UNIVERSITÀ DEGLI STUDI DI PADOVA

Università degli Studi di Padova

Dipartimento di Fisica e Astronomia "Galileo Galilei"

Ph.D. Course in Physics - XXXVI cycle

Studies on neutrino oscillation parameters Δm_{21}^2 and $\sin^2\theta_{12}$ at nuclear reactors with the JUNO experiment

Coordinator:
Prof. Giulio Monaco

Supervisor:
Prof. Marco Grassi

Ph.D. Candidate:
Beatrice Jelmini

To the people I love
To the people I know
To the people I've just met
To the people I'll cross paths with

To my people

Abstract

Neutrino oscillations are a well-established quantum phenomenon and have been experimentally verified by many different experiments in the last decades. There are still open questions on the topic; one of them is the determination of the neutrino mass ordering (NMO). To address this question, the Jiangmen Underground Neutrino Observatory (JUNO) has been proposed and is currently under construction in China. Furthermore, JUNO is expected to reach an unprecedented sub-percent precision in the measurement of three of the oscillation parameters that are used to model neutrino oscillations. In this work, we focus on some experimental issues relevant to the neutrino oscillation analysis and provide the expected JUNO precision in the measurement of the *solar* oscillation parameters, Δm_{21}^2 and $\sin^2 \theta_{12}$.

JUNO will detect electron antineutrinos ($\overline{\nu}_e$) produced inside nuclear reactors as a by-product of the fission processes happening inside the cores. A good understanding and modelling of the source are of paramount importance, even though it constitutes a great challenge. In this work, we present a model of the reactor spectrum and flux which accounts for all recent measurements from short-baseline reactor experiments, which show discrepancies with respect to the various models available in the literature.

The neutrino oscillation analysis relies on the calorimetric measurement of the energy of the electron antineutrinos. The interaction of an $\overline{\nu}_e$ with the liquid scintillator target mass is followed by the emission of scintillation and Cherenkov light; the light is detected by a system of PMTs generating a signal which is finally processed by the front-end and readout electronics. Any non-linear behavior in this chain of processes could distort the spectrum and lead to a wrong determination of the NMO and to biases in the measurement of the oscillation parameters. A known source of non-linearity is the intrinsic non-linearity in the emission of light by the liquid scintillator, which is mainly due to the quenching effect. In this work, we propose a model, based on Geant4, to describe the non-linear relation between the energy deposited in the detector by the antineutrino and the emitted light. Another known source of non-linearity is the instrumental non-linearity of the PMT system and of the readout electronics, thus a thorough characterization of the two hardware systems is of paramount importance. A test protocol was developed and used to thoroughly characterize the readout electronics during mass production; the test protocol is presented in detail.

Finally, we provide JUNO expected sensitivity to the measurement of Δm_{21}^2 and $\sin^2 \theta_{12}$ after the first year of data-taking; the impact of the main sources of systematic uncertainties is also investigated.

Contents

List of Figures

List of Tables

Introduction

Neutrino oscillations are a well-established quantum phenomenon and have been experimentally verified by many different experiments in the last decades, as briefly presented in the first part of chapter 1. Furthermore, the 2015 Nobel Prize in Physics was awarded *"for the discovery of neutrino oscillations, which shows that neutrinos have mass"*. The phenomenon of neutrino oscillations is based on the difference between the flavor eigenstates, ν_α, which are produced and detected through weak interactions, and the mass eigenstates, ν_i, which propagate in the vacuum or in matter according to the Schroedinger equation. A neutrino produced with flavor α can thus be detected as a neutrino with flavor β with the probability $P(\nu_\alpha \to \nu_\beta)$, derived in the second part of chapter 1, which depends on the neutrino energy and the distance between the source and the detector and displays an oscillatory behavior. The oscillation probability depends on three mixing angles, θ_{ij}, which parametrize the mixing between the flavor and mass eigenstates, and three mass-squared differences, $\Delta m_{ij}^2 = m_i^2 - m_j^2$, with m_i being the mass of the mass eigenstate ν_i, which determine the frequencies of the oscillatory pattern.

The Jiangmen Underground Neutrino Observatory (JUNO) is a multi-purpose experiment, currently under construction in China, that will detect electron antineutrinos from reactors with the main goal of improving our knowledge of neutrino oscillations. Indeed, JUNO is expected to measure three of the oscillation parameters (Δm_{21}^2, Δm_{31}^2, and $\sin^2 \theta_{12}$) with an unprecedented sub-percent precision and to determine the neutrino mass ordering, *i.e.*, the order of the masses of the three mass eigenstates, with a 3σ significance in about six years of data-taking. The JUNO experiment is introduced in chapter 2.

This work aims to estimate the expected precision that the JUNO experiment can reach in the measurement of the *solar* oscillation parameters, Δm_{21}^2 and $\sin^2 \theta_{12}$, after one year of data-taking. To this end, I focused on some experimental issues relevant to the analysis that could possibly spoil JUNO results if not properly addressed.

In the analysis of the reactor electron antineutrino spectrum, a good understanding and modelling of the source is of paramount importance. Reactor electron antineutrinos are produced inside nuclear cores from the β decays of neutron-rich fission products from the fission of four main isotopes: ^{235}U, ^{239}Pu, ^{238}U, and ^{241}Pu. The proper modelling of the antineutrino flux and spectrum from reactors constitutes a great challenge, because we have only partial knowledge of all the processes happening inside a nuclear reactor, and the nuclear databases used to evaluate a prediction are incomplete. Furthermore, recent measurements

from short-baseline reactor experiments show discrepancies with respect to the various models available in literature. I worked on the evaluation of a model of the reactor spectrum and flux which accounts for all recent measurements and is needed to achieve JUNO ambitious physics goals; this work is presented in chapter 3. I also propose a treatment of the uncertainties based on covariance matrices, even though further studies should be carried out.

The neutrino oscillation analysis relies on the measurement of the energy of antineutrinos coming from nuclear reactors; in fact, JUNO can be considered as a calorimeter. The interaction of an electron antineutrino with the liquid scintillator target mass is followed by the emission of scintillation and Cherenkov light; the light propagates and is detected by a system of PMTs generating a signal which is finally processed by the front-end and readout electronics, before being stored. Any non-linear behaviour in this chain of processes could distort the oscillatory pattern of the spectrum and lead to a wrong determination of the neutrino mass ordering and in biases in the measurement of the oscillation parameters.

The quenching effect of the liquid scintillator is responsible for a non-linear relation between the antineutrino energy and the amount of emitted light. I developed a model based on Geant4 which describes the non-linearity due to quenching of electrons, gammas, and positrons; the model is presented in chapter 4. The model has only one free parameter, which is also a parameter used in the JUNO Monte Carlo simulation software. By means of the calibration data from γ sources, the model could also be used to fine tune the value of this parameter in the simulation framework.

An additional source of non-linearity is given by the instrumentation used to detect the light and process the signal: the PMTs and the readout electronics; in this work, I focus only on the latter. To estimate the possible non-linearity of the electronics, a thorough characterization of all boards was carried out in parallel to mass production. The test protocol which I developed for the mass testing is described in chapter 5.

Finally, in chapter 6 I present the analysis of the reactor antineutrino spectrum and provide JUNO expected sensitivity after one year of data-taking for the measurement of the *solar* oscillation parameters, Δm_{21}^2 and $\sin^2 \theta_{12}$. I also investigated in detail the impact of the background uncertainties and of the uncertainty on the reactor flux. After one year of data-taking, JUNO is expected to reach a sub-percent precision on the measurement of Δm_{21}^2, and significantly improve the current precision on $\sin^2 \theta_{12}$.

Chapter 1

History and theory of neutrino oscillations

The phenomenon of *neutrino oscillations* is a quantum effect that has been experimentally confirmed and studied in the last few decades. In fact, the Nobel Prize in Physics 2015 was awarded to Takaaki Kajita, from the Super-Kamiokande experiment in Japan, and to Arthur B. McDonald, from the SNO experiment in Canada, *"for the discovery of neutrino oscillations, which shows that neutrinos have mass"* [1].

In section 1.1, we present the historical developments and the most important experimental results that led to the discovery and verification of neutrino oscillations. Then, in section 1.2, we discuss the theoretical 3-ν oscillation framework and provide the evaluation of the oscillation probability in vacuum and in matter. Finally, in section 1.2.3, we present some open questions concerning neutrino oscillations and massive neutrinos, which will be addressed with the new generation of experiments, such as the JUNO experiment.

For further reference about both the theoretical treatment and the historical background, see M. Tanabashi *et al.*, *Review of Particle Physics* [2, Chap. 14].

1.1 A bit of history

We now propose a brief historical description of the most important achievements in the field of neutrino oscillations. We start by presenting the solar neutrino problem (SNP) and the atmospheric neutrino anomaly which arose from the first experiments detecting solar and atmospheric neutrinos, respectively. Then, we point out how both problems could be solved with neutrino oscillations and present some experimental verification for these solutions. Then, we briefly introduce neutrino experiments at accelerators, which constitute a complementary approach to experiments at nuclear reactors, to which the JUNO experiment belongs.

1.1.1   The solar neutrino problem and its solution

Solar neutrinos are produced by thermonuclear reactions that take place inside the sun. The reactions are part of the pp chain and CNO cycle, which fuse four protons to produce an helium atom with the emission of two positrons and two electron neutrinos: $4p \rightarrow {}^4\text{He} + 2e^+ + 2\nu_e$. The fluxes of neutrinos emitted in the various reactions of the chain are displayed in Fig. 1.1, where the fluxes are prediction from the Standard Solar Model (SSM), initially developed by J. Bahcall [3]. The model describes the structure and evolution of the sun and, before the first solar neutrino experiment, was strongly supported by data from helioseismology.

The first experiment that tried to detect solar neutrinos was Homestake by R. Davis, Jr., in the late 1960s [4]. Homestake employed a radiochemical technique and was able to measure the rate of solar neutrinos integrated over time. The detector was filled with C_2Cl_4 and neutrinos were detected through the following reaction: $\nu_e + {}^{37}\text{Cl} \rightarrow e^- + {}^{37}\text{Ar}$. The produced argon was then chemically extracted, and the Auger electrons emitted from electron capture of ^{37}Ar were counted in a low-background proportional chamber. Since the threshold of the neutrino capture by ^{37}Cl is 814 keV, Homestake was mainly sensitive to the ^{7}Be and ^{8}B neutrinos (see Fig. 1.1). The final measured rate was 2.56 SNU, about a third of the SSM prediction of 8.46 SNU, where $1\,\text{SNU} = 10^{-36}$ captures/s/atom. The discrepancy between the measured and predicted values was known as the *solar neutrino problem* (SNP).
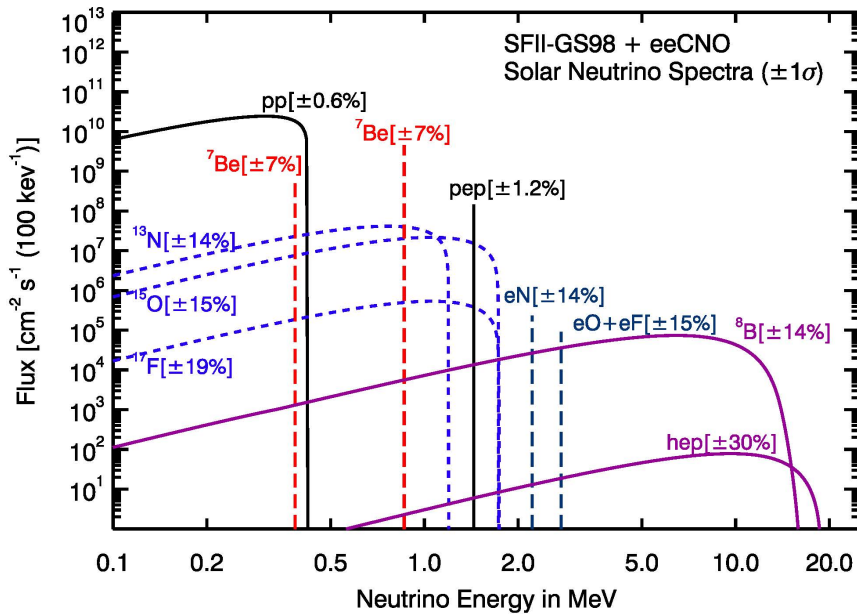
Figure 1.1. Spectrum of solar neutrino fluxes predicted by recent Standard Solar Model calculation [5].

A lower energy threshold could be reached in radiochemical experiments that employed gallium and detected neutrinos through the following reaction: $\nu_e + {}^{71}\text{Ga} \rightarrow e^- + {}^{71}\text{Ge}$. The threshold of this reaction is 233 keV, so experiments with gallium allowed for the detection of pp neutrinos, which have the most abundant flux according to the SSM (see Fig. 1.1). Two experiments employed gallium: the SAGE experiment [6] in Baksan, Russia, used about 50 t of liquid metallic gallium

as a target; the GALLEX experiment [7] at Laboratori Nazionali del Gran Sasso (LNGS), Italy, used 101 t of GaCl$_3$, containing a total of 30.3 t of gallium. Both experiments observed almost half of the expected capture rate of solar neutrinos, with a measured value of 65.4 SNU for SAGE and 69.3 SNU for GALLEX, against a predicted value of 127.9 SNU.

The deficit measured by the radiochemical experiments with gallium supported the SNP. Therefore, either the SSM was wrong, although supported by helioseismology, or something was happening to the neutrinos while traveling from the production point inside the sun to the Earth. Combined with the results of the Homestake experiment with chlorine, SAGE and GALLEX results pointed out that the deficit of the measurements with respect to the prediction is energy-dependent. Radiochemical experiments are limited by the fact that they measure a rate integrated in time and cannot provide any directional information.

Kamiokande and Super-Kamiokande

The Kamiokande experiment [8], in Japan, was the first experiment to realize real-time measurements of solar neutrinos and consisted of a 3000-t water Cherenkov detector, with a 6.5 MeV energy threshold, thus being sensitive only to ^{8}B neutrinos. Solar neutrinos were detected through elastic scattering (ES) on the electrons of the detector: $\nu_x + e^- \to \nu_x + e^-$. With respect to radiochemical experiments, Kamiokande could detect all neutrino flavors since the ES reaction occurs via both charged and neutral current weak interactions. The successor of Kamiokande, the Super-Kamiokande (Super-K) [9] experiment, consists of a water Cherenkov detector with 50 kt of pure water and is characterized by an energy threshold of 3.5 MeV, thus it is sensitive only to ^{8}B neutrinos. Super-K is still taking data and its latest results (2016 [10]) show a measured flux of $2.345 \cdot 10^6 \, \mathrm{cm}^{-2} \, \mathrm{s}^{-1}$, compared to a SSM prediction of $5.46 \cdot 10^6 \, \mathrm{cm}^{-2} \, \mathrm{s}^{-1}$, thus providing a confirmation of the results from the radiochemical experiments. Furthermore, since Kamiokande and Super-K are able to reconstruct the trajectory of the recoil electron and, thus, provide directional information on the incoming neutrino, they showed for the first time that the detected neutrinos were indeed coming from the sun.

SNO

The Sudbury Neutrino Observatory (SNO) was an experiment in Canada and consisted of 1000 t of heavy water (D$_2$O). Thanks to the presence of the deuterium, SNO was able to detect solar neutrinos via three interactions:

- Elastic scattering (ES) with an electron, $\nu_x + e^- \to \nu_x + e^-$, via both charged and neutral current interactions, as in Kamiokande. Since the electron neutrino is the only one interacting through charged current, ν_e has a total cross section about six times greater than that of ν_μ and ν_τ, so a combined flux of all flavors is measured: $\phi_{\mathrm{ES}} = \phi(\nu_e) + 0.15 \, (\phi(\nu_\mu) + \phi(\nu_\tau))$.

- Charged current (CC) interaction with the deuteron: $\nu_e + d \to p + p + e^-$. Only electron neutrinos can be detected through this channel, thus

     providing a measurement of the electronic component of the flux: $\phi_{\mathrm{CC}} = \phi(\nu_e)$.

- Neutral current (NC) interaction with the deuteron: $\nu_x + d \to p + n + \nu_x$. The energy required to break apart the deuteron is about $2\,\mathrm{MeV}$ and the reaction is sensitive to all neutrino flavors with equal cross section, thus providing a measurement of the total flux: $\phi_{\mathrm{NC}} = \phi(\nu_e) + \phi(\nu_\mu) + \phi(\nu_\tau)$.

Due to the threshold of about $2\,\mathrm{MeV}$, SNO was sensitive only to $^8\mathrm{B}$ neutrinos.

The total flux of the $^8\mathrm{B}$ neutrinos measured by SNO, $\phi_{\mathrm{NC}} = 5.25{\cdot}10^6\,\mathrm{cm}^{-2}\,\mathrm{s}^{-1}$, was finally in agreement with the SSM prediction, thus suggesting that something was happening to the neutrinos before reaching the Earth. The NC results of 2002 [11] established the existence of a non-ν_e component in the solar neutrino flux and provided an explanation for the low measured rate in the previous experiments: some of the ν_e's produced inside the sun oscillate into ν_μ's or ν_τ's before reaching the Earth. The solution to the solar neutrino problem is thus neutrino oscillations in matter. The flavor transition $\nu_e \to \nu_\mu, \nu_\tau$ is indeed favored by the high electron density in the inner part of the sun, and can be described with a mass-squared difference $\Delta m^2 \sim 7.5 \cdot 10^{-5}\,\mathrm{eV}^2$ and a mixing angle $\sin^2\theta \sim 0.3$.

Borexino

The Borexino experiment at LNGS, Italy, provided further confirmation of the solution to the solar neutrino problem. The detector consisted of $300\,\mathrm{t}$ of ultra-pure liquid scintillator with an energy resolution of $5\,\%$ at $1\,\mathrm{MeV}$ and an energy threshold of $0.19\,\mathrm{MeV}$. It detected solar neutrinos via the elastic ν-e scattering in real time. Thanks to the very low energy threshold, the experiment reported the first real-time detection of $^7\mathrm{Be}$ neutrinos. Borexino also measured for the first time the fluxes of pp and pep neutrinos, with measured fluxes of $\phi_{\mathrm{pp}} = 6.1{\cdot}10^{10}\,\mathrm{cm}^{-2}\,\mathrm{s}^{-1}$ and $\phi_{\mathrm{pep}} = 1.27{\cdot}10^8\,\mathrm{cm}^{-2}\,\mathrm{s}^{-1}$ [12], respectively, and neutrinos from the CNO cycle, with a measured flux of $\phi_{\mathrm{CNO}} = 6.7 \cdot 10^8\,\mathrm{cm}^{-2}\,\mathrm{s}^{-1}$ [13].

Together with the data from other solar experiments, Borexino's data are important to study the matter effect in neutrino oscillations, and its measurement [14, 15] of the various solar neutrino fluxes have been proven consistent with the solution to the solar neutrino problem.

1.1.2   The atmospheric neutrino anomaly and its solution

Atmospheric neutrinos are produced by the decay of hadrons generated in the interactions of the cosmic rays with the Earth's atmosphere. The decay of pions constitute the dominant decay chain:

$$\pi^+ \to \mu^+ + \nu_\mu \qquad \mu^+ \to e^+ + \nu_e + \bar{\nu}_\mu,$$
$$\pi^- \to \mu^- + \bar{\nu}_\mu \qquad \mu^- \to e^- + \bar{\nu}_e + \nu_\mu.$$

From these decay chain, the ratio of the number of neutrinos of muonic flavor over the number of neutrinos of electronic flavor, $R = (\nu_\mu + \bar{\nu}_\mu)/(\nu_e + \bar{\nu}_e)$, is expected to be equal to 2 at low energies ($\sim 1\,\mathrm{GeV}$).

Detectors for atmospheric neutrinos are located on or just below the Earth's surface. Since atmospheric neutrinos are produced everywhere in the atmosphere, their flight distance can vary from 15 km for neutrinos produced above the detector (downward-going), to about 13 000 km for those produced on the other side of the planet and traveling through the Earth (upward-going). One can expect that the zenith angle distributions (the path length distribution) between downward-going and upward-going neutrinos are symmetric for energy above 1 GeV.

In order to reduce the uncertainty, early experiments reported a double ratio, *i.e.*, the ratio between the observed and expected value of the ratio R: $\tilde{R} = R_{\mathrm{obs}}/R_{\mathrm{exp}}$, which is anticipated to be equal to 1. Early atmospheric neutrino experiments reported a significantly lower value of $\tilde{R}$, which suggested either a deficit in the number of ν_μ's, or an excess in the number of ν_e's, or both; this is the so-called *atmospheric neutrino anomaly*.

Kamiokande [16] was among these experiments and also provided a first indication of the zenith angle dependence of the muon disappearance probability, but the results were not conclusive.

Super-Kamiokande

Super-Kamiokande provided a solution to the atmospheric neutrino anomaly. In 1998, it reported evidence for neutrino oscillations in atmospheric neutrinos [17] by measuring the zenith angle distribution.

The observed events were divided into e-like and μ-like events, based on the flavor identification of the final-state charged lepton following a neutrino interaction; each category was further divided into different energy ranges. The results showed that the observed zenith angle distributions for the e-like events were in agreement with the expectation at all energies, thus excluding the idea of an excess of ν_e's as an explanation for the atmospheric ν anomaly. On the other hand, the distribution for the μ-like events deviated significantly from the expectation. The results pointed out a deficit of upward-going events, which was also energy-dependent.

The atmospheric neutrino anomaly can be explained with the flavor transition $\nu_\mu \to \nu_\tau$ as the dominant oscillation mode in atmospheric neutrinos; since Super-K cannot detect ν_τ's, it cannot provide direct evidence for this. The asymmetry in the zenith angle distribution can be explained by the fact that the baseline for downward-going neutrinos is too short for the oscillation to occur, while upward-going neutrinos have a long enough baseline. The corresponding oscillation parameters were found to be $\Delta m^2 \sim 2.5 \cdot 10^{-3}\,\mathrm{eV}^2$ and $\theta \sim 45°$. Super-K's results were confirmed by other atmospheric neutrino observations.

The fact that $\nu_\mu \to \nu_\tau$ is the dominant oscillation mode for atmospheric neutrinos has been verified only recently by the OPERA experiment through the detection of accelerator neutrinos, as explained in the next section.

1.1.3 Neutrino experiments at accelerators

For experiments at accelerators, the neutrino beam is obtained by accelerating protons and by colliding them onto a target, thus producing pions and kaons

which then decay into neutrinos. Given that pions are the most abundant product, the neutrino beam is mainly composed of either muon neutrinos or antineutrinos, depending on whether positive or negative pions are selected. In fact, it is possible to select the dominant composition of the beam by inverting the direction of current in the magnetic horns, which are also used to focus the pion and kaon beam. Experiments can thus study the disappearance of muon (anti-)neutrinos and the appearance of electron (anti-)neutrinos. The neutrino beam is produced with an energy of the order of $1\,\mathrm{GeV}$ to $10\,\mathrm{GeV}$. Given that the first oscillation maximum driven by the atmospheric mass splitting is at $L/E \approx 500\,\mathrm{km/GeV}$, the baseline of experiments at accelerators ranges from a few hundreds to thousand of kilometer.

The first generation of experiments, like K2K, MINOS, and OPERA, was mainly meant to confirm the existence of neutrino oscillations and study the physics of atmospheric neutrino oscillations; as an example, we briefly mention the OPERA experiment, since it was the first one observing ν_τ appearing in a ν_μ beam. A second generation of experiments, comprising T2K and Noνa, has been built with the main goal to search for CP violation in neutrino oscillations. DUNE and Hyper-Kamiokande, which are currently under construction, constitute the third generation of experiments at accelerators, and besides the further investigation of long-baseline neutrino oscillations, they will have a rich physics program.

Experiments at accelerators also have the sensitivity to determine the neutrino mass ordering by exploiting the matter effect, providing a complementary approach to the determination in the vacuum which can be achieved with a reactor experiment like JUNO (see next section).

OPERA

The OPERA experiment was a long-baseline experiment installed at LNGS and used the CERN Neutrinos to Gran Sasso (CNGS) beamline to study the appearance of ν_τ's in a beam of ν_μ's. The CNGS neutrino beamline provided a neutrino beam with energy of the order of $10\,\mathrm{GeV}$ from CERN to LNGS for a baseline of about $732\,\mathrm{km}$. The latest results from 2018 [18] reported the observation of ν_τ events, thus confirming that the oscillation mode $\nu_\mu \to \nu_\tau$ is the dominant one for atmospheric neutrinos. OPERA's results also suggests a $\Delta m^2 \sim 2.7 \cdot 10^{-3}\,\mathrm{eV}^2$ for the atmospheric sector, consistent with other oscillation experiments.

1.1.4   Oscillation experiments at nuclear reactors

Nuclear reactors are very intense sources of electron antineutrinos produced inside the cores by β decay of fission fragments, with a flux of $2 \cdot 10^{20}$ $\bar{\nu}_e$ per second per GW of thermal power. Oscillation experiments at nuclear reactors employ a liquid scintillator contained in a spherical or cylindrical vessel as the primary antineutrino target, and exploit the inverse beta decay as the detection process: $\bar{\nu}_e + p \to e^+ + n$ (more details on the interaction mechanism are provided in the next chapters). Experiments at nuclear reactors are disappearance experiments

and are used to investigate the survival probability $P(\bar{\nu}_e \rightarrow \bar{\nu}_e)$, that will be derived in section 1.2.2.

A list of past, current, and future reactor experiments with a baseline greater than 1 km is reported in Table 1.1; the reactor thermal power, the baseline, and the detector target mass are also listed. Among experiments at reactors, KamLAND can be considered as a long-baseline experiment, with an average baseline of $L = 180$ km. Since the neutrino flux from reactors is isotropic and decreases with the baseline as L^{-2}, experiments with baseline longer than a few hundred kilometers suffer from low statistics; if longer baselines are needed, oscillation experiments with accelerator neutrinos should be employed (see section 1.1.3). Double Chooz (France), RENO (Korea), and Daya Bay (China) are short-baseline experiments with $L \sim O(1 \text{ km})$ and provided the first measurement of θ_{13} in 2012; we briefly present Daya Bay only, since we will use its latest results in chapter 3. JUNO, with a mean baseline of about $L \sim 50$ km, can be considered as a medium-baseline experiment.

There are also several experiments with a very short baseline, ~ 10 m, built with the main goal to investigate oscillations at a scale of $\delta m^2 \sim 1 \text{ eV}^2$), involving a fourth neutrino beyond the 3-ν oscillation framework presented in section 1.2. In the context of the study presented in this manuscript, we are not interested in physics beyond the 3-ν oscillation framework; nonetheless it is worth mentioning very short baseline experiments at reactors because, as a secondary results, they can provide a precise measurement of the reactor antineutrino spectrum, as it will be mentioned in chapter 3.

Table 1.1. List of experiments which study neutrino oscillations with reactor antineutrinos, with a baseline greater than 1 km [2].

Name	Reactor power [GW]	Baseline L [km]	Detector mass [t]	Year
KamLAND	various	180 (avg.)	1000	2001 –
Double Chooz	4.25×2	1.05	8.3	2011 – 2018
RENO	2.9×6	1.65	20×4	2011 – 2020
Daya Bay	2.8×6	1.38	16	2011 –
JUNO	26.6 (tot.)	53 (avg.)	20 000	2024 (exp.) –

KamLAND

The KamLAND experiment is located in the Kamioka mine in Japan and can detect electron antineutrinos from more than 50 nuclear power stations with a flux-weighted average baseline $L_0 = 180$ km. The detector consists of 1000 t of ultra-pure liquid scintillator contained in a 13-m diameter spherical balloon [19]. The detector is instrumented with an array of 1879 PMTs, with a total photo-cathode coverage of 34 % and an energy resolution of $\sim 7.5 \%/\sqrt{E[\text{MeV}]}$.

In 2002 [19], KamLAND provided evidence for reactor $\bar{\nu}_e$ disappearance at 99.95 % confidence level and provided a measurement of the solar oscillation parameters, Δm_{21}^2 and $\sin^2 \theta_{12}$, complementary to the measurement by solar exper-

iments. It was also the first experiment to provide a first "picture" of neutrino oscillations, thanks to the wide range of baselines, as shown in Fig. 1.2 [20]. The figure shows the ratio of the observed $\bar{\nu}_e$ spectrum to the expectation spectrum in the hypothesis of no-oscillation as a function of L_0/E: a clear oscillatory signature can be seen.
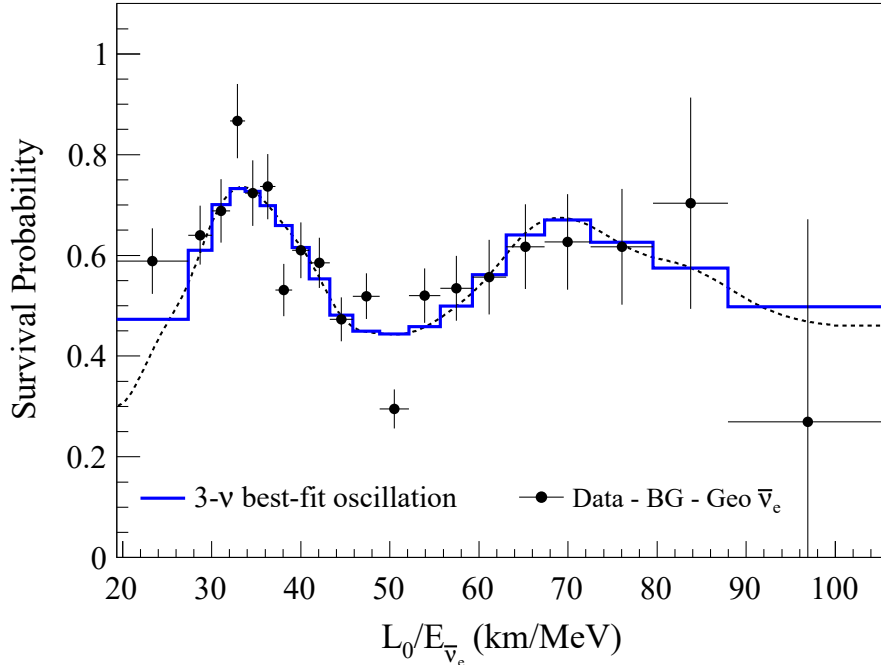
Figure 1.2. Ratio of the observed $\bar{\nu}_e$ spectrum to the expectation in the hypothesis of no oscillation as a function of L_0/E for the KamLAND data. $L_0 = 180\,\text{km}$ is the flux-weighted average reactor baseline [20].

Daya Bay

The Daya Bay (DYB) experiment is located in China and consists of several antineutrino detectors (ADs) positioned in a near and a far sites [21]. The use of a near and a far site allows for the cancellation of reactor-related systematic uncertainties and part of the detection-related ones. At the near site, the ADs are not sensitive to neutrino oscillations, while at the far site, the ADs are able to see a deficit in the neutrino spectrum due to neutrino oscillations. As the far site is concerned, DYB consists of four detectors, containing 20 t of gadolinium-doped LS each, at a baseline of 1.65 km. Light generated by the IBD interactions inside the liquid scintillator target are detected by about 200 PMTs and with an energy resolution of $(7.5/\sqrt{E[\text{MeV}]} + 0.9)\%$.

Due to the short baseline $L \sim O(1\,\text{km})$, the survival probability depends only on one mixing angle and one mass splitting, which are parameters used to describe neutrino oscillations, as it will be explained in section 1.2. Short-baseline reactor experiments, like Daya Bay, are thus sensitive only to the atmospheric component of the oscillations and are suitable for a precise measurement of θ_{13}.

In 2012, DYB [21], together with the Double Chooz [22] and RENO [23] experiments, reported an indication of reactor electron antineutrinos disappearance

and established a non-zero value of θ_{13}. They reported the ratio of observed values over the prediction with no oscillation; the ratio from DYB [24] is shown in Fig. 1.3, together with the detected spectrum.
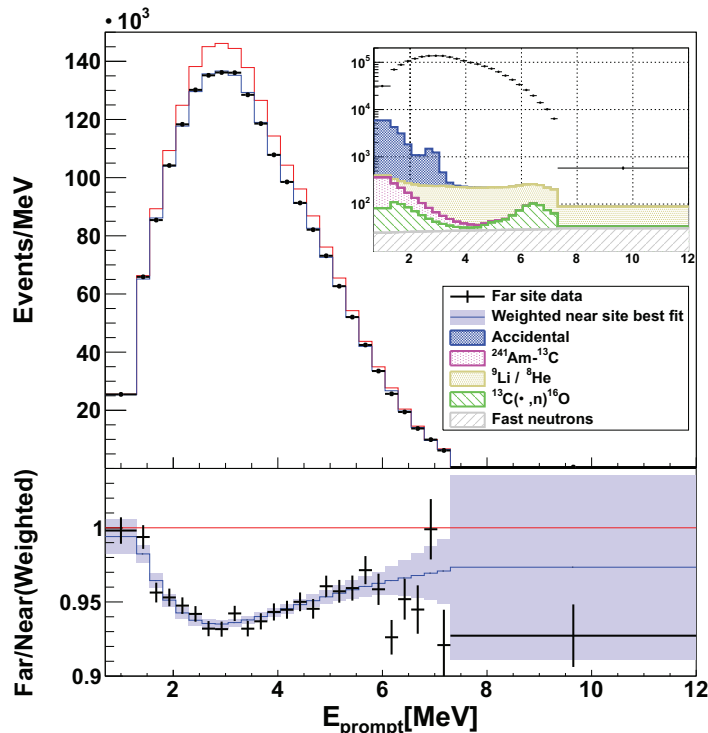
Figure 1.3. The background-subtracted spectrum at the far site (black points) and the expectation derived from near-site measurements excluding (red line) or including (blue line) the best-fit oscillation. The bottom panel shows the ratios of data over predictions with no oscillation. The inset shows the background components on a logarithmic scale [24].

JUNO

The JUNO experiment, with a mean baseline of 52.5 km and an expected resolution of 3 % at 1 MeV, has a significant sensitivity to the determination of the neutrino mass ordering and has been mainly proposed to achieve this physics goal. Chapter 2 is devoted to a thorough description of the experiment and its physics prospects beyond the reactor electron antineutrino analysis.

1.2 3-ν oscillation framework

In the Standard Model (SM) of particle physics, neutrinos are fermions and interact only through weak interactions. Neutrinos and antineutrinos are described as spin-1/2 left-handed and right-handed leptons, respectively, and are massless.

With respect to the symmetry group $SU(2)_L$ which describes the weak interactions, neutrinos are spin-1/2 left-handed leptons and are part of a doublet

together with the respective left-handed charged lepton; there are three families of left-handed leptons:

$$\begin{pmatrix} \nu_e \\ e \end{pmatrix}_{\mathrm{L}}, \quad \begin{pmatrix} \nu_\mu \\ \mu \end{pmatrix}_{\mathrm{L}}, \quad \begin{pmatrix} \nu_\tau \\ \tau \end{pmatrix}_{\mathrm{L}}.$$

Neutrinos are produced in weak interactions with a definite flavor, that is, they are flavor eigenstates and are always produced with, or absorbed to give, a charged lepton of the same flavor; flavor eigenstates are labeled ν_e, ν_μ, and ν_τ. Since the mass eigenstates differ from the flavor eigenstates, a neutrino can be produced at the source with a flavor and be detected with a different one after traveling a distance L: this phenomenon is known as *neutrino oscillations*. Mass eigenstates are usually labeled ν_1, ν_2, and ν_3 and have mass m_1, m_2, and m_3, respectively.

Neutrino oscillations have been observed by various experiments in the last decades and solved both the solar neutrino problem and the atmospheric neutrino anomaly, as described in section 1.1. For the oscillations to occur, neutrinos must be massive, so every attempt to introduce massive neutrinos leads to an extension of the SM.

In the rest of this manuscript, we work in natural units, thus $c = \hbar = 1$.

1.2.1   The mixing matrix

The minimal model that can explain the experimental observations of neutrino oscillations requires the mixing between the three ν flavors of the SM and the three distinct mass eigenstates:

$$\begin{pmatrix} \nu_e \\ \nu_\mu \\ \nu_\tau \end{pmatrix} = U_{\mathrm{PMNS}} \begin{pmatrix} \nu_1 \\ \nu_2 \\ \nu_3 \end{pmatrix}, \tag{1.1}$$

where U is the 3×3 complex mixing matrix, whose general expression is:

$$U_{\mathrm{PMNS}} = \begin{pmatrix} U_{e1} & U_{e2} & U_{e3} \\ U_{\mu 1} & U_{\mu 2} & U_{\mu 3} \\ U_{\tau 1} & U_{\tau 2} & U_{\tau 3} \end{pmatrix}. \tag{1.2}$$

The neutrino mixing matrix U is analogous to the CKM matrix that describes the mixing between quarks: the matrix can be written following a standard parameterization as a sequence of three rotation matrices and a complex phase with a total of four independent parameters. Since the Dirac or Majorana nature of the neutrino is yet to be established, a matrix with two complex phases is added to the parameterization. Thus, the final form is:

$$U = \begin{pmatrix} 1 & 0 & 0 \\ 0 & c_{23} & s_{23} \\ 0 & -s_{23} & c_{23} \end{pmatrix} \cdot \begin{pmatrix} c_{13} & 0 & s_{13}\,e^{-i\delta_{\mathrm{CP}}} \\ 0 & 1 & 0 \\ -s_{13}\,e^{i\delta_{\mathrm{CP}}} & 0 & c_{13} \end{pmatrix} \cdot \begin{pmatrix} c_{12} & s_{12} & 0 \\ -s_{12} & c_{12} & 0 \\ 0 & 0 & 1 \end{pmatrix} \cdot$$
$$\cdot \begin{pmatrix} e^{i\eta_1} & 0 & 0 \\ 0 & e^{i\eta_2} & 0 \\ 0 & 0 & 1 \end{pmatrix}, \tag{1.3}$$

where $c_{ij} = \cos\theta_{ij}$ and $s_{ij} = \sin\theta_{ij}$. The matrix U has a total of six independent parameters: θ_{12}, θ_{13}, and θ_{23} are the three mixing angles; δ_{CP} is the CP-violation phase which accounts for a possible violation of the CP symmetry by the weak interaction in the lepton sector; η_1 and η_2 are the two Majorana phases which have physical meaning only if the neutrino is a Majorana particle and play no role in neutrino oscillations, so they are neglected in the rest of this work.

After multiplying the matrices, the matrix U for ν oscillations can be written as:

$$U = \begin{pmatrix} c_{12}c_{13} & s_{12}c_{13} & s_{13}\,e^{-i\delta_{CP}} \\ -s_{12}c_{23} - c_{12}s_{23}s_{13}\,e^{i\delta_{CP}} & c_{12}c_{23} - s_{12}s_{23}s_{13}\,e^{i\delta_{CP}} & s_{23}c_{13} \\ s_{12}s_{23} - c_{12}c_{23}s_{13}\,e^{i\delta_{CP}} & -c_{12}s_{23} - s_{12}c_{23}s_{13}\,e^{i\delta_{CP}} & c_{23}s_{13} \end{pmatrix}. \quad (1.4)$$

This matrix is also referred to as the Pontecorvo-Maki-Nakagawa-Sakata (PMNS) mixing matrix.

In the case of three Dirac neutrinos, the matrix U is unitary, hence satisfies the following requirement:

$$U^\dagger U = I, \qquad \text{or} \quad U^\dagger = U^{-1} = (U^*)^T.$$

This is not true in the case of three Majorana neutrinos. However, since the deviation from unitarity is small, for all practical purposes, U is unitary independently of whether neutrinos are Dirac or Majorana particles [2, Chap. 14, p. 8].

1.2.2   Calculation of the oscillation probability

To compute the expression of the oscillation probability [25], we first calculate the most general survival probability in the vacuum; then, the equation for the case of the JUNO experiment, which we are interested in, is given; finally, we include the matter effect.

A neutrino produced at the source (at space-time point $x = 0 = (0,0)$) with flavor α is a linear coherent superposition of the mass eigenstates:

$$|\nu_\alpha(0)\rangle = \sum_k U_{\alpha k} |\nu_k(0)\rangle, \quad (1.5)$$

where U is the unitary mixing matrix of Eq. (1.4). In what follows, a Greek index is used to identify flavor eigenstates, $\nu_\alpha \equiv \nu_e, \nu_\mu, \nu_\tau$, while a Latin index is used for mass eigenstates, $\nu_k \equiv \nu_1, \nu_2, \nu_3$.

The mass eigenstates propagate according to the Schroedinger equation:

$$i\frac{\partial}{\partial t}|\nu_k(x)\rangle = -\frac{1}{2m_k}\frac{\partial^2}{\partial x^2}|\nu_k(x)\rangle, \quad \text{for } k = 1,2,3. \quad (1.6)$$

No potential is considered in the equation since, for now, we are interested in neutrino oscillations in the vacuum. Solutions to this equation are plane waves:

$$|\nu_k(x)\rangle = e^{-i(E_k t - \boldsymbol{p}_k \cdot \boldsymbol{x})}|\nu_k(0)\rangle = e^{-i\phi_k}|\nu_k(0)\rangle, \quad \text{for } k = 1,2,3, \quad (1.7)$$

where we defined the phase $\phi_k = p_k x$, with $p_k = (E_k, \boldsymbol{p}_k)$ the 4-momentum of the neutrino mass state ν_k and $x = (t, \boldsymbol{x})$ the space-time vector.

The evolution of the initial state with flavor α is thus:

$$|\nu_\alpha(x)\rangle = \sum_k U_{\alpha k} |\nu_k(x)\rangle = \sum_k U_{\alpha k} \, e^{-i\phi_k} |\nu_k(0)\rangle. \tag{1.8}$$

By inverting Eq. (1.5), we can express the mass eigenstates as a linear combination of the flavor eigenstates:

$$|\nu_k(0)\rangle = \sum_\gamma U_{\gamma k}^* |\nu_\gamma(0)\rangle. \tag{1.9}$$

By using Eq. (1.9), we can rewrite Eq. (1.8) by expressing the flavor state α at a space-time point $x = (t, \boldsymbol{x})$ in terms of the flavor eigenstates at the source:

$$|\nu_\alpha(x)\rangle = \sum_\gamma \sum_k U_{\alpha k} \, e^{-i\phi_k} U_{\gamma k}^* |\nu_\gamma(0)\rangle. \tag{1.10}$$

Finally, we can write the transition amplitude for the detection of a neutrino of flavor β at a distance L from the source, where a neutrino of flavor α was originally produced:

$$\begin{aligned}
A(\nu_\alpha(0) \to \nu_\beta(L)) &= \langle \nu_\beta(L) \,|\, \nu_\alpha(0) \rangle \\
&= \sum_\gamma \sum_k U_{\beta k}^* \, e^{+i\phi_k} U_{\gamma k} \langle \nu_\gamma(0) \,|\, \nu_\alpha(0) \rangle \\
&= \sum_k U_{\beta k}^* \, e^{+i\phi_k} U_{\alpha k}.
\end{aligned} \tag{1.11}$$

where we used the orthogonality of the flavor states, $\langle \nu_\gamma(0) \,|\, \nu_\alpha(0) \rangle = \delta_{\gamma\alpha}$, and the fact that neutrinos are very relativistic particles, so $t \simeq L$.

The oscillation probability is given by:

$$\begin{aligned}
P(\nu_\alpha \to \nu_\beta) &= |A(\nu_\alpha(0) \to \nu_\beta(L))|^2 \\
&= \left| \sum_k U_{\beta k}^* \, e^{+i\phi_k} U_{\alpha k} \right|^2 \\
&= \left| U_{\beta 1}^* U_{\alpha 1} \, e^{+i\phi_1} + U_{\beta 2}^* U_{\alpha 2} \, e^{+i\phi_2} + U_{\beta 3}^* U_{\alpha 3} \, e^{+i\phi_3} \right|^2.
\end{aligned} \tag{1.12}$$

Since neutrinos are relativistic particles, $E_k, p_k \gg m_k$, we can rewrite the energy as:

$$E_k = \sqrt{p_k^2 + m_k^2} = p_k \sqrt{1 + \frac{m_k^2}{p_k^2}} \approx p_k \left(1 + \frac{m_k^2}{2p_k^2} \right) \approx p_k + \frac{m_k^2}{2E_k}. \tag{1.13}$$

By using $t \approx x \approx L$, where L is the distance between the source and the detection point, and Eq. (1.13), the phase can be written as:

$$\phi_k = E_k t - p_k x \approx p_k L + \frac{m_k^2}{2E_k} L - p_k L = \frac{m_k^2}{2E_k} L. \tag{1.14}$$

Using the complex relation $|z_1 + z_2 + z_2|^2 = |z_1|^2 + |z_2|^2 + |z_3|^2 + 2\Re(z_1 z_2^* + z_1 z_3^* + z_2 z_3^*)$ and Eq. (1.14), we can now expand Eq. (1.12) to obtain the general expression of the oscillation probability for a neutrino of flavor α to be detected as a neutrino of flavor β after traveling a distance L:

$$P(\nu_\alpha \to \nu_\beta) = \delta_{\alpha\beta} - 4 \sum_{k>j} \Re(U_{\alpha k}^* U_{\beta k} U_{\alpha j} U_{\beta j}^*) \sin^2(\Delta_{kj}) +$$
$$+ 2 \sum_{k>j} \Im(U_{\alpha k}^* U_{\beta k} U_{\alpha j} U_{\beta j}^*) \sin(2\Delta_{kj}), \quad (1.15)$$

where the argument of the trigonometric functions is:

$$\Delta_{kj} = \Delta m_{kj}^2 \frac{L}{4E} = 1.27 \Delta m_{kj}^2 \frac{L[\mathrm{m}]}{E[\mathrm{MeV}]}, \quad \text{for } k > j. \quad (1.16)$$

The mass-squared differences $\Delta m_{kj}^2 = m_k^2 - m_j^2$ with $k > j$ are important parameters for neutrino oscillations and drive the oscillatory terms in the probability. On the other hand, the mixing angles θ_{jk}, which are hidden in the matrix elements, are responsible for the amplitude of the oscillations.

Survival probability for electron antineutrinos from reactors

Experiments that study neutrino oscillations can be divided into two categories: *appearance* and *disappearance* experiments. The former study the appearance of neutrinos of flavor β in an original flux or beam of neutrinos of flavor α, thus measuring the probability in Eq. (1.15) for $\beta \neq \alpha$. On the contrary, the latter start with a pure flux or beam of neutrinos of flavor α and look at how many of them have disappeared at a distance L. Disappearance experiments measure the probability in Eq. (1.15) with $\beta = \alpha$; the probability $P(\nu_\alpha \to \nu_\alpha)$ is also known as survival probability.

We are particularly interested in the expression of $P(\nu_\alpha \to \nu_\alpha)$ since the JUNO experiment is a disappearance experiment, which detects electron antineutrinos produced in nuclear reactors. For $\beta = \alpha$, the imaginary part of Eq. (1.15) is null and the probability reduces to:

$$P(\nu_\alpha \to \nu_\alpha) = 1 - 4 \sum_{k>j} \Re(U_{\alpha k}^* U_{\alpha k} U_{\alpha j} U_{\alpha j}^*) \sin^2\left(1.27 \Delta m_{kj}^2 \frac{L}{E}\right)$$
$$= 1 - 4 \sum_{k>j} |U_{\alpha k}|^2 |U_{\alpha j}|^2 \sin^2\left(1.27 \Delta m_{kj}^2 \frac{L}{E}\right) \quad (1.17)$$

Since there is no imaginary part, the survival probability is independent of the CP-violation phase δ_{CP}; as a consequence, disappearance experiments are not suited to directly study CP-violation in the lepton sector. The expanded form of

the survival probability is:

$$P(\nu_\alpha \to \nu_\alpha) = 1 - 4\,|U_{\alpha2}|^2|U_{\alpha1}|^2 \sin^2\left(1.27\,\Delta m_{21}^2\frac{L}{E}\right)$$
$$- 4\,|U_{\alpha3}|^2|U_{\alpha1}|^2 \sin^2\left(1.27\,\Delta m_{31}^2\frac{L}{E}\right) \qquad (1.18)$$
$$- 4\,|U_{\alpha3}|^2|U_{\alpha2}|^2 \sin^2\left(1.27\,\Delta m_{32}^2\frac{L}{E}\right).$$

Since we are interested in neutrinos of electronic flavor, $\alpha = e$, we can use the matrix U of Eq. (1.4) to evaluate the survival probability for electron antineutrino. Finally, by using the trigonometric relation $2\sin\theta\cos\theta = \sin(2\theta)$, we can write:

$$P(\nu_e \to \nu_e) = \; 1 - \cos^4(\theta_{13})\sin^2(2\theta_{12})\sin^2(\Delta_{21})$$
$$- \cos^2(\theta_{12})\sin^2(2\theta_{13})\sin^2(\Delta_{31}) \qquad (1.19)$$
$$- \sin^2(\theta_{12})\sin^2(2\theta_{13})\sin^2(\Delta_{32}),$$

where $\Delta_{kj} = 1.27\,\Delta m_{kj}^2\frac{L}{E}$ and $\Delta m_{kj}^2 = m_k^2 - m_j^2$, with $k > j$.

Under the CPT theorem, we have $P(\bar\nu_e \to \bar\nu_e) = P(\nu_e \to \nu_e)$, so Eq. (1.19) is the survival probability for an electron antineutrino to be detected as an electron antineutrino at a distance L from the source. This equation is thus valid for disappearance experiments at reactors, like the JUNO experiment.

The electron antineutrino survival probability $P(\bar\nu_e \to \bar\nu_e)$ as a function of L/E_ν for the normal (NO) and inverted (IO) orderings, introduced in the next section, is shown in Fig. 1.4. Given an intermediate baseline of about $52.5\,\mathrm{km}$ and that reactor electron antineutrino energy ranges between 1 and $10\,\mathrm{MeV}$, JUNO will cover the region around the first minimum of the slow oscillation, driven by Δm_{21}^2. As it can be seen in the figure, the fast oscillations driven by the atmospheric term, Δm_{32}^2, have a smaller amplitude compared to the slow oscillation driven by the solar term, Δm_{21}^2. In order to resolve the fine structure of the oscillation pattern, an energy resolution better than $\Delta m_{21}^2/|\Delta m_{32}^2| \approx 3\,\%$ is necessary and is one of the main requirements of the JUNO experiment.

For short baselines, $L \sim O(1\,\mathrm{km})$, Eq. (1.19) reduces to [21]:

$$P(\bar\nu_e \to \bar\nu_e) \simeq 1 - \sin^2(2\theta_{13})\sin^2\left(1.27\Delta m_{31}^2\frac{L}{E}\right), \qquad (1.20)$$

thus depending only on one mixing angle, θ_{13}, and one mass splitting, Δm_{31}^2. For this reason, short-baseline reactor experiments, like Daya Bay introduced earlier, are well suited for a precise measurement of θ_{13}. On the other hand, a medium-baseline reactor experiment like JUNO will not be able to improve the state-of-the-art measurement of θ_{13}.

Observations on the survival probability and the oscillation parameters

The survival probability of Eq. (1.19) has a total of four independent parameters: two mixing angles, θ_{12} and θ_{13}, and two mass-squared differences Δm_{kj}^2. In fact,
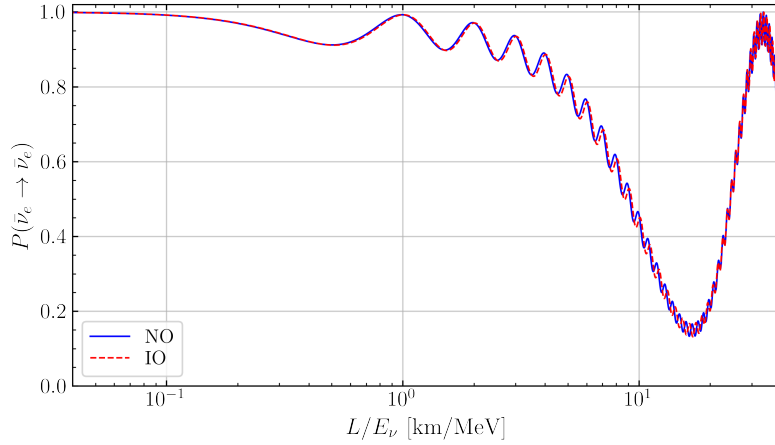
Figure 1.4. Survival probability for electron antineutrinos as a function of L/E_ν for the normal (blue) and inverted (red) orderings. Oscillation parameters from NuFIT 5.2 (2022) [26, 27] are used.

only two out of the three Δm_{kj}^2 are independent since they have to satisfy the following relation:

$$\Delta m_{21}^2 + \Delta m_{32}^2 + \Delta m_{13}^2 = 0. \tag{1.21}$$

From experiments studying neutrino oscillations, we know that $\Delta m_{21}^2 > 0$, while the sign of $\Delta m_{32/31}^2$ is still unknown. There are thus two possible orderings for the spectrum of neutrino masses: normal ordering (NO), where $m_1 < m_2 < m_3$, and inverted ordering (IO), where $m_3 < m_1 < m_2$. The true mass ordering is one of the current open issues about massive neutrinos (see section 1.2.3).

Table 1.2. Oscillation parameters from NuFIT 5.2 (2022) [26, 27].

Parameter	Value
Δm_{21}^2	$7.41 \cdot 10^{-5}\,\text{eV}^2$
$\sin^2 \theta_{12}$	0.303
Δm_{31}^2 (NO)	$2.511 \cdot 10^{-3}\,\text{eV}^2$
Δm_{32}^2 (IO)	$-2.498 \cdot 10^{-3}\,\text{eV}^2$
$\sin^2 \theta_{13}$ (NO)	0.02203
$\sin^2 \theta_{13}$ (IO)	0.02219

The values of the oscillation parameters from a recent global fit [26, 27] are listed in Table 1.2. Throughout this work, we use the notation by I. Esteban *et al.* [26, 27], where the two independent mass splittings are the smallest and the largest ones for each mass ordering. The smallest mass splitting is $\Delta m_{21}^2 \sim 7 \cdot 10^{-5}\,\text{eV}^2$ for both normal (NO) and inverted (IO) orderings. This parameter is responsible for the slow or *solar* component of the oscillation pattern. The largest mass splitting depends on the mass ordering and is labeled as $\Delta m_{3\ell}^2$, where:

- $\ell = 1$ ($\Delta m_{3\ell}^2 = \Delta m_{31}^2 > 0$) for NO;
- $\ell = 2$ ($\Delta m_{3\ell}^2 = \Delta m_{32}^2 < 0$) for IO.

$\Delta m_{3\ell}^2 \sim 3 \cdot 10^{-3}\,\mathrm{eV}^2$ drives the fast or *atmospheric* component of the oscillation pattern. A schematic representation of the mass splitting for the two mass orderings is shown in Fig. 1.5.
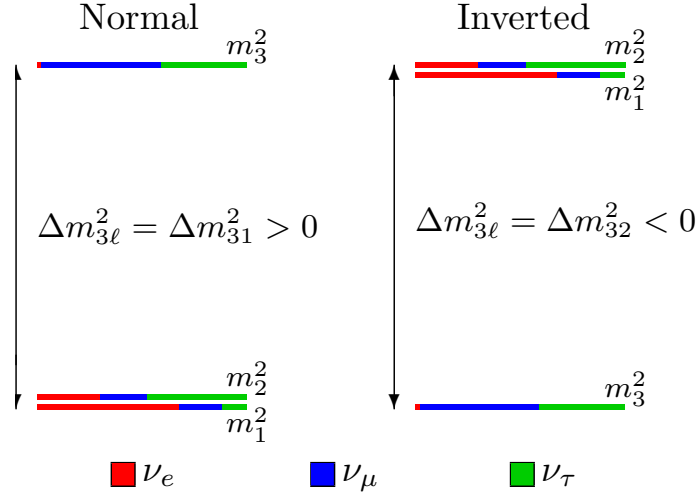
Figure 1.5. Schematic of the mass splittings for the two orderings, accordingly to the notation by I. Esteban *et al.* [26, 27]. The colored bars represent how much the flavor eigenstates are mixed to obtain the mass eigenstates; the matrix U of Eq. (1.4) has been considered.

Sometimes in the literature, the determination of the neutrino mass ordering is referred to as the determination of the neutrino mass hierarchy (MH). In fact, depending on the values of the lightest neutrino, the mass spectrum can be further classified in: normal hierarchical spectrum (NH), $m_1 \ll m_2 < m_3$; inverted hierarchical spectrum (IH), $m_3 \ll m_1 < m_2$; quasidegenerate spectrum (QD), $m_1 \simeq m_2 \simeq m_3$. The neutrino spectrum may or may not be hierarchical with what we know so far about the neutrino absolute mass scale. Therefore, it is more precise to address this problem as the determination of the neutrino mass ordering.

The matter effect

Until now, we have considered neutrino oscillations in the vacuum. The oscillation probability may change if neutrinos travel through matter and thus move in a potential a, which acts differently on the different flavor eigenstates. This is known as *matter effect* or *neutrino oscillations in matter*. The phenomenon depends on the energy of the traveling neutrino and the electron density of the traversed matter. Indeed, electron neutrinos can interact in matter via neutral and charged current, while the other two neutrino flavors, ν_μ and ν_τ, interact only via neutral current; hence, neutrino flavors interact differently in the matter and experience different potentials a_α. The matter effect plays a critical role in the study of the solar sector of neutrino oscillations since the electron neutrinos are produced inside the sun, where the matter density is high. In fact, as already seen

in section 1.1.1, the solar neutrino problem could be explained by the transition $\nu_e \to \nu_\mu, \nu_\tau$ which is enhanced by the matter effect in the sun.

For a reactor experiment with a medium baseline of about 50 km, the matter effect has a small impact, nonetheless, it cannot be neglected given JUNO challenging physics goals. In fact, neglecting the matter effect could introduce a bias in the measurement of the solar oscillation parameters, $\sin^2\theta_{12}$ and Δm^2_{21} [28]. One possible to way to get the survival probability in matter is to use the same analytical form as the survival probability in the vacuum, Eq. (1.19), and use the oscillation parameters in matter, which are obtained by a perturbative expansion of the oscillation parameters in terms of the matter potential [28]. In the end, the survival probability in matter can be written as:

$$
\begin{aligned}
P_{\text{matter}}(\nu_e \to \nu_e) = \ & 1 - \cos^4(\tilde{\theta}_{13})\sin^2(2\tilde{\theta}_{12})\sin^2(\tilde{\Delta}_{21}) \\
& - \cos^2(\tilde{\theta}_{12})\sin^2(2\tilde{\theta}_{13})\sin^2(\tilde{\Delta}_{31}) \\
& - \sin^2(\tilde{\theta}_{12})\sin^2(2\tilde{\theta}_{13})\sin^2(\tilde{\Delta}_{32}),
\end{aligned}
\tag{1.22}
$$

where $\tilde{\Delta}_{kj} = 1.27\,\Delta \tilde{m}^2_{kj}\frac{L}{E}$, and the tilde on top identifies the perturbative expansion of the oscillation parameters.

The potential which is introduced in the Schroedinger equation of Eq. (1.6) and which is affecting only $\bar{\nu}_e$ during propagation can be written as:

$$
a = -2\sqrt{2}G_F N_e E_\nu
\tag{1.23}
$$

where G_F is the Fermi constant, N_e is the electron density, and E_ν is the antineutrino energy in units of MeV. The potential can also be approximated as a function of the matter density:

$$
a \approx 1.52 \cdot 10^{-4}\left(\frac{Y_e\,\rho}{\text{g/cm}^3}\right)\left(\frac{E_\nu}{\text{GeV}}\right)\text{eV}^2,
\tag{1.24}
$$

where $\rho = 2.45\,\text{g/cm}^3$ is the matter density for the JUNO experiment [29], and $Y_e \approx 0.5$ is the number of electrons per nucleon.

It is found that for the JUNO analysis it is enough to expand the oscillation parameters up to the second order in the matter potential [28]. The expansion of the solar oscillation parameters is given in the following equations:

$$
\sin^2\tilde{\theta}_{12} \simeq \sin^2\theta_{12}\cdot\left[1 + 2c_{12}^2\left(\frac{c_{13}^2\,a}{\Delta m^2_{21}}\right) + 3c_{12}^2\cos 2\theta_{12}\left(\frac{c_{13}^2\,a}{\Delta m^2_{21}}\right)^2\right],
\tag{1.25}
$$

and

$$
\Delta\tilde{m}^2_{21} \simeq \Delta m^2_{21}\left[1 - \cos 2\theta_{12}\left(\frac{c_{13}^2\,a}{\Delta m^2_{21}}\right) + 2s_{12}^2 c_{12}^2\left(\frac{c_{13}^2\,a}{\Delta m^2_{21}}\right)^2\right].
\tag{1.26}
$$

As far as the mixing angle θ_{13} is concerned, it can be rewritten as:

$$
\sin^2\tilde{\theta}_{13} \simeq \sin^2\theta_{13}\cdot\left[1 + 2c_{13}\left(\frac{a}{\Delta m^2_{ee}}\right)\right],
\tag{1.27}
$$

where:
$$\Delta m_{ee}^2 = c_{12}^2 \Delta m_{31}^2 + s_{12}^2 \Delta m_{32}^2. \tag{1.28}$$

Finally, the two largest mass splittings can be expanded as:

$$\Delta \tilde{m}_{31}^2 \simeq \Delta m_{31}^2 \cdot \left[1 - \left(\frac{a}{\Delta m_{31}^2} \right) \left(c_{12}^2 c_{13}^2 - s_{13}^2 - s_{12}^2 c_{12}^2 c_{13}^2 \left(\frac{c_{13}^2 a}{\Delta m_{21}^2} \right) \right) \right], \tag{1.29}$$

and

$$\Delta \tilde{m}_{32}^2 \simeq \Delta m_{32}^2 \cdot \left[1 - \left(\frac{a}{\Delta m_{32}^2} \right) \left(s_{12}^2 c_{13}^2 - s_{13}^2 + s_{12}^2 c_{12}^2 c_{13}^2 \left(\frac{c_{13}^2 a}{\Delta m_{21}^2} \right) \right) \right]. \tag{1.30}$$

Figure 1.6 shows the fractional difference between the probability in matter and in the vacuum. As already mentioned, the difference in the probability is small, up to about 4 %, nonetheless the matter effect cannot be neglected since it introduces a shift in the measurement of the oscillation parameter values.
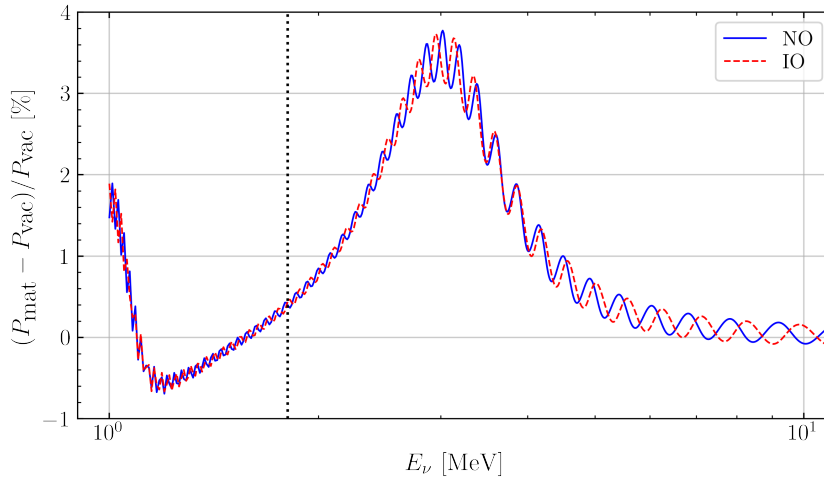
Figure 1.6. Fractional difference of the electron antineutrino survival probability in matter and in the vacuum versus the antineutrino energy. The matter effect is up to 4 % at about 3 MeV. The dotted vertical line refers to the IBD threshold. Oscillation parameters from NuFIT 5.2 (2022) [26, 27] are used.

1.2.3   Open questions on massive neutrinos

Here, we present some of the open issues related to the physics of massive neutrinos, which will be addressed in the next generation of experiments. When possible, we point out whether the issue can be directly or indirectly addressed by the JUNO experiment [30].

Determination of the mass ordering
We know that $\Delta m_{21}^2 > 0$, while the sign of the atmospheric splitting $\Delta m_{31/32}^2$ is still unknown. There are thus two possible orderings for the masses of the mass eigentstates: normal ordering, with $m_1 < m_2 < m_3$, and inverted

ordering, with $m_3 < m_1 < m_2$; a graphical representation of the two mass orderings is shown in Fig. 1.5. It is fundamental to determine the MO since the sign of $\Delta m^2_{31/32}$ can have an impact in different fields, from particle physics to astrophysics and cosmology. For example, the MO is crucial in the understanding of the origin of the neutrino masses and mixing, in the prediction of the supernova nucleosynthesis, or in the cosmological probe of the neutrino mass scale.

The JUNO experiment has been designed to measure the MO using precision spectral measurements of reactor antineutrino oscillations. With respect to long-baseline accelerator experiments and atmospheric experiments, which could also resolve the MO, JUNO will study oscillations in the vacuum, thus being independent of the matter effect.

Precision measurements of the oscillation parameters
From the latest global analysis by I. Esteban *et al.* [26, 27], the current precision of all mixing angles and mass-squared differences lies between 1.3 % and 5 %. JUNO, as a standalone experiment, has the potential to obtain unprecedented sub-percent precision for three oscillation parameters, namely Δm^2_{21}, $\sin^2 \theta_{12}$, and the atmospheric splitting $\Delta m^2_{31/32}$.

CP-violation phase
The CP-violation phase δ_{CP} of the mixing matrix U models the violation of the CP-symmetry in weak interactions in the lepton sector. We have already observed in Eq. (1.17) that δ_{CP} does not appear in the survival probability of a disappearance experiment; thus, it can only be studied in appearance experiments.

Since JUNO is a disappearance experiment, it cannot directly measure the value of the CP-violation phase. However, JUNO results on the MO determination could help resolve the degeneracy between the MO and the CP phase measurements, which emerges in long- or medium-baseline accelerator experiments. A determination of the MO independent of δ_{CP} is thus necessary for the future of neutrino physics.

Dirac or Majorana particle?
By definition, a Dirac particle is distinguishable from its antiparticle since they have opposite lepton numbers, while a Majorana particle is its own antiparticle. Whether massive neutrinos are Dirac or Majorana particles is still unknown. A way to determine the nature of neutrinos is to study the reaction called *double-beta decay* ($\beta\beta$ decay), where a nucleus undergoes two beta decays with the emission of a neutrino and an antineutrino. If neutrinos were Majorana particles, it would be possible to observe *neutrinoless double-beta decay* ($0\nu\beta\beta$ decay); so far, no convincing evidence for an occurrence of the $0\nu\beta\beta$ decay has been established.

By determining the MO, JUNO could help determine the goals of the search for neutrinoless double-beta decay. In fact, the chance to observe the reaction with the next generation of $0\nu\beta\beta$ experiments is greatly enhanced if the MO is inverted.

Absolute mass of the neutrino

The neutrino absolute mass scale is currently unknown. Since oscillation experiments are sensitive to the neutrino mass-squared differences, they cannot measure the absolute mass of neutrinos, that can, however, be measured by experiments studying the end-point of the electron spectrum emitted in a beta decay. In synergy with neutrinoless double-beta decay experiments, JUNO could help constrain the value of the lightest neutrino mass.

The information on the lightest neutrino mass could also determine whether the neutrino mass spectrum is hierarchical or not, that is, if it is the case of a normal hierarchical spectrum (NH), $m_1 \ll m_2 < m_3$; an inverted hierarchical spectrum (IH), $m_3 \ll m_1 < m_2$; or a quasi-degenerate spectrum (QD), $m_1 \simeq m_2 \simeq m_3$.

Unitarity of the mixing matrix

JUNO precision measurements of the oscillation parameters could be used to test the unitarity of the mixing matrix U. By the combination of the precision results of JUNO, Daya Bay, and SNO, it could be possible to test the unitarity relation

$$|U_{e1}|^2 + |U_{e2}|^2 + |U_{e3}|^2 = 1$$

with a precision of 2.5 % [30, p. 43].

The test of the unitarity of the 3×3 PMNS matrix is important in probing or constraining possible new physics associated with the mixing between the three active SM neutrinos and sterile neutrinos.

Octant of θ_{23}

From the current measurements of the oscillation parameters, the value of $\theta_{23} = 45°$ is allowed within the experimental uncertainties, thus suggesting a maximal mixing in the μ-τ sector. Since many mass models depend on the value of θ_{23}, the determination of the octant of this mixing angle could serve as a model discriminator. The JUNO experiment is not sensitive to this parameter, so it cannot address this issue. At the same time, the large uncertainty characterizing θ_{23} is not going to affect JUNO physics goals.

The determination of the MO and the precision measurements of the oscillation parameters are themselves significant goals that can be achieved with JUNO as a standalone experiment. Furthermore, JUNO results could be used in combination with results from other experiments to help addressing other questions, such as the measurement of the CP-violation phase δ_{CP}, the determination of the Dirac or Majorana nature and the absolute mass scale of neutrinos, and the test of the unitarity of the mixing matrix U.

Chapter 2

The JUNO experiment

JUNO (Jiangmen Underground Neutrino Observatory) is a multipurpose experiment located in Southern China. The experiment will detect electron antineutrinos ($\overline{\nu}_{e}$) produced from the β decay of fission products inside the cores of nuclear reactors, with the main aim to study neutrino oscillations and answer to some open questions about the physics of massive neutrinos, *e.g.*, the neutrino mass ordering (MO).

Section 2.1 is dedicated to the description of the JUNO experiment, with a focus on the different hardware systems composing the detector; while section 2.2 provides an overview of the physics prospects of the JUNO experiment beyond the analysis of reactor antineutrinos. More detailed information about the experiment and the physics goals can be found in several available publications [30–32].

At the moment of writing, the experiment is still under construction, and the first data-taking is expected to begin in 2024; the status of the construction for each JUNO system is given throughout the chapter. The JUNO collaboration is composed of 74 institutions from 17 different countries worldwide.

2.1 The detector

JUNO is a 20 kt liquid scintillator detector with a shell structure as shown in the schematic of Fig. 2.1. JUNO design is based on the experience of previous liquid scintillator neutrino detectors, like the ones introduced in section 1.1, although JUNO will be the biggest among them. Organic liquid scintillators for large detectors are usually chosen for various characteristics, such as high light yield, high attenuation length, good stability, low toxicity, and availability in huge amounts at relatively low cost. The different components of the JUNO experiment are presented in the following sections.

2.1.1 The central detector

A key component of JUNO central detector (CD) is the stainless steel structure which provides the mechanical support for many other components, like the acrylic vessel, the PMTs, and the electronics. The steel structure has a spherical shape with a diameter of 40.1 m, and was the first part of JUNO to be installed
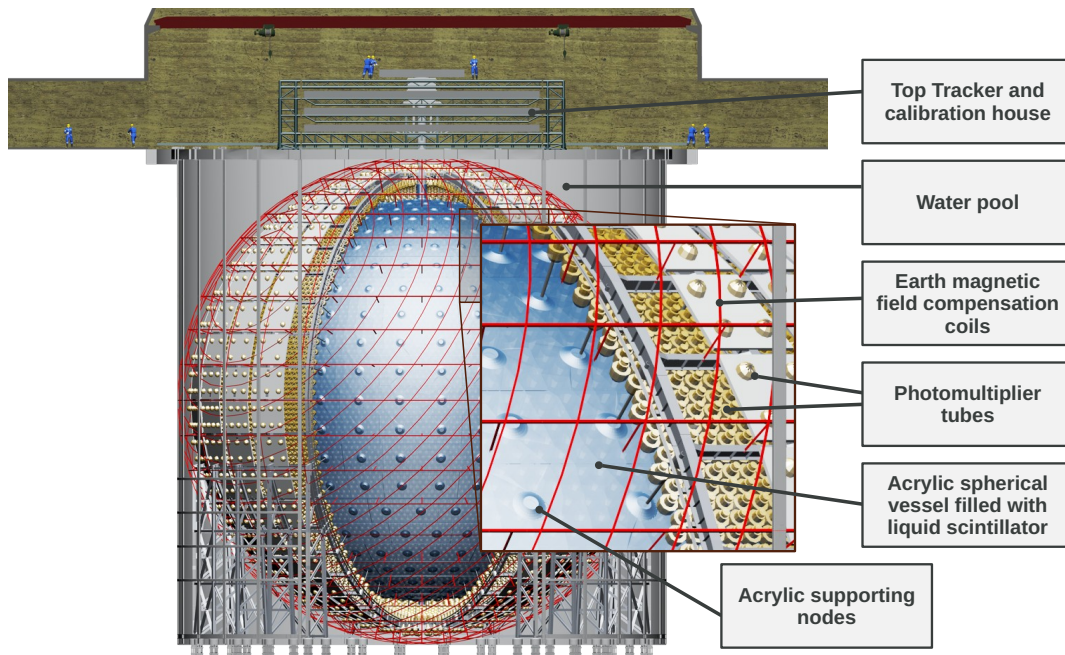
Figure 2.1. Schematic view of the JUNO detector [29].

in the experimental hall. Figure 2.2a shows a picture of the supporting structure at the end of the installation, which was completed in June 2022.

The 20 kt of liquid scintillator are contained in a spherical acrylic vessel, with a thickness of 12.4 cm and an inner diameter of 35.4 m. The acrylic material has to be transparent to the optical photons produced by particle interactions inside the liquid scintillator: a light transparency greater than 96 % is expected. Figure 2.2b was taken in January 2023 at the beginning of the acrylic vessel installation, and shows the first top acrylic panels connected to the stainless steel structure through steel connecting rods.

Both the stainless steel support structure and acrylic vessel has to meet stringent requirements in term of radiopurity, especially the vessel since it will be directly in contact with the liquid scintillator. The radiopurity requirement for the acrylic is a contaminant concentration of less than 10^{-12} g/g for ^{238}U, ^{232}Th, and ^{40}K.

A system of inward-facing PMTs is installed on the stainless steel structure and is better described in section 2.1.4. The acrylic sphere and the supporting structure are immersed in a cylindrical water pool, which shields against the environmental radioactivity and is part of the veto system (see section 2.1.3). In this configuration, the water is allowed to pass through the supporting structure and reach the acrylic sphere, surrounding the system of PMTs. As a result, water serves as a buffer liquid to protect the LS from the radioactivity of the PMT glass. Furthermore, a layer of Tyvek reflection foils is installed to optically separate the central detector from the water pool and increase the light collection efficiency [33].

(a) *Stainless steel structure.* **(b)** *Acrylic vessel installation.*
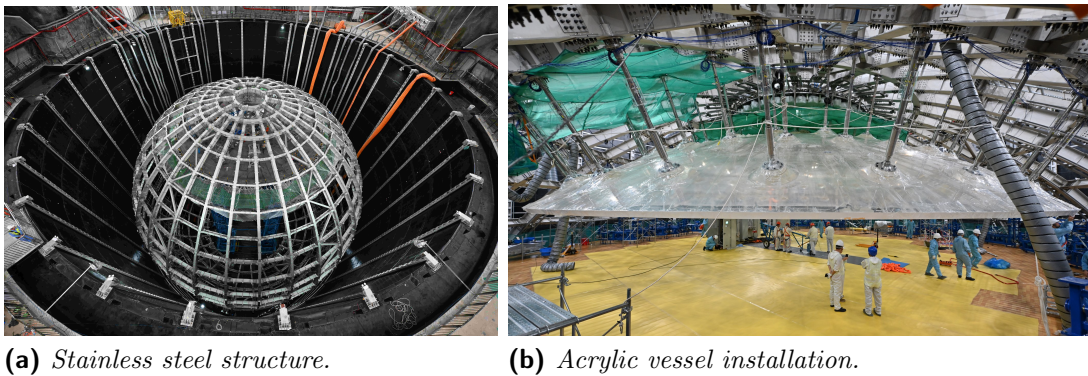
Figure 2.2. **(a)** Picture of the stainless steel structure of JUNO central detector, whose installation was completed in June 2022. **(b)** Picture taken during the installation of the first top layers of the acrylic vessel. The rods connecting the acrylic panels to the stainless steel structure are clearly visible. The presence of workers gives an idea of JUNO dimensions.

2.1.2   The liquid scintillator

The scintillator used in JUNO is an organic liquid scintillator (LS). Linear alkyl-benzene (LAB) is used as the solvent due to a good light yield ($\sim 10^4\,\gamma/\mathrm{MeV}$) and its excellent transparency. The latter is related to the attenuation length of the scintillator, and JUNO's LAB is characterized by a measured attenuation length of 25 m to 30 m at a wavelength of 430 nm, comparable with the diameter of the detector [34]. A molecule of LAB is a straight alkyl chain of 10 to 13 carbons attached to a benzene ring 10, so the chemical formula is $C_6\,H_5\,C_n\,H_{2n+1}$ with n ranging from 10 to 13. Two hydrogen atoms are attached to each carbon in the chain and can be regarded to as *free protons* and constitute the main target for reactor electron antineutrinos. Since 20 kt of LS are contained in the inner vessel, and the mass fraction of hydrogen and carbon atoms is 12 % and 88 %, respectively, the number of free proton targets in JUNO is $N_p \simeq 1.44 \cdot 10^{33}$.

The solvent is doped with 2.5 g/L of 2,5-diphenyloxazole (PPO), acting as the primary fluor, and 3 mg/L of p-bis-(o-methylstyryl)-benzene (bis-MSB), a wavelength shifter, to obtain the final mixture [31, 35], characterized by a density of 0.859 g/mL [30]. The light emission following the deposition of energy by a charged particle in the LS comes from a chain of radiative processes transferring energy from the excited molecules of the solvent to the fluor and finally to the wavelength shifter, which emits optical photons with a distribution peaked at 430 nm in a characteristic time of about 4.4 ns.

The liquid scintillator is required to have as low an intrinsic background as possible. The target radiopurity differs for different analysis goals, for example, the analysis of reactor antineutrinos relies on the coincidence between a prompt signal and a delayed signal so the residual background can be suppressed by the application of selection cuts (see section 6.2.2); on the other hand, the analysis of solar neutrinos is characterized by a single signal coming from the elastic scattering of neutrinos on electrons of the medium, thus in this case a lower contaminant concentration is required. The requirements for the two physics

analyses are summarized in Table 2.1.

Table 2.1. The table summarizes the radiopurity target for JUNO liquid scintillator for two different analyses: the analysis of reactor antineutrinos and the analysis of solar neutrinos. All contaminant concentrations are given in units of g/g.

[g/g]	$^{238}\mathrm{U}/^{232}\mathrm{Th}$	$^{40}\mathrm{K}$	$^{210}\mathrm{Pb}$
Reactor $\bar{\nu}_e$	$< 10^{-15}$	$< 10^{-16}$	$< 10^{-22}$
Solar ν_e	$< 10^{-17}$	$< 10^{-18}$	$< 10^{-24}$

To meet the radiopurity requirements, a purification process comprising several steps was developed: (1) the alumina filtration step is meant to improve the optical properties of the LAB; (2) the distillation process is meant to remove heavy metals and improve the transparency; (3) the water extraction is meant to remove heavy elements like U, Th, and K; (4) the gas stripping is meant to remove volatile impurities such as Ar, Kr, and Rn. The first two step are performed only on the LAB, while the last two steps are performed underground after the LS mixing to obtain the final mixture.

Finally, before filling JUNO central detector with the LS, an Online Scintillator Internal Radioactivity Investigation System (OSIRIS) [36] has been developed to check and monitor the radiopurity requirements. OSIRIS is equipped with 64 20-inch PMTs with a photocoverage of about 9 % facing a tank with 20 t of JUNO liquid scintillator. With a photoelectron yield of 280 PE/MeV, it is expected to reach an energy resolution of 6 % at 1 MeV. OSIRIS is expected to reach the U/Th sensitivity for the reactor analysis in a few days, while 2-3 weeks are needed for the solar neutrino analysis.

2.1.3   The veto system

The JUNO veto system comprises two systems: the Cherenkov water pool and the Top Tracker.

The acrylic sphere and the stainless steel structure are immersed in a cylindrical water pool, which serves as a Cherenkov detector and shields against the environmental radioactivity, which constitutes a background. The water pool is 44 m high and has a diameter of 43.5 m and is filled with 35 kt of ultrapure water. 2400 20-inch veto PMTs are installed on the supporting structure facing outwards to detect the Cherenkov light produced by passing muons; even though the detector is located about 650 m (1800 m.w.e.) underground, a residual rate of cosmogenic muons of 0.004 Hz/m² is expected. The water pool is also meant to keep the temperature uniform and stable at $(21 \pm 1)\,°C$.

Cosmic muons are produced in the atmosphere by cosmic rays and constitute one of the primary forms of background. For this reason, a Top Tracker has been designed [37] to precisely track muons and study cosmogenic backgrounds, as will be explained in chapter 6. The Top Tracker is located above the water pool, event though it will cover only about 50 % of the surface. It is composed of existing strips of plastic scintillator from the OPERA experiment [38] which will

be placed in three horizontal layers. A schematic drawing of JUNO Top Tracker is shown in Fig. 2.3.
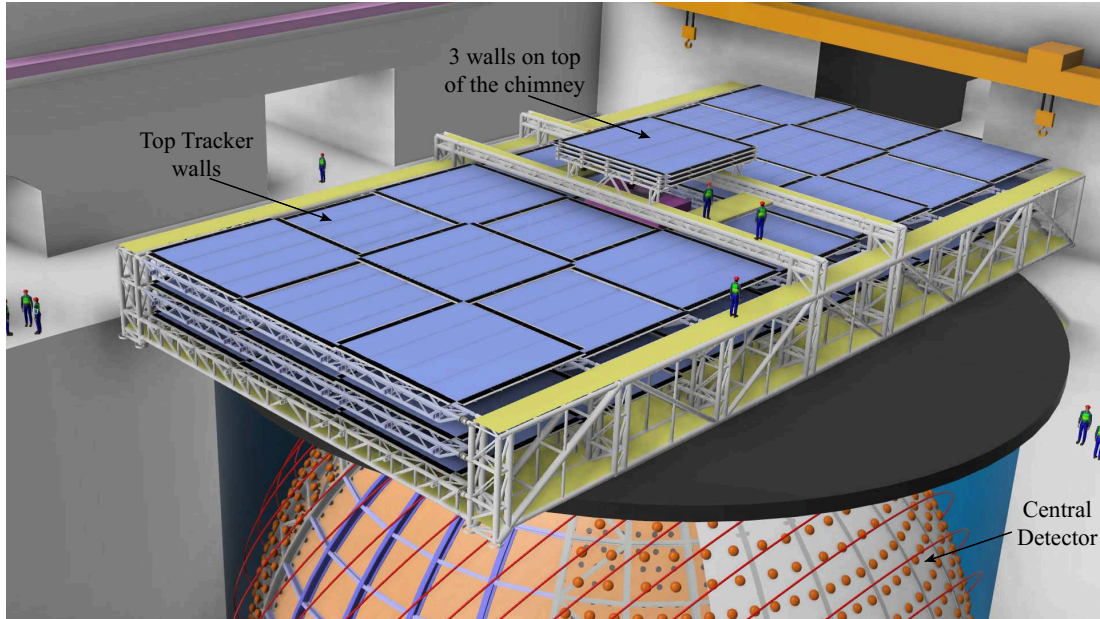
Figure 2.3. Schematic view of JUNO Top Tracker [37].

2.1.4 The PMT system

The PMT system comprises a total of 20 012 20-inch PMTs to be installed on the stainless steel supporting structure [39]: 17 612 of them face inwards to detect the scintillation light emitted in the liquid scintillator, while the remaining 2400 face outwards to detect the Cherenkov light emitted in the veto water pool. Among them, 15 012 PMTs are micro-channel plate PMTs produced by Northern Night Vision Technology (NNVT), while 5000 are dynode PMTs by Hamamatsu Photonics K. K. (HPK). The 20-inch PMTs of the central detector provide a photocoverage of 75.2 %. The waveform coming from the 20-inch PMTs are acquired and digitized by the readout electronics, which will be described in detail in chapter 5. Given the large size of the 20-inch PMTs, with a diameter of about 50 cm, the photoelectron produced by a photon at the PMT photocathode can be affected in its flight to the the anode by the Earth's magnetic field; for this reason, a set of 32 circular coils are installed on the supporting structure to compensate for the Earth's magnetic field and minimize the impact on the PMT photon detection efficiency (PDE).

All 20-inch PMTs have been produced, potted and thoroughly characterized in an extensive testing campaign; all details and results can be found in [40]. NNVT PMTs are characterized by a very high quantum efficiency (QE) of 30.1 % and a good transit time spread (TTS) of 7.0 ns, while HPK PMTs are much faster, with a TTS of 1.3 ns, and also have a high QE of 28.5 %. From the testing campaign, the measured PDE, which is given by the product between the QE and the collection efficiency, is greater than 28 % and meets JUNO requirement of a

PDE of at least 27 %. The distributions of the PDE for all PMTs, NNVT PMTs, and HPK PMTs are shown in Fig. 2.4a in black, red, and blue, respectively; the mean values and the standard deviations are also given. The multiplication step of the 20-inch PMTs is characterized by a gain of 10^7.

(a) *Measured PDE distribution.*

(b) *Measured DCR distribution.*
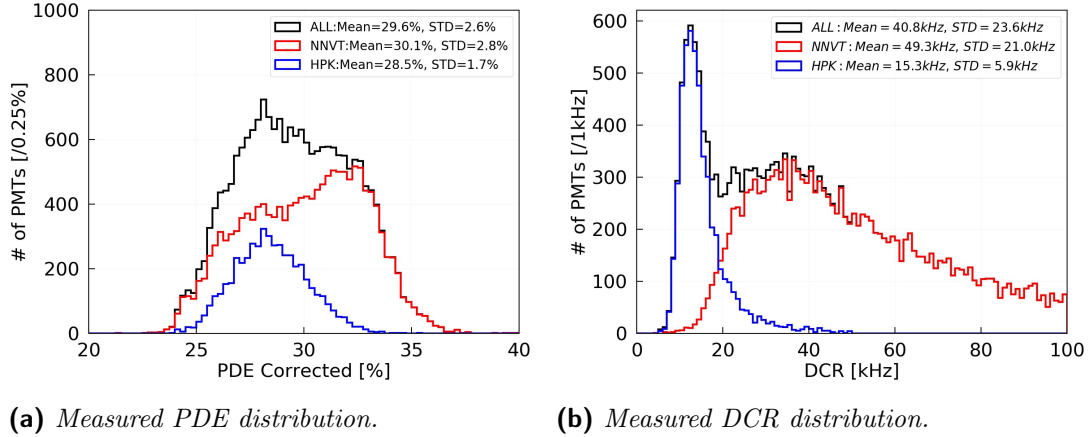
Figure 2.4. Distributions of the **(a)** PDE and **(b)** DCR for all PMTs, NNVT PMTs, and HPK PMTs in black, red, and blue, respectively. The mean values and the standard deviations are also given. For the PDE, the values were corrected after a re-calibration of the testing setup, which showed a degradation of the performance due to aging [40].

The photocoverage and the PDE enter in the evaluation of the number of detected photoelectrons (PE) which constitutes JUNO final observable, so they contribute to the stochastic term a of the energy resolution, Eq. (4.17) in section 4.2. Furthermore, the dark count rate (DCR), which was measured to be 49.3 kHz and 15.3 kHz for NNVT and HPK PMTs, respectively, contributes to the noise term c. The distribution of the DCR for all PMTs, NNVT PMTs, and HPK PMTs are shown in Fig. 2.4b in black, red, and blue, respectively; the mean values and the standard deviations are also given.

In addition to the 20-inch PMTs, the PMT system comprises 26 000 3-inch PMTs [41] facing inwards, so that the total photocoverage of the central detector increases to 77.9 %. The 3-inch PMT system is meant to be used as a linear reference to calibrate the channel-wise non-linearity of the 20-inch PMTs, as explained in section 2.1.5. The 3-inch PMTs are placed in the spaces between the 20-inch PMTs, in the configuration shown in Fig. 2.5a; Figure 2.5b shows the first layers of the 20-inch and 3-inch PMTs installed on the stainless steel structure facing the acrylic vessel.

2.1.5   The calibration system

To achieve the goal of determining the neutrino mass ordering and measure three of the oscillation parameters with unprecedented precision, JUNO needs to meet very stringent requirements and an excellent understanding of the energy detector response is needed. In particular, to resolve the oscillation pattern in the reactor

(a) *PMT configuration.*   **(b)** *PMT installation.*
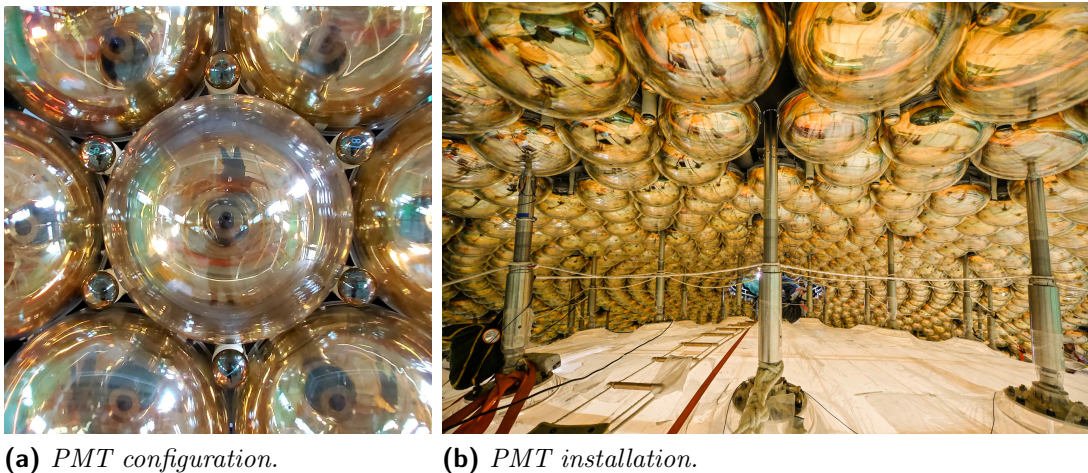
Figure 2.5. (a) Configuration of the 20-inch and 3-inch PMTs. **(b)** Picture taken during the installation of the first top layers of PMT system. Both 20-inch and 3-inch PMTs installed on the stainless steel structure and facing the acrylic vessel are clearly visible.

$\overline{\nu}_e$ energy spectrum, JUNO is required to reach an energy resolution of 3 % at 1 MeV and to keep systematic uncertainties on the energy scale below 1 % [42].

A more detailed discussion on the energy resolution and the physics non-linearity can be found in chapter 4; here, we focus on the hardware used for the calibration of the JUNO experiment.

As shown in the schematic of Fig. 2.6a, the calibration system of the JUNO experiment consists of four main subsystems:

Automatic Calibration Unit (ACU)

The ACU [43] is designed to deploy the calibration sources inside the liquid scintillator along the vertical axis z, with an expected positioning precision of 1 cm. The ACU will be used to regularly deploy a neutron source, multiple gamma sources, and a pulsed UV laser source [44], with the aim of monitoring the stability of the energy scale and the position non-uniformity of the detector response over time.

Cable Loop System (CLS)

The CLS [45] is designed to deploy sources off-axis by means of two cables with adjustable length attached to the source, with one of them passing through an anchoring point on the internal surface of the sphere. In JUNO, we plan to install two CLSs in two opposite half-planes. Sources will be deployed with an expected positioning precision of 3 cm. This system is meant to calibrate the position non-uniformity of the detector response.

Guide Tube system (GT)

The GT [46] will be used to deploy sources along a longitudinal circle through a tube looped outside of the acrylic sphere, with an expected positioning precision of 3 cm. This subsystem will be mainly used to calibrate the non-uniformity of the detector response at the CD boundary.

(a) *Schematic of the calibration hardware for JUNO.*

(b) *Schematic of the source assembly.*
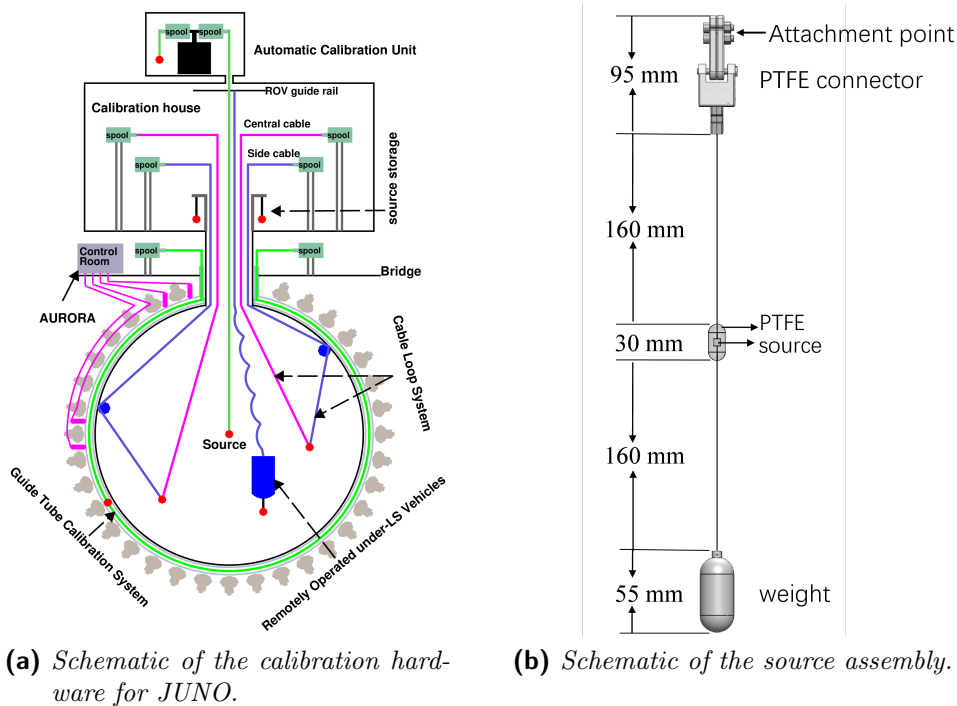
Figure 2.6. Hardware for the calibration of the JUNO experiment [42]: **(a)** schematic showing the position and the functioning of the calibration house and of the four subsystems of the calibration hardware; **(b)** design of the mechanical structure that will contain the calibration sources.

Remotely Operated Vehicle (ROV)

The ROV [47] is designed to deploy sources in the whole liquid scintillator volume with an expected positioning precision of 3 cm. It is intended as a supplemental system in case of significant local effects that cannot be calibrated by the other systems, or in case of a significant azimuthal dependence identified during data-taking.

In Fig. 2.6a, the AURORA system is also shown, even though it is not part of the calibration hardware. It is a laser diode system with the main goal of monitoring the properties of the liquid scintillator, such as the attenuation and scattering lengths.

Figure 2.6b shows the design of the mechanical structure used to deploy the calibration sources. The source is contained in a cylindrical stainless steel shell, which is attached at the top to a connector through a 160 mm long wire, while at the bottom a weight of about 100 g is attached to maintain the tension of the wire. All components of the assembly are covered in a highly reflective Polytetrafluoroethylene (PTFE) layer, to reduce the absorption of optical photons by the assembly itself and thus reducing the impact of the shadowing effect on the source energy spectrum. The effect of the source assembly on the energy spectrum is studied in detail in section 4.3.

Dual Calorimetry Calibration (DCC)

Other than the physics non-linearity that will be covered in detail in chapter 4, there is also the contribution of the instrumental non-linearity, which includes the non-linear response of the readout system, comprising the PMT system and the electronics; more details on the study of the electronics linearity are given in chapter 5.

The instrumental non-linearity manifests itself in each single channel, so that channel-level non-linearities convolve into an event-level instrumental non-linearity, which is also position dependent. To calibrate the channel-level non-linearity, a novel technique that exploits the presence of the two independent photosensor systems has been developed: the Dual Calorimetry Calibration (DCC) [42, 48]. As seen in section 2.1.4, the different sizes of the PMTs translate into different working regimes. As far as reactor events are concerned, 20-inch PMTs are characterized by a dynamic range up to 100 PE, displaying a non-linear response over this range; the full waveform is acquired and digitized, and then the charge is extracted by charge reconstruction algorithms. On the other hand, 3-inch PMTs are small enough and almost work in the single-PE regime, with a dynamic range up to 2 PE; their response is linear in the working range and the charge is evaluated through PE counting.

In this way, the 3-inch PMT system can be used as a linear reference to calibrate the channel-level non-linearity for each 20-inch PMT channel. In the current calibration strategy, the DCC is performed by means of a tunable UV laser placed at the detector center, so that the position non-uniformity can be neglected. It is demonstrated that, in an extreme hypothetical scenario with a channel-level non-linearity of 50 % at 100 PE, the event-level non-linearity can be improved from 2 % to less then 0.3 %.

2.1.6   JUNO location

The JUNO experiment is located in Jinji town, Kaiping city, Jiangmen city, Guangdong province, in China, as shown in Fig. 2.7. The experiment will be installed about 650 m (1800 m.w.e.) underground to reduce the cosmogenic background produced by cosmic rays impacting on the terrestrial atmosphere.

Two Nuclear Power Plants (NPPs) will provide most of the electron antineutrino flux to be detected in JUNO: the Yangjian (YJ) NPP and the Taishan (TS) NPP, which consist of 6 and 2 reactor cores, respectively. The 6 reactor cores of the Yangjian NPP have a thermal power of 2.9 GW each, while the 2 of the Taishan NPP have a thermal power of 4.6 GW each, for a total of 26.6 GW.

The JUNO site is located about 53 km away from the two NPPs since this is the optimal baseline for the determination of the neutrino mass ordering, according to preliminary studies [30, 49]. In fact, the baseline has been chosen to maximize the electron antineutrino disappearance in JUNO and hence minimize the survival probability for $\overline{\nu}_e$ of equation (1.17).

For an accurate analysis of the reactor $\overline{\nu}_e$ spectrum for the determination of the neutrino mass ordering, the actual baseline distribution of the reactor cores should be taken into account. The baselines and the thermal powers of the 8 near
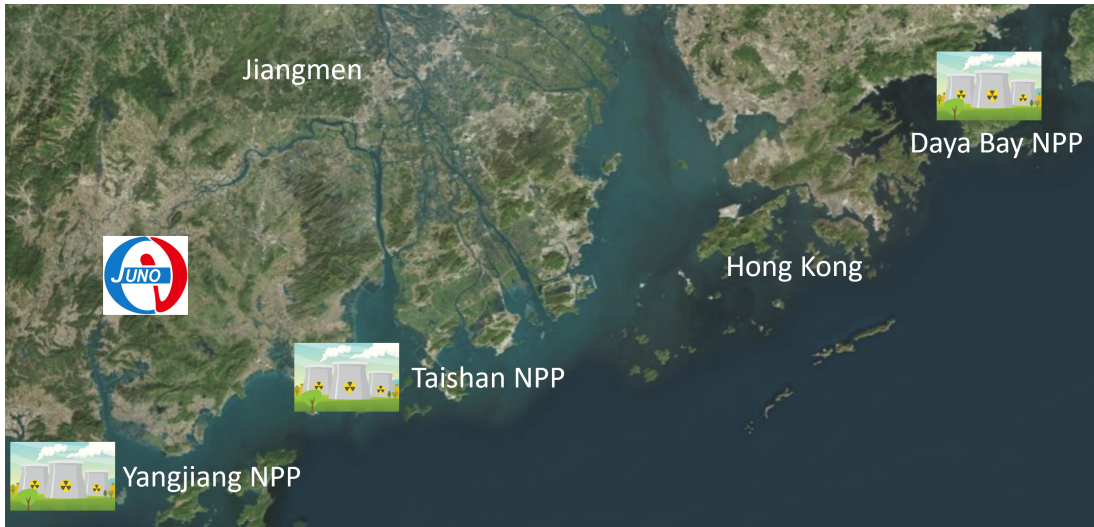
Figure 2.7. Location of the JUNO experiment in Jiangmen city, Guangdong province, in China. The nuclear power plants which provide JUNO with the electron antineutrino flux are also shown.

reactor cores of the Yangjian and Taishan nuclear power plants are summarized in Table 2.2.

Table 2.2. The table summarizes the thermal powers and the baselines from the JUNO detector for the 8 nuclear reactor cores of the Yangjian (YJ) and Taishan (TS) NPPs, which contribute to the JUNO electron antineutrino flux. The contribution from DYB is also considered [29, 31].

Core	YJ-C1	YJ-C2	YJ-C3	YJ-C4	YJ-C5	YJ-C6	TS-C1	TS-C2	DYB
Power [GW]	2.9	2.9	2.9	2.9	2.9	2.9	4.6	4.6	17.4
Baseline [km]	52.74	52.82	52.41	52.49	52.11	52.19	52.77	52.64	215

As can be seen in Fig. 2.7, there is another distant NPP in the region around JUNO: the Daya Bay (DYB) NPP, which contributes to the antineutrino flux with a thermal power of about 17.4 GW and is located 215 km from the JUNO site, as listed in Table 2.2. Due to the long baseline, JUNO is not able to resolve the fast oscillation pattern, hence the Daya Bay NPP does not contribute to the NMO determination; nonetheless, the DYB flux affects the spectral shape, so it must be included in the analysis.

Nuclear power plants with a baseline greater than 300 km do not contribute to the oscillation analysis and are considered as a background, contributing about one signal event per day (see section 6.1.2 for more on backgrounds).

2.1.7 Taishan Antineutrino Observatory (TAO)

For the analysis of the reactor electron antineutrino spectrum, it is important to have a good reference for the unoscillated spectrum. Current models are in disagreement with recent data (see chapter 3 and [50–54] for more details), so a data-driven input would boost JUNO sensitivity. For these reasons, a satellite

experiment has been designed and is currently under construction: the Taishan Antineutrino Observatory (TAO).

TAO is placed about 44 m from one of the two cores of the Taishan nuclear power plant, and given the very short baseline and high flux from reactors, it is characterize by a very high statistics, with about 4000 expected reactor electron antineutrino signals per day. TAO is a Gadolinium-doped liquid scintillator detector with a target mass of 2.8 t. The inner surface of the acrylic vessel containing the liquid scintillator is covered by about $10\,\mathrm{m}^2$ of Silicon Photomultiplier (SiPM) with a PDE of about 50 % to detect the scintillation light produced after a neutrino interaction, for a total photocoverage of 94 %. The detector is operated at $-50\,^\circ\mathrm{C}$ to reduce the dark noise of the SiPM and the energy resolution is expected to be better than 2 % at 1 MeV. A schematic drawing of TAO is shown in Fig. 2.8 and more details can be found in [55].

A prototype of TAO is currently under construction at the Institute of High Energy Physics (IHEP), Beijing, China, and will be transported and installed at the Taishan nuclear power plant in 2024. Given the very high statistics, TAO is expected to provide a model-independent reference spectrum for JUNO after about one year of data-taking.
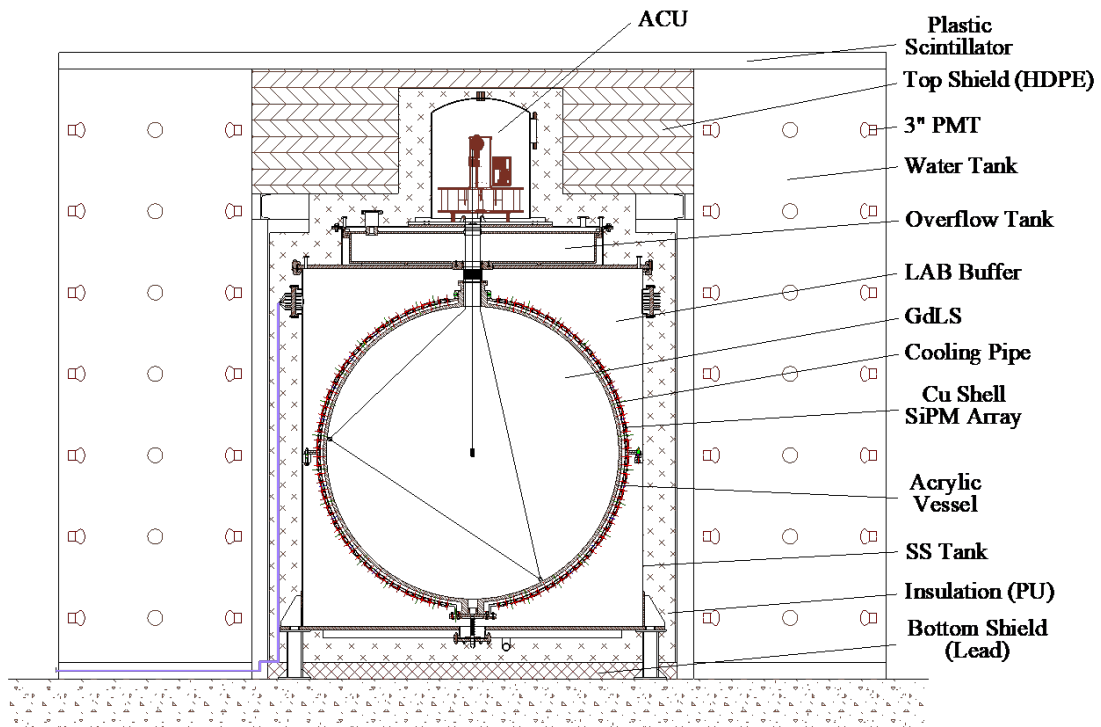
Figure 2.8. Schematic of the Taishan Antineutrino Observatory [31], JUNO satellite experiment located close to one of the Taishan reactor core.

2.2   Physics prospects beyond reactor electron antineutrinos

Although the JUNO experiment was mainly proposed to determine the neutrino mass ordering [56] and measure the values of some of the oscillation parameters with an unprecedented sub-percent precision [29], the physics program that can be addressed with JUNO is extensive. A brief summary of the physics prospects beyond the reactor analysis is now given; for a more detailed overview see [31], while for specific information see the references cited for each topic.

Geo-neutrinos

Geo-neutrinos are electron antineutrinos from the β decay of nuclides which are part of the decay chains of ^{238}U and ^{232}Th, which are stored inside the Earth. Given the fact that they have the same signature, they constitute an irreducible background to reactor electron antineutrinos (see section 6.1.2). Nonetheless, geo-neutrinos may themselves bring fundamental insights into the composition and internal structure of the Earth. By detecting geo-neutrinos, it would be possible to address questions such as the composition of the Earth, the chemical layering in the mantle, the nature of mantle convection, and the radiogenic contribution to the terrestrial heat flow. About 400 events per year are expected; JUNO will reach a precision on the flux of about 5 % in 10 years, with the current precision being greater than 15 %. A paper on this analysis is under preparation.

Solar neutrinos

Electron neutrinos are emitted in the fusion processes occurring inside the Sun through the pp and CNO chains. They may be used to test the MSW matter effect and improve the knowledge of solar physics, such as the metallicity problem, the fundamental physics of the sun, and will help to compare solar models with the data from helioseismology. JUNO is expected to detect solar neutrinos in the intermediate and high-energy ranges. In the former case, JUNO could improve Borexino results in a few years for neutrinos from ^{7}Be, pep, and CNO, depending on the radiopurity scenario [57]; in the latter case, JUNO is expected to reach a 5 % precision on the flux from ^{8}B in about 10 years of data-taking, and could also provide an independent measurement of the solar oscillation parameters, Δm_{21}^2 and $\sin^2 \theta_{12}$ [58, 59].

Atmospheric neutrinos

JUNO can perform the first measurement of atmospheric neutrinos with a liquid scintillator detector, and could provide significant insights on the flux in the 100 MeV to 10 GeV energy range. JUNO is able to discriminate the neutrino flavor, thus is expected to provide the ν_e and ν_μ spectra with a precision of 10 % to 25 % in 5 years of data-taking [60]. The detection of atmospheric neutrinos may also provide an independent determination of the mass ordering through matter effect in the Earth, and may help to determine the octant of the atmospheric mixing angle θ_{23}.

Core-Collapse Supernova

A galactic Core-Collapse Supernova (CCSN) emits 99% of its energy in the form of neutrinos and antineutrinos of any flavors. The rate of galactic CCSN is about 3 per century, so during its lifetime, JUNO has the potential to detect neutrinos from one SN explosions and determine the flavor content of the flux, the energy spectrum, and the time evolution of the signal, bringing insights into the mechanism of stellar core collapse [61].

Diffuse Supernova Neutrino Background

The JUNO experiment has also the potential to detect $\overline{\nu}_e$ from Supernovae explosions and observe for the first time the Diffuse Supernova Neutrino Background (DSNB). The measurement of the DSNB, *i.e.*, the integrated neutrino flux from all past core-collapse events in the visible universe, will provide information on the cosmic star-formation rate, the average core-collapse neutrino spectrum, and the rate of failed supernovae. JUNO is expected to see a few DSNB events per year in the energy range from $10\,\mathrm{MeV}$ to about $30\,\mathrm{MeV}$, which is not dominated by reactor or atmospheric $\overline{\nu}_e$. JUNO has a discovery potential of 3σ in about 3 years of data-taking, considering the nominal model; in case of no observation of the DSNB, it will provide more stringent limits and exclude some of the models [62]

Exotic physics

JUNO has also the potential to provide insights in more exotic physics, like the detection of dark matter at the MeV scale [63], the observation of the proton decay through the channel $p \rightarrow \nu + K^+$ [64], or look for damping signatures [65].

Chapter 3

Antineutrino production at nuclear reactors

A nuclear reactor core yields on average 6 electron antineutrinos per fission, *i.e.*, about $2 \cdot 10^{20}$ antineutrinos per second per GW of thermal power. More than 99% of the neutrinos are produced from β decay of neutron-rich fission products from the fission of four isotopes: ^{235}U, ^{239}Pu, ^{238}U, and ^{241}Pu. The neutrino flux and spectrum for each isotope are obtained by the superposition of thousands of β spectra from all possible β-decay branches of the fission fragments. The resulting isotopic spectra are the main ingredients for the prediction of the unoscillated spectrum at the source for an experiment at reactors, like JUNO; deformations due to neutrino oscillations are then applied to the unoscillated spectrum for the neutrino oscillation analysis.

The model used so far in reactor experiments to evaluate the unoscillated reactor flux and spectrum is the so-called Huber-Mueller (HM) model, which is introduced later in this chapter. However, some discrepancies between this model and data from recent short-baseline reactor experiments have been observed, thus indicating that the HM model is not able to properly reproduce the expected reactor spectrum. In particular, data displays a deficit of about 5% in the flux normalization with respect to the prediction [50]; furthermore, a distortion in the spectral shape at about $5\,\mathrm{MeV}$ has been observed by several experiments in the last decade [51–54]. Given the ambitious physics goals in the analysis of neutrino oscillations, JUNO needs a very precise and accurate modelling of the reactor antineutrino flux and spectrum. For this reason, a satellite detector, TAO (see section 2.1.7), is currently under construction very close to one of the Taishan nuclear cores to measure the reactor antineutrino flux and spectrum and provide a reference for JUNO. TAO will start data-taking at the same time as JUNO and will provide the reference flux and spectrum only after a few years. So, we need to investigate a new approach to evaluate the spectrum prediction for the first years of data-taking when TAO reference will not be available; this topic is the focus of this chapter.

The chapter is divided as the following: in section 3.1, we introduce the equation to evaluate the prediction of JUNO oscillated spectrum, where the reactor unoscillated spectrum is one of the ingredients; section 3.2 is dedicated to a review of the reactor isotopic spectra available in literature; then, the receipt to

evaluate JUNO spectrum is provided in section 3.3; in section 3.4, the time evolution of the spectrum is investigated; section 3.5 is dedicated to the uncertainty treatment; finally, we conclude in section 3.6.

3.1 Prediction of the reactor antineutrino flux and spectrum

The prediction for the expected reactor spectrum in JUNO is given by the following equation:

$$S^\nu(E_\nu) = N_p \cdot \sigma_{\text{IBD}}(E_\nu) \cdot \epsilon \cdot \int_0^T dt \sum_r \frac{S_r^\nu(E_\nu, t) \cdot P_{ee}(E_\nu, L_r)}{4\pi L_r^2}, \qquad (3.1)$$

where $S^\nu(E_\nu)$ is the total oscillated spectrum, expressed in units of number of antineutrinos per unit of energy [N_ν/MeV], and is obtained by summing the unoscillated antineutrino spectrum at each reactor r, $S_r^\nu(E_\nu, t)$. Each reactor spectrum is multiplied by the survival probability $P_{ee}(E_\nu, L_r)$, Eq. (1.19), and by a suppression factor due to the fact that the flux scales as the inverse of the squared of the distance, L_r; the baselines L_r are summarized in Table 2.2.

The quantity σ_{IBD} is the cross section of the interaction of an electron antineutrino with a proton through the inverse beta decay (IBD) process, introduced at the end of this section, and $N_p = 1.44 \cdot 10^{33}$ is the number of free protons in the liquid scintillator, while $\epsilon = 82.2\,\%$ is the IBD selection efficiency [29], as obtained by applying the selection cuts explained in section 6.2.2.

In Eq. (3.1), we operate an integration in time over the data-taking period T to take into account the time evolution of the unoscillated reactor spectrum, which will be the focus of section 3.4. The unoscillated reactor spectrum for reactor r is defined as:

$$S_r^\nu(E_\nu, t) = \frac{W_r(t)}{\sum_i f_{ir}\langle e_i \rangle} \sum_i f_{ir} S_i^\nu(E_\nu), \qquad (3.2)$$

and is expressed in units of number of antineutrinos per unit of energy per unit of time [N_ν/(MeV s)]. The reactor thermal power $W_r(t)$ is listed in Table 2.2 for the main reactor cores contributing to the total flux and may vary with time.

In a reactor core, there are four main isotopes undergoing fission and contributing to the antineutrino flux: ^{235}U, ^{239}Pu, ^{238}U, and ^{241}Pu. The fission fraction f_{ir} of isotope i for reactor r is defined as the number of fissions of isotope i over the total number of occurring fissions; ^{235}U is the dominant isotope, with the largest fission fraction. Fission fractions may differ for different cores depending on the fuel composition and, in general, are time-dependent: f_{235} decreases during a burn-up cycle while f_{239} and f_{241} increase with an almost fixed ratio; f_{238} is almost constant (see section 3.4 for more details). The quantity $\langle e_i \rangle$ is the mean energy released per fission for isotope i. Table 3.1 lists the values of the expected mean fission fractions for the JUNO experiment [29, 31] and the mean energies per fission [66].

Finally, $S_i^\nu(E_\nu)$ is the isotopic spectrum, *i.e.*, the electron antineutrino energy distribution per fission for each isotope i, expressed in units of number of antineutrinos per unit of energy per fission $[N_\nu/(\text{MeV fission})]$; sections 3.2 and 3.3 are dedicated to a thorough analysis of the spectra available in literature and the construction of the model for JUNO, respectively.

Table 3.1. List of the expected mean fission fractions for JUNO [29, 31], the effective fission fractions for Daya Bay [67], and the mean fission energies for the four main isotopes undergoing fission [66].

Isotope	JUNO f_i	Daya Bay f_i	$\langle e_i \rangle$ [MeV]
^{235}U	0.58	0.564	202.36
^{239}Pu	0.30	0.304	211.12
^{238}U	0.07	0.076	205.99
^{241}Pu	0.05	0.056	214.26

IBD cross section

An electron antineutrino enters the detector and interacts mostly with a free proton of the liquid scintillator (see section 2.1.2) through inverse beta decay (IBD), thus producing a positron and a neutron:

$$\bar{\nu}_e + p \longrightarrow e^+ + n. \tag{3.3}$$

This process has a threshold on the incoming antineutrino energy of $E_\nu^{\text{th}} \approx m_n - m_p + m_e \approx 1.806\,\text{MeV}$, where m_n, m_p, and m_e are the masses of the neutron, proton, and positron, respectively. An approximated equation for the IBD cross section is given by Strumia and Vissani in [68]:

$$\sigma_{\text{IBD}}(E_\nu) \approx 10^{-43} \, p_e \, E_e \, E_\nu^{a + b \ln E_\nu + c \ln^3 E_\nu} \quad [\text{cm}^2] \tag{3.4}$$

where p_e and $E_e = E_\nu - \Delta$ are the positron momentum and energy, respectively, with $\Delta = m_n - m_p \approx 1.293\,\text{MeV}$ being the mass difference between the neutron and proton, E_ν is the incoming antineutrino energy, and $a = -0.07056$, $b = 0.02018$, and $c = -0.001953$. The approximation of Eq. (3.4) is valid for $E_\nu \lesssim 300\,\text{MeV}$, so it is valid for antineutrinos from reactors since they have typical energies of a few MeV. The IBD cross section increases as a function of the antineutrino energy, as shown in Fig. 3.1.

3.2 Isotopic spectra

In this section, we review the available isotopic spectra, $S_i^\nu(E_\nu)$, which can be used in Eq. (3.2) to evaluate the unoscillated reactor spectrum.
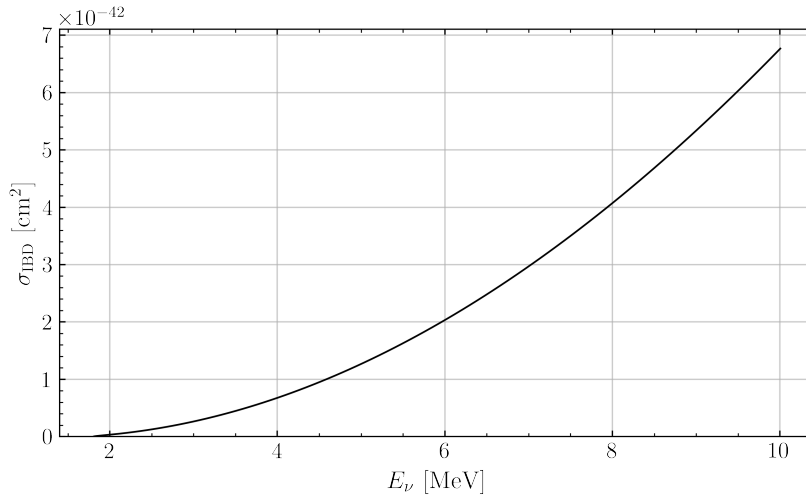
Figure 3.1. Cross section of the IBD process as a function of the electron antineutrino energy E_ν. The process has a threshold of $E_\nu > 1.806\,\text{MeV}$.

3.2.1   Conversion method

The conversion method is based on the measurements of β spectra done at the Institut Laue–Langevin (ILL), France, in the 1980's by means of a high resolution magnetic spectrometer [69–72]. Thermal neutrons were used to induce fission on ^{235}U, ^{239}Pu, and ^{241}Pu, and the energy of the electrons emitted by the β decay of the fission products was measured to obtain the total β spectrum for each isotope. Then, each β spectrum is converted into a $\overline{\nu}_e$ spectrum by solving an inversion or unfolding problem; refer to [73] for more details. The most recent conversion of the ILL β spectra to $\overline{\nu}_e$ spectra was done by Huber in 2011 [73]. The spectra are tabulated in the energy range from 1.875 MeV to 8.125 MeV with a bin width of 250 keV, and are shown in Fig. 3.2. These spectra are used in the standard Huber-Mueller (HM) model, which will be introduced later in section 3.3.

There are several sources of uncertainties in the conversion method, which are also tabulated in [73] and, as an example, are listed in the appendix in Table A.1 for ^{241}Pu. The sources of uncertainties strictly related to the inversion procedure are fully uncorrelated between bins (thus translating into a diagonal covariance matrix), while the uncertainties coming from the data normalization and from theory are fully correlated between bins (thus translating into a covariance matrix with non-null off-diagonal elements). The dominating uncertainties are the one from the normalization of the data and the statistical uncertainty from the conversion procedure, as it can also be seen in Table A.1.

At ILL, it was not possible to measure the β spectrum for ^{238}U because the cross section for fission induced by thermal neutrons is several orders of magnitude lower than for the other isotopes, as shown in Fig. 3.3. Nonetheless, fission on ^{238}U can be induced with fast neutrons, as it has been done in more recent time, as described in the next section.
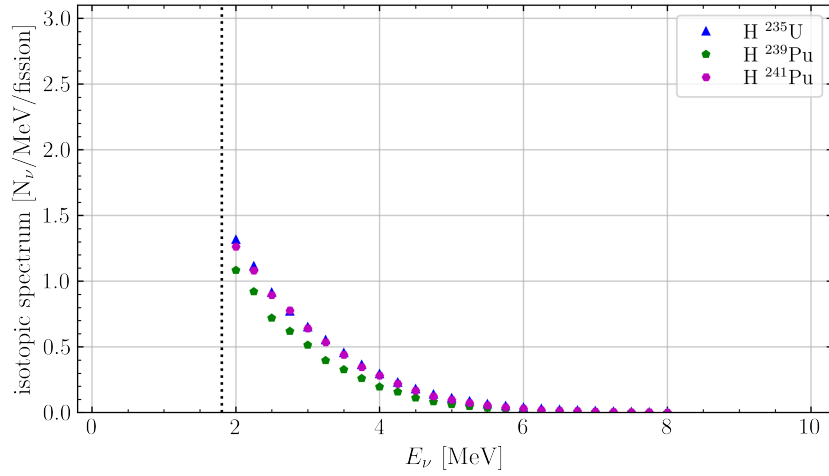
Figure 3.2. Available tabulated data obtained by conversion method of the ILL measured β spectra for ^{235}U, ^{239}Pu, and ^{241}Pu by Huber [73]. Data are tabulated with a bin width of $250\,$keV in the energy range from $1.875\,$MeV to $8.125\,$MeV. The vertical dotted line corresponds to the IBD threshold at $1.806\,$MeV.
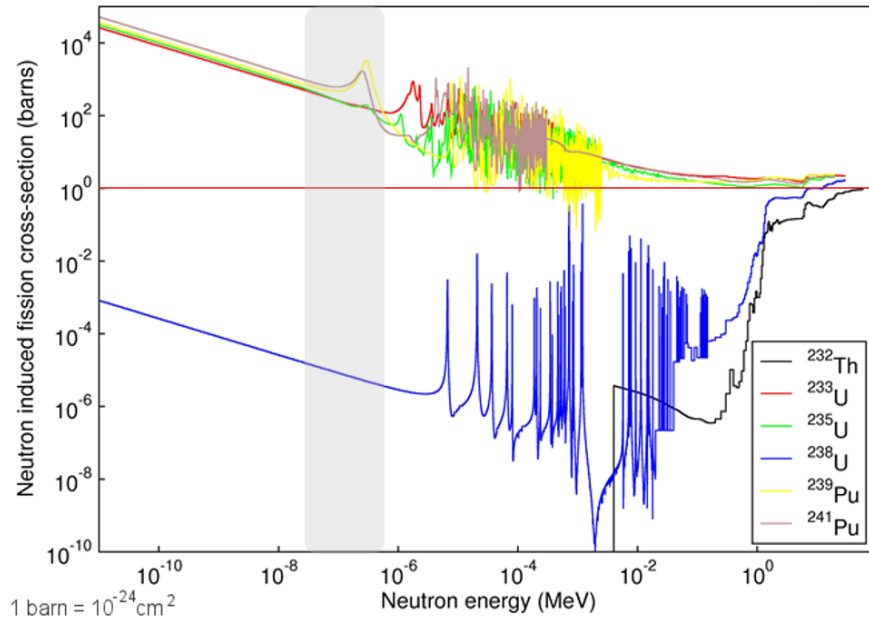
Figure 3.3. Fission cross section for ^{232}Th, ^{233}U, ^{235}U, ^{238}U, ^{239}Pu, and ^{241}Pu as a function of the neutron energy [74]. The vertical gray band corresponds to the energy range of thermal neutrons, used to induce fission of ^{235}U, ^{239}Pu, and ^{241}Pu at ILL. Fission of ^{238}U can be induced by using fast neutrons, with an energy above $1\,$MeV.

Non-equilibrium contribution to the antineutrino flux

It is important to note that the ILL data were taken with a rather short irradiation time, 12 h for ^{235}U, and 36 h for ^{239}Pu and ^{241}Pu. After this time, equilibrium was not reached, since there are several fission products with lifetime of a few days, which will continue to accumulate and provide an additional contribution to the neutrino flux. The non-equilibrium contribution has been evaluated by Mueller *et al.* [75] and is provided in tabulated data as relative corrections to the reference spectrum for several irradiation time. The correction due to the non-equilibrium effect is of the order of a few percent and is relevant below 3.5 MeV.

3.2.2 Recent measurement of the ^{238}U spectrum

In 2014, the first measurement of the β spectra for ^{238}U was performed by Haag *et al.* [76] at Garching, Germany, thus the first isotopic spectrum for ^{238}U from the conversion method was evaluated.

In this experiment, two target foils of natural uranium (0.7 % ^{235}U, 99.3 % ^{238}U) were irradiated, one with thermal neutrons to induce fission of ^{235}U and the other one with fast neutrons to induce fission of ^{238}U. The β spectrum for ^{235}U was measured and was normalized bin-wise to the measurement of the ^{235}U β spectrum done at ILL. Then, the same normalization was applied to the ^{238}U spectrum to reduce systematic uncertainties; in this way, the Garching ^{238}U β spectrum is fully correlated to the ^{235}U ILL measurement. The ^{238}U β spectrum is finally converted to an antineutrino spectrum and tabulated, and an estimation of the uncertainties is also provided.

The antineutrino isotopic spectrum for ^{238}U from the conversion method is shown in Fig. 3.4 in the energy range from 2.875 MeV to 7.625 MeV with a bin width of 250 keV. The spectrum starts almost 1 MeV above the IBD threshold due to the irreducible and indeterminable background of 2.2 MeV γ-rays from the neutron capture by the detector itself.

Furthermore, to minimize the non-equilibrium effect, the first 11 h of irradiation were not considered, and only the subsequent 42 h were used to determine the ^{238}U spectrum.

3.2.3 New normalization of ^{235}U and ^{238}U spectra

Recently, the ratio of the cumulative β spectra stemming from the fission of ^{235}U and ^{239}Pu has been measured at the Kurchatov Institute (KI), Russia [77]. The measured ratio, $R = S_{235}/S_{239}$, is shown in Fig. 3.5a in red, as a function of the total electron energy. The ratio is systematically lower than the one from the ILL data, shown in blue in the same figure.

By comparing the result obtained by this experiment and the measurement performed by the Daya Bay and RENO experiments, the difference in the ratio can be explained as an overestimation of the normalization of the ILL data for the ^{235}U β spectrum [78]. So, the ^{235}U β spectrum is renormalized by using the KI ratio of Fig. 3.5a. The new estimation of the ^{235}U antineutrino spectrum from the conversion of the renormalized ILL data is provided by Kopeikin *et al.* in [78]
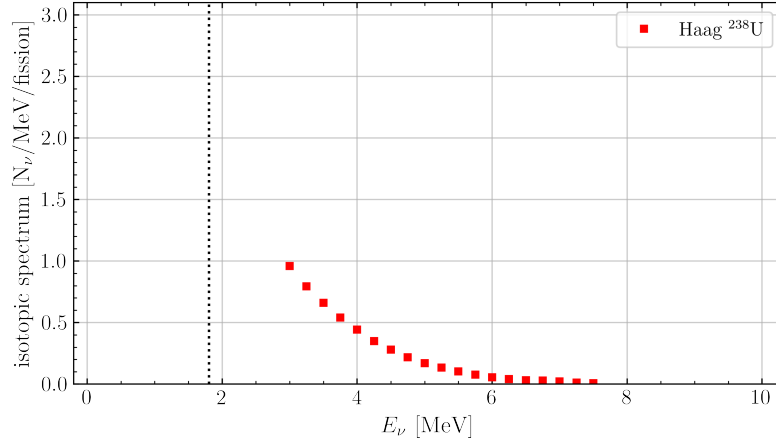
Figure 3.4. Tabulated data of the isotopic spectrum for ^{238}U obtained by conversion of the measured β spectrum by Haag *et al.* [76]. The data are given with a bin width of 250 keV in the energy range from 2.875 MeV to 7.625 MeV. The vertical dotted line corresponds to the IBD threshold at 1.806 MeV. The first point is above the IBD threshold due to background at low energy.

and shown in blue in Fig. 3.5b, in the energy range from 1.875 MeV to 8.125 MeV with a bin width of 250 keV.
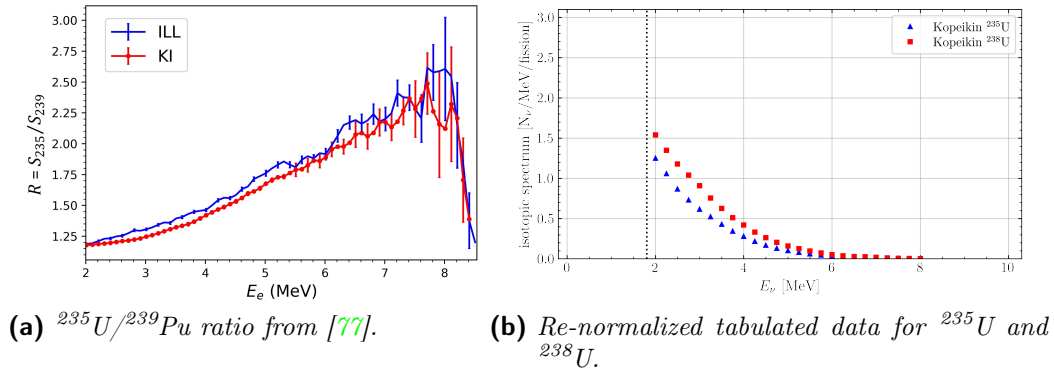
(a) $^{235}U/^{239}Pu$ *ratio from [77].*

(b) *Re-normalized tabulated data for* ^{235}U *and* $^{238}U.$

Figure 3.5. **(a)** Ratio of the cumulative β spectra of ^{235}U and ^{239}Pu from ILL [69–72] (in blue) and recent KI [77] (in red) data. **(b)** Re-normalized tabulated data for ^{235}U and ^{238}U from Kopeikin *et al.* [78]. Data are provided with a bin width of 250 keV in the energy range from 1.875 MeV to 8.125 MeV. The vertical dotted line corresponds to the IBD threshold at 1.806 MeV.

As explained in section 3.2.2, the antineutrino spectrum of ^{238}U measured by Haag *et al.* was obtained by fixing the normalization of the experimental data to the ILL ^{235}U data. Thus, the ^{238}U β spectrum presented in the previous section has to be re-normalized as well, and then converted to provide a new estimation for the ^{238}U antineutrino spectrum. The tabulated data are given in [78] and shown in red in Fig. 3.5b. Below 3 MeV, where the experiment at Garching could not provide a measurement of the spectrum, the spectrum is extended with previous data from [79].

3.2.4   Summation method

The summation, or *ab initio*, method calculates the neutrino flux from first principles and can provide a spectrum for all four main isotopes undergoing fission: ^{235}U, ^{239}Pu, ^{238}U, and ^{241}Pu. The method evaluates the $\overline{\nu}_\text{e}$ spectrum by summing together all beta decay branches from all fission products, and heavily relies on nuclear tabulated data (branching ratios, fission yields), which are sometimes incomplete or inaccurate. Furthermore, it's difficult to provide uncertainties to the spectra evaluated with this method.

The ^{238}U isotopic spectrum by Mueller *et al.* [75] is tabulated in Table A.2 in the appendix and shown in Fig. 3.6a in the energy range from 1.875 MeV to 8.125 MeV with a bin width of 250 keV. Several sources of uncertainties are also provided and listed in Table A.2; these uncertainties can be fully correlated, partially correlated, or fully uncorrelated between bins. The major source of uncertainty is given by the missing information of nuclear databases, with the uncertainty ranging from 10 % at low energies up to more than 20 % in the high energy part of the spectrum.

A more recent *ab initio* evaluation for the reactor $\overline{\nu}_\text{e}$ spectrum was provided by Estienne *et al.* in 2019 [80], and will be referred to as the "Estienne-Fallot" (EF) method in the rest of the manuscript; the spectra are shown in Fig. 3.6b in the energy range from 0 MeV to 10.1 MeV with a bin width of 100 keV. In this case, an updated uncertainty budget is not provided.
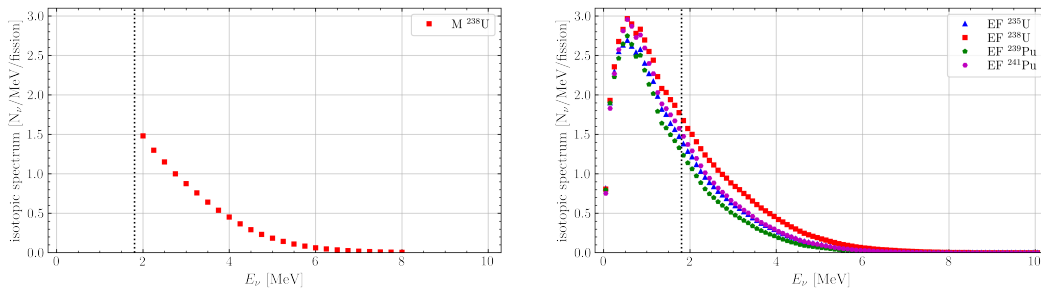
(a) *Tabulated data from Mueller* et al. *[75].*   **(b)** *Tabulated data from Estienne* et al. *[80].*

Figure 3.6. **(a)** Tabulated data from Mueller *et al.* [75] in the energy range from 1.875 MeV to 8.125 MeV with a bin width of 250 keV. **(b)** Most recent tabulated data obtained by the summation method for all isotopes by Estienne *et al.* [80] in the energy range from 0 MeV to 10.1 MeV with a bin width of 100 keV. The vertical dotted line corresponds to the IBD threshold at 1.806 MeV.

3.2.5   Direct measurement of the antineutrino spectrum

In recent years, isotopic spectra have become available from the direct detection of reactor electron antineutrinos by detectors at short distance from reactors, *e.g.*, the Daya Bay experiment (introduced in section 1.1.4). The Daya Bay experiment is able to separate the contributions from the various isotopes thanks to the time evolution of the fission fractions during a burn-up cycle; the time evolution will

be presented in detail in section 3.4. The Daya Bay experiment provided the first ^{235}U and ^{239}Pu spectra in prompt energy[1] in 2019 [81], and then applied an unfolding procedure to bring the spectra to antineutrino energy [67], so that other experiments could use them to build their prediction. The unfolding procedure is needed to remove the contribution of the detector response which is different for each experiment.

Since ^{241}Pu is the isotope with the lowest fission fraction, and does not change much during one burn-up cycle, it is difficult to separate its contribution from the other isotopes. For this reason, and to reduce the uncertainties, a combination of the two plutonium spectra is extracted, referred to as *Pu_combo*: $S_{\mathrm{pu\_combo}} = S_{239} + 0.183 \cdot S_{241}$, where the factor 0.183 is the average ratio of the fission fraction of ^{241}Pu to ^{239}Pu, based on Daya Bay data. Due to the fact that the *Pu_combo* spectrum is extracted with a fixed factor, it can only be used in the prediction for other experiments which are characterized by a similar fission fraction ratio of ^{241}Pu to ^{239}Pu, which is the case for the JUNO experiment.

Figure 3.7a shows the tabulated data provided by the Daya Bay experiment for the isotropic antineutrino spectra: the total spectrum in black, ^{235}U in blue, and *Pu_combo* in red; the spectra are provided in the supplemental material of [67]. In Fig. 3.7b, the spectra are weighted by the IBD cross section, Eq. (3.4). Data are provided with a bin width of 250 keV from 1.8 MeV to 7.8 MeV, while the last bin is from 7.8 MeV to 9.5 MeV, with the bin center at 8.65 MeV. The total spectrum corresponds to the Daya Bay effective fission fractions listed in Table 3.1, which were obtained by taking into account the distance between the reactor cores and the detectors, and the time-dependent thermal power of each core. Uncertainties are also provided in the form of a covariance matrix which includes the correlation between the three spectra and can be found in the supplemental material of [67].

In the extraction of Daya Bay spectra, the non-equilibrium effect (see section 3.2.1 and the contribution of the spent nuclear fuel (see paragraph below) are considered as additional contributions, thus they are not included in the tabulated spectra [81].

There are other experiments close to research reactors like PROSPECT [82] and STEREO [83]. Given that research reactors are characterized by a fuel with highly enriched uranium, these experiments can mainly extract the spectrum for ^{235}U. Since Daya Bay is providing the uncertainties as a covariance matrix between the three unfolded spectra, introducing a spectrum from another experiment will highly complicate the treatment of uncertainties, so input spectra from other experiments are not considered in this work.

Spent nuclear fuel   Every few months, part of the core is re-fuelled with fresh fuel, and the spent fuel is placed in water pools close to the reactor cores. Even though fission is no more induced, there are still long-lived isotopes that accumu-

---

[1]The prompt energy is defined as the reconstructed energy of the prompt signal, *i.e.*, the energy deposited by the final-state positron produced by the IBD interaction of an electron antineutrino with a proton of the liquid scintillator. More details about the reconstructed energy and the prompt signal can be found in sections 4.2 and 6.1.1, respectively.

(a) *Daya Bay isotopic spectra.*

(b) *Daya Bay weighted isotopic spectra.*
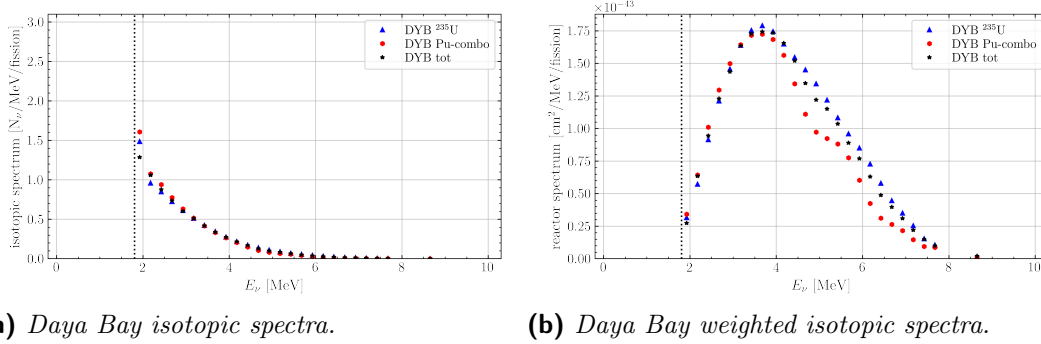
Figure 3.7. Available **(a)** isotopic spectra and **(b)** isotopic spectra weighted by the IBD cross section from the direct measurement of reactor electron antineutrinos by the Daya Bay experiment [67]. Data are provided with a bin width of 250 keV in the energy range from 1.8 MeV to 7.8 MeV, while the last bin is from 7.8 MeV to 9.5 MeV, with the bin center at 8.65 MeV. The spectrum of ^{238}U is not shown since it is not directly measured by the Daya Bay experiment.

lated during the operation of the core and can contribute to the antineutrino flux. The contribution of the spent nuclear fuel (SNF) was estimated by the Daya Bay experiment [81] and contribute a few percent in the energy region below 4 MeV.

3.3 Prediction for JUNO antineutrino spectrum at the source

Interpolation and extrapolation of the tabulated data

JUNO will use a much finer binning than the one of the tabulated data available in literature, in fact the bin width will be of the order of 10 keV rather than 100 keV. For this reason, it is important to properly interpolate the tabulated data with a function that doesn't add non-physical features. Furthermore, JUNO spectrum covers a broader energy range, adding bins at low energy below the first available data point, as well as at higher energies; for this reason, a proper extrapolation function must be used.

It was found that a good way to interpolate and extrapolate tabulated data is through an exponential inter-/extrapolation, which consists of a linear inter-/extrapolation of the logarithm of the data. The exponential inter-/extrapolation is used throughout the rest of the chapter. Furthermore, for better visualization, the isotopic spectra are multiplied by the IBD cross section of Eq. (3.4) before being plotted.

Building the model

There are two main models that can be used to evaluate the prediction for the total antineutrino reactor spectrum.

The first model, also referred to as "vanilla model", consists of a weighted sum of the single isotopic spectra, where the weight is given by the respective fission fraction:

$$S_{\text{JUNO}} = f_{235}S_{235} + f_{239}S_{239} + f_{238}S_{238} + f_{241}S_{241}, \qquad (3.5)$$

where f_i are JUNO fission fractions averaged over one burn-up cycle and are listed in Table 3.1. The model can be evaluated by using different inputs for the isotopic spectra. If the spectra for ^{235}U, ^{239}Pu, and ^{241}Pu are taken from Huber and the ^{238}U spectrum from Mueller *et al.*, we refer to this model as the *conversion summation mixed model*, or *Huber-Mueller (HM) model*, which is also the standard reactor model used so far by reactor experiments. If we use all spectra from Estienne *et al.*, we obtain a *pure summation model*, also referred to as *Estienne-Fallot (EF) model*.

The second model relies on the total spectrum measured by another reactor experiment, for example the Daya Bay experiment, and corrections are applied to take into account the differences in the fission fractions between JUNO and Daya Bay:

$$S_{\text{JUNO}} = S_{\text{total}} + \Delta f_{235}S_{235} + \Delta f_{239}S_{\text{pu\_combo}} + \Delta f_{238}S_{238} + (\Delta f_{241} - 0.183\Delta f_{239})S_{241}, \tag{3.6}$$

where S_{total}, S_{235}, and $S_{\text{pu\_combo}}$ are the unfolded spectra from Daya Bay, while S_{238} and S_{241} are taken from Mueller and Huber, respectively; $\Delta f_i = f_i^{JUNO} - f_i^{DYB}$ are the differences in the average fission fractions between JUNO and Daya Bay, where f_i^{DYB} are Daya Bay effective fission fractions (averaged over time and over the distance between the reactor cores and the detectors) and are listed in Table 3.1. This model will be referred to as the *antineutrino-driven model*, and, for brevity, as the *Daya Bay (DYB) model* since the spectra are taken from the Daya Bay experiment.

The antineutrino-driven model can also be expressed in matrix notation, which will be useful in the uncertainty treatment, as:

$$S_{\text{JUNO}} = R \cdot \begin{pmatrix} S_{\text{total}} \\ S_{235} \\ S_{\text{pu\_combo}} \\ S_{238} \\ S_{241} \end{pmatrix}, \qquad (3.7)$$

where R is the transformation matrix defined as:

$$\begin{aligned} R &= \left(\begin{array}{c|c|c|c|c} I_{25} & \Delta f_{235}I_{25} & \Delta f_{239}I_{25} & \Delta f_{238}I_{25} & (\Delta f_{241} - 0.183 \times \Delta f_{239})I_{25} \end{array} \right) \\ &= \left(\begin{array}{ccc|ccc|ccc|ccc|ccc} 1 & & & \Delta f_{235} & & & \Delta f_{239} & & & \Delta f_{238} & & & \cdots & & \\ & \ddots & & & \ddots & & & \ddots & & & \ddots & & & \ddots & \\ & & 1 & & & \Delta f_{235} & & & \Delta f_{239} & & & \Delta f_{238} & & & \cdots \end{array} \right), \end{aligned} \tag{3.8}$$

where I_a is the $a \times a$ identity matrix, and Δf_i are the difference in the fission fractions as defined above. The vertical vector on the right of Eq. (3.7) is a vector collecting, in the given order, the input spectra of the model; since all

inputs spectra are given in 25 tabulated bins, the vector has dimension 125×1. Following the same reasoning, $\boldsymbol{R}$ is a 25×125 matrix, and the final spectrum is a 25×1 vector.

The comparison between different models is shown in Fig. 3.8. The spectrum from the EF model, thus based on the summation method, is shown as a dashed red line, while the standard HM model is shown in dashed-dotted blue. The prediction obtained with the antineutrino-driven model is shown in black, and, as expected, it shows a deficit in the absolute normalization, and a bump in the spectral shape at about 5 MeV, if compared to the HM model. For comparison, the HM model with corrections from the Daya Bay experiment is also shown in green; the corrections are computed as the ratio between the measurement and the prediction in Daya Bay [84], thus this model is corrected for the normalization deficit and the spectral bump. A good agreement between the antineutrino-driven prediction and the prediction based on the corrected HM model can be seen.
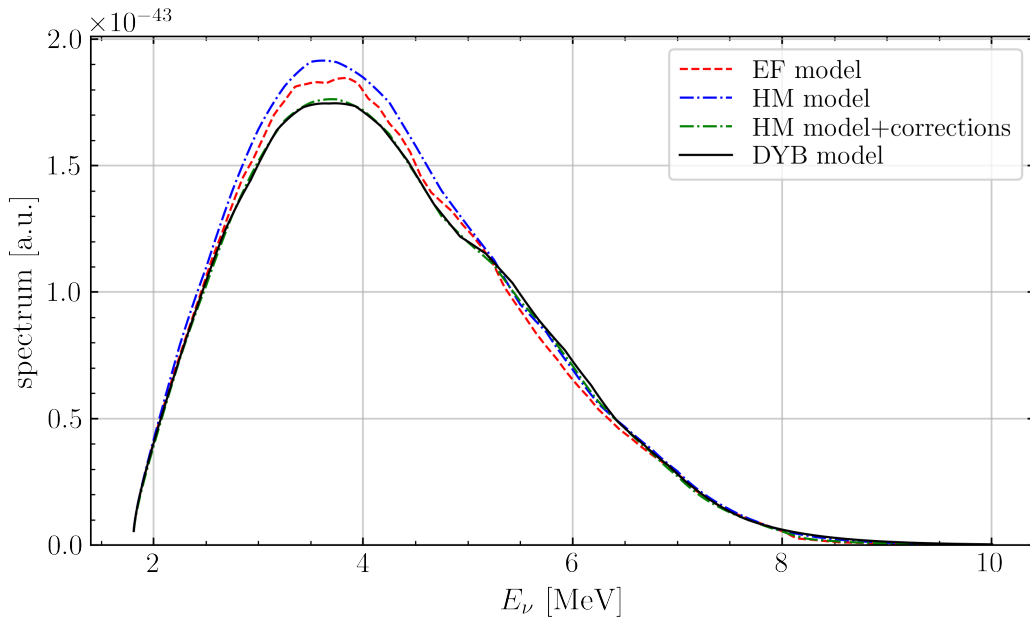
Figure 3.8. Comparison between different prediction of the JUNO spectrum based on the vanilla (red and blue) and antineutrino-driven (black) models. The HM model with corrections from the Daya Bay experiment taking into account the observed deficit in the normalization and spectral distortion is also shown in green.

Final receipt for JUNO reactor spectrum prediction

The model selected to be used in the oscillation analysis described in chapter 6 is the antineutrino-driven prediction of Eq. (3.6) since it naturally includes the deficit in the normalization and the spectral distortion at about 5 MeV, without the need of further corrections. For the analysis of the reactor spectrum in the first year of data-taking, the total, ^{235}U, and *Pu_ combo* spectra are taken from the Daya Bay experiment; for ^{241}Pu, the spectrum from the conversion method by Huber is used, while for ^{238}U the *ab initio* spectrum by Estienne *et al.* is used.

The choice of the *ab initio* spectrum for ^{238}U instead of a recent one from the conversion method is driven by the fact that the Garching spectrum displays the wrong normalization and the spectrum at low energies is missing; the spectrum from Kopeikin is excluded because it combines different measurements and it would be extremely difficult to get a consistent uncertainty budget. For the same reason, spectra provided by other reactor experiments, such as PROSPECT and STEREO, are excluded.

The choice of the antineutrino-driven model is also driven by the fact that TAO, JUNO satellite experiment introduced in section 2.1.7, is under construction close to one reactor core at the Taishan nuclear power plant. In fact, TAO is expected to provide a reference spectrum after about one year of data-taking, which can be used for the prediction of the JUNO spectrum, replacing the total spectrum from the Daya Bay experiment.

3.3.1 Mean cross section per fission

The cross section per fission, or IBD yield, for isotope i is defined as the integral of the isotopic spectrum $S_i^\nu(E_\nu)$ multiplied by the IBD cross section σ_{IBD}:

$$\sigma_i = \int_{E_{\mathrm{th}}}^{E_{\mathrm{max}}} dE_\nu\, S_i^\nu(E_\nu) \cdot \sigma_{\mathrm{IBD}}(E_\nu), \qquad (3.9)$$

where $E_{\mathrm{th}} = 1.806\,\mathrm{MeV}$ is the threshold of the IBD cross section, and E_{max} is the upper extreme of the integration, so the value of the IBD yield depends on the integration interval. The quantity to be integrated, $S_i^\nu \cdot \sigma_{\mathrm{IBD}}$, is shown in Fig. 3.9 for the four isotopes, where the isotopic spectra are taken from the HM model; the values of the IBD yield for the four isotopes are listed in Table 3.2. As it can be seen in the plot and by the values in the table, ^{238}U has the largest IBD yield, *i.e.*, it produces the largest number of neutrino interactions per fission compared to the other isotopes. Despite this, the number of fission processes from ^{238}U is low since fission of ^{238}U is mostly induced by fast neutrons, as explained in section 3.2.1, while neutrons inside nuclear reactors are mainly thermal neutrons. For this reason, its contribution to the antineutrino flux is less than $10\,\%$.

Table 3.2. IBD yields of the four isotopes undergoing fission; the isotopic spectra from the HM model are used.

Isotope	σ_i 10^{-43} [cm^2/fission]
^{235}U	6.64
^{239}Pu	4.36
^{238}U	10.12
^{241}Pu	6.04

The mean cross section per fission is obtained by weighing the IBD yield of each isotope with the respective fission fraction f_i:

$$\langle\sigma\rangle_f = \sum_i f_i\,\sigma_i. \qquad (3.10)$$
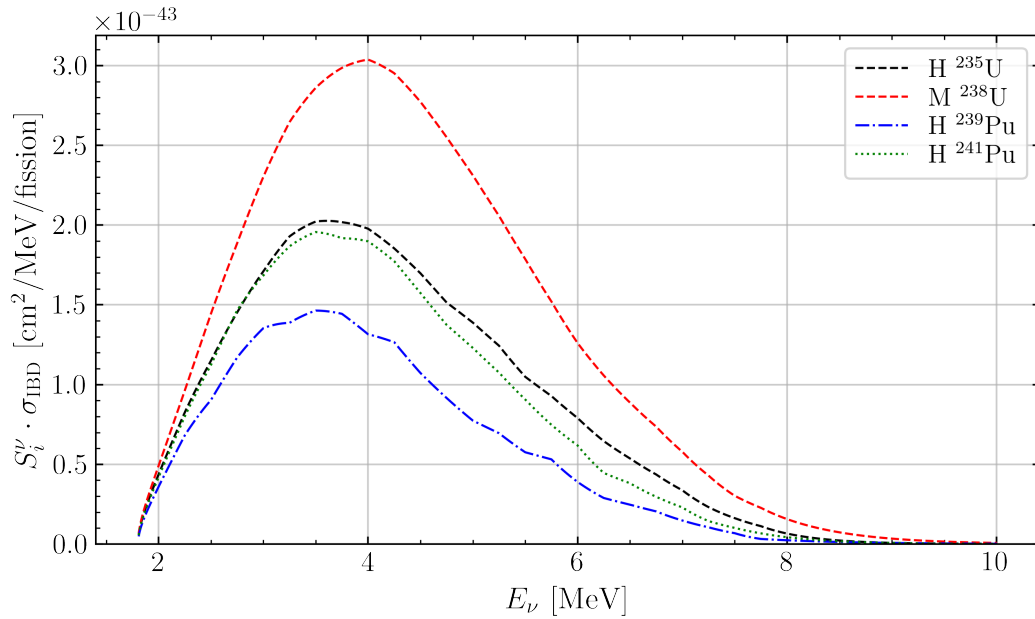
Figure 3.9. Product of the isotopic spectra $S_i^{\nu}(E_{\nu})$, taken from the HM model, and the IBD cross section σ_{IBD}. The integration of this quantity provides the cross section per fission of each isotope.

Both the IBD yield and the mean cross section per fission are expressed in units of area per fission [cm²/fission].

The mean cross section per fission is usually introduced to fix the absolute normalization of the reactor neutrino flux and to allow comparison between different models and experimental results. Given that the fission fractions change with time, $\langle\sigma\rangle_f$ also varies with time, while the IBD yields of Eq. (3.9) are fixed in time.

For the JUNO experiment, the following values were evaluated for the mean cross section per fission for the two models: $6.15 \cdot 10^{-43}$ cm²/fission for the HM model, and $5.83 \cdot 10^{-43}$ cm²/fission for the antineutrino-driven model, where the fission fractions in Table 3.1. These values can be compared to the ones measured by short-baseline reactor experiments: $\langle\sigma\rangle_f = (5.89 \pm 0.07) \cdot 10^{-43}$ cm²/fission for Daya Bay [85], and $\langle\sigma\rangle_f = (5.71 \pm 0.06) \cdot 10^{-43}$ cm²/fission for Double Chooz [54]. As expected, the value obtained with the antineutrino-driven model is consistent with the measured values.

It is worth to note that the ratio of the antineutrino-driven value to the vanilla value is 0.948, which is consistent with the observed 5 % deficit in the normalization of the flux based on recent reactor data compared to the standard HM model.

3.4   Time evolution

Fresh fuel is made up of Low Enriched Uranium (LEU), with different enrichment for the two nuclear power plants closest to JUNO: 95.55 % of ^{238}U and 4.45 % of ^{235}U for the Yangjian cores, while 97.02 % of ^{238}U and 2.98 % of ^{235}U for the Tais-

han cores; these values are taken from [86]. During the operation of the reactor core, ^{235}U undergoes fission induced by thermal neutrons, thus its concentration and contribution to the neutrino flux decrease with time. As already seen, ^{238}U mainly undergoes fission with fast neutrons; anyway, thermal neutrons can be captured producing ^{239}Pu and ^{241}Pu, so the concentration of these two isotopes increases with time as well as their contribution to the neutrino flux.

Usually, we are not interested in the changes of the composition of the fuel, rather in the changes of the fission fractions, which are not directly proportional to the changes of the isotope concentration. Indeed, the neutron flux slightly varies in time, contributing to the changes of the fission fractions.

Every 12-18 months, depending on the nuclear power plant, the core is re-fuelled with fresh fuel and a new burn-up cycle starts. The burn-up is the measure of how much energy is extracted from a primary nuclear fuel source, and is expressed in units of [MW d/tU] (energy per tonnes of initial Uranium in the fuel). The evolution of the fission fractions during one burn-up cycle for the Daya Bay experiment is shown in Fig. 3.10a [84]. Actually, only from 1/4 to 1/3 of the fuel is replaced with fresh fuel, and this explains why the fission fraction of ^{239}Pu is not zero at the beginning of the cycle. Since the contribution of ^{239}Pu increases during one cycle, the fission fraction of ^{239}Pu, f_{239}, is sometimes used as a unit of burn-up, hence of time, as in Fig. 3.10b.
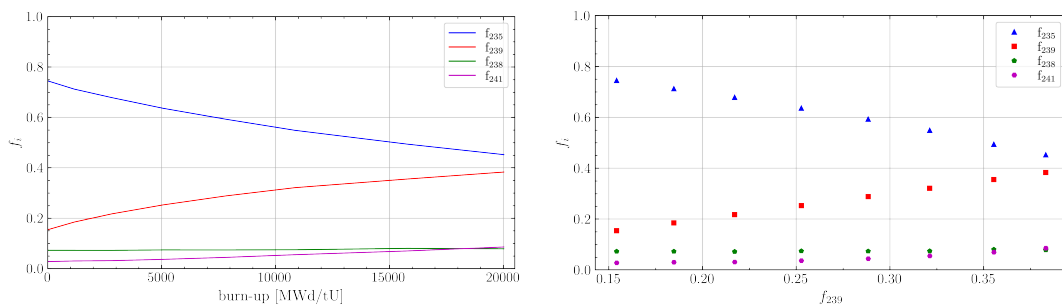
(a) *Fission fraction evolution as a function of burn-up.*

(b) *Fission fraction evolution as a function of f_{239}.*

Figure 3.10. **(a)** Evolution of the fission fractions during one burn-up cycle for one reactor core [84]. **(b)** Evolution of the fission fractions during one burn-up cycle as a function of f_{239} for a single core.

The spectrum at different times during one burn-up cycle, thus corresponding to different values of ^{239}Pu fission fraction f_{239}, are shown in Figs. 3.11a and 3.11b for the HM model and the antineutrino-driven model, respectively. The top panels show the spectral shape, while the bottom panels show the relative difference with respect to the spectrum at the beginning of the burn-up cycle, with $f_{239} = 0.1542$. From Fig. 3.11, it is clear that the changes in the fission fractions have an impact both on the rate and shape of the spectrum, as will be further discuss in sections 3.4.1 and 3.4.2, respectively.
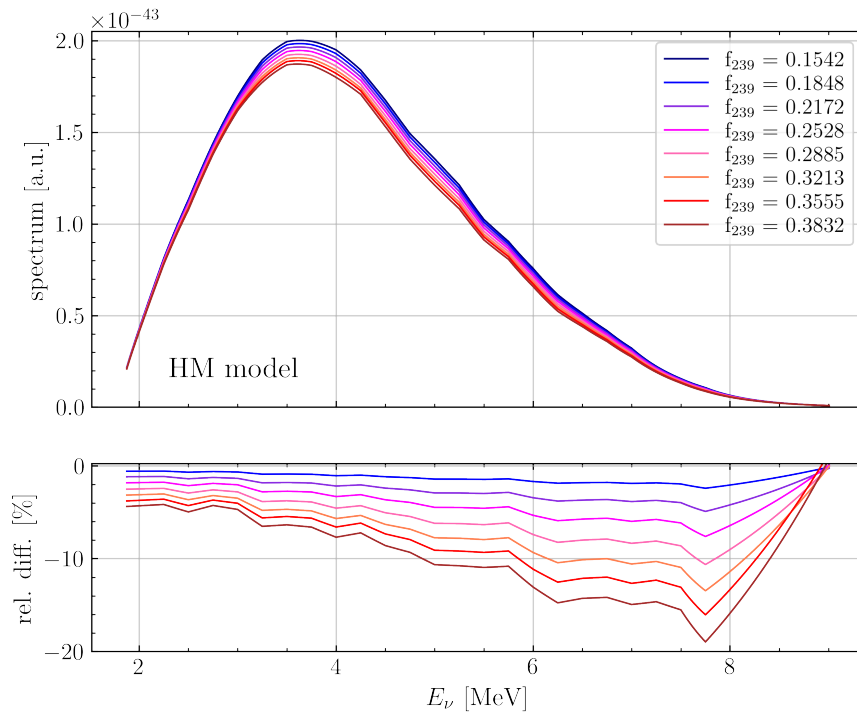
(a) *Spectral shape evolution for the HM model.*
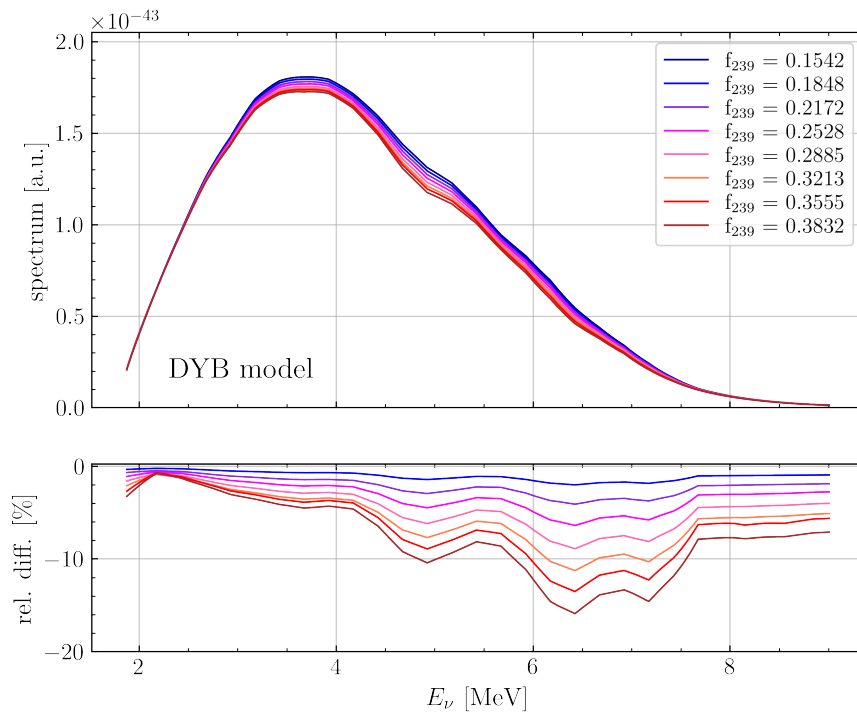
(b) *Spectral shape evolution for the antineutrino-driven model.*

Figure 3.11. Evolution of the reactor spectrum during one burn-up cycle for **(a)** the HM model and **(b)** the antineutrino-driven model. The top panels show the spectrum for different values of f_{239}, while bottom panels show the relative difference with respect to the spectrum at the beginning of the cycle ($f_{239} = 0.1542$). The spectral shapes are shown for a single core.

3.4.1 Evolution of the antineutrino rate

Now, we estimate the changes in the antineutrino rate due to the time evolution of the fission fractions.

As seen in section 3.3.1, the number of neutrino interactions induced by the fission of each isotope is fixed in time, while the mean cross section per fission has a time dependence as a result of the evolving fission fractions: its evolution in time is shown in Fig. 3.12a for the HM model (red) and for the antineutrino-driven model (blue and green). For the latter, two different values of the upper integration limit were used to show that the value of $\langle\sigma\rangle_f$ depends on the integration interval used in Eq. (3.9). As expected, the HM model overestimates the value of $\langle\sigma\rangle_f$ by 5 %–6 % over the whole burn-up cycle. For comparison, measured values from the Daya Bay experiment from [87] are also shown in black. Taking the antineutrino-driven model with the largest integration interval (blue points), the mean cross section per fission decreases by 6.48 % during one burn-up cycle.

Another quantity which varies with time is the fission rate:

$$R_f = \frac{W_{\mathrm{th}}}{\langle E\rangle_f}, \tag{3.11}$$

where W_{th} is the thermal power, which the nuclear power plant tries to keep as constant as possible during operation, and we assume to be constant in time. The quantity $\langle E\rangle_f$ is the mean energy per fission, which explicitly depends on the fission fractions:

$$\langle E\rangle_f = \sum_i f_i\langle e_i\rangle, \tag{3.12}$$

with i running over the four main isotopes undergoing fission, and $\langle e_i\rangle$ being the mean energies per fission of the four isotopes, as listed in Table 3.1. The time evolution of the fission rate is shown in Fig. 3.12b, where the thermal power of a Taishan core, $W_{\mathrm{th}} = 4.6\,\mathrm{GW}$, is used, and a reactor duty cycle of 100 % is assumed. During one burn-up cycle, the fission rate decreases by about 1.31 %. A similar result is obtained by considering the thermal power of a Yangjian core, $W_{\mathrm{th}} = 2.9\,\mathrm{GW}$.

Finally, we can combine the mean cross section per fission of Eq. (3.10) and the fission rate of Eq. (3.11) to get the antineutrino rate:

$$R_\nu = \frac{N_p\epsilon}{4\pi L^2} \cdot R_f \cdot \langle\sigma\rangle_f, \tag{3.13}$$

where $N_p = 1.44\cdot10^{33}$ is the number of target protons, $\epsilon = 82.2\,\%$ is the detection efficiency [29], and L is the detector baseline from the reactor. For a Taishan core, with $W_{\mathrm{th}} = 4.6\,\mathrm{GW}$ and $L = 52.77\,\mathrm{km}$, the time evolution of the antineutrino rate over a burn-up cycle is shown in Fig. 3.12c. At the beginning of the cycle, the antineutrino rate is 25.10 IBD/d, while at the end of the cycle it goes to 23.16 IBD/d, showing a 7.70 % decrease. The values reported here are obtained without applying neutrino oscillations; in fact, considering neutrino oscillations, R_ν reduces to about 7.5 IBD/d. A similar result is obtained for a Yangjian core.

JUNO results on the reactor spectrum analysis depends on the amount of data collected, in fact current sensitivities are estimated assuming a statistics of about

10^5 IBD events in 6 years of data-taking, so it is important to take into account the reduction of the antineutrino flux over time to have an accurate estimation of the statistics.

3.4.2   Evolution of the spectral shape

As shown in Fig. 3.11, the spectral shape is also affected by the time evolution of the fission fractions, and the spectral change is energy-dependent. The changes in the spectral shape can be evaluated more quantitatively with the procedure used by the Daya Bay experiment in [85, 87].

The procedure is the following.

1. We calculate the spectrum at different burn-up times, corresponding to 8 different values of the ^{239}Pu fission fraction, f_{239}: 0.1542, 0.1848, 0.2172, 0.2528, 0.2885, 0.3213, 0.3555, 0.3832.

2. The antineutrino energy range is divided into 6 energy bins: 1.88-3 MeV, 3-4 MeV, 4-5 MeV, 5-6 MeV, 6-7 MeV, and 7-9 MeV.

3. For each energy bin, the mean cross section per fission σ_j is evaluated for each spectrum corresponding to a different value of f_{239}, where j identifies the energy bin. The integration interval in Eq. (3.10) is given by the limits of the energy bin.

4. For each bin, we evaluate $\overline{\sigma}_j$ as the mean of σ_j.

5. For each bin, the ratio $\sigma_j/\overline{\sigma}_j$ is plotted as a function of f_{239}, as shown in Fig. 3.13 for the antineutrino-driven (blue) and the HM (red) models; each panel corresponds to one of the energy bins defined in the first bullet point.

6. A linear fit is performed to get the slope, $(\overline{\sigma}_j)^{-1} d\sigma_j/df_{239}$, which quantify the changes of the spectrum over time at different energies. The best fit lines are also shown as dotted lines in Fig. 3.13.

7. Finally, the values of the slope are plotted as a function of the antineutrino energy in Fig. 3.14.

The procedure above is performed both for the HM model and the antineutrino-driven model. Figure 3.14 shows that the changes in the spectral shape are indeed energy-dependent, and the spectrum is more affected by the time evolution of the fission fractions at high energies. Furthermore, the HM model, shown in red, displays a steeper slope over the whole energy range, compared to the antineutrino-driven model, shown in blue. For each point, the horizontal bar corresponds to the width of the energy bin, while the vertical bar shows the uncertainty on the slope.

The uncertainty on the slope is evaluated by means of ToyMC spectra. The procedure above, from step 1. to step 6., is repeated 10 000 times. Each time, the spectra at point 1. are sampled from the nominal spectra by including uncertainties in the form of the covariance matrix $\boldsymbol{V}_{\text{JUNO}}$ of Eq. (3.14) (introduced in the next section); the function `scipy.stats.multivariate_normal.rvs` from the `scipy` package is used. The values of the slopes that are found at each repetition
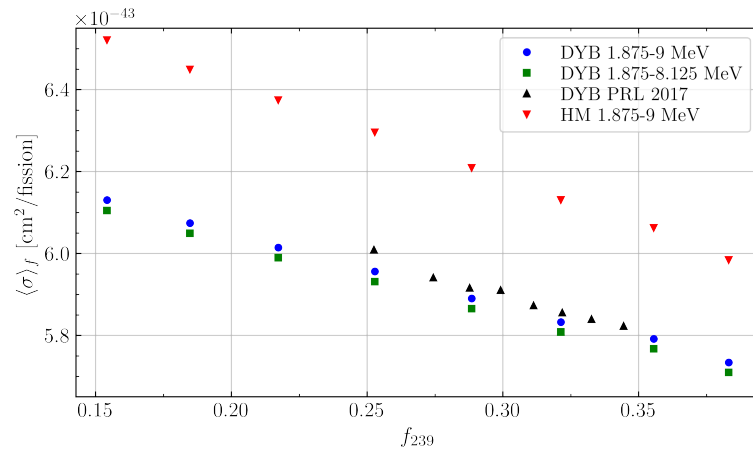
(a) *Time evolution of the mean cross section per fission, $\langle\sigma\rangle_f$.*
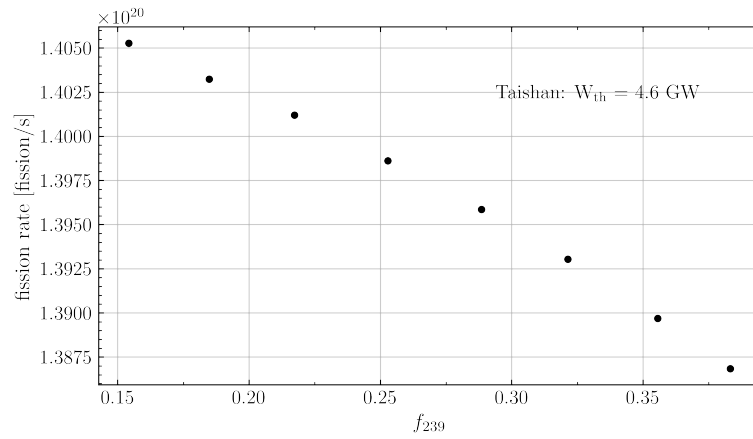
(b) *Time evolution of the fission rate, R_f.*
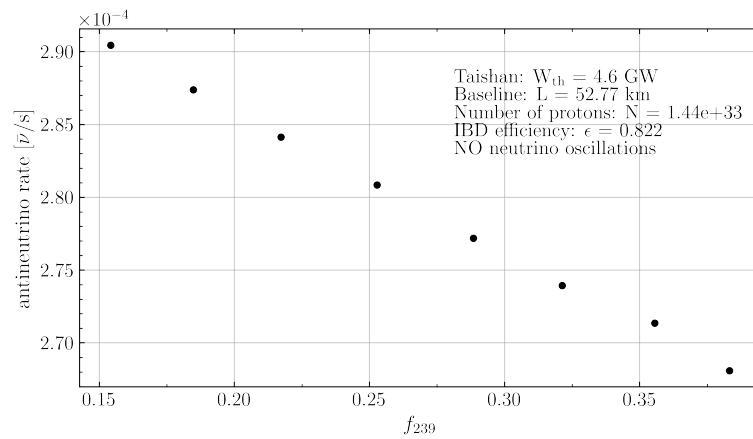
(c) *Time evolution of the antineutrino rate, R_ν.*

Figure 3.12. **(a)** Time evolution of the mean cross section per fission, Eq. (3.10), during one burn-up cycle for different models and integration intervals. **(b)** Time evolution of the fission rate, Eq. (3.11), during one burn-up cycle for a Taishan core. **(c)** Time evolution of the antineutrino rate, Eq. (3.13), for a Taishan core. The fission fraction of ^{239}Pu, f_{239}, is used as the unit of time. See the text for more details.
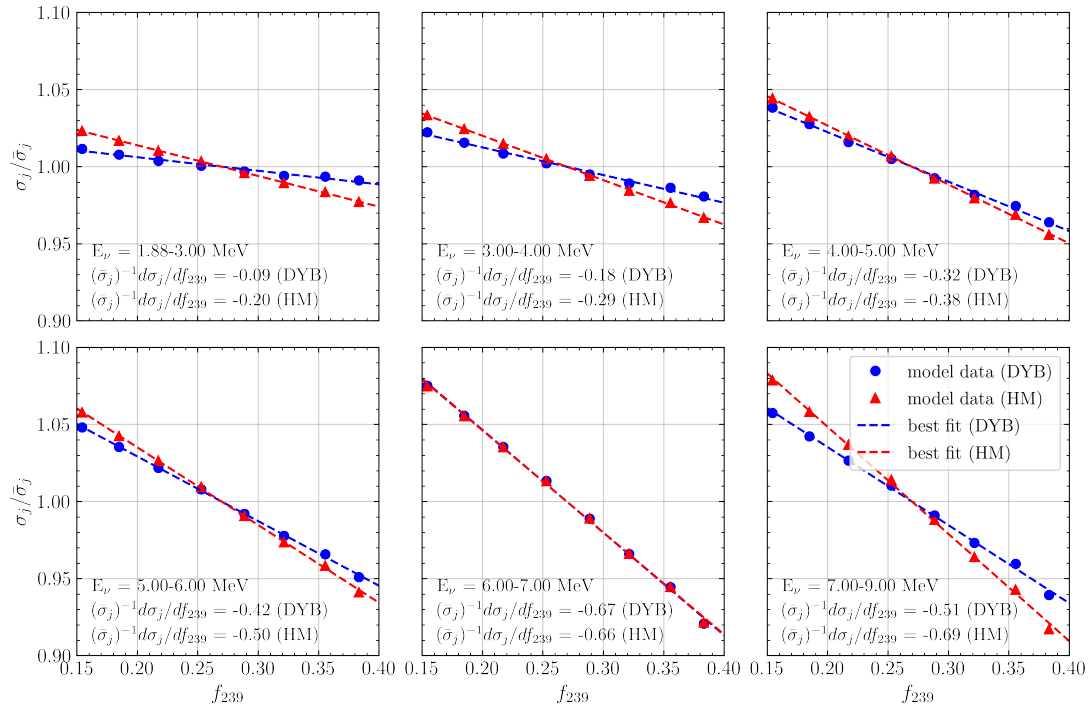
Figure 3.13. Change in the spectral shape in the 6 energy bins for the antineutrino-driven (blue) and HM (red) models. Each panel shows the ratio $\sigma_j/\overline{\sigma}_j$ as a function of f_{239}. The best fit lines from the linear fit are also shown. In the fifth panel, corresponding to the energy bin from $6\,\mathrm{MeV}$ to $7\,\mathrm{MeV}$, the two lines are overlapping.

are used to fill an histogram, one for each energy bin. Finally, the standard deviation of the values in the histogram is taken as the slope uncertainty for that energy bin.

The behavior of the antineutrino-driven model in the last two points in Fig. 3.14 might be explained by the fact that Daya Bay tabulated data present a wider last bin, thus it may be related to the interpolation and extrapolation procedures.
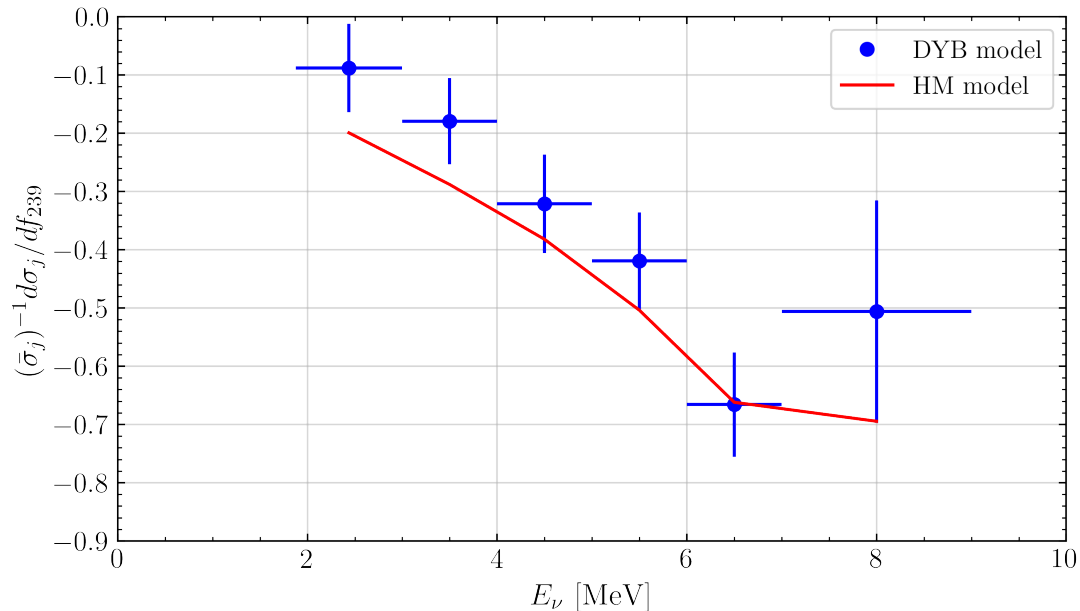
Figure 3.14. Spectral shape change, $(\overline{\sigma}_j)^{-1}d\sigma_j/df_{239}$, as a function of the antineutrino energy, for the antineutrino-driven (blue) and HM (red) models.

3.5 Uncertainty treatment

To use the predicted reactor spectrum to extract the neutrino oscillation parameters, it is important to provide a proper uncertainty budget together with the predicted spectrum. This topic is now detailed. First, we introduce the uncertainty propagation which employs the matrix notation introduced in section 3.3, equations (3.7) and (3.8); then, the uncertainties on the tabulated spectra are described; finally, a study on the 2D interpolation of the covariance matrix to match JUNO finer binning is presented.

3.5.1 Uncertainty propagation

It is convenient to use the matrix notation introduced previously to propagate the uncertainties on the input spectra to the predicted spectrum. We can use the fact that the covariance matrix of a random vector $\boldsymbol{Y} = \boldsymbol{R} \cdot \boldsymbol{X}$ obtained by applying a transformation matrix $\boldsymbol{R}$ to another random vector $\boldsymbol{X}$ with covariance $\boldsymbol{V}_{\mathrm{X}}$ can be written as $\boldsymbol{V}_{\mathrm{Y}} = \boldsymbol{R} \cdot \boldsymbol{V}_{\mathrm{X}} \cdot \boldsymbol{R}^{T}$. Thus:

$$\boldsymbol{V}_{\mathrm{JUNO}} = \boldsymbol{R} \cdot \boldsymbol{V}_{\mathrm{inputs}} \cdot \boldsymbol{R}^{T}, \tag{3.14}$$

where $\boldsymbol{R}$ is the transformation matrix of Eq. (3.8), and $\boldsymbol{V}_{\text{JUNO}}$ is the covariance matrix of JUNO prediction from the antineutrino-driven model, Eqs. (3.6) and (3.7).

The structure of the input covariance matrix $\boldsymbol{V}_{\text{inputs}}$ is displayed in Fig. 3.15, where the big box corresponds to the 75×75 bin covariance matrix provided by the Daya Bay experiment, and the small boxes are all 25×25 bin matrices, with the matrices related to the ^{238}U and ^{241}Pu spectra along the diagonal. The "off-diagonal" matrices are null matrices; in fact, the correlations between the Daya Bay spectra, the ^{238}U spectrum and the ^{241}Pu spectrum are null since these inputs are independent from each other.
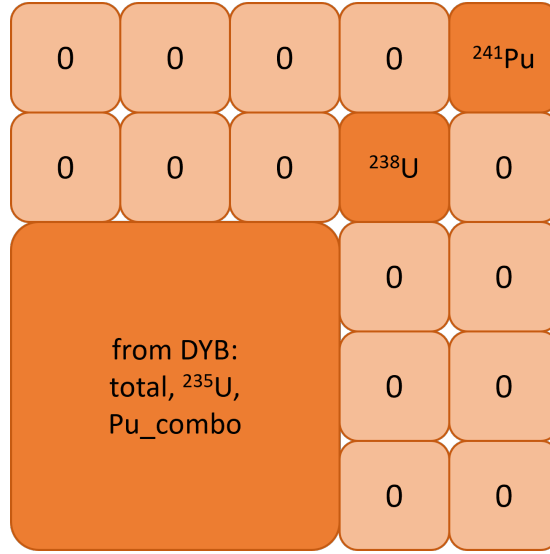
Figure 3.15. Structure of the input covariance matrix $\boldsymbol{V}_{\text{inputs}}$ to be used in Eq. (3.14).

3.5.2   Covariance matrices of the input spectra

From the several sources discussed in section 3.2, uncertainties are given in different formats: tabulated uncorrelated uncertainties between bins; tabulated fully correlated uncertainties between bins; or already in the form of a covariance matrix with partial correlations.

Bin-uncorrelated uncertainties correspond to a diagonal covariance matrix, with the diagonal elements equal to the uncertainty squared: $\sigma_{ii} = \sigma_i^2$, where the index i runs over bins. The covariance matrix for the bin-correlated contributions presents non-null off-diagonal elements and is obtained by exploiting the definition of the covariance: $\sigma_{ij} = \rho_{ij} \cdot \sigma_i \cdot \sigma_j$, where ρ_{ij} is the correlation coefficient between the i-th and j-th bin. Since the bins are fully correlated, it implies that $\rho_{ij} = 1 \; \forall i, j$, thus $\sigma_{ij} = \sigma_i \cdot \sigma_j$.

The uncertainties are provided as relative uncertainties. To obtain an absolute uncertainty, each matrix element σ_{ij} is multiplied by the value of the isotopic spectrum S: $V_{ij} = \sigma_{ij} \cdot S_i \cdot S_j$. To have the uncertainty for the reactor spectrum, the elements of the covariance matrix are further multiplied by the IBD cross

section[2] ξ^{IBD} of Eq. (3.4): $V_{ij} = \sigma_{ij} \cdot S_i \cdot S_j \cdot \xi_i^{\mathrm{IBD}} \cdot \xi_j^{\mathrm{IBD}}$.

In the rest of the chapter, covariance matrices are displayed using a power law scale instead of a linear scale, so that the structure of the off-diagonal elements, which are smaller with respect to the diagonal elements, can still be distinguished.

Plutonium-241

The uncertainties for the ^{241}Pu spectrum are taken from Huber [73] and are listed in Table A.1 in the appendix, with different columns corresponding to different contributions. Two sources of uncertainties, strictly related to the inversion procedure, are uncorrelated between bins, while the uncertainties coming from the data normalization and from theory are fully correlated between bins. The binning is the same as the one of the spectrum: 25 bins from 1.875 MeV to 8.125 MeV with a bin width of 250 keV.

The covariance matrix is evaluated for each uncertainty contribution as explained above; the total covariance matrix is finally obtained as the sum of the single covariance matrices, and is shown in Fig. 3.16a. The total correlation matrix, obtained from the total covariance matrix as $\rho_{ij} = \sigma_{ij}/\sigma_i\sigma_j$, is also shown in Fig. 3.16b. The covariance matrix of Fig. 3.16a is used to fill the 25x25 bin matrix related to ^{241}Pu in the input covariance matrix $\boldsymbol{V}_{\mathrm{inputs}}$ of Fig. 3.15.
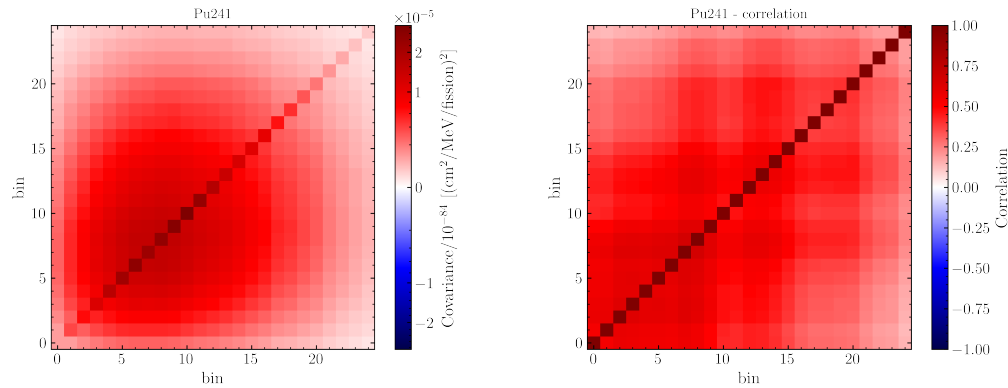
(a) ^{241}Pu covariance matrix.

(b) ^{241}Pu correlation matrix.

Figure 3.16. **(a)** Covariance matrix and **(b)** correlation matrix for ^{241}Pu in the original binning [73].

Uranium-238

In the reactor spectrum prediction, we use the spectrum from Estienne *et al.* [80] for ^{238}U. Since Estienne *et al.* did not provide a new estimation of the uncertainty budget, and given that their spectrum it's just an updated version of the one from Mueller *et al.* [75], we decided to use the relative uncertainties from the latter.

---

[2]Even though the Greek letter σ is used to identify the IBD cross section throughout this work, here we use the Greek letter ξ to avoid confusion with σ as a symbol for uncertainties.

The uncertainties for ^{238}U are thus taken from Mueller *et al.* and are listed in Table A.2 in the appendix. Analogous to ^{241}Pu, the uncertainties for ^{238}U are also divided into uncorrelated and fully correlated, even though the contributions have different origins given that for ^{238}U the summation method is used. The major source of uncertainty is given by the missing information of nuclear databases. The binning of the matrix is the same as the one of the spectrum provided in the reference: 25 bins from $1.875\,\text{MeV}$ to $8.125\,\text{MeV}$ with a bin width of $250\,\text{keV}$. The total covariance matrix is shown in Fig. 3.17a and is used to fill the 25x25 bin matrix related to ^{238}U in the input covariance matrix $\boldsymbol{V}_{\text{inputs}}$ of Fig. 3.15. The total correlation matrix is also shown in Fig. 3.17b; compared to ^{241}Pu, there is almost no correlation between bins of the ^{238}U spectrum.

In Fig. 3.17, the uncertainty obtained from the propagation of the uncertainties in the nuclear databases is considered as uncorrelated between bins. Actually, this source of uncertainty induces partial correlations at low energies, below $3.5\,\text{MeV}$. It is found that the effect of the partial correlation induced by this uncertainty source can be neglected in the following study; see section A.3 in the appendix for more details.

In this isotope, to obtain the absolute value starting from the relative uncertainty value, the covariances are multiplied by the value of the isotopic spectrum from Estienne *et al.*, which is the one selected for the reactor spectrum prediction; since Estienne's spectrum is provided with a different binning, the spectrum is first interpolated and then used to get the absolute uncertainty value. The multiplication with the IBD cross section is also applied.

(a) ^{238}U covariance matrix.   (b) ^{238}U correlation matrix.
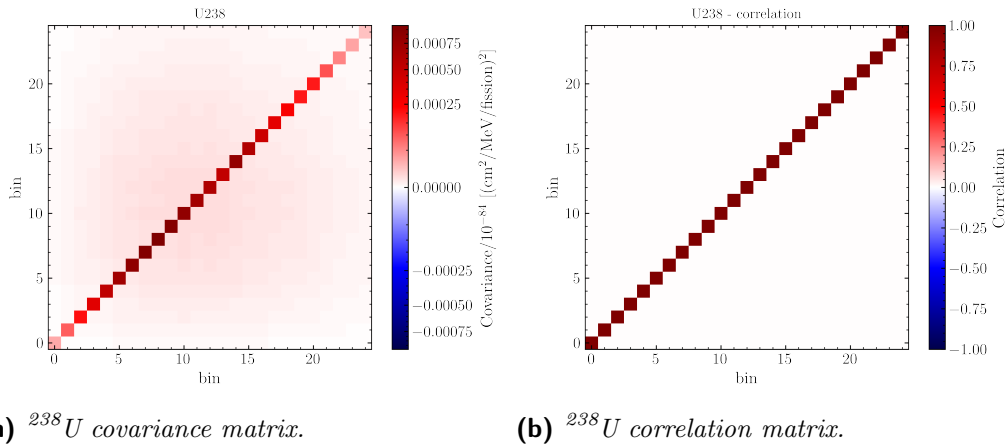
Figure 3.17. (a) Covariance matrix and (b) correlation matrix for ^{238}U in the original binning [75].

Daya Bay

The covariance matrix for the spectra from the Daya Bay experiment is directly provided by the Daya Bay collaboration in the supplemental material of [67]. The matrix is already in units of $(\text{cm}^2/\text{MeV/fission})^2$, so no further manipulation is required. The covariance matrix is shown in Fig. 3.18a, while the corresponding

correlation matrix is shown in Fig. 3.18b. The matrix of Fig. 3.18a is used to fill the 75x75 bin matrix related to the Daya Bay spectra in the input covariance matrix $\boldsymbol{V}_{\text{inputs}}$ of Fig. 3.15.

The three 25x25 blocks along the diagonal correspond to the covariance matrices for the total spectrum S_{total}, the ^{235}U spectrum S_{235}, and the *Pu_combo* spectrum $S_{\text{pu\_combo}}$, respectively. The off-diagonal blocks incorporate the correlations among the three spectra.

Daya Bay spectra are provided in 25 bins; the first 24 bin centers range from 1.8 MeV to 7.8 MeV with a bin width 250 keV, while the last bin is centered at 8.65 MeV with a bin width of 1.7 MeV, incorporating the high energy part of the spectrum in one bin.
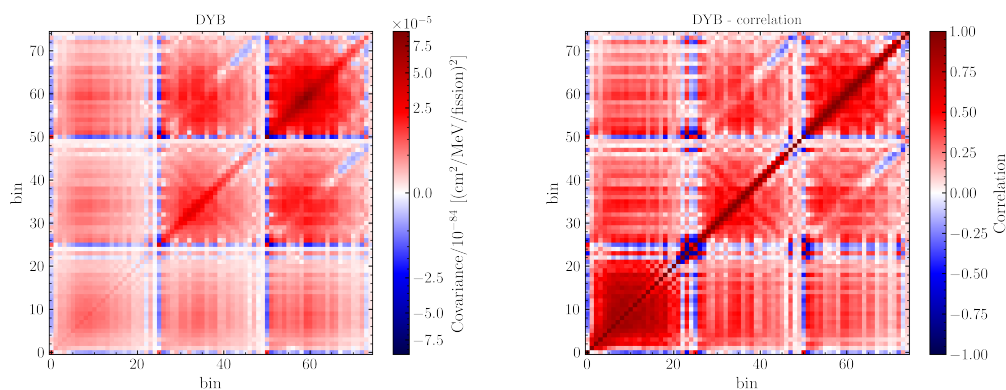
(a) *Daya Bay covariance matrix.*   **(b)** *Daya Bay correlation matrix.*

Figure 3.18. **(a)** Covariance matrix and **(b)** correlation matrix for Daya Bay in the original binning [67]. The diagonal 25x25-bin blocks correspond to the total spectrum S_{total}, the ^{235}U spectrum S_{235}, and the *Pu_combo* spectrum $S_{\text{pu\_combo}}$, respectively.

3.5.3   Interpolation of the covariance matrix

As already mentioned in section 3.3, JUNO will use a smaller bin width, thus it is crucial to find a way to interpolate the covariance matrix to match the desired binning. This task is not trivial, and several methods are investigated in this section. As an example and for simplicity, we work on the covariance matrices of ^{241}Pu and ^{238}U, and try to double the bin number, thus going from 25 to 50.

First, we try several multivariate methods which are already available in several python packages; then, we try the interpolation of the tabulated uncertainties; finally, we investigate several methods based on ToyMC samples.

Multivariate methods

Several multivariate methods which directly perform a 2D interpolation are tested. Results for ^{241}Pu and ^{238}U are shown in Figs. 3.19 and 3.20, respectively; as a reference, the original covariance matrix is shown on panel **(a)**, at the top left.

The matrices in panels **(b)** and **(c)** are obtained by means of the following `scipy` function: `scipy.interpolate.interp2`. The matrix in panel **(d)** is evaluated with the Inverse Distance Weighted (IDW) interpolation, which is usually used with a known scattered set of points. The value assigned to an unknown point is calculated with a weighted average of the values available at the known points, where the weights are the inverse of the distance between the unknown point and the known points. The matrix in panel **(e)** is obtained with the Radial Basis Function (RBF) interpolation, which is based on the weighted sum of radial basis functions.

It can be seen by eye that the multivariate methods described above introduce patterns that are not there in the original matrix, especially for ^{238}U, where negative off-diagonal elements appear. The method with the best performance seems to be the 2D linear interpolation, but it still introduces an oscillatory pattern along the main diagonal.
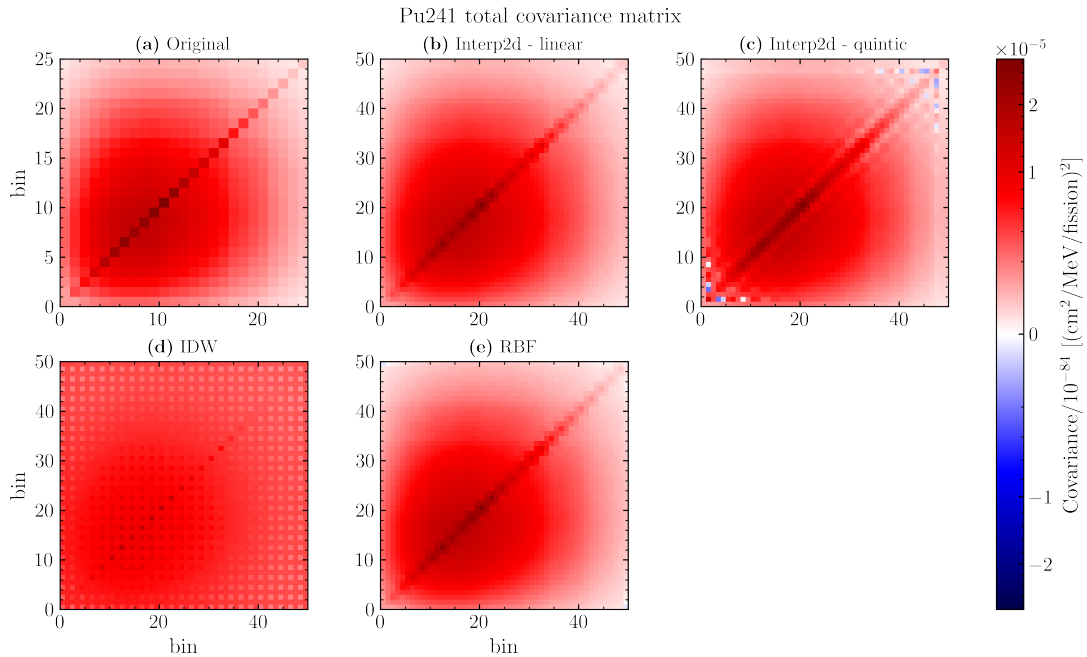
Figure 3.19. Comparison between the covariance matrices obtained by several multivariate methods for ^{241}Pu: for **(b)** and **(c)**, a 2-dimensional interpolation from the `scipy` package is used; for **(d)**, the Inverse Distance Weighted (IDW) interpolation is used; for **(e)**, the Radial Basis Function (RBF) interpolation is used. The matrix in the original binning is shown in panel **(a)**. See the text for more details.

1D interpolation of the tabulated uncertainties

The 1D uncertainty interpolation method exploits the fact that the uncertainties from the conversion and summation methods are provided in tables and performs the desired interpolation directly on the uncertainty vectors. A linear interpolation on the available data is used. This method can be used only on ^{241}Pu and ^{238}U, since the Daya Bay uncertainty is provided in the form of a matrix.
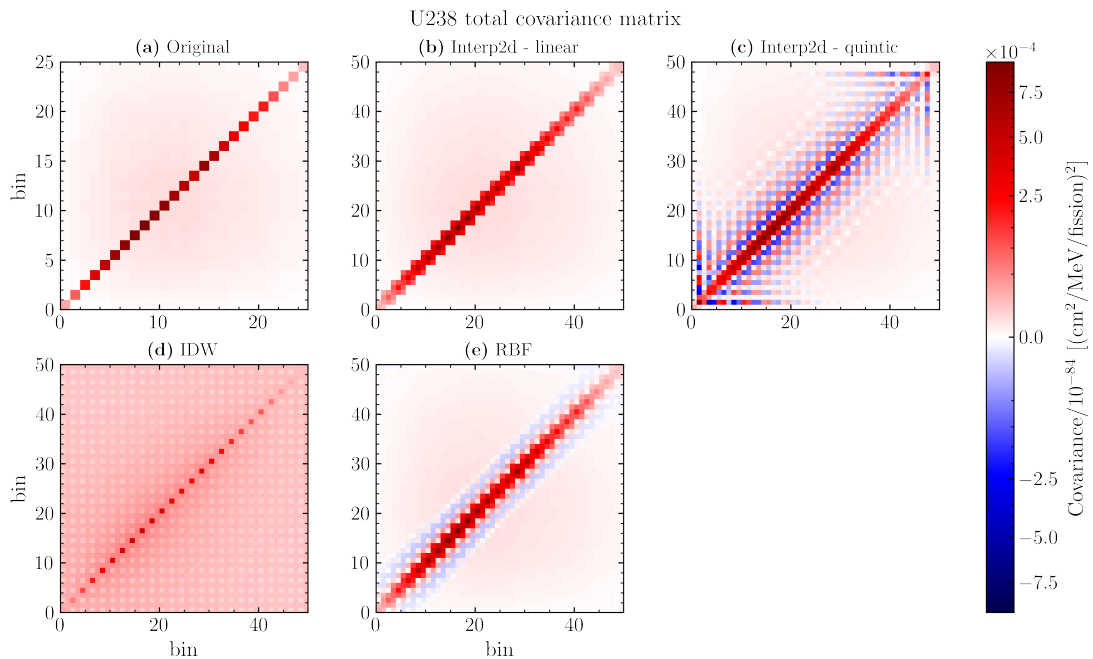
Figure 3.20. Comparison between the covariance matrices obtained by several multivariate methods for ^{238}U: for **(b)** and **(c)**, a 2-dimensional interpolation from the `scipy` package is used; for **(d)**, the Inverse Distance Weighted (IDW) interpolation is used; for **(e)**, the Radial Basis Function (RBF) interpolation is used. The matrix in the original binning is shown in panel **(a)**. See the text for more details.

The covariance matrices resulting from this method are shown in panel **(b)** of Figs. 3.21 and 3.22 for ^{241}Pu and ^{238}U, respectively. For both isotopes, this method seems to be able to reproduce the original matrix (in panel **(a)** of the same figures), without introducing unwanted correlation features or oscillating values along the diagonal, as displayed by the other methods.

ToyMC-based methods

Two methods that are based on the simulation of many toy pseudo-experiments are now presented, where the sampled spectra are obtained from the original tabulated spectrum and the covariance matrix. In what follows, we refer to the original tabulated spectrum for ^{241}Pu and ^{238}U as Asimov spectrum, to distinguish it from the sampled spectra.

A number of samples (about 10k) are generated starting from the Asimov dataset taking the covariance matrix into consideration by means of a function from the `scipy` package: `scipy.stats.multivariate_normal.rvs`.

Interpolation of ToyMC spectra In the first ToyMC-based method, each sampled spectrum is interpolated using the exponential interpolation presented in section 3.3 to match the new binning. Then, the covariance matrix with the new binning is obtained from the interpolated spectra using the definition of the
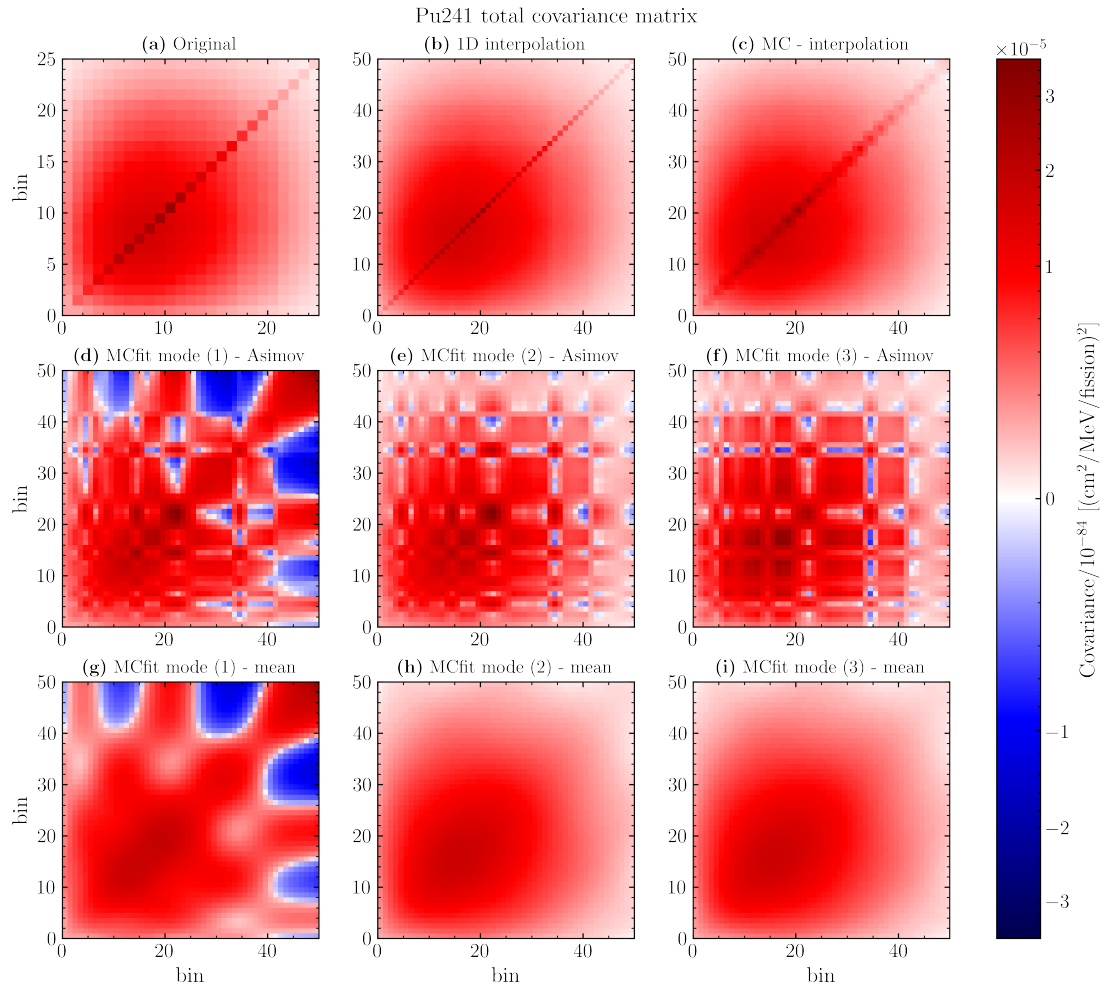
Figure 3.21. Comparison of the MC methods and the 1D-interpolation method for
^{241}Pu. The matrix in the original binning is shown in panel **(a)**. The
matrix from the 1D interpolation of the tabulated data is shown in panel
(b), while the one from the interpolation of ToyMC sampled spectra is
shown in panel **(c)**. The second and third rows show the matrices obtained
by fitting the ToyMC sampled spectra, with the three columns from left
to right corresponding to the fitting modes (1), (2), and (3), respectively.
The Asimov dataset and the mean spectrum are used as the expectation
value in the second (panels **(d)**, **(e)**, and **(f)**) and third (panels **(g)**, **(h)**,
and **(i)**) row, respectively.
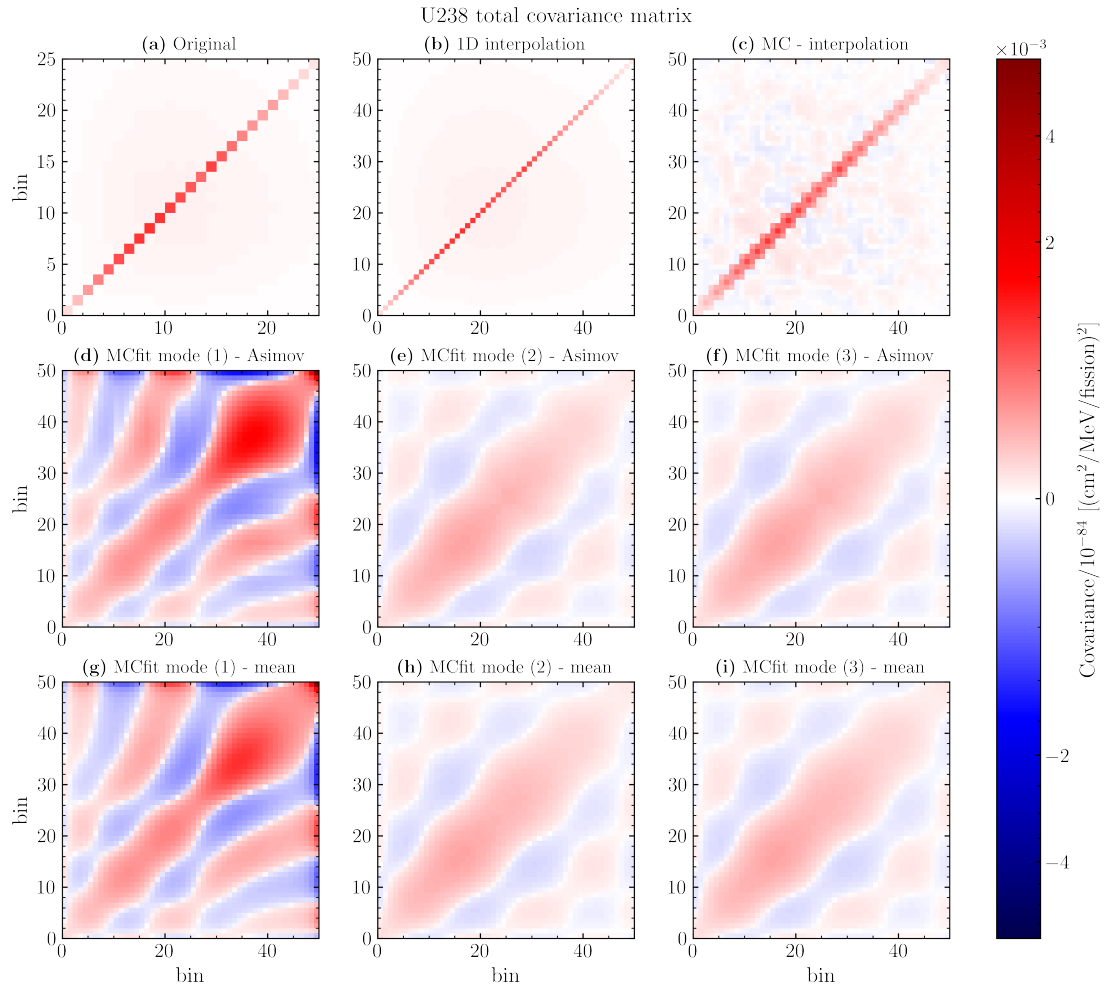
Figure 3.22. Comparison of the MC methods and the 1D-interpolation method for ^{238}U. The matrix in the original binning is shown in panel **(a)**. The matrix from the 1D interpolation of the tabulated data is shown in panel **(b)**, while the one from the interpolation of ToyMC sampled spectra is shown in panel **(c)**. The second and third rows show the matrices obtained by fitting the ToyMC sampled spectra, with the three columns from left to right corresponding to the fitting modes (1), (2), and (3), respectively. The Asimov dataset and the mean spectrum are used as the expectation value in the second (panels **(d)**, **(e)**, and **(f)**) and third (panels **(g)**, **(h)**, and **(i)**) row, respectively.

covariance matrix:

$$V^{ij} = \frac{1}{N} \sum_{n=1}^{N} \left(x_n^i - E[x^i] \right) \left(x_n^j - E[x^j] \right), \quad i,j = 1, ..., 25 \qquad (3.15)$$

where i and j run over the number of bins of the new binning configuration, the sum is over the number of samples N, x_n^i is the i-th value of the n-th sampled spectrum, and $E[x^i]$ is the expectation value for the i-th entry. The Asimov spectrum is also interpolated and used as the expectation value; this also justifies the N at the denominator instead of $(N-1)$.

The matrices resulting from this method are shown in panel **(c)** in Figs. 3.21 and 3.22 for ^{241}Pu and ^{238}U, respectively. The results are similar to the one obtained with the multivariate methods: an oscillating behavior of the values along the diagonal is clearly visible for ^{241}Pu, while negative elements appear for ^{238}U.

Fit of ToyMC spectra In the second ToyMC-based method, each sampled spectrum is fitted using a parametric function already used in literature to parametrize the isotopic spectra, *i.e.*, the exponential of a polynomial of fifth order [73, 75]:

$$f(E_\nu) = \exp\left(\sum_{\alpha=0}^{5} p_\alpha \, E_\nu^\alpha \right) \qquad (3.16)$$

where p_α are free parameters of the fit. As an example, Fig. 3.23a shows 10 sampled spectra for ^{241}Pu.

(a) *Example sampled spectra.*   **(b)** *Best-fit curves.*
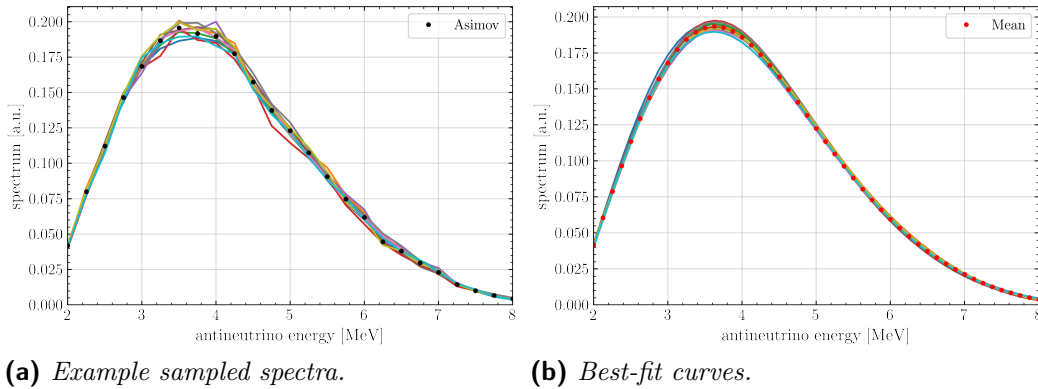
Figure 3.23. **(a)** Example of 10 spectra sampled from ^{241}Pu with the original binning. The Asimov spectrum is also shown as black dots. **(b)** Best fit curves of the 10 sampled spectra, obtained with fitting mode (3) (see text for more details), shown with the new binning. The mean of the fit curves from all samples spectra is shown as red dots.

The sampled spectra are fitted using the `scipy.optimize.curve_fit` function. Three different fitting modes are used: (1) a χ^2-like function with no uncertainty (equivalently, a χ^2 fit with the uncertainty at the denominator fixed to 1); (2) a standard χ^2 fit, where the uncertainties are taken equal to the square root of

the diagonal values of the covariance matrix; (3) a χ^2 fit taking into account the whole covariance matrix. The same set of sampled spectra is used with the three fitting modes. As an example, Fig. 3.23b shows the best-fit curves obtained by fitting the sampled spectra of Fig. 3.23a with the fitting mode (3). The best-fit functions are then evaluated in the new binning configuration and are finally used to evaluate the covariance matrix through Eq. (3.15), similarly to what is done for the interpolation method.

First, the Asimov spectrum, shown in black in Fig. 3.23a, is used as the expectation value in Eq. (3.15) and the resulting covariance matrices for the three fitting modes are shown in the middle row of Figs. 3.21 and 3.22 for ^{241}Pu and ^{238}U, respectively; panels **(d)**, **(e)**, and **(f)** correspond to fitting modes (1), (2), and (3), respectively. These matrices show features that are not present in the original matrix, probably introduced by the difference in smoothness between the Asimov and the fit function, as further investigated in section A.2 in the appendix. It is worth noticing that for ^{238}U there is no much difference between the fitting modes (2), shown in panel **(e)**, and (3), shown in panel **(f)**, since the covariance matrix is almost diagonal.

Then, the mean spectrum from all best-fit curves is evaluated and is shown in red in Fig. 3.23b, and is found to be different from the Asimov dataset; nonetheless, it seems to be a better representative of the best-fit curves, as further investigated in section A.2 in the appendix. So, the mean spectrum is used as the expectation value in Eq. (3.15) and the resulting matrices are shown in the bottom row of Figs. 3.21 and 3.22 for ^{241}Pu and ^{238}U, respectively; panels **(g)**, **(h)**, and **(i)** correspond to fitting modes (1), (2), and (3), respectively. For ^{241}Pu, the matrix in panel **(g)** is still not matching the original matrix, and this is probably related to the fact that no uncertainty is used in the fit. On the other hand, the matrices in panels **(h)** and **(i)** show a good resemblance with the original matrix, as far as the correlation pattern is concerned, but are not able to reproduce the diagonal. Contrary to ^{241}Pu, for ^{238}U we see no improvement in using the mean spectrum instead of the Asimov one as the expectation value. This is probably due to the fact that the original covariance matrix is almost diagonal, and this method works fine to reproduce the correlation between bins but not the diagonal contribution, as seen in the case of ^{241}Pu.

From the consideration above, the best fit configuration is number (3), where the full covariance matrix is used in the χ^2, and the mean spectrum is to be preferred as the expectation value in Eq. (3.15). Nonetheless, we can conclude that the use of a smooth fit function allows us to reproduce the correlation between bins, while it gives no information on bin-to-bin uncorrelated uncertainties along the main diagonal.

Comparison

We can look at the uncertainty bands generated by the re-binned matrices to check if they can qualitatively reproduce the uncertainty of the original covariance matrix. In the following, we take into account the methods which showed good performances: the 1D interpolation of the tabulated uncertainty, the interpolation of ToyMC samples, and the fit of ToyMC samples with fitting mode (3) and with

the mean spectrum as expectation value, corresponding to the matrix in panel
(i).

For the original covariance matrix (25 bins) and each of the tree methods listed
above (50 bins), 10k spectra are generated by means of the following function from
the `scipy` package: `scipy.stats.multivariate_normal.rvs`. The generated
spectra are then collected in a heat map, as shown in Figs. 3.24 and 3.25 for
^{241}Pu and ^{238}U, respectively; the Asimov spectrum is also shown as black dots.
For ^{241}Pu, all heat maps look quite similar by eye, while for ^{238}U some differences
can be seen: for instance, the ToyMC interpolation method displays an oscillatory
behavior at the edges of the uncertainty bands, while the ToyMC fit method
displays a much narrower distributions of the generated spectra.
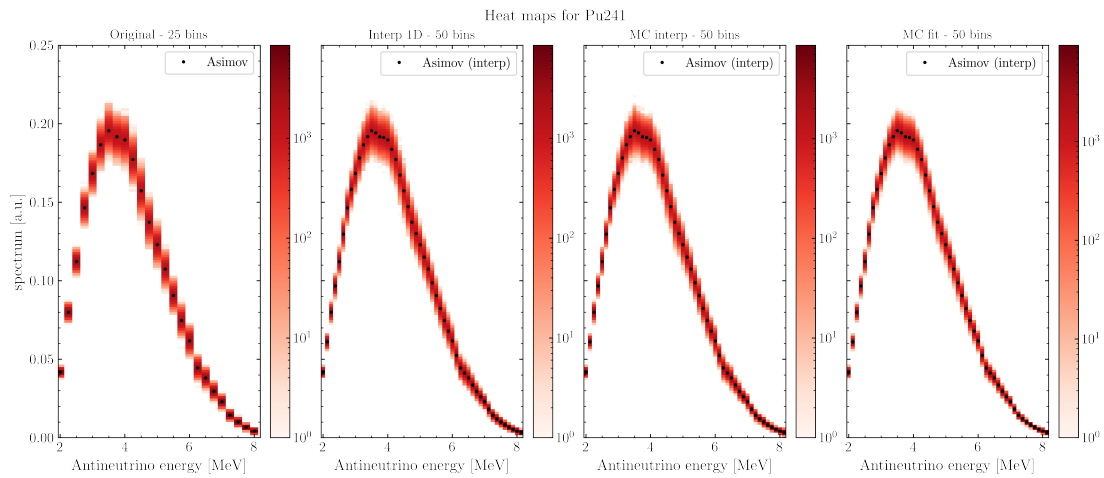
Figure 3.24. Heat maps evaluated from the generated spectra for ^{241}Pu with, from
left to right, the original covariance matrix, the matrix from the 1D-
interpolation method, the matrix from the ToyMC interpolation method,
and the matrix from the ToyMC fit method. The Asimov spectrum is also
shown.

To better visualize the differences in the heat maps, we compute the 16-
th, 50-th (or median), and 84-th percentile curves for each energy bin for all
generated datasets. The curves are shown in Figs. 3.26 and 3.27 for ^{241}Pu and
^{238}U, respectively. For ^{241}Pu, the 1D uncertainty interpolation and the ToyMC
interpolation method both reproduce the curves from the original matrix, with
relative differences over most of the energy range within 1 % and 2 %, respectively,
even though the latter display an oscillatory behavior. On the other hand, the
ToyMC fit method properly reproduces the median but differs for the 16-th and
84-th percentile curves up to 5 %.

For ^{238}U, the 1D uncertainty interpolation is performing well, with a relative
difference well within 1 % over most of the energy range. On the other hand,
the ToyMC interpolation method displays an oscillatory behavior in the relative
difference, showing that it is not able to reproduce the uncertainty band for the
new energy points. Finally, it can be seen by eye that the ToyMC fit method is
giving a narrower energy band, with a relative difference greater than 2 % over
the whole energy range.
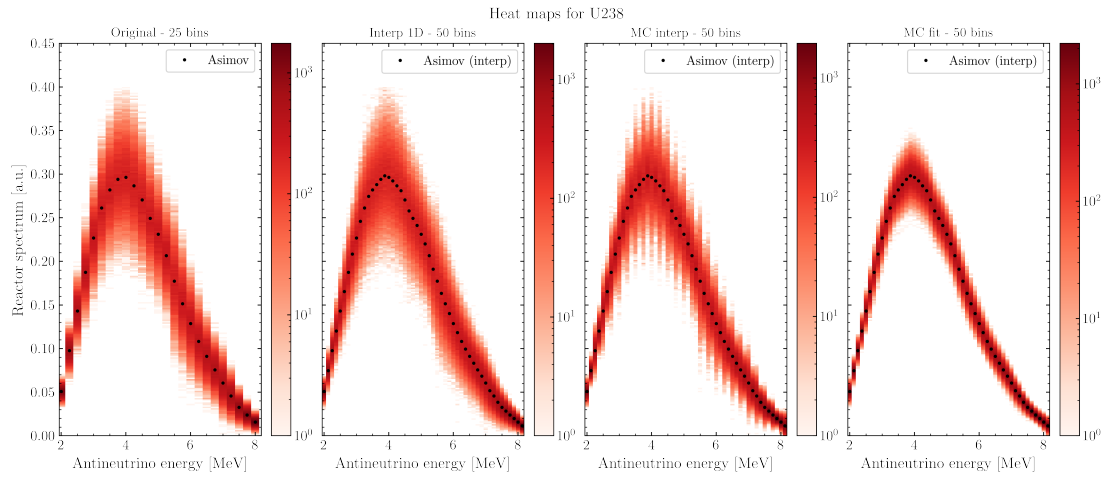
Figure 3.25. Heat maps evaluated from the generated spectra for ^{238}U with, from left to right, the original covariance matrix, the matrix from the 1D-interpolation method, the matrix from the ToyMC interpolation method, and the matrix from the ToyMC fit method. The Asimov spectrum is also shown.
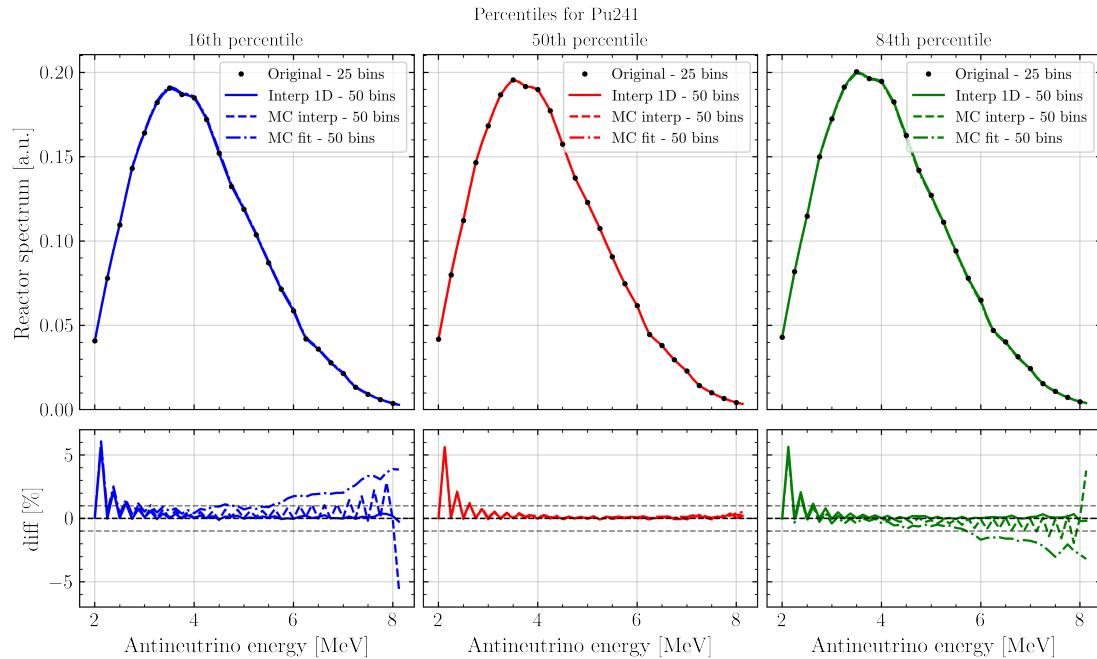
Figure 3.26. Comparison of the 16-th (left), 50-th (middle), and 84-th (right) percentile curves for ^{241}Pu between the original covariance matrix and three rebinned matrices. Relative differences below $1\,\%$ are obtained over most of the energy range by comparing the original matrix with the one from the 1D uncertainty interpolation; the matrix from the MC interpolation method displays an oscillatory behavior, with an amplitude within $2\,\%$ over most of the energy range. On the other hand, the matrix from the MC fit method seems to produce the same median, but different 16-th and 84-th percentile curves, with a relative difference increasing with energy up to $\sim \pm 5\,\%$.
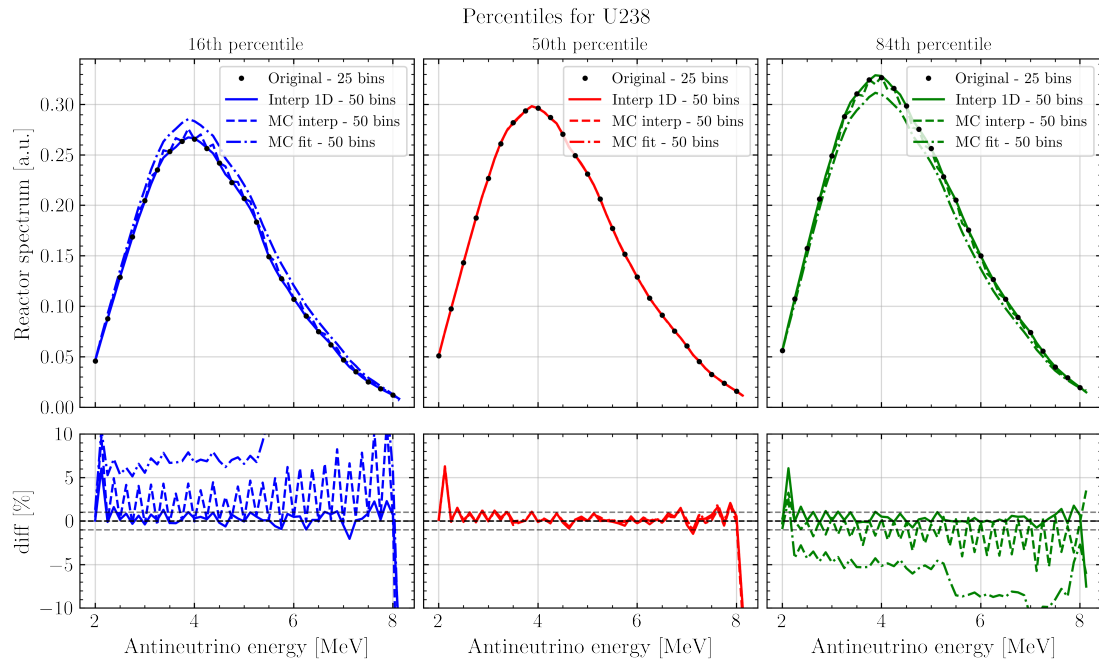
Figure 3.27. Comparison of the 16-th (left), 50-th (middle), and 84-th (right) percentile
curves for ^{238}U between the original covariance matrix and three re-binned
matrices. Relative differences below 1 % are obtained by comparing the
original matrix with the one from the 1D uncertainty interpolation, while
an oscillatory behavior is clearly visible for the matrix from the MC inter-
polation method. On the other hand, the matrix from the MC fit method
seems to produce the same median, but different 16-th and 84-th per-
centile curves, with a relative difference greater than 5 % over most of the
energy range.

3.6   Results and discussion

In this chapter, a method to evaluate the prediction for JUNO reactor spectrum based on recent data from the Daya Bay experiment were presented. This method is to be preferred to the standard HM method since it takes into account the proper flux normalization and the spectral distortion, without the need of additional corrections.

The effect of the changes in the fuel composition, and thus in the fission fractions, during one operational cycle of a reactor core were also investigated, showing that both the rate and shape of the antineutrino spectrum are affected.

Finally, we focused on the evaluation of the uncertainty budget of the prediction of the reactor spectrum. In particular, great effort was devoted to study the 2D interpolation of the covariance matrix in order to match JUNO finer binning. We found that the 1D uncertainty interpolation works fine, but only for tabulated data, so either fully correlated or uncorrelated uncertainties between bins can be treated in this way, while for the Daya Bay spectra it cannot be used since a full matrix with non-trivial correlations is provided. As far as the two ToyMC-based methods are concerned, the one interpolating the samples spectra introduces an oscillating behavior along the main diagonal, while the one fitting the spectra is giving narrower uncertainty bands. The study on the uncertainty presented here does not provide a definite answer yet and further studies are needed.

Chapter 4

Detection of final state particles in a liquid scintillator detector

One of the main challenges for the JUNO experiment is to get a good understanding of the detector response, *i.e.*, all those processes which transform the antineutrino energy E_ν to the final observable, the reconstructed energy E_{rec}. In particular, the non-linear relation between the energy deposited in the detector and the light emission by the liquid scintillator, also known as liquid scintillator non-linearity (LSNL), plays a critical role in the detector response. In fact, it can distort the spectral shape and the oscillation pattern thus affecting the neutrino oscillation analysis, in particular the determination of the neutrino mass ordering. For this reason, a great effort is devoted in modelling the non-linearity, with the additional goal of using the model to tune JUNO Monte Carlo simulation software.

With respect to previous studies [88–90], the model presented in this work is completely based on Geant4 [91–93], all particles (e^-, γ, and e^+) are treated with the same approach, and the only free parameter is the Birks' constant, used in the semi-empirical Birks' law to describe the non-linearity introduced by the scintillation process: the quenching effect. A model with the Monte Carlo production cut value as an additional free parameter is also investigated. The value of the free parameter is tuned by comparing the model to the JUNO calibration data, which will be obtained by means of gamma sources deployed in the detector [42]; since JUNO is currently under construction, mock data from Monte Carlo simulations are used in this work.

In section 4.1, we briefly cover the interaction of radiation with matter, introducing concepts and quantities that will be useful in the rest of the chapter; in section 4.2, a description of the detector response, connecting the antineutrino energy E_ν to the reconstructed energy E_{rec}, is given, and the role of the liquid scintillator non-linearity is highlighted; section 4.3 focuses on the calibration sources and the effect on the energy spectrum due to the presence of a mechanical structure around the source; finally, in section 4.4, we introduce a Geant4-based model of the detector response which treats all particles (e^-, γ, and e^+) in the same way; we conclude in section 4.5.

4.1   Radiation-matter interaction

In this section, we present a brief summary of the interaction of electrons, gammas, and positrons with matter; for a more detailed description see [2, Chapter 34].

All plots shown in this section are specific for JUNO liquid scintillator, whose composition and properties can be found in Tables B.1 and B.2, respectively.

Interaction of electrons with a medium

At low energy, an electron loses its kinetic energy T^{e^-} through collisions with other electrons in the medium. The mean energy loss per mass per unit area dE/dx, or mass stopping power, is described by the Møller equation:

$$\left\langle -\frac{dE}{dx} \right\rangle = \frac{1}{2} K \frac{Z}{A} \frac{1}{\beta^2} \left[\ln \frac{m_e c^2 \beta^2 \gamma^2 m_e c^2 (\gamma - 1)}{2I^2} + \right.$$
$$\left. + (1 - \beta^2) - \frac{2\gamma - 1}{\gamma^2} \ln 2 + \frac{1}{8} \left(\frac{\gamma - 1}{\gamma} \right)^2 - \delta(E) \right], \quad (4.1)$$

where x is the mass per unit area[1], $K = 0.307\,\text{MeV cm}^2/\text{mol}$ is a constant obtained from fundamental constants, Z and A are the atomic number and atomic mass of the absorber, γ is the Lorentz factor, β is the velocity of the electron with respect to the speed of light in vacuum, m_e is the electron mass, I is the mean excitation energy of the absorber, and $\delta(E)$ is the density effect correction which is relevant at high energies. The mass stopping power is expressed in units of $\text{MeV cm}^2/\text{g}$ and is almost the same for all materials, with a slow decrease as a function of Z; the linear stopping power, in units of MeV/cm, can be obtained by multiplying the mass stopping power by the absorber density ρ in units of g/cm^3. The mean mass stopping power as described by Eq. (4.1) for JUNO liquid scintillator is shown in blue in Fig. 4.1.

During the energy loss through ionization, it may happen that an electron is knocked out of an atom of the medium; these electrons are secondary particles produced during ionization and are known as *δ-rays*. After production, they lose energy in the medium through ionization.

Above a critical energy that depends on the medium, electrons start losing energy through Bremsstrahlung, producing low-energy photons with a continuum spectrum, thus introducing a term in Eq. (4.1) which increases with the electron kinetic energy. The radiative contribution to the mean mass stopping power is shown in red in Fig. 4.1, and as it can be seen, the term is several order of magnitudes lower at low energies, and it becomes non-negligible above about 10 MeV.

---

[1]We follow the notation used in the Review of Particle Physics by the Particle Data Group [2]. The quantity x denotes a mass per unit area in g/cm^2 and not a length, so that dE/dx is the *mass* stopping power in units of $\text{MeV cm}^2/\text{g}$. The *linear* stopping power is denoted by $\rho dE/dx$, in MeV/cm, where ρ is the density in g/cm^3.

The total mean mass stopping power is shown in black in Fig. 4.1. In the absence of any leakage effect, an electron deposits all its kinetic energy in the absorber, so that $E_{\text{dep}}^{e^-} = T^{e^-}$.
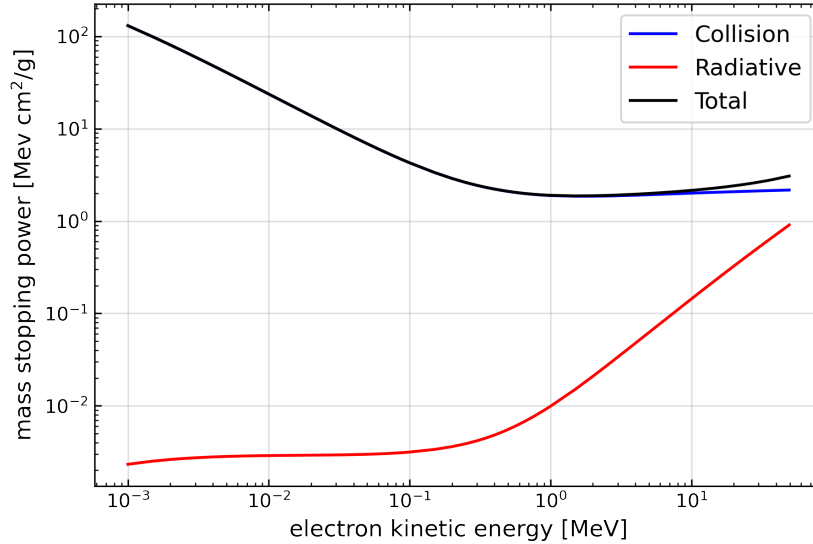
Figure 4.1. Mean mass stopping power for electrons in JUNO liquid scintillator, from [94], in the energy range relevant for the reactor spectrum analysis. The collision and radiative terms are shown in blue and red, respectively, while the total mean mass stopping power is shown in black. The density effect, relevant at high energies, is included in the ionization term. The radiative term becomes significant at high energies, above a few megaelectronvolts.

Interaction of gammas with a medium

Gammas are neutral particles, so they cannot directly ionize a medium, thus they release their energy by producing secondary charged particles, *i.e.*, electrons and positrons. Several processes are involved in the production of secondary electrons and positrons; the relative cross section of each process is shown in Fig. 4.2, while a brief description is given here:

Photoelectric absorption
The gamma ray is absorbed by an atom or molecule of the medium and an electron is emitted. The electron has a kinetic energy equal to the energy of the gamma minus the binding energy of the electron to the atom or molecule. The photoelectric absorption dominates at low energies, below about 20 keV for JUNO liquid scintillator, as shown in Fig. 4.2.

Incoherent scattering
The gamma ray scatters on an electron of the medium, losing a fraction of its energy which is transferred to the electron. The incoherent, or Compton, scattering dominates at high energies, above about 20 keV for JUNO liquid scintillator.

Coherent scattering

The gamma photon scatters on an electron of the medium without losing energy. The coherent, or Rayleigh, scattering is a sub-dominant process and is not relevant since we are interested in the processes which involve energy loss by the gamma.

Pair production

A photon produces an electron-positron pair near a nucleus or another electron, which recoils to satisfy energy and momentum conservation. The energy threshold of this process is twice the rest mass of the electron, about 1.022 MeV, and the respective cross section increases with energy.
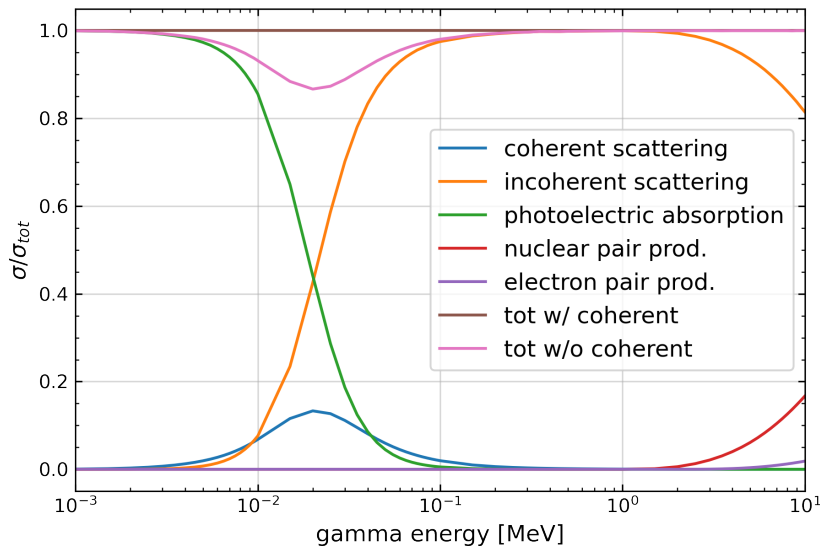
Figure 4.2. Gamma cross section in JUNO liquid scintillator, from [95]. The cross section of each process is normalized to the total cross section. Below about 20 keV, photons are mainly absorbed through photoelectric absorption, while at higher energies, they interact through incoherent, or Compton, scattering; above $2m_e \sim 1.022$ MeV, photons start converting into an electron-positron pair, with the respective cross section increasing with energy.

Figure 4.3 shows the distribution of the kinetic energy of the secondary charged particles, $P^\gamma(T^{e^\pm})$, produced by the interaction of a γ with JUNO liquid scintillator, based on the interactions just explained. The distributions for three representative γ energies are shown. The distributions are usually obtained through Monte Carlo simulations based on the Geant4 toolkit [91–93], as it is done by the Daya Bay experiment [88]. Alternatively, a semi-analytical method has been proposed in [89]; however, it does not include all interactions so it presents issues in retrieving the right total deposited energy.

Finally, the energy deposited by a γ can be evaluated as the sum of the energies deposited by all secondary charged particles:

$$E_{\text{dep}}^\gamma = \int_0^{T_{\max}^{e^\pm}} P^\gamma(T^{e^\pm}) \cdot T^{e^\pm} \, dT^{e^\pm}, \tag{4.2}$$
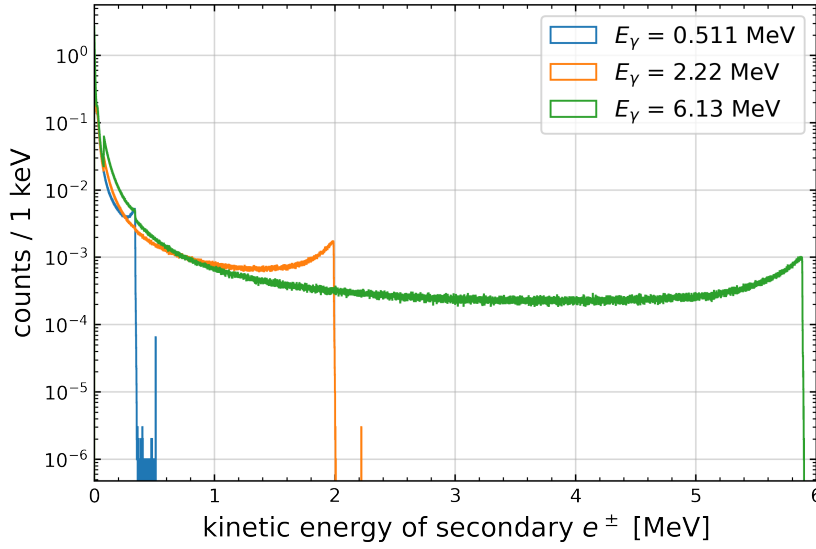
Figure 4.3. Distribution of the kinetic energy of the secondary charged particles produced by the interaction of a γ with JUNO liquid scintillator. The distributions are shown for three representative γ energies and are obtained through Geant4 Monte Carlo simulations.

where $P^\gamma(T^{e^\pm})$ is taken from simulations. In the end, the energy deposited by a γ is equal to the gamma initial energy, $E^\gamma_{\text{dep}} = E^\gamma$, nonetheless the deposited energy as defined in Eq. (4.2) will be useful in the definition of the visible energy later in this chapter.

Interaction of positrons with a medium

Similar to electrons, positrons lose their kinetic energy through collisions with the electrons of the medium. Given the fact that electrons and positrons are not identical particles, the energy loss of a positron is different from Eq. (4.1) and is described by the Bhabha equation:

$$\left\langle -\frac{dE}{dx} \right\rangle = \frac{1}{2} K \frac{Z}{A} \frac{1}{\beta^2} \left[\ln \frac{m_e c^2 \beta^2 \gamma^2 m_e c^2 (\gamma - 1)}{2 I^2} + \right.$$
$$\left. + 2 \ln 2 - \frac{\beta^2}{12} \left(23 + \frac{14}{\gamma + 1} + \frac{10}{(\gamma + 1)^2} + \frac{4}{(\gamma + 1)^3} \right) - \delta(E) \right]. \quad (4.3)$$

After releasing its kinetic energy in the medium through collisions, a positron annihilates with an electron of the medium producing two $511\,\text{keV}$ gamma rays. The energy deposited by the two gamma rays can be treated as discussed above. Finally, the total energy deposited by a positron can be written as:

$$E^{e^+}_{\text{dep}} = T^{e^+} + 2 \cdot 0.511\,\text{MeV}. \quad (4.4)$$

4.2   From particle interaction to light detection

In chapter 3, we focused on the model of the reactor spectrum at the source, expressed as a function of the electron antineutrino energy, E_ν, which is not the

final observable to be used in JUNO analysis. In fact, the final observable, the reconstructed energy E_{rec}, is related to the antineutrino energy through a chain of three main processes:

$$E_\nu \xrightarrow{\text{IBD kinematics}} E_{\text{dep}} \xrightarrow{\text{Light emission}} E_{\text{vis}} \xrightarrow{\text{Light detection}} E_{\text{rec}}, \qquad (4.5)$$

which are now briefly described. We refer to the chain of processes in Eq. (4.5) as the detector response.

In this work, we assume no energy leakage, so that particles deposit their whole energy in the scintillator. Furthermore, we neglect any positional non-uniformity in the detector response.

4.2.1   IBD kinematics

As already seen in section 3.1, an incoming antineutrino interacts with a proton of the liquid scintillator through the IBD process, thus producing a positron and a neutron. In the analysis of reactor antineutrinos, we are interested in the final-state positron, since its energy is proportional to the antineutrino energy, E_ν. The positron releases its kinetic energy through ionization and eventually annihilates with an electron producing two $511\,\text{keV}$ gamma rays. If we neglect the recoil of the neutron in the final state, the whole antineutrino energy E_ν is transferred to the positron, so that we have a univocal relation between E_ν and the deposited energy E_{dep}, which is given by the sum of the positron kinetic energy T_{e^+} and the two annihilation gammas:

$$E_{\text{dep}}^{e^+} = T^{e^+} + 2\,m_e \simeq E_\nu - 0.782\,\text{MeV}, \qquad (4.6)$$

where $m_n - m_p - m_e \approx 0.782\,\text{MeV}$.

What happens in reality is that a small fraction of E_ν is transferred to the final-state neutron which recoils. The neutron recoil introduces a smearing effect, thus spoiling the univocal relationship between E_ν and E_{dep}: a distribution of possible positron energy, and thus E_{dep}, corresponds to each initial antineutrino energy. The distribution of the positron energy follows a "top hat" distribution [96], with a spread increasing with E_ν, as shown in Fig. 4.4.

4.2.2   Light emission: Liquid scintillator non-linearity

The second step in the detector response chain connects the deposited energy E_{dep} to the visible energy E_{vis}, which is defined as the amount of light produced in a liquid scintillator by the passage of a particle, and is defined differently for e^-, γ, and e^+. E_{vis} is usually not linearly proportional to the deposited energy. In fact, there are two independent effects contributing to the non-linear response of the liquid scintillator, also called liquid scintillator non-linearity (LSNL): the quenching effect, which is characteristic of the light produced by the scintillation process, and the Cherenkov effect.
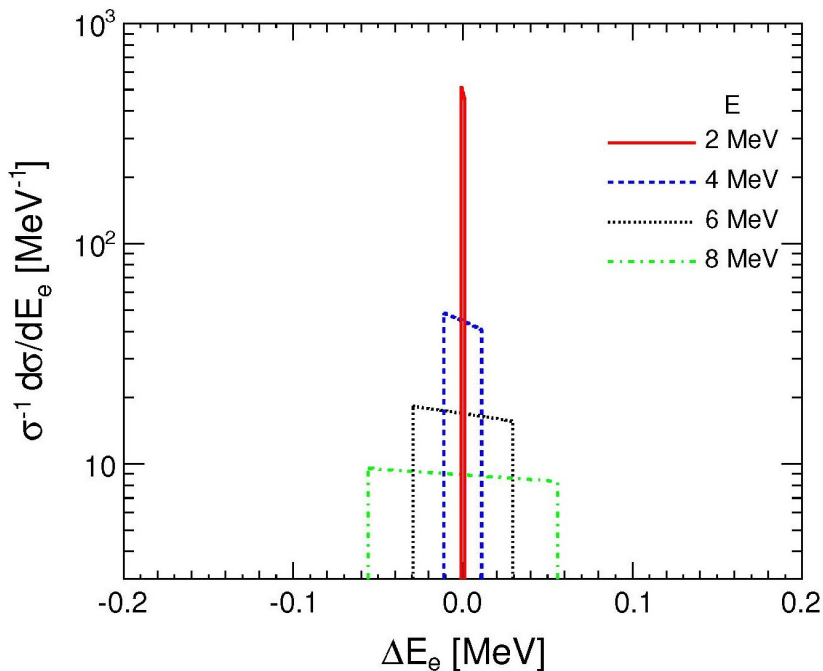
Figure 4.4. Smearing introduced by the nucleon recoil in the IBD interaction, from [96]. Here E is the initial antineutrino energy. ΔE_e represents the positron energy with respect to the median value of each distribution.

Quenching effect

Scintillation light is produced by the de-excitation of the molecules of the liquid scintillator after the passage of a charged particle, which loses its kinetic energy T through ionization, as already explained in section 4.1. If the local energy deposit by the charged particle is high, it might happen that the liquid scintillator reaches a saturation condition, and less scintillation light is produced. This effect, called quenching, is characteristic only of the collision term and is most relevant at low energies, where the mean mass stopping power is higher, as shown in Fig. 4.1.

The quenched energy, *i.e.*, the deposited kinetic energy actually contributing to the light emission through scintillation, can be evaluated by integrating the semi-empirical Birks' law [97]:

$$E_{\text{quenched}} = \int_0^T \frac{1}{1 + k_B \frac{dE}{dx}\big|_{E'}} dE', \qquad (4.7)$$

where k_B is the Birks' constant, specific for each material and to be measured experimentally, and dE/dx is the mean mass stopping power from Møller, Eq. (4.1), and from Bhabha, Eq. (4.3), for electrons and positrons, respectively. The quenched energy for a γ as in the equation above is not defined, since a γ does not directly ionize the medium and a mean mass stopping power is not provided.

Then, we can define the ratio between the quenched energy and the energy deposited through ionization, *i.e.*, the kinetic energy of the particle T:

$$R^{e^\pm}(T^{e^\pm}; k_B) = \frac{E_{\text{quenched}}^{e^\pm}}{T^{e^\pm}}, \qquad (4.8)$$

where E_{quenched} is from Eq. (4.7). This ratio represents the fraction of the energy deposited through ionization contributing to the light emission through scintillation, and is different for electrons and positrons. Figure 4.5 shows several curves of the scintillation non-linearity described by Eq. (4.8) for different values of the Birks' constant. As it can be seen, the higher the value of the Birks' constant, the more the particle kinetic energy is quenched and the less scintillation light is emitted. Furthermore, it can be seen that quenching is more effective at low energies, where the local energy deposition is higher, as explained in section 4.1.
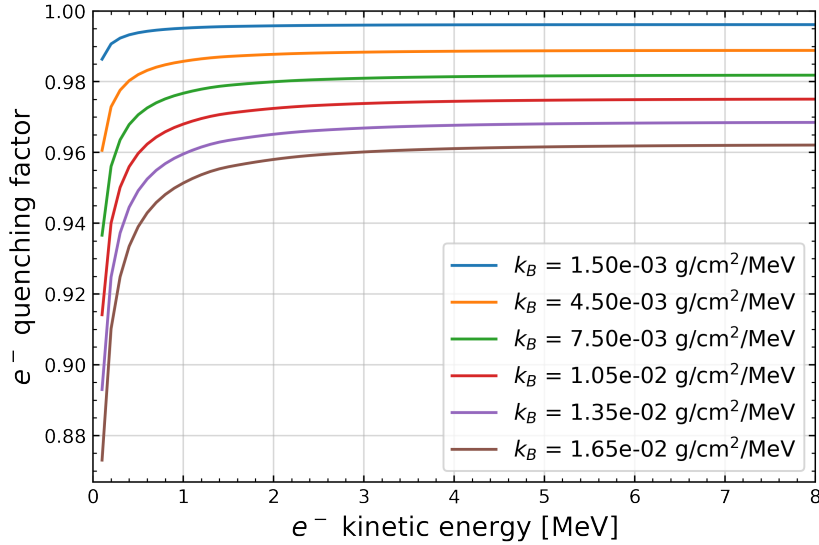
Figure 4.5. Scintillation non-linearity curves due to the quenching effect in JUNO liquid scintillator for several values of the Birks' constant, k_B.

It is relevant to note that in the integration of the Birks' law, Eq. (4.7), the contribution of energetic δ-rays and gammas from Bremsstrahlung produced as secondary particles is not included. Furthermore, they are usually more quenched than the primary electron due to their lower energies.

Cherenkov effect

If a charged particle traversing a material has a velocity which is higher than the group velocity of light in that material, then Cherenkov photons are emitted.

The number of optical photons emitted by the Cherenkov effect follows the Frank-Tamm formula [98]:

$$\frac{d^2 N_{\text{CherenkovOP}}}{dx d\lambda} = \frac{2\pi \alpha z^2}{\lambda^2} \left(1 - \frac{1}{\beta^2 n^2(\lambda)},\right) \tag{4.9}$$

where x is the particle track length, λ is the wavelength of the emitted photon, α is the fine-structure constant, z is the atomic number of the charged particle, $\beta = v/c$, and $n(\lambda)$ is the refractive index of the medium. The Cherenkov effect depends on the particle velocity, hence the particle energy, constituting an additional source of energy non-linearity. It depends also on the refractive index of the medium, which is a function of the photon wavelength and is usually not known

with precision, thus introducing a large uncertainty in the number of emitted Cherenkov photons.

The contribution of the Cherenkov effect to the visible energy, described by an energy-dependent effective factor f_C, is usually determined through MC simulation:

$$f_C(T) = \frac{N_{\text{CherenkovOP}}^{\text{detected}}}{T} \tag{4.10}$$

where T is the particle kinetic energy, and $N_{\text{CherenkovOP}}^{\text{detected}}$ is the number of optical photons produced by Cherenkov effect, Eq. (4.9), and actually detected. In fact, Cherenkov light is emitted in the UV spectrum, so many Cherenkov optical photons are absorbed by the liquid scintillator and then re-emitted in the visible spectrum so that they can be detected by the PMTs. Since there is great uncertainty in the absorption and re-emission probabilities, $N_{\text{CherenkovOP}}^{\text{detected}}$ and the Cherenkov factor f_C depend on the implementation of these processes in the simulation; with real data, the contribution of Cherenkov light could be determined through calibration. Figure 4.6 shows several curves of the Cherenkov effect summed with the quenching effect, for different values of the Cherenkov factor; for reference, the curve corresponding to the quenching only case is shown as blue dots. Currently, the default Cherenkov factor is 52 % and was obtained by measurements of JUNO liquid scintillator in one detector of the Daya Bay experiment [99].
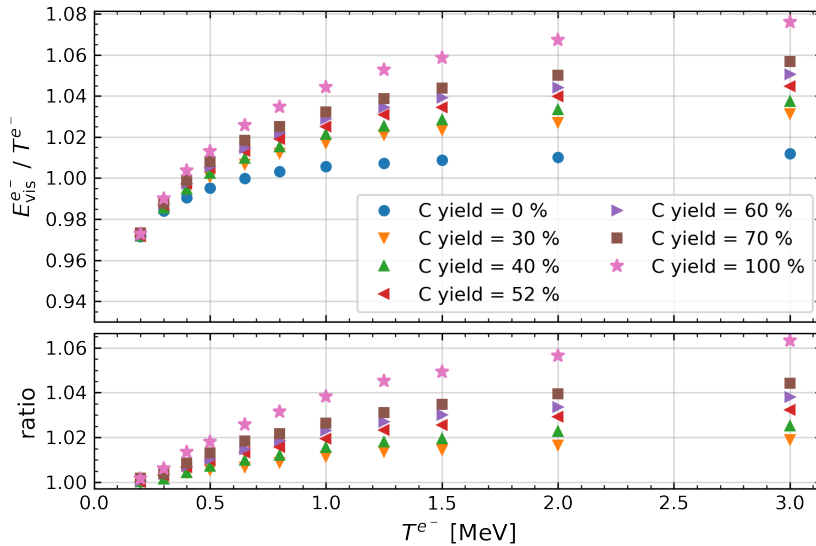
Figure 4.6. Light emission curves for an electron obtained with different values of the Cherenkov factor used in the simulation. The normalization of the vertical scale is anchored at the γ line at 2.22 MeV from neutron capture on hydrogen. The blue dots represent the case in which the Cherenkov factor is set to zero, thus only the quenching effect is included; the bottom panel shows the ratio to the 0 % Cherenkov factor curve. Plot by R. M. Guizzetti.

Visible energy of electrons

In the end, for an electron with deposited energy $E_{\text{dep}}^{e^-} = T^{e^-}$, there are two contributions to the visible energy:

$$E_{\text{vis}}^{e^-} = R^{e^-}(T^{e^-}; k_B) \cdot T^{e^-} + f_C(T^{e^-}) \cdot T^{e^-}, \qquad (4.11)$$

where R is the quenching ratio of Eq. (4.8), and f_C is the Cherenkov factor of Eq. (4.10). Quenching and the Cherenkov effect are two physically separate and independent processes, hence it is possible to sum them together. The ratio of the total visible energy to the deposited energy for electrons is shown in Fig. 4.6.

In this work, we focus on the non-linear response introduced by the quenching effect and we don't take into account the Cherenkov effect, so that we can write the quenching factor for electrons as:

$$f_q^{e^-} = \frac{E_{\text{vis}}^{e^-}}{T^{e^-}} = R^{e^-}(T^{e^-}; k_B), \qquad (4.12)$$

where we used the fact that $E_{\text{vis}} = E_{\text{quenched}}$ if we neglect Cherenkov light. The quenching factor above represents the fraction of the electron kinetic energy contributing to the light production through scintillation.

Visible energy of gammas

As far as gammas are concerned, quenching affects the secondary charged particles produced by the interactions explained in section 4.1; in particular, given the γ energies of interest in this study (see section 4.3), quenching mainly affects Compton electrons. The visible energy of a gamma can thus be obtained by summing over all initial kinetic energies of the secondary particles, with each energy weighted by the corresponding quenching factor, $R^{e^\pm}$, from Eq. (4.8):

$$E_{\text{vis}}^{\gamma} = \int_0^{T_{\text{max}}^{e^\pm}} P^\gamma(T^{e^\pm}) \cdot T^{e^\pm} \cdot R^{e^\pm}(T^{e^\pm}; k_B) \, dT^{e^\pm}, \qquad (4.13)$$

where $P^\gamma(T^{e^\pm})$ is the energy distribution of the secondary charged particles produced by a gamma, as introduced in section 4.1. Finally, the quenching factor for a gamma can be defined as the ratio between the γ visible energy and the γ deposited energy:

$$f_q^\gamma = \frac{E_{\text{vis}}^\gamma}{E_{\text{dep}}^\gamma}, \qquad (4.14)$$

where E_{vis}^γ and E_{dep}^γ are taken from Eq. (4.13) and (4.2), respectively. The γ quenching factor represents the fraction of the γ energy contributing to the scintillation light through ionization by the secondary charged particles.

Visible energy of positrons

Following Eq. (4.4), the visible energy for a positron can be obtained by summing two terms:

$$E_{\text{vis}}^{e^+} = T^{e^+} \cdot R^{e^+}(T^{e^+}; k_B) + 2 \cdot f_q^\gamma(511\,\text{keV}) \cdot 511\,\text{keV}, \qquad (4.15)$$

where the first one comes from the quenching of the positron deposited kinetic energy, with the quenching ratio R^{e^+} defined in Eq. (4.8), and the second one is the visible energy of the two annihilation gammas, with the γ quenching factor from Eq. (4.14). Finally, we can define the quenching factor for positrons as:

$$f_q^{e^+} = \frac{E_{\mathrm{vis}}^{e^+}}{E_{\mathrm{dep}}^{e^+}}, \tag{4.16}$$

where the visible and deposited energies are defined in Eq. (4.15) and (4.4), respectively. The quenching factor represents the fraction of the energy deposited by the positron, as the sum of the kinetic energy and the annihilation gammas, which contributes to the scintillation light emission.

4.2.3 Light detection: Energy resolution

In the last step of detector response chain, energy resolution relates the visible energy, E_{vis}, to the reconstructed energy, E_{rec}, which is JUNO final observable. E_{rec} is evaluated as $E_{\mathrm{rec}} = Y_{\mathrm{PE}} \cdot N_{\mathrm{PE}}$, where N_{PE} is the number of detected photoelectrons (PE), and $Y_{\mathrm{PE}} = 1665\,\mathrm{PE/MeV}$ is the PE yield [56, 99], a normalization constant which translates N_{PE} into an energy in units of MeV. The PE yield is obtained by simulating the neutron capture on hydrogen atoms at the detector center, so it is anchored to the γ line at $2.22\,\mathrm{MeV}$; the most recent and updated version of JUNO Monte Carlo simulation framework was used to obtain this value.

The relation between the visible and reconstructed energies is not univocal and a distribution of E_{rec} corresponds to a given E_{vis}. In particular, the distribution is usually a Gaussian, with the width given by the standard three-parameter parametrization:

$$\frac{\sigma_E}{E_{\mathrm{vis}}} = \sqrt{\left(\frac{a}{\sqrt{E_{\mathrm{vis}}}}\right)^2 + b^2 + \left(\frac{c}{E_{\mathrm{vis}}}\right)^2}, \tag{4.17}$$

where a, b, and c model the stochastic term, the constant term, and the noise term, respectively, and all energies are expressed in units of MeV.

The stochastic term a is related to the intrinsic fluctuations of the quantum processes involved in the light generation, like the optical photon emission in the liquid scintillator, and detection, like the photoelectron production in the PMTs. The constant term b includes the modeling of any instrumental effects which produce response variation in the detector, such as the geometry, or temperature gradients; it is dominated by the position non-uniformity of the detector response. Finally, noise is introduced by the readout chain, *e.g.*, the dark noise of the PMTs; once the dark noise of the PMTs is measured, the noise term c can be evaluated and is fixed.

Since the stochastic term a is fixed by the stochastic processes involved in the light production and detection, and the noise term c is fixed by the DCR of the PMTs, one should work to keep b as small as possible. An optimization of the calibration campaign to keep the energy resolution within the requirement of $3\,\%$ at $1\,\mathrm{MeV}$ is extensively presented in [42]. From a more recent study on JUNO

energy resolution [99], the expected energy resolution at $1\,\mathrm{MeV}$ is $2.95\,\%$, with $a = 2.614\,\%$, $b = 0.64\,\%$, and $c = 1.205\,\%$.

Finally, the spectrum in E_{rec} can be obtained from the convolution of the spectrum in E_{vis} and the energy resolution:

$$S(E_{\mathrm{rec}}) = \int_{E_{\mathrm{th}}}^{\infty} dE_{\mathrm{vis}}\, S(E_{\mathrm{vis}}) \cdot G(E_{\mathrm{rec}}; E_{\mathrm{vis}}, \sigma_E), \qquad (4.18)$$

where $G(E_{\mathrm{rec}}; E_{\mathrm{vis}}, \sigma_E)$ is the Gaussian distribution evaluated in E_{rec}, centered in E_{vis}, and with width given by Eq. (4.17). The convolution is evaluated over the range of visible energy, with the lower threshold of about $1\,\mathrm{MeV}$.

4.3   Calibration sources

For the energy calibration of the JUNO experiment, we plan to use several radioactive γ and neutron sources spanning the energy range from $0.662\,\mathrm{MeV}$ to $6.13\,\mathrm{MeV}$; a complete list is given in Table 4.1. To cover the high energy part of the spectrum for the reactor antineutrino analysis, we plan to use the continuous β-decay spectrum of the cosmogenic $^{12}\mathrm{B}$, which is characterized by a Q-value of $13.4\,\mathrm{MeV}$; this calibration source is not considered in this work, and more information can be found in [42]. Furthermore, the use of sources at lower energies for the solar neutrinos analysis is under investigation, but is beyond the scope of this work so they will not be covered here. The hardware that will be used to deploy the sources inside JUNO was already described in section 2.1.5.

Table 4.1. List of the calibration sources to be used in the calibration campaign by the JUNO experiment [42].

Source	Source type	Energy
$^{137}\mathrm{Cs}$	γ	$0.662\,\mathrm{MeV}$
$^{54}\mathrm{Mn}$	γ	$0.835\,\mathrm{MeV}$
$^{60}\mathrm{Co}$	γ	$1.173\,\mathrm{MeV} + 1.333\,\mathrm{MeV}$
$^{40}\mathrm{K}$	γ	$1.461\,\mathrm{MeV}$
$^{68}\mathrm{Ge}$	e^+	$0.511\,\mathrm{MeV} + 0.511\,\mathrm{MeV}$ (from e^+ annihilation)
$^{241}\mathrm{Am}\text{-}^9\mathrm{Be}$	n, γ	n $+ 4.43\,\mathrm{MeV}$ ($^{12}\mathrm{C}^*$)
$^{241}\mathrm{Am}\text{-}^{13}\mathrm{C}$	n, γ	n $+ 6.13\,\mathrm{MeV}$ ($^{16}\mathrm{O}^*$)
$(\mathrm{n},\gamma)\mathrm{p}$	γ	$2.2\,\mathrm{MeV}$
$(\mathrm{n},\gamma)^{12}\mathrm{C}$	γ	$4.94\,\mathrm{MeV}$ or $3.68\,\mathrm{MeV} + 1.26\,\mathrm{MeV}$

Gamma sources

Figures 4.7, 4.8 and 4.9 show the decay schemes of JUNO γ sources.

As shown in Fig. 4.7a, $^{137}\mathrm{Cs}$ undergoes β decay to $^{137}\mathrm{Ba}^*$ with a branching ratio of $94.36\,\%$; then, $^{137}\mathrm{Ba}^*$ decays to the ground state emitting a γ of $0.662\,\mathrm{MeV}$ with a branching ratio of $85\,\%$. The isotope $^{54}\mathrm{Mn}$ decays through electron capture to $^{54}\mathrm{Cr}^*$, which then decays to the ground state with the emission of a γ of $0.835\,\mathrm{MeV}$, as shown in Fig. 4.7b.

The decay scheme of ^{60}Co is a bit more complicated and is shown in Fig. 4.8a. ^{60}Co decays 99.88 % of the time through β^- emission to the third excited state of ^{60}Ni, at 2.506 MeV above the ground state. Almost all the time, the excited state decays to the ground state with the emission of two γ rays, with energies of 1.173 MeV and 1.333 MeV. These two γ rays will be observed as a single event, nonetheless they will be quenched individually and differently, and this must be taken into account in the evaluation of the physics non-linearity.

As shown in Fig. 4.8b, most of the time ^{40}K undergoes β decay to the ground state of ^{40}Ca, without emitting any γ ray. The relevant γ ray of 1.461 MeV is produced from the decay of ^{40}Ar* to its ground state after the decay of ^{40}K through electron capture; this process has a branching ratio only of 10.55 %.

Finally, ^{68}Ge always decays to the ground state of ^{68}Ga through electron capture, which is itself an unstable isotope. ^{68}Ga has several decay modes to the excited states and the ground state of ^{68}Zn. The decay mode we are interested in is the decay to the ground state with the emission of a positron, which annihilates producing two 0.511 MeV γ rays; this decay mode has a branching ratio of 87.68 %. In Fig. 4.9, only the decay scheme of ^{68}Ga is shown.

(a) *Decay scheme of ^{137}Cs.*   (b) *Decay scheme of ^{54}Mn.*
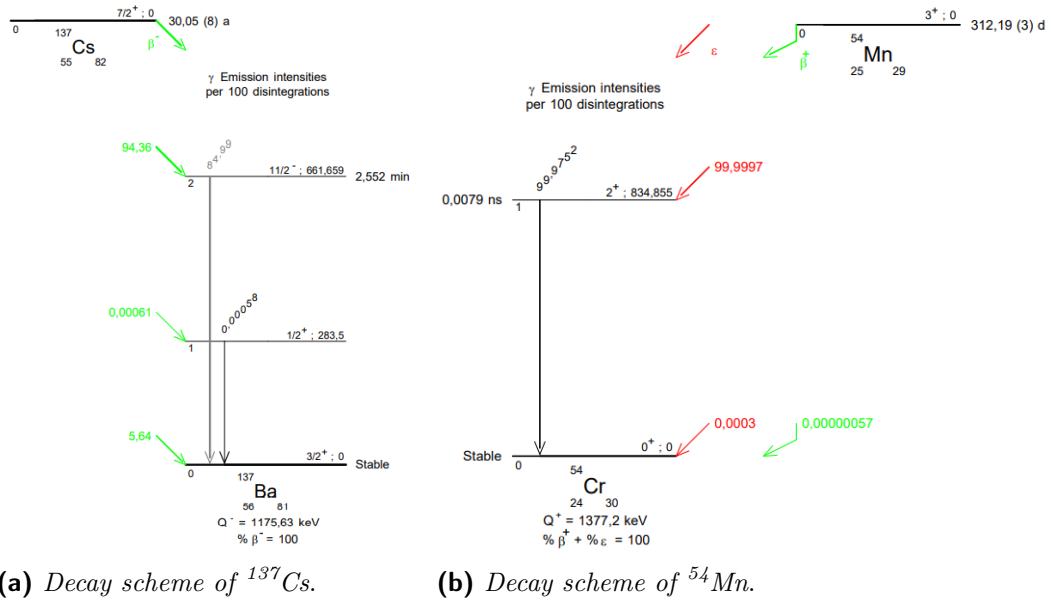
Figure 4.7. Decay schemes of JUNO radioactive sources: (a) ^{137}Cs and (b) ^{54}Mn [100].

Neutron sources

In JUNO, we plan to use two neutron sources: ^{241}Am-^{9}Be and ^{241}Am-^{13}C. In both sources, ^{241}Am decays to ^{237}Np with the emission of low-energy X-rays and an α particle, which is subsequently captured by ^{9}Be or ^{13}C, respectively. In the final state after the α capture, we are left with a neutron and an atom of ^{12}C or ^{16}O, respectively, either in the ground state or in an excited state. In the latter case, ^{12}C* decays to the ground state with the emission of a γ ray of 4.43 MeV, while ^{16}O* decays emitting a γ ray of 6.13 MeV.
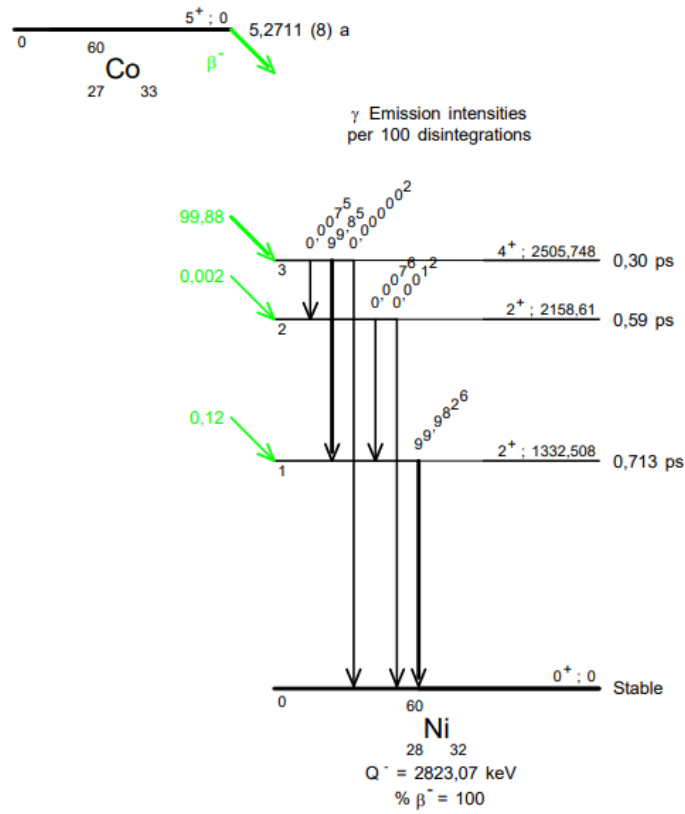
(a) *Decay scheme of ^{60}Co.*
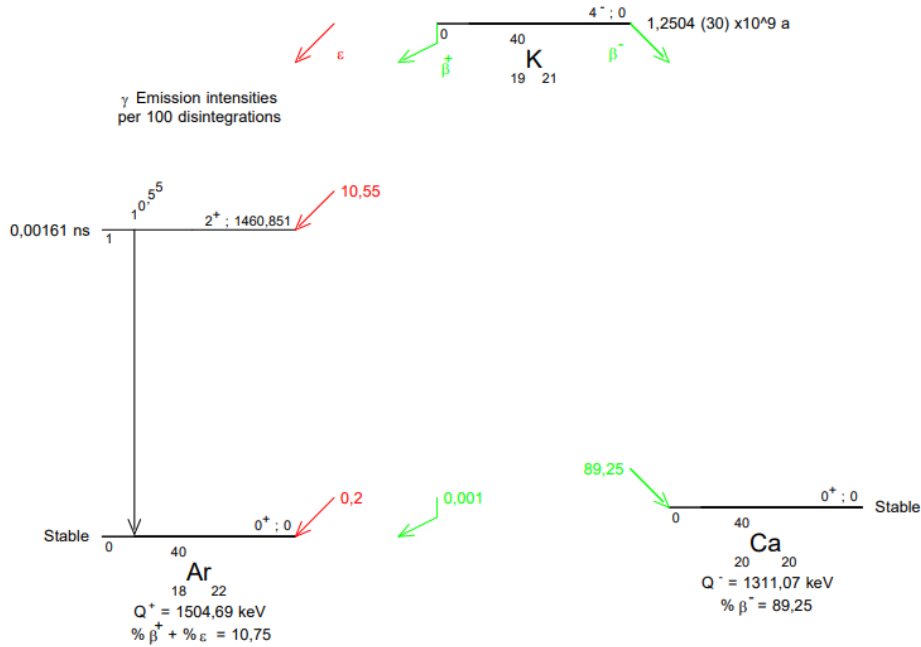
(b) *Decay scheme of ^{40}K.*

Figure 4.8. Decay schemes of JUNO radioactive sources: (a) ^{60}Co and (b) ^{40}K [100].
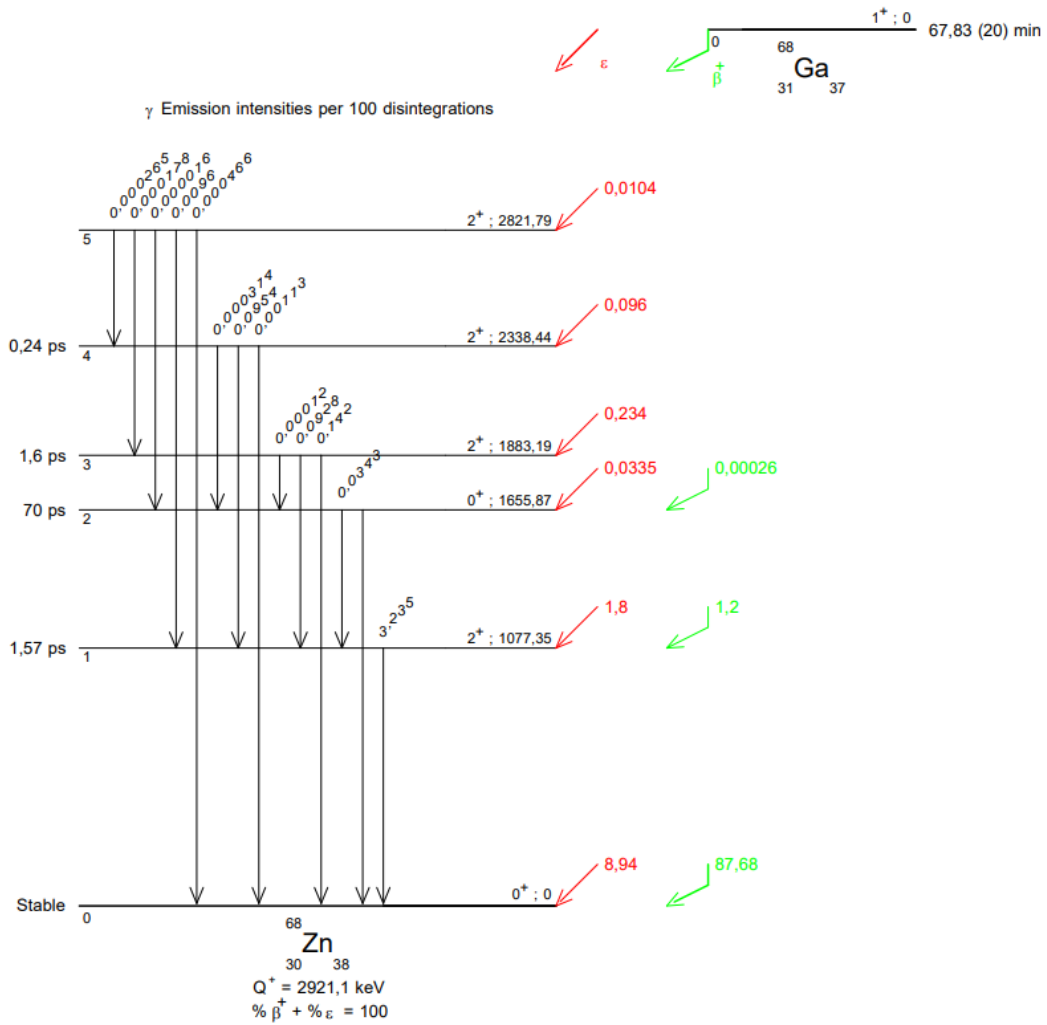
Figure 4.9. Decay scheme of the ^{68}Ge radioactive source. Only the decay scheme of ^{68}Ga is shown [100], since ^{68}Ge decays to the ground state of ^{68}Ga through electron capture, so without the emission of electrons or gammas.

The neutrons produced by these two sources undergo neutron capture by hydrogen atoms in the liquid scintillator, with the emission of a γ ray of 2.22 MeV. 1 % of the time, neutrons are captured by ^{12}C atoms, followed by the emission of a 4.94 MeV γ or two γ rays with energy of 3.68 MeV and 1.26 MeV, with branching ratios of 67.5 % and 32.1 %, respectively.

Effect of the source assembly on the energy spectrum

Before deployment in JUNO liquid scintillator, all sources will be enclosed in a source assembly which was described in section 2.1.5 and shown in Fig. 2.6b. In the case of absence of the source assembly, we expect to observe a peak in the distribution of the detected PE, which corresponds to the monochromatic γ energy and whose width is determined by the energy resolution of the detector; as an example, the peak from ^{54}Mn is shown in blue in Fig. 4.10a. The presence of a mechanical structure used to deploy the source might introduce a bias in the position of the peak due to two effects: the energy loss and shadowing effects.

The energy loss effect refers to the fact that the γ might undergo Compton scattering inside the cylindrical stainless steel shell enclosing the source with the scattered electron not reaching the liquid scintillator, thus only a fraction of the initial γ energy is deposited in the liquid scintillator, hence biasing the peak position towards lower energies and producing a shoulder at the left of the peak, clearly visible in Fig. 4.10a. The shadowing effect refers to the fact that the optical photons produced in the liquid scintillator might be absorbed by the assembly structure, despite the high reflectivity of the material; similarly to the case of the energy loss effect, shadowing results in a bias in the position of the γ peak. An example of the energy spectrum with the source simulated inside of the assembly is shown in red in Fig. 4.10a for ^{54}Mn; by comparing the two spectra, both the shift of the peak and the shoulder are clearly visible. We try to parametrize both the peak and the shoulder to estimate the impact of these effects.

The peak, which should be monochromatic but smeared by the energy resolution, is fitted with a Gaussian, with the width given by the energy resolution. There are several functions that can be used to fit the shoulder at low energies [101]; a complete study can be found in [102], here we present the main results. The best function, in terms of $\chi 2$, which can parametrize the shoulder is a step function convoluted with the energy resolution, *i.e.*, the complementary error function. In the end, we determine the position of the peak by modelling the source spectrum with the following distribution:

$$f(x) = C \cdot \exp -\frac{(x - \mu)^2}{2\sigma^2} + P_1 \cdot \left(0.5 \cdot \mathrm{erfc}\, \frac{x - \mu}{\sqrt{2}\sigma} \right) \qquad (4.19)$$

where C and P_1 are two normalization constants, μ and σ are the central value and the width of the Gaussian peak. An example is shown in Fig. 4.10b for the ^{54}Mn source, where the best fit curve is shown in red; residuals are also shown in the bottom panel.
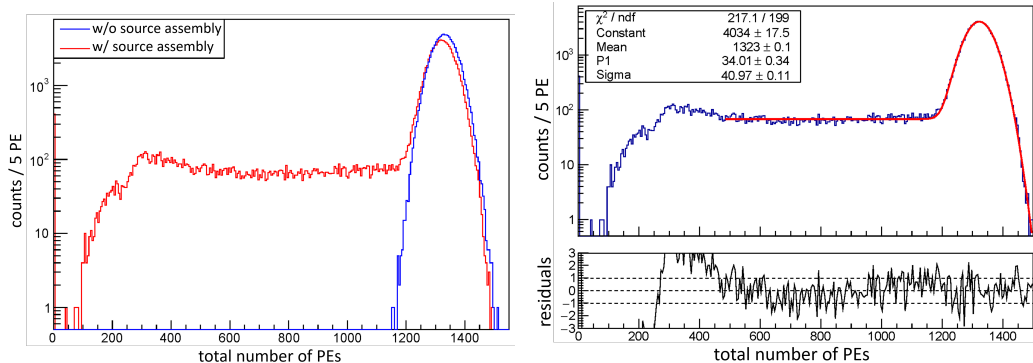
(a) ^{54}Mn *spectrum.*   **(b)** *Fit of the* ^{54}Mn *spectrum.*

Figure 4.10. **(a)** Energy spectrum of the ^{54}Mn gamma source without (blue) and with (red) the source assembly. The shift to the left in the position of the peak due to the presence of the enclosure is clearly visible. The spectrum obtained with the source assembly also displays the shoulder at the left of the peak due to the energy loss and shadowing effects. **(b)** Fit of the ^{54}Mn spectrum using Eq. (4.19). Residuals are also shown in the bottom panel. Plots by R. M. Guizzetti [102].

4.4 Geant4-based model of the light emission

In this section, we investigate a new method to build a model of the emission of scintillation light. The aim of the study is to have a model with only one free parameter, the Birks' constant k_B, and use the model to fit calibration data and obtain the value of k_B for JUNO liquid scintillator. The best-fit value can then be used for MC tuning as an input for JUNO MC simulation software. In particular, we are interested in the model for positrons, since they constitute the signal of the reactor antineutrino analysis.

Existing approaches [88–90] base the description of the light emission from positrons on the light emission from gammas, which itself is based on the light emission from electrons, as seen in section 4.2.2. However, these approaches fail to properly account for all secondary particles produced in the medium, for example, the contribution of gammas from Bremsstrahlung by electrons and positrons is not included, so there is missing energy in the model. Furthermore, the description of the light emissions of e^-, γ, and e^+ are highly interrelated, *e.g.*, high energy gammas might undergo pair production thus producing a positron, which then annihilates producing gammas. A semi-analytical model as the one proposed in section 4.2.2 and based on the definitions of the visible energy for e^-, γ, and e^+ in Eq. (4.11), (4.13), and (4.15), is thus complicated and incomplete.

In contrast, the method we present in this work treats e^-, γ, and e^+ in the same way, applying exactly the same procedure to evaluate the visible energy. This approach exploits a stand-alone Geant4 [91–93] MC simulation framework, so that all relevant processes in radiation-matter interaction are accounted for, and secondary particles are properly treated.

The model is based on the fact that radiation-matter interactions in Geant4 are divided in steps, and it is possible to track the primary particle and all sec-

ondary particles until all their energy is deposited in the medium. Furthermore, at each step it is possible to get several quantities, *e.g.*, the length of the step and the amount of energy deposited in that step. A schematic example is shown in Fig. 4.11, where the primary particle is the γ on the bottom left, which doesn't ionize the medium. After a step, Geant4 evaluates the probability of a Compton scattering happening and samples the energies of the final-state γ' and electron. The ionization process of the electron is implemented in steps, only three are shown in the figure; one step is highlighted in green. For each step, the relevant quantities that are needed in this work are the step length, dx, and the amount of energy lost through ionization in the step, dE.
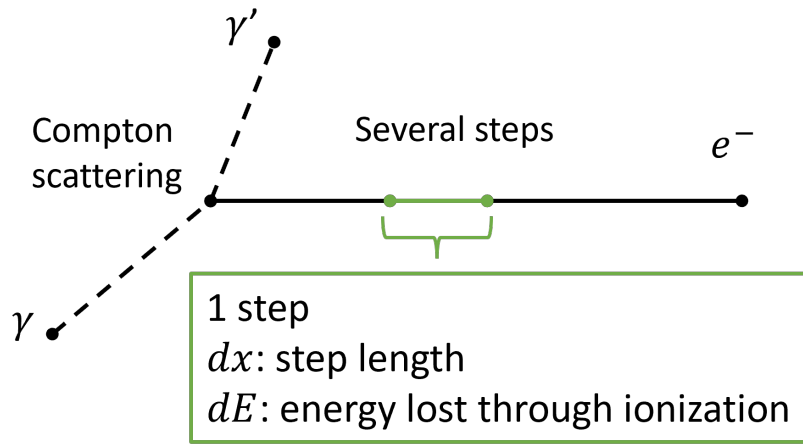
Figure 4.11. Working principle of a Geant-4 simulation. γ is an incoming gamma ray, interacting via Compton scattering, thus we are left with a new gamma ray with lower energy, γ', and an electron, which loses energy through ionization. The ionization process is implemented in steps, each characterized by a different step length, dx, and energy loss, dE. As an example, three steps are shown, and one is highlighted in green.

We start by describing the model for γ and its tuning based on mock calibration data, section 4.4.1, then we test the model on e^-, section 4.4.2, and finally we apply the model on e^+, section 4.4.3.

4.4.1   Tuning the model on γ calibration sources

In this section, we start building the model for gammas, since JUNO will use γ calibration sources to anchor the energy scale and study the detector response. To simplify the model, we consider single γ peaks even when multiple gammas are emitted simultaneously, *e.g.*, for ^{60}Co and for the neutron capture on carbon atoms. Hence, we simulated one million γ events for each of the following energies: 0.511 MeV, 0.662 MeV, 0.835 MeV, 1.173 MeV, 1.26 MeV, 1.333 MeV, 1.461 MeV, 2.22 MeV, 3.68 MeV, 4.43 MeV, 4.94 MeV, and 6.13 MeV. Each event was simulated inside a box of liquid scintillator with a side length of 10 m, in this way the event is fully contained inside the box without energy leakage. The liquid scintillator mixture used in the simulation is the same as the one implemented in

JUNO simulation framework; it is summarized in Table B.1. Other properties of the liquid scintillator are listed in Table B.2.

As already anticipated, we are interested in dE, the energy lost through ionization in one step of the simulation by a charged particle. We then get the length of the step, dx, which is given in units of cm, and multiply it by the density of the liquid scintillator, $\rho = 0.859\,\mathrm{g/cm^3}$ [30], to get a mass per unit area in $\mathrm{g/cm^2}$, as required by the notation introduced at the beginning of the chapter in section 4.1. Then, we evaluate the mass stopping power dE/dx in units of $\mathrm{MeV\,cm^2/g}$ for the given step. The procedure is performed for each step of each secondary charged particle produced in the simulation; in case of a primary electron or positron, the same procedure is done also on the ionization steps of the primary electron or positron. Finally, we fill a histogram with the value of dE/dx, and each entry is weighted by the corresponding value of the deposited energy dE, as depicted in the simplified scheme of Fig. 4.12a.

In Fig. 4.12a, the green box corresponds to a single entry of the histogram, in particular, to the i-th entry of the j-th dE/dx bin; as an example, the green box corresponds to the entry of the step highlighted in green in Fig. 4.11. By summing over i, we get the deposited energy in each single bin, which corresponds to the red box in Fig. 4.12a:

$$dE_j = \sum_i^{N_j} dE_{ij}, \tag{4.20}$$

where N_j is the number of entries in the j-th bin. By summing over all bins, we get the total deposited energy:

$$E_{\mathrm{dep}} = \sum_j^{N_{\mathrm{bins}}} dE_j = \sum_j^{N_{\mathrm{bins}}} \sum_i^{N_j} dE_{ij}, \tag{4.21}$$

where N_{bins} is the total number of bins in the histogram. We have checked that the deposited energy evaluated from the dE/dx histogram is within $0.3\,\%$ from the expected value, i.e., the initial γ energy, for all energies. An example of a dE/dx histogram for $E_\gamma = 6.13\,\mathrm{MeV}$ is shown in Fig. 4.12b. Each histogram is divided into $60\,000$ bins, from 0 to $600\,\mathrm{MeV\,cm^2/g}$, so with a bin width of $0.01\,\mathrm{MeV\,cm^2/g}$.

Then, we can apply Birks' law, which is applied outside of the simulation framework so that the Birks' constant can be changed and is not a hard-coded quantity. The underlying idea of the model is that all entries in each dE/dx bin are quenched by the same factor, which depends on dE/dx and the value of the Birks' constant, as in Eq. (4.7). In the end, we can directly apply the respective factor to the content of each bin, and evaluate the visible energy:

$$E_{\mathrm{vis}} = \sum_j^{N_{\mathrm{bins}}} \frac{dE_j}{1 + k_B \left(dE/dx\right)_j}, \tag{4.22}$$

where we sum over all bins and dE_j is the quantity defined in Eq. (4.20). Finally, for each initial γ energy, the quenching factor describing the scintillation non-

(a) *Simplified scheme of the dE/dx distribution.*

(b) dE/dx *distribution for $E_\gamma = 6.13\,\text{MeV}$.*
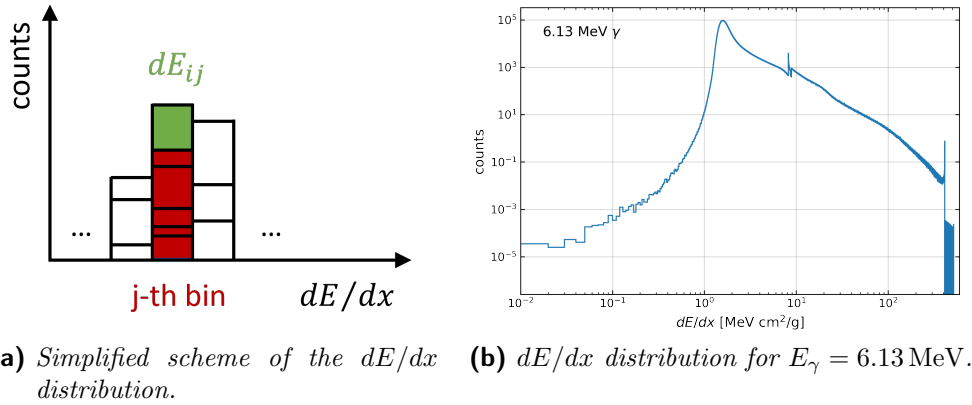
Figure 4.12. **(a)** Simplified scheme of the dE/dx distribution, with a single entry and one bin highlighted in green and red, respectively. **(b)** Example of the dE/dx distribution for $E_\gamma = 6.13\,\text{MeV}$, obtained by simulating 10^6 gammas. The two sharp peaks in the distribution are most likely related to the production cut set in the Monte Carlo software.

linearity is defined as:

$$f_q = \frac{E_{\text{vis}}}{E_{\text{dep}}}, \tag{4.23}$$

where E_{quenched} and E_{dep} are taken from Eq. (4.22) and (4.21), respectively. The quenching factor defined above corresponds to the one that was defined for gammas in Eq. (4.14), and the same definition holds for electrons, Eq. (4.12), and positrons, Eq. (4.16).

Since k_B is a free parameter in Eq. (4.22), it is possible to evaluate the γ quenching factor for different values of the Birks' constant; the γ quenching factor can be collected into a lookup table, like the one shown in Fig. 4.13 for a few representative values of k_B, ranging from $1.5 \cdot 10^{-3}\,\text{g/(cm}^2\,\text{MeV)}$ to $2.15 \cdot 10^{-2}\,\text{g/(cm}^2\,\text{MeV)}$ in steps of $1.0\,\text{g/(cm}^2\,\text{MeV)}$. As expected, the higher the value of k_B, the more quenched the γ energy.

As already mentioned, this model can be used to fit the calibration data in order to get the value of the Birks' constant which better describes the real liquid scintillator quenching, and use this value as an input of the MC simulation software. A simple χ^2 fit is used:

$$\chi^2 = \sum_\gamma \left(\frac{M^\gamma(k_B) - D^\gamma}{\sigma^\gamma} \right)^2, \tag{4.24}$$

where M^γ is the energy of the γ calibration peak predicted by the model presented in this work, $M^\gamma(k_B) = f_q^\gamma(k_B)\,E^\gamma$, while D^γ and σ^γ come from the calibration data, and k_B is the only free parameter. The sum runs over the γ peaks listed at the beginning of this section.

Since the JUNO experiment is still under construction and there are no real data available, we can perform a closure test by producing mock data with the same stand-alone G4 simulation framework and fitting the model to the mock data, while keeping in mind that the ultimate goal is the tuning of JUNO Monte
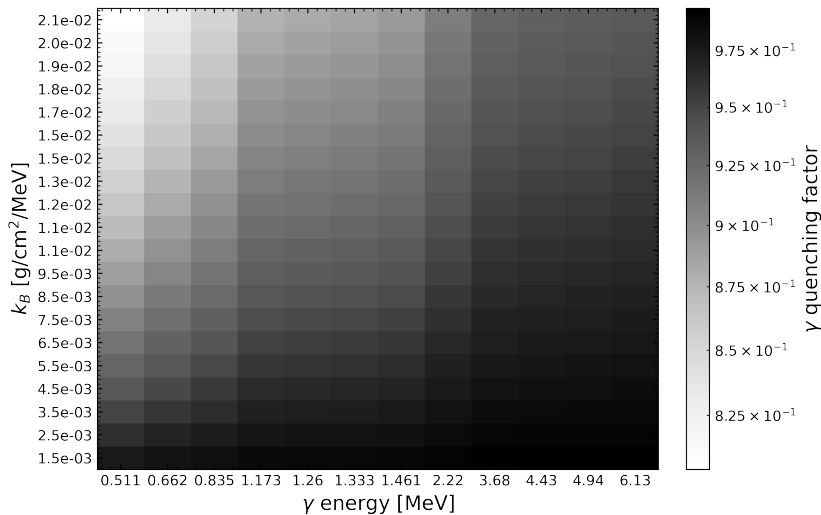
Figure 4.13. Lookup table for the γ quenching factor, evaluated with the G4-based model. It is possible to evaluate the quenching factor affecting each γ calibration source for different values of the Birks' constant k_B.

Carlo simulation framework through γ calibration sources. Mock data are obtained with a hard-coded value of $k_B = 6.5 \cdot 10^{-3}\,\mathrm{g/(cm^2\,MeV)}$, and we take the mean and the standard deviation of the mean of the quenched energy distribution as D^γ and σ^γ. The result of the fit is shown in Fig. 4.14, with the mock data as black squared, and the best fit values from the G4-based model as red circles. The best fit value of the Birks' constant is $k_B = (6.4329 \pm 0.0003) \cdot 10^{-3}\,\mathrm{g/(cm^2\,MeV)}$, less than $1\,\%$ from the real input value, and the residuals are well within $0.1\,\%$, as shown in the bottom panel of Fig. 4.14. This model has slightly better performances with respect to the approach presented in [90], which shows similar residuals but finds a best fit value for the Birks' constant more than $11\,\%$ from the true input value.

4.4.2   Testing the model on electrons

Before going to positrons, we test the G4-based model for the scintillation nonlinearity on electrons. We repeat the steps presented in section 4.4.1 up to the evaluation of the electron quenching factor, Eq. (4.23), for a selected list of representative electron kinetic energies: from $0.1\,\mathrm{MeV}$ to $1\,\mathrm{MeV}$ in steps of $0.1\,\mathrm{MeV}$, and from $1\,\mathrm{MeV}$ to $10\,\mathrm{MeV}$ in steps of $1\,\mathrm{MeV}$. The lookup table for the e^- quenching factor is shown in Fig. 4.15a for a few representative values of k_B, ranging from $1.5 \cdot 10^{-3}\,\mathrm{g/(cm^2\,MeV)}$ to $2.15 \cdot 10^{-2}\,\mathrm{g/(cm^2\,MeV)}$ in steps of $1.0 \cdot 10^{-3}\,\mathrm{g/(cm^2\,MeV)}$. The lookup table for electrons might also become useful when considering the continuous β spectrum of the cosmogenic $^{12}\mathrm{B}$ that will be used to calibrate the energy response up to $12\,\mathrm{MeV}$.

We can now compare the model to mock data. Mock data are obtained by simulating 10^6 electrons for each of the energy listed above; the Geant4 stand-alone simulation framework with the Birks' constant set to $k_B = 6.5 \cdot 10^{-3}\,\mathrm{g/(cm^2\,MeV)}$ is used. As it was done for gammas, we take the mean of the quenched energy
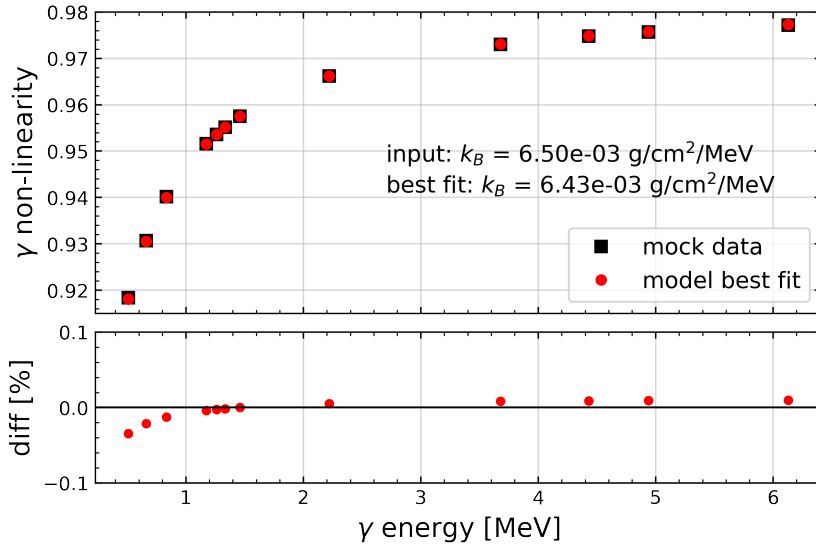
Figure 4.14. Fit of the model to the single peaks of the γ calibration sources. The mock data are shown as black squares, while the best fit points as red circles. The bottom panel shows the relative difference of the best fit points with respect to the mock data.

distribution as the estimate of the peak position from the mock data; these values are shown as black squares in Fig. 4.15b. The model prediction is evaluated for $k_B = 6.43 \cdot 10^{-3}$ g/(cm^2 MeV), the best-fit value of the Birks' constant, so that we can test how much the model calibrated on the γ sources in the previous section is able to describe the light emission of electrons. The predicted values are shown as red circles in Fig. 4.15b. In the bottom panel, the relative difference of the model prediction with respect to the mock data is shown. With the exception of the first point at 0.1 MeV at almost 0.2 %, the relative difference is well within 0.1 % up to 10 MeV, thus the model calibrated on gammas is able to describe the e^- non-linearity with good accuracy.

(a) *Lookup table for e^- f_q.*

(b) *Model-data comparison for e^-.*
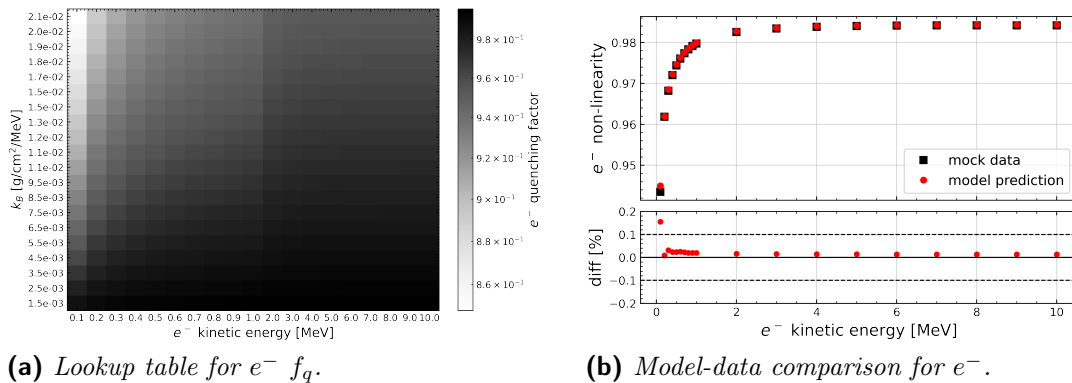
Figure 4.15. **(a)** Lookup table for the e^- quenching factor. **(b)** Comparison of the prediction from the G4-based model (red circles) to mock data (black squares) for e^-. The bottom panel shows the relative difference of the model prediction with respect to the mock data.

4.4.3   Applying the model to positrons

Finally, we apply the model to positrons, since they constitute the signal in the reactor electron antineutrino analysis. We follow the same procedure for e^+ as explained in section 4.4.2 for e^-. We consider the following positron kinetic energies: from $0.0\,\mathrm{MeV}$ to $1\,\mathrm{MeV}$ in steps of $0.1\,\mathrm{MeV}$, and from $1\,\mathrm{MeV}$ to $10\,\mathrm{MeV}$ in steps of $1\,\mathrm{MeV}$; we consider also a null kinetic energy since the positron can be produced at rest if the $\overline{\nu}_e$ energy is at the threshold of the IBD interaction.

Figure 4.16a shows the lookup table for the positron quenching factor, for different values of the Birks' constant, ranging from $1.5 \cdot 10^{-3}\,\mathrm{g/(cm^2\,MeV)}$ to $2.15 \cdot 10^{-2}\,\mathrm{g/(cm^2\,MeV)}$ in steps of $1.0 \cdot 10^{-3}\,\mathrm{g/(cm^2\,MeV)}$.

Similarly to what was done for electrons, Fig. 4.16b shows the comparison between the mock data and the model prediction for positrons. Mock data are obtained by simulating 10^6 positrons for each of the energy listed above; the Geant4 stand-alone simulation framework with the Birks' constant set to $k_B = 6.5 \cdot 10^{-3}\,\mathrm{g/(cm^2\,MeV)}$ is used. The mean of the quenched energy distribution is taken as the estimate of the peak position from the mock data; these values are shown as black squares in Fig. 4.16b. The predicted values, shown as red circles in Fig. 4.16b, are evaluated for $k_B = 6.43 \cdot 10^{-3}\,\mathrm{g/(cm^2\,MeV)}$, the best-fit value of the Birks' constant. In the bottom panel, the relative difference of the model prediction with respect to the mock data is shown. The relative difference is well within $0.1\,\%$ over the whole range of positron kinetic energy, showing that the model calibrated on gammas gives an accurate description of the positron non-linearity.

(a) *Lookup table for e^+ f_q.*   **(b)** *Model-data comparison for e^+.*
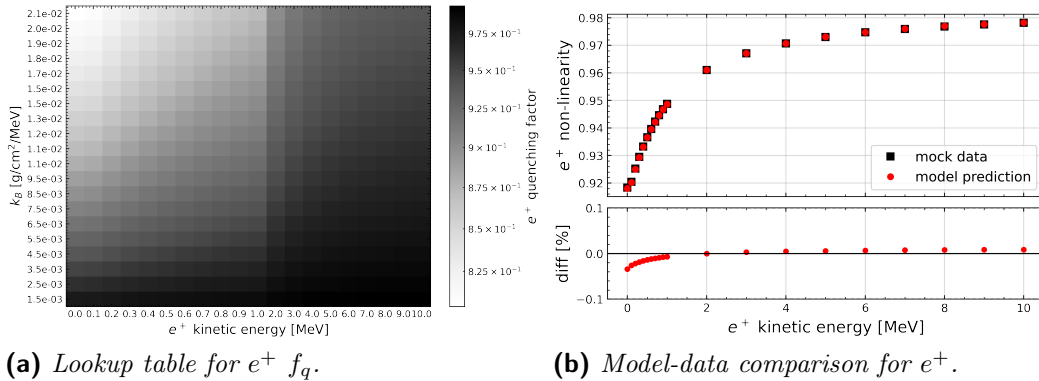
Figure 4.16. **(a)** Lookup table for the e^+ quenching factor. **(b)** Comparison of the prediction from the G4-based model (red circles) to mock data (black squares) for e^+. The bottom panel shows the relative difference of the model prediction with respect to the mock data.

4.4.4   Possible future work

The method presented so far only describes the non-linearity of the light emission through the scintillation process. As presented in section 4.2.2, the Cherenkov effect can introduced an additional non-linearity, so future studies could focus in trying to incorporate this effect into the non-linearity model. Furthermore, it

could be possible to include this model as one of the possible implementations of the LSNL in a fitting framework, and it would be interesting to compare the results obtained with different non-linearity methods.

In addition, it might also be interesting to study the effect of the production cut in the Geant4 simulations on the model, as already investigated by the Daya Bay experiment [88]. In the following section, we present a preliminary study on this topic.

MC production cut as an additional free parameter

The output of a G4-based simulation depends on the production cut, which sets a cut in the production of secondary particles for those processes with divergences at low energies, *i.e.*, ionization and Bremsstrahlung; the production cut is needed because of the limited computational time and resources that would be otherwise required. The production cut is given as a threshold length, l_{cut}, which is then converted into an energy threshold depending on the material and the particle; values for JUNO liquid scintillator can be found in Table B.3. At one step, if the particle has not enough energy to produce secondary particles that will travel at least the set threshold length, the energy loss in discrete steps is stopped, no more secondaries are produced, and the particle is tracked down to zero energy considering a continuous energy loss. Thus, the number of secondary particles and their energy distribution, and hence the distribution of dE/dx, depends on the value of the production cut, which represents another input of the MC simulation framework and could be highly correlated with the Birks' constant k_B.

We include the production cut as a free parameter in our model by simulating particles and getting the dE/dx distributions for different values of the production cut: $1000\,\mu\text{m}$, $100\,\mu\text{m}$, $10\,\mu\text{m}$, and $1\,\mu\text{m}$. In the default JUNO simulation framework, the default values are $1000\,\mu\text{m}$ for γ and $100\,\mu\text{m}$ for e^- and e^+, while in our simulation we set the same cut for all particles. Since we simulate only four values of the production cut, a linear 1D interpolation is performed to get intermediate values.

We define a new χ^2 formula:

$$\chi^2 = \sum_\gamma \left(\frac{M^\gamma(k_B, l_{\text{cut}}) - D^\gamma}{\sigma^\gamma} \right)^2, \tag{4.25}$$

where M^γ is now the prediction from the model with two parameters: k_B and the production cut, l_{cut}, which are left free in the fit. The mock data considered in this study are obtained with the Geant4 stand-alone simulation framework with $k_B = 6.5 \cdot 10^{-3}\,\text{g}/(\text{cm}^2\,\text{MeV})$ and $l_{\text{cut}} = 100\,\mu\text{m}$.

As expected, the two parameters are highly correlated, with a linear correlation coefficient of 0.87; the 2D contour plots at $68\,\%$, $90\,\%$, and $99\,\%$ are shown in Fig. 4.17. The best fit values are $k_B = (6.4026 \pm 0.0007) \cdot 10^{-3}\,\text{g}/(\text{cm}^2\,\text{MeV})$ and a production cut of $l_{\text{cut}} = (97.61 \pm 0.04)\,\mu\text{m}$, which are actually a few sigmas far from the MC real input values. The origin of the discrepancy is still under investigation.
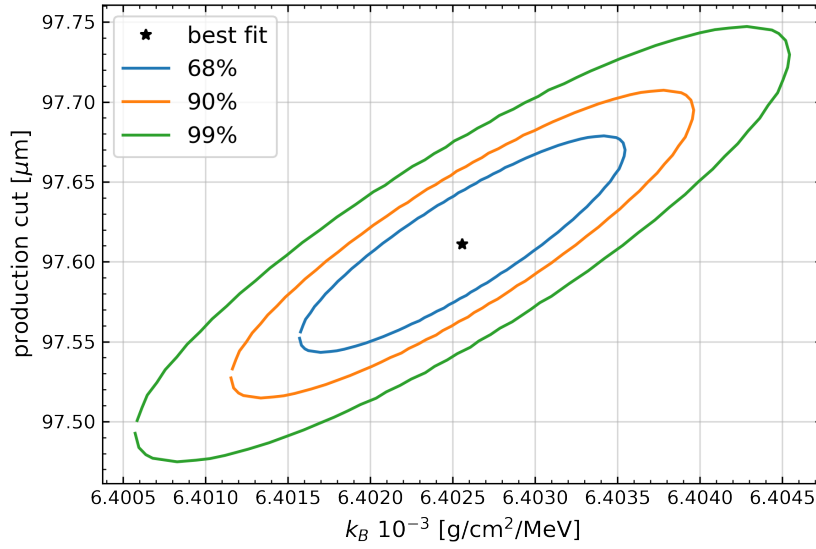
Figure 4.17. Contour plot of k_B and the production cut. The two parameters are highly correlated, with a linear correlation coefficient of 0.87. The best fit values are: $k_B = (6.4026 \pm 0.0007) \cdot 10^{-3} \, \mathrm{g}/(\mathrm{cm}^2 \, \mathrm{MeV})$ and $l_{\mathrm{cut}} = (97.61 \pm 0.04) \, \mu\mathrm{m}$; these values are several sigmas far from the real input values of $6.5 \cdot 10^{-3} \, \mathrm{g}/(\mathrm{cm}^2 \, \mathrm{MeV})$ and $100 \, \mu\mathrm{m}$.

4.5 Results and discussion

In this chapter, a novel method based on a simple output of Geant4 simulations was presented to model the scintillation non-linearity with just one free parameter, the Birks' constant k_B. The model was built starting from the γ non-linearity, and was then tuned using mock calibration data to obtain the value of the Birks' constant, $k_B = (6.4329 \pm 0.0003) \, \mathrm{g}/(\mathrm{cm}^2 \, \mathrm{MeV})$, which was found to be within $1\,\%$ from the input value, showing better performance with respect to previous approaches [90].

The model was then applied to the e^- and e^+ non-linearity, so that all particles are treated with the same approach. Figure 4.18 shows the non-linearity curves of e^- (blue), γ (orange), and e^+ (green) with $k_B = (6.4329 \pm 0.0003) \, \mathrm{g}/(\mathrm{cm}^2 \, \mathrm{MeV})$ as a function of the particle kinetic energy (4.18a) and the total deposited energy (4.18b). For electrons and gammas, the deposited energy is equal to the kinetic energy of the particle, while for positrons the deposited energy also includes the two $0.511 \, \mathrm{MeV}$ gammas from the positron annihilation, as in Eq. (4.4). For all particles, the comparison between the model prediction and the mock data shows a relative difference within $0.1\,\%$, providing a good consistency check of the model.
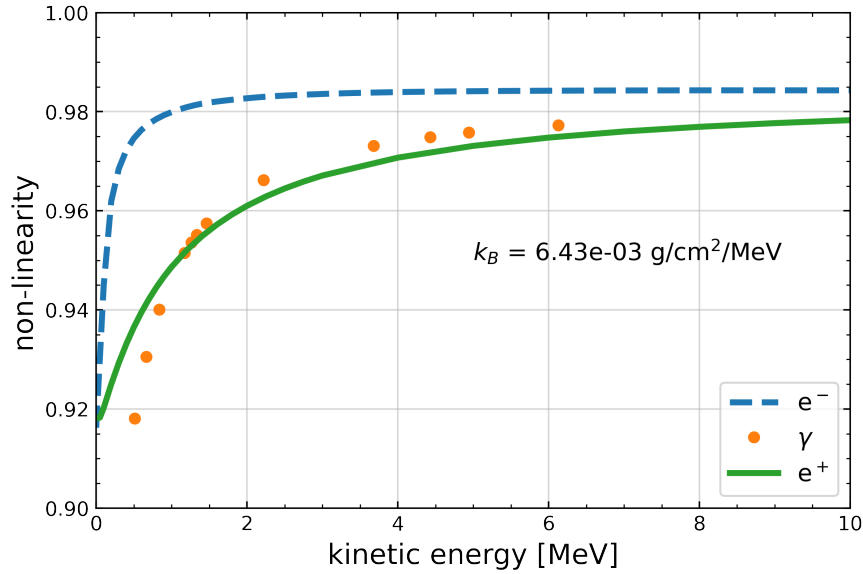
(a) *Non-linearity curves versus kinetic energy.*
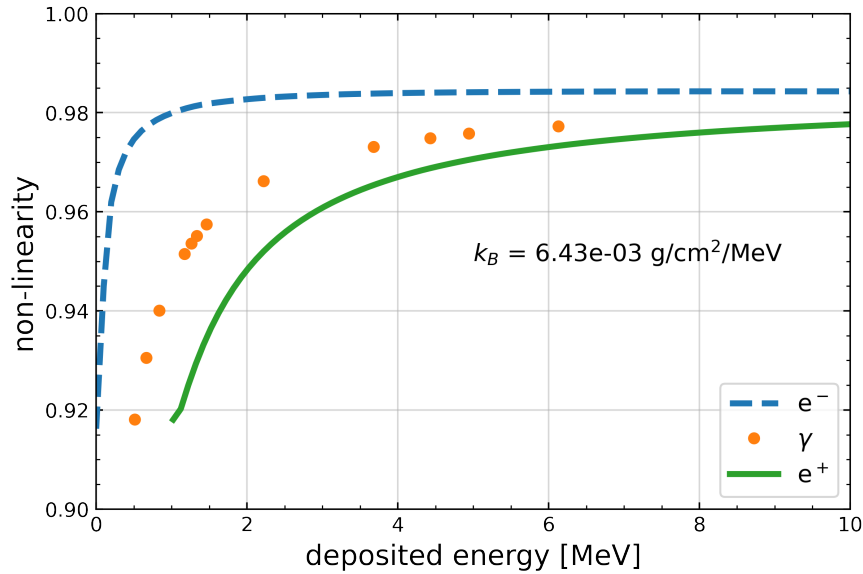
(b) *Non-linearity curves versus deposited energy.*

Figure 4.18. Non-linearity curves for e^- (blue), γ (orange), and e^+ (green) as a function of **(a)** the particle kinetic energy and **(b)** the total deposited energy, obtained with the value of the Birks' constant from the fit on the γ calibration sources, $k_B = 6.43 \cdot 10^{-3}\,\mathrm{g/(cm^2\,MeV)}$.

Chapter 5

Mass testing of JUNO 20-inch PMT readout electronics

The scintillation and Cherenkov light produced by the interaction of an electron antineutrino in the liquid scintillator is detected by the 20-inch and 3-inch PMT system described in section 2.1.4. The 20-inch PMT output current is sampled and processed by the JUNO 20-inch PMT underwater readout electronic system [103–105] Spotting hardware failures and evaluating the performance of the underwater readout electronics before the actual installation is of paramount importance, because it will be impossible to repair or to change an electronics module after its deployment. Furthermore, the required loss rate of the electronics channels is less than 0.5% in 6 years [31]. In addition, a thorough characterization of the readout electronics is essential in the evaluation of JUNO observable: the reconstructed energy, E_{rec}. In fact, a possible non-linearity of the electronics channels, which is referred to as *instrumental non-linearity* in contrast to the intrinsic non-linearity of the liquid scintillator light emission process, could distort the spectrum and spoil the neutrino mass ordering determination. Furthermore, it is also important to check the stability of the electronics over time, since any change in the performance could affect the reconstruction and introduce a bias in E_{rec}, thus affecting JUNO physics analyses.

To this end, we designed and developed a dedicated test protocol [106–108] used during the mass production, at a dedicated facility in Kunshan, China. The protocol could also be used during the installation procedure to check if anything went wrong during the installation and to verify that the electronics performance didn't change.

The rest of the chapter is organized as follows: in section 5.1 we describe the JUNO 20-inch PMT readout electronics; in section 5.2 we discuss the mass production and the mass testing setup at the dedicated facility in Kunshan, China; in section 5.3 a detailed description of the developed test protocol is presented; conclusions are drawn in section 5.4.

5.1   JUNO 20-inch PMT readout electronics
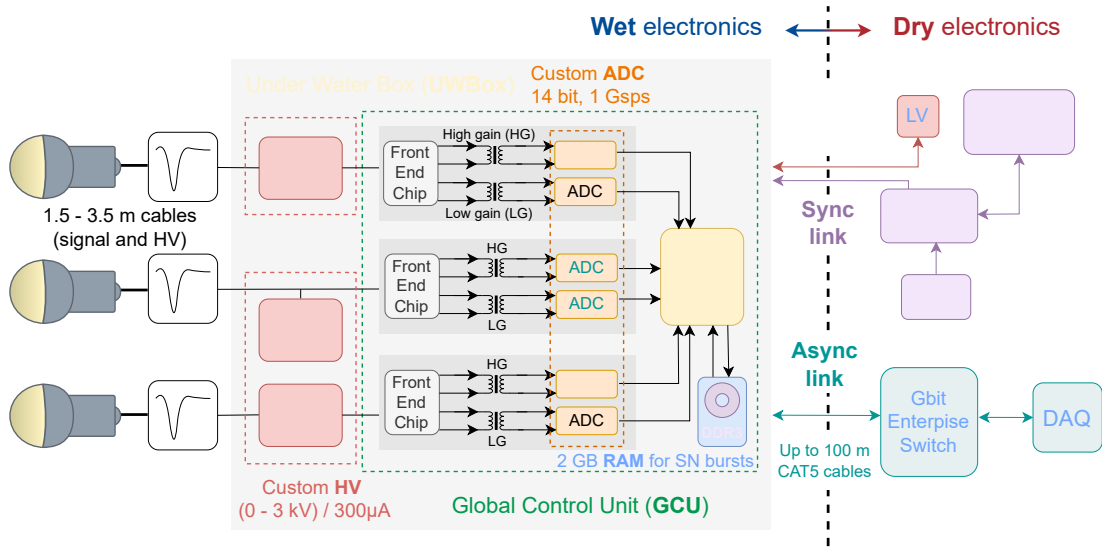
Figure 5.1. JUNO 20-inch PMT readout electronics schematic [109]. A description of the different parts is given in the text.

A schematic of the JUNO 20-inch PMT electronics is given in Fig. 5.1. Only details relevant for the test protocol are provided here, while more detailed descriptions can be found in [109–111];

Three 20-inch PMTs are connected through 50 Ω, coaxial cables to the *front-end* (FE), or *wet*, electronics [110], which is located very close to the PMT output, and hosted inside a stainless steel, water-tight box: the Under Water Box (UW-Box). In total, the JUNO detector is instrumented with 6681 UWBoxes, 5878 for the central detector and 803 for the Cherenkov water pool, as part of the JUNO veto system. Each UWBox contains three High Voltage Units (HVUs), which are programmable modules providing the bias voltage to the PMT voltage divider, and a motherboard incorporating the front-end and readout electronics components: the Global Control Unit (GCU).

Each GCU implements three readout channels, one for each connected 20-inch PMT. The PMT analog signal reaching the GCU is processed by a custom Front-End Chip (FEC), which duplicates the input signal and injects it in two parallel streams with different gains, referred to as *high-gain stream* and *low-gain stream* (see Fig. 5.1). The signal from each stream is converted to a digital waveform by a 14-bit, 1 GS/s, custom flash Analog-to-Digital Converter (ADC). The usage of two flash ADCs per readout channel has been driven by the design requirement of providing a wide dynamic range in terms of reconstructed photo-electrons (PE) [109]. The digital signal is further processed by a Xilinx Kintex-7 FPGA (XC7K325T), which has the task of generating trigger primitives, reconstructing the charge, timestamp tagging, and temporarily storing the signal before sending it to the data acquisition (DAQ).

The electronics inside the UWBox has two independent connections to the *dry* electronics: a *synchronous link* (S-link) for the connection to the *back-end*

(BE) electronics, which provides the clock and synchronization to the boards and handles the trigger primitives; and an *asynchronous link* (A-link) which is fully dedicated to the DAQ and slow-control, or Detector Control System (DCS). A modified dedicated version of the 1588 protocol [112] is used to keep all the boards synchronized and correct time delays due to the cable length difference. Through the A-link, the IPBus Core protocol [113] is used for data transfer [111], slow control monitoring, and electronics configurations. These connections are realized using commercially available CAT-5 and CAT-6 Ethernet cables for the A-link and S-link, respectively; the length of the cables ranges between 30 m and 100 m. An additional, low-resistance, power cable will bring power to the electronics inside the UWBox.

The three channels of each GCU are independent up to the FPGA. This means that any misbehavior happening before the FPGA will not impact the neighboring channels, while a misbehavior of the FPGA or of the connections to the dry electronics will result in the loss of three channels.

For the purpose of the electronics mass testing described here, GCUs were operated in a self-trigger mode, where all channels trigger in parallel and where all readout boards send their locally triggered waveforms to the DAQ, independently of each other, whenever a signal exceeds a given threshold. In this configuration, the BE trigger electronics and the S-link were only used to provide the UWBox with the clock needed to operate properly.

5.1.1 Internal test pulse generator

Each GCU is equipped with three independent test pulse generator circuits, one per channel; a schematic of the circuit is presented in Fig. 5.2. The main components of the circuit are a 16-bit digital-to-analog converter (DAC), a switch, and a RC circuit acting as a differentiator, or high-pass filter, with $C_1 = 390$ pF and $R_2 = 24.9\,\Omega$, with a 5 % and 1 % tolerances, respectively; the values of C_1 and R_2 were chosen to produce a signal mimicking a PMT signal.

The amplitude of the generated pulse can be adjusted via the IPbus protocol [113] by changing the input digital amplitude of the DAC (A_{DAC}), which uses a reference voltage of 5 V to convert the digital value to a voltage value. The pulse is generated by closing the switch and connecting the node between the DAC and the differentiator to ground, generating a step voltage, as shown in Fig. 5.2. The step function goes through a differentiator, or high-pass filter, generating a PMT-like pulse which is injected directly into the FEC of the channel. The switch is also controlled via the IPbus protocol: to generate one pulse, we need to close and then open again the switch, hence two IPbus commands are needed; in this way it is possible to control the frequency at which the switch is closed/opened and the test pulses are generated.

The injected input charge, which is the area of each generated pulse, corresponds to the charge accumulated by the capacitor C_1 under a potential difference equal to the DAC output, evaluated as follows:

$$Q_{\mathrm{in}} = A_{\mathrm{DAC}} \cdot \frac{5\,\mathrm{V}}{2^{16}} \cdot C_1, \tag{5.1}$$
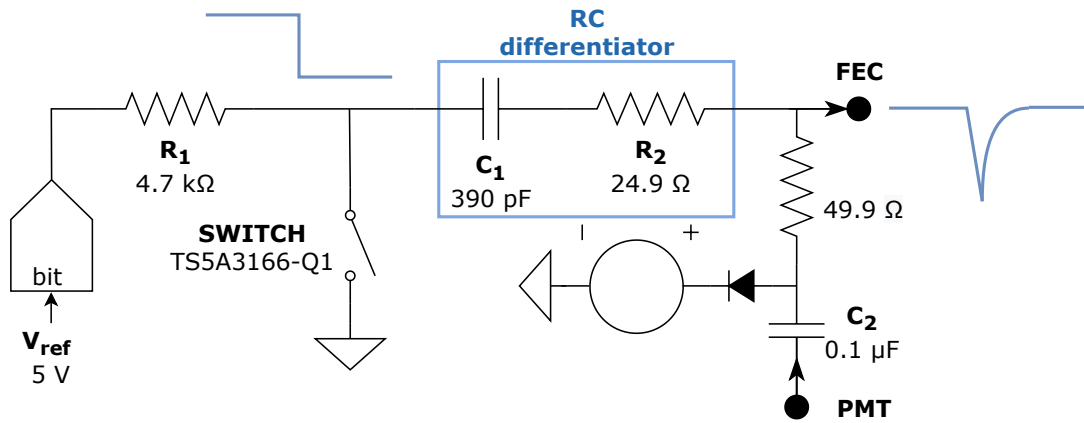
Figure 5.2. Schematic of the internal test pulse generator. Each channel is equipped with one internal generator circuit, which is connected directly to the Front-End Chip (FEC). The main components of the circuit are a 16-bit digital-to-analog converter (DAC), a switch, and a RC circuit with $C_1 = 390\,\mathrm{pF}$ and $R_2 = 24.9\,\Omega$. The connection from the PMT to the FEC is also shown; arrows are used to indicate the direction of the signals.

where Q_{in} is in unit of pC if C_1 and A_{DAC} are in units of pF and DAC counts, respectively. The value $5\,\mathrm{V}/2^{16} \simeq 76\,\mathrm{\mu V}/\mathrm{DAC}$ counts is the conversion factor from DAC counts to a tension in volts.

5.2 Mass production and testing at the Kunshan site

A facility in Kunshan (昆山), China, was devoted to the mass production and testing of the 20-inch PMT readout electronics, composed of a total of 6950 boards.

5.2.1 Production process

During mass production, the first step was the welding of the stainless steel bellows to the UWBoxes, followed by a leakage test. Following this, the cables for the S-link, A-link, and the power line were threaded through the bellows. The GCU board and the three HV units were then assembled inside the UWBox and soldered to the cables. The electronics in each box was then tested for at least five days. If it passed the tests, the box was finally laser welded, and - following a further leakage test - was put into store before being sent to the JUNO experimental site. A picture of an assembled UWBox before laser welding is shown in Fig. 5.3a.

Before the beginning of the mass production, tests were performed on a small number of boxes to assess the possible damage and risks from the laser welding procedure; it was found that no damage is expected from this procedure. Nonetheless, a shorter version of the tests was performed on each board after the laser welding.
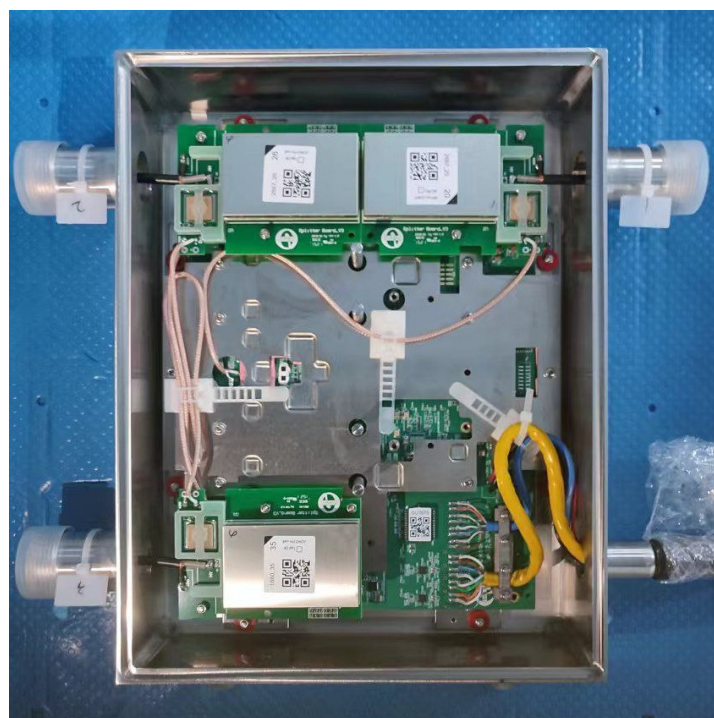
(a) *Assembled UWBox before laser welding.*

(b) *Shelf with UWBoxes in the testing room in Kunshan.*

Figure 5.3. **(a)** Picture of an assembled Underwater Box before laser welding. The three HVUs are clearly visible, one near each of the connectors at which the 20-inch PMTs will be connected. The GCU board is located on the bottom. **(b)** A shelf full of UWBoxes in the testing room at the Kunshan facility. In the front of the picture, a rack with power supplies, switches, and back-end and trigger electronics is also visible.

5.2.2   Testing of the GCUs

During the test, the assembled UWBoxes and the bellows were located on shelves in a dedicated testing room, as shown in Fig. 5.3b; in the front of the picture, a rack with power supplies, switches for the network connection, and the trigger electronics is also visible. The room had space to locate a maximum number of 344 GCUs on nine shelves. All the tests described in Section 5.3 were performed in parallel on all the GCUs available in the testing room.

The test procedure was automatized in order to minimize human errors during the shifts. Shifts were organized exploiting time zone differences between China, where the boxes were located, and Europe, so that the European part of the collaboration could take part in the mass testing remotely, since it was not possible to travel to China due to COVID-19 restrictions. During daytime in China, local shifters were in charge of assembling between 40 and 60 new UWBoxes per day and replacing them in the testing room. At the end of the Chinese working day, an European shifter took over to perform the tests; in this way it was possible to have shifts covering all 24 hours each day. Data analysis on the acquired data from the tests was performed on the following day, in order to provide a fast feedback on the tested boards. The mass testing of all 6950 GCUs lasted for about 10 months from October 2021 to July 2022. Figure 5.4 shows the cumulative number of tested boards as a function of time.
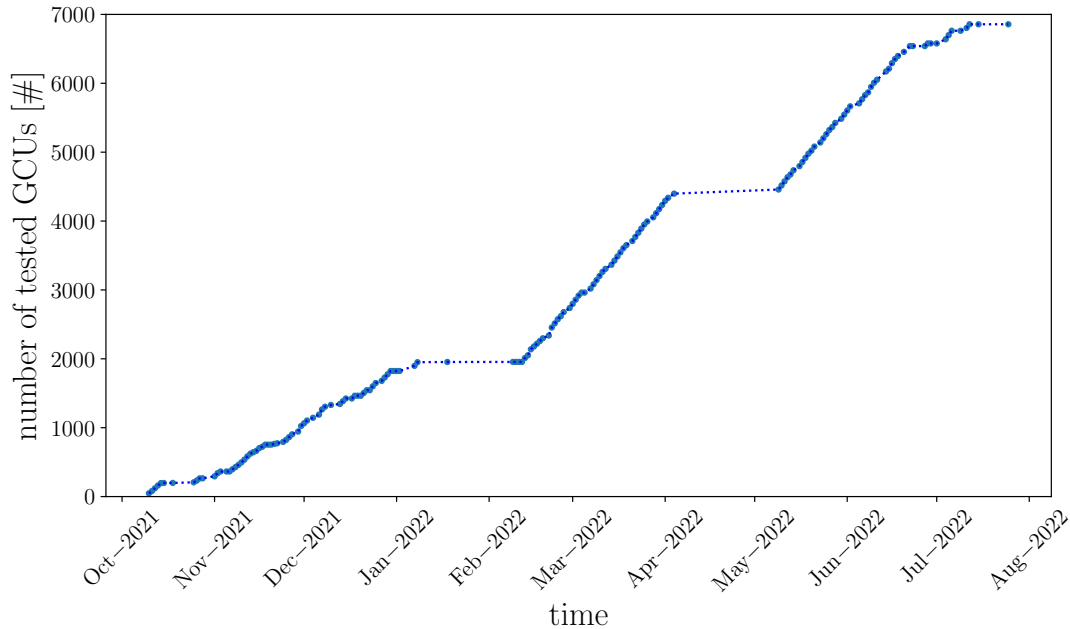
Figure 5.4. Cumulative number of tested GCUs as a function of time. The production and testing campaign started in October 2021 and ended in July 2022. A total of 6900 boards were tested. Two breaks in the production, the first due to Chinese New Year Holidays and the second due to a COVID-19 outbreak, are clearly visible.

5.2.3 Network and connection details at the Kunshan site

Figure 5.5 shows a scheme of the connections in the testing room at the Kunshan site. In the testing room, GCUs were connected to the BECs in batches of 40 in order to provide the clock to the tested boards through the synchronous link. A total of 9 BECs were needed; the BECs were then connected to the trigger electronics. For the asynchronous link, 40 GCUs were connected to a level 1 (L1) switch through a 1 Gb link, for a total of nine L1 switches; L1 switches were then connected to a level 2 (L2) switch through a 4x10 Gb link; the L2 switch was finally connected to the DAQ server via a 4x100 Gb link. The DAQ server consisted of a Dell PowerEdge C6400, with a total of 24 cores and 48 threads, a 2.7 GHz processor and 192 GB RAM. The ControlHub software was installed on the server in order to access the electronics devices through the IPbus protocol [113].
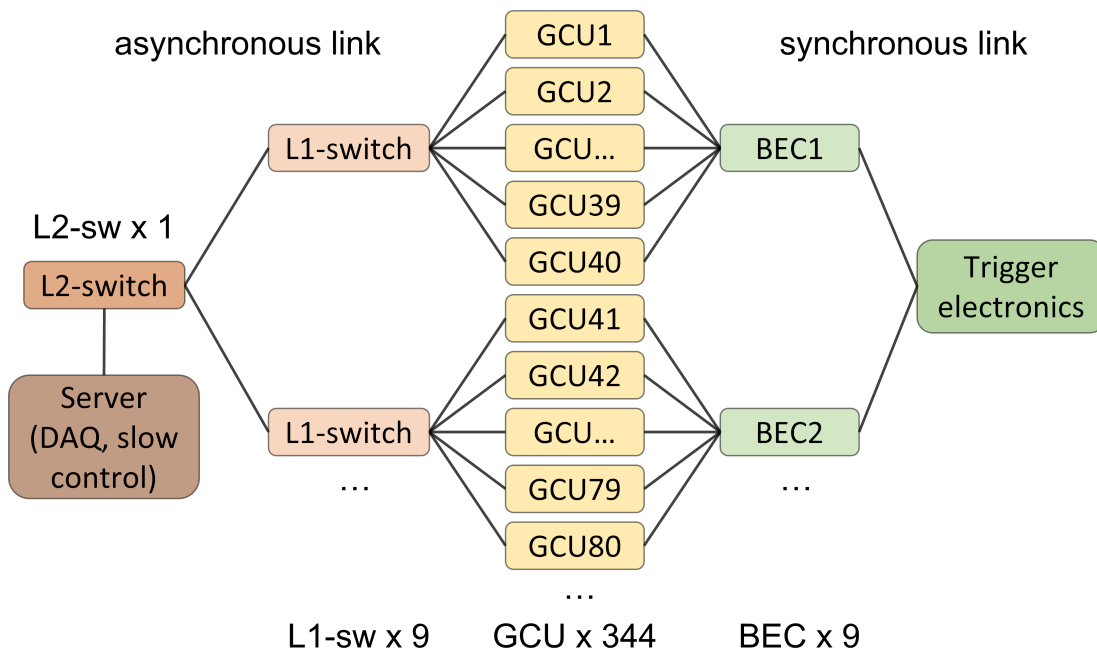
Figure 5.5. Schematic of the network connections at the Kunshan site. On the right part, the connection to the trigger electronics via the synchronous link is shown; on the left, the connection to the server through the asynchronous link is shown. In the current configuration of the Kunshan site, it is possible to test up to 344 GCUs in parallel.

A dedicated local network was used for the communication between the GCUs and the server. Each GCU is identified by a 4-digit ID number, ranging from 0001 to 7700. The GCU ID number defines the MAC address associated to the Kintex 7 FPGA of the GCU, which in turn defines the univocal IP address which is used to communicate with the electronics board. The IP address is 10.7.XX.XX/19, where the last two blocks correspond to the GCU ID in hexadecimal notation.

5.3   Test protocol for the 20-inch PMT readout electronics

We designed and implemented the test protocol [106, 107] according to the following criteria:

- it had to be controlled remotely and to be run in parallel to the production line;

- it had to be easy to operate, in order to have non-expert shifters being able to join the testing campaign;

- it had to provide the shifter with a fast and visual feedback of the performance of the tested components.

The test protocol was performed on each electronics card after all the components had been fitted, as described in Section 5.2.1, and before the UWBox was finally sealed. The protocol consisted of several steps:

(1) a connection test, to check that the board was reachable through the local network;

(2) a linearity and (3) a stability tests investigating the properties of the digitized waveforms to validate the performance and the reliability of the whole readout chain;

(4) a DCS test to monitor the temperature and the status of the board.

Each test is presented in more detail in section 5.3.3.

The tests of step (2) were performed separately on the high-gain and on the low-gain streams. Input signals were generated in both cases by the internal test pulse generator, but either the high-gain stream, or the low-gain stream was selected for the readout of the digitized waveform.

5.3.1   Properties of the digitized waveform

Figure 5.6 shows an example of a digitized waveform generated by the internal test pulse generator described in Section 5.1.1, where the high-gain stream was selected. During the tests, the length of the readout window, $i.e.$, the portion of the waveform which is sampled, is fixed to 304 samples which correspond to 304 ns, given the flash ADC sampling frequency of 1 GS/s.

For each digitized waveform, baseline and noise are evaluated. The baseline, B, is defined as the average of the first 85 samples; the noise, σ_{baseline}, is defined as the standard deviation computed on the same samples.

Another property which is monitored during the test is the waveform integrated charge. The waveform integrated charge, Q_{out}, corresponds to the shadowed region in Fig. 5.6 and it is evaluated offline as in the following equation:

$$Q_{\text{out}} = \sum_{i}^{N_s} \frac{75\,\mu\text{V} \cdot (B - N_i) \cdot \Delta t_s}{R}, \tag{5.2}$$
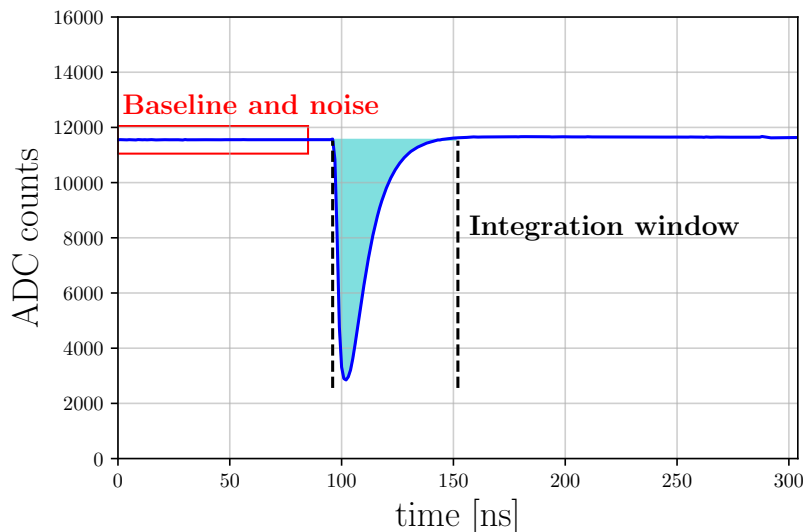
Figure 5.6. Example of a digitized waveform from GCU 3133 channel 0, generated with the internal test pulse generator, as described in Section 5.1.1, and obtained by selecting the high-gain stream. The first 85 samples are used to evaluate the values of the baseline and the noise. The limits of the charge integration window are shown as dashed black lines.

where N_s is the number of samples in the integration window, N_i is the amplitude in ADC counts of the i-th bin, B the baseline value as defined above, $75\,\mu V$ is the voltage corresponding to 1 ADC count, $R = 50\,\Omega$ is the input impedance, and Δt_s is the width of a single bin; in our case $\Delta t_s = 1\,ns$. The integration window, shown in Fig. 5.6, starts 5 ns before the minimum, or peak, of the waveform, and extends out to 50 ns after the minimum.

In Eq. (5.2), the conversion factor between ADC counts and voltage, equal to $75\,\mu V$/ADC count, is a characteristic of the flash ADCs, and it is the same for the high-gain and low-gain streams. In this way, Eq. (5.2) does not take into account the gain of the amplification step in the FEC, which in turn has to be determined through the linearity test of the test protocol, as explained in Section 5.3.3.

5.3.2 Configuration of the GCUs

The following GCU parameters needed to be set through the slow control before each test:

1. the length of the readout window;

2. the value of the pre-trigger;

3. the value of the trigger threshold;

4. the trigger mode.

For the mass production tests, we fixed the length of the readout window to 304 ns to optimize the total size of the acquired data. The pre-trigger is the time

interval between the beginning of the readout window and the moment at which the signal exceeds the threshold, *i.e.*, the region that precedes the pulse.

There are two possibilities for the trigger threshold: the threshold is either fixed to a given value in ADC counts, and is the same for all channels; or it is evaluated for each channel in terms of $\sigma_{\mathrm{baseline}}$ from the baseline. During the tests, the trigger threshold was fixed to a common value for all channels. The trigger modes were described in Section 5.1. During the tests, the trigger mode was set to the locally-triggered configuration in which channels trigger independently from each other with the BE trigger electronics not employed.

5.3.3   The test protocol

In this section, the four tests composing the test protocol for the 20-inch PMT readout electronics are presented.

Connection test

The first step of the test protocol is the connection test, meant to check that all the GCUs are properly connected to the local network and responding. A non-responding board would imply either that the cables are not properly plugged in, which is an easy issue to solve, or that the assembling procedure had not been successful, thus requiring further investigation on the production side.

For this test, we used the default Linux `ping` command and sent 100 56-byte packets in 1 s from the DAQ server to each GCU, so that it was possible to test in a few seconds the connection to the local network of hundreds of boards. The IP addresses were automatically recovered by the input GCU ID number, as explained in section 5.2.3. The `ping` command directly calculates the mean response time and its standard deviation, which were both stored, together with the fraction of lost packets.

As a quick visual feedback for the shifter, the mean response time and its standard deviation were recovered and plotted versus the GCU ID number; an example with a batch of 160 GCUs is shown in Fig. 5.7. The mean response time depends on the length of the asynchronous link cables and on the network configuration.

Linearity test

The linearity test was meant to test the linear response of the two flash ADCs serving each channel and evaluate the gain factors of the two data streams in the FEC. The test was performed by generating PMT-like signals with the internal test pulse circuit described in Section 5.1.1. Before this test, the channel linearity was studied with external physics sources and by reading PMT signals on a small set of boxes [109, 114].

For the test, values of the test pulse amplitude were chosen to cover a wide range. For the high-gain stream, the range starts at 1 PE up to about 160 PE, before the beginning of the saturation regime. For the low-gain stream, the range starts at about 90 PE up to the maximum possible value of the DAC,
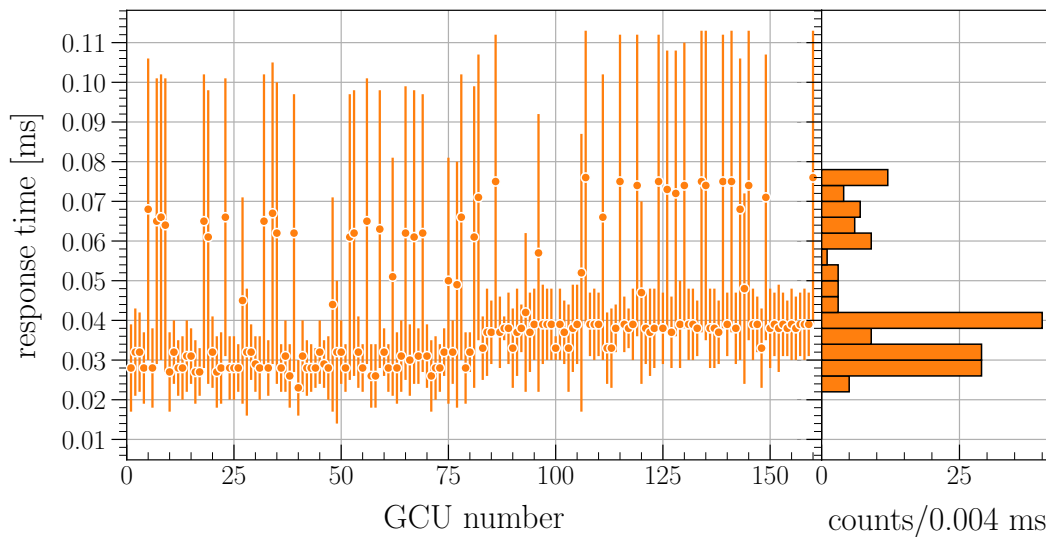
Figure 5.7. Connection test results for a batch of 160 GCUs [107]. The plot on the left shows the mean response time and its standard deviation for each GCU; the plot on the right shows the distribution of the response time of the batch of GCUs. A step in the response time is visible around GCU 80, pointing at differences in cable lengths and network configuration between the first 80 GCUs and the other 80 boards of the batch. Large values of the uncertainty are caused by large variation in the response time.

corresponding to about 1200 PE. The two ranges overlap, allowing us to check the cross range between the two streams. The frequency of pulse generation and the acquisition time were set to provide more than 2000 waveforms for each linearity point. Parameter settings, test pulse generation, and data acquisition were completely automatized.

Raw data were then processed and saved in `ROOT` [115] files as `TTree` objects. For each channel and each input DAC amplitude, the integrated output charge was evaluated according to Eq. (5.2); the evaluated values were then collected into a histogram and the mean value was taken as the output charge corresponding to the given input DAC amplitude; the data for the two streams are shown in Fig. 5.8a for one channel of a typical GCU. Finally, for each channel, a quadratic fit was done for both data streams to extract the gain factor of the two FEC streams, with the fit function defined as:

$$Q_{\text{out}} = c_2 \cdot Q_{\text{in}}^2 + G \cdot Q_{\text{in}} + c_0, \qquad (5.3)$$

where Q_{out} and Q_{in} are the output and input charge defined by Eq. (5.2) and (5.1), respectively, G is the dimensionless gain of the FEC stream, c_0 is the intercept, and c_2 is the coefficient of the quadratic term. A quadratic function was used because the response is not perfectly linear, due to the integral non-linearity (INL) which is characteristic of ADCs and DACs; we expect the quadratic term to be subdominant with respect to the linear term. The gain G is expected to be less than 1; the reason for this design choice is that the FEC input signal is expected to reach amplitudes exceeding the typical flash ADC dynamic range, hence the necessity to attenuate and not amplify the signal.
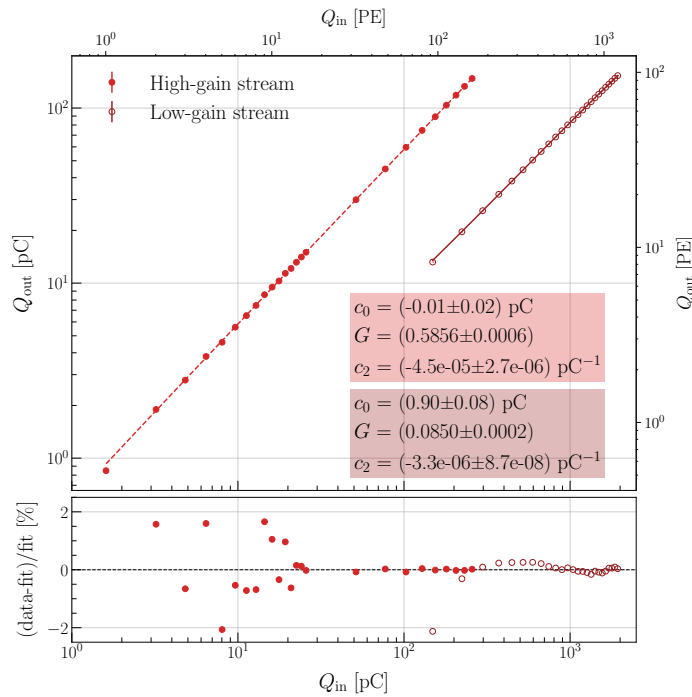
(a) *Quadratic fit of the data from the linearity test.*
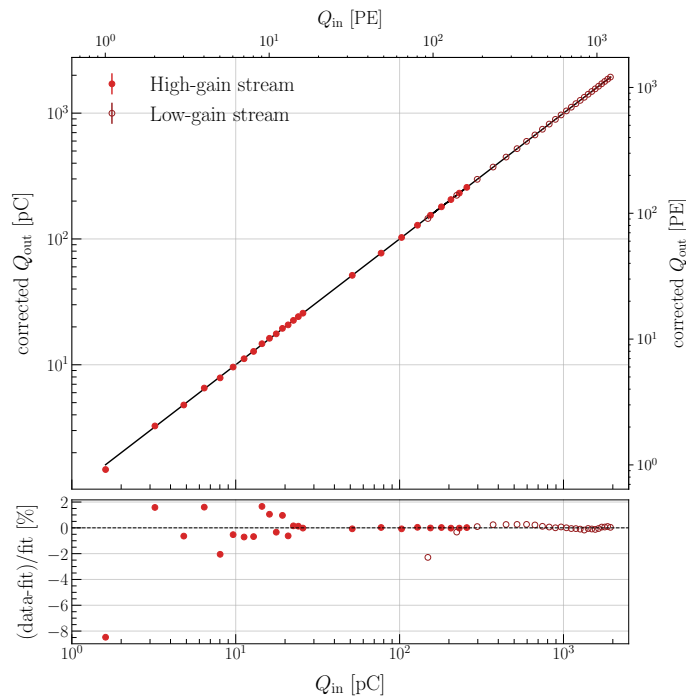
(b) *Corrected gain.*

Figure 5.8. **(a)** Results from the linearity test for one channel of a typical GCU for the high-gain (full circles) and low-gain (empty circles) streams. The input charge is evaluated by using Eq. (5.1), while the output charge is evaluated through Eq. (5.2). The fit is performed using the function in Eq. (5.3). **(b)** Output charge corrected for the gain obtained from the quadratic fit: the two streams now lie on the same line. Charges are also expressed in number of PEs on the secondary axes, where $1\,\text{PE} = 1.6\,\text{pC}$.

Figure 5.8a shows the results of the linearity test for one channel of a typical GCU for the high-gain stream (full circles) and the low-gain stream (empty circles). A quadratic fit was done on both streams, yielding the following results:

- for the high-gain stream, in the range [1.6, 257] pC: $c_0 = (-0.01 \pm 0.02)\,\mathrm{pC}$, $G = 0.5856 \pm 0.0006$, and $c_2 = (-4.5 \pm 0.3) \cdot 10^{-5}\,\mathrm{pC}^{-1}$.

- for the low-gain stream, in the range [149, 1934] pC: $c_0 = (0.90 \pm 0.08)\,\mathrm{pC}$, $G = 0.0850 \pm 0.0002$, and $c_2 = (-3.3 \pm 0.9) \cdot 10^{-6}\,\mathrm{pC}^{-1}$.

Figure 5.8b shows the corrected charge, which is obtained by first evaluating the output charge through Eq. (5.2) and then correcting with the gain obtained from the quadratic fit; as it can be seen, the two data streams lie on the same line after the gain correction. The bottom panel shows the residuals of the corrected output charge with respect to a linear fit; the dispersion at low values of the input charge could be explained as low SNR, while the non-linearity at high charge is typical for an ADC. In the figure, input and output charges are expressed in picocoulombs on the primary axes and in terms of number of photo-electrons (PE) on the secondary axes, with $1\,\mathrm{PE} = q_e \cdot G_{\mathrm{PMT}} = 1.6\,\mathrm{pC}$, where q_e is the electron charge, and $G_{\mathrm{PMT}} = 10^7$ is the assumed nominal PMT gain of the 20-inch PMTs in JUNO [31, 40].

During the analysis, we also checked the saturation amplitude of the high-gain stream, while for the low-gain stream we could not reach saturation with the internal test pulse generator. In the high-gain configuration, channels saturate for an input signal of about 16500 DAC counts, corresponding to an input charge of about $450\,\mathrm{pC} \simeq 280\,\mathrm{PE}$. Data points above the saturation threshold are not used in the fit and are not shown in Fig. 5.8.

Stability test

The stability test consists in firing the internal test pulse generator with a fixed amplitude over a time period lasting several hours, and to check that the waveform properties listed below do not change. The input amplitude was set to 12000 DAC counts for the high-gain stream and to 45000 DAC counts for the low-gain stream. The frequency of the test pulses was set to 1 Hz, while the data acquisition time was determined by the available time during the shift.

The waveform monitored parameters are: baseline, noise, minimum value of the waveform, and minimum position in the readout window. The baseline and noise are obtained as described in Section 5.3.1. These quantities were obtained by processing raw data and saved in `ROOT` files as `TTree` objects.

As an example, Figs. 5.9a and 5.9b show the results of the stability test for the baseline value and the noise of a typical GCU, respectively. The values of the baseline and the noise as a function of time are shown for the three channels in three different panels; distributions of the values are shown as well. From Fig. 5.9a, we can see that the baseline values for the three channels lie between 11600 and 11615 ADC counts, well within the acceptance range of [11000, 12000] ADC counts. The accepted noise level is between 2 and 4.5 ADC counts, corresponding to about 0.03 PE and 0.08 PE respectively, and, as can be seen in Fig. 5.9b, the evaluated values lie within these limits.
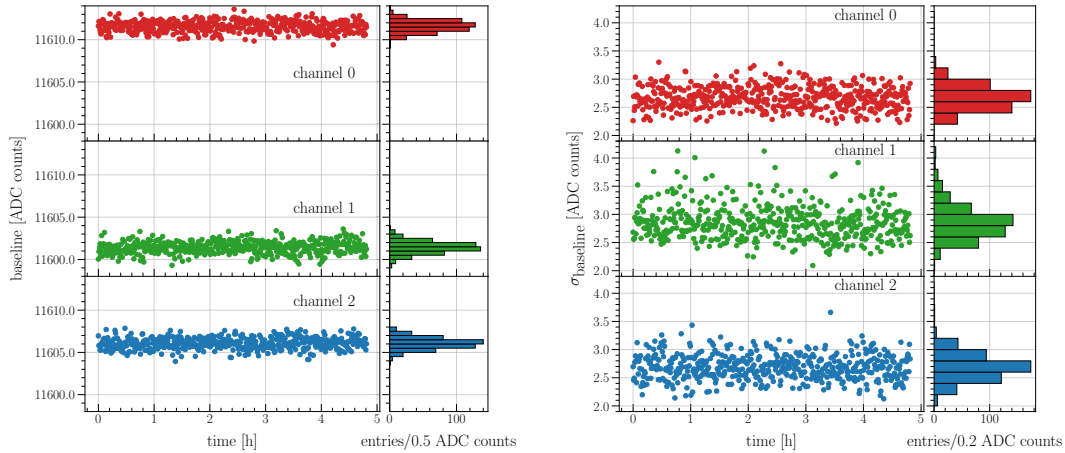
(a) *Results of the stability test for the baseline.***(b)** *Results of the stability test for the noise.*

Figure 5.9. Evolution of the **(a)** baseline and **(b)** noise over a 5-hour stability run for the three channels of a typical GCU [107]. The plots in the left panel show the baseline and noise evaluated on single waveforms as a function of time; the plots in the right panel show the distribution of the baseline and noise values. For all three channels, both the baseline value and the noise are within the acceptance intervals.

Slow control monitoring

The slow control monitoring is meant to read several internal parameters and sensors installed on the GCU and to monitor the overall status of the board. All sensors were read through the IPbus protocol [113] in parallel to the DAQ and over the same transport layer.

For each GCU, the following parameters were read during the slow control monitoring: the temperature of the FPGA, the temperature and the high voltage value of each HVU, and several FPGA internal reference voltages [116].

As an example, Fig. 5.10 shows a plot of the evolution of the FPGA temperature for five GCUs. For all GCUs, the FPGA temperature is stable over time. The difference in the absolute values is due to the different positions of the GCUs on the racks in the testing room (see Section 5.2). The testing room was equipped with an air conditioning system with a constant temperature of about 26 °C.

5.3.4   Storing the test results into a database

The information on the configuration and parameters used for the tests, together with the results of the tests, are saved in a MySQL database which is available on the local server at the Kunshan site. Storing this kind of information is important to have an history of the performance of each GCU, and to compare the results during mass production with the tests foreseen for the upcoming installation and commissioning phases.

Figure 5.11 is obtained by accessing the local database and shows the value
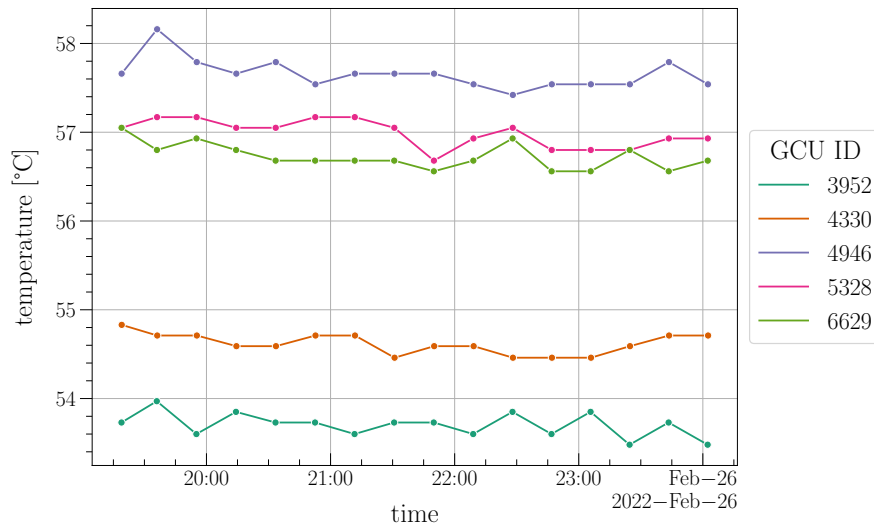
Figure 5.10. The figure shows the evolution of the FPGA temperature for 5 GCUs, recorded from the slow control monitoring. The different temperature values are due to the different positions of the GCUs in the testing room in the dedicated facility at Kunshan.

of the noise from the stability test for several days and runs for GCU 3333; each panel shows results for one of the three GCU channels. The runs shown in the figure span a time period of more than 25 days, during which the noise is stable and within the acceptance range.

Figures 5.12a and 5.12b show the distributions of the high-gain and the low-gain values, respectively, obtained in the linearity test by using Eq. (5.3). The distribution for the high-gain stream has a mean of 0.599 and a standard deviation of 0.007, while the distribution for the low-gain stream has a mean of 0.0883 and a standard deviation of 0.0013.

5.4 Results

A total of 6950 devices were tested in about ten months. Only eight GCUs were discarded on the basis of the tests presented in this chapter and the criteria shown in Table 5.1. Another 56 GCUs were discarded due to issues that arose during the assembling procedure. In total, 6886 GCUs were accepted, while only 64 were rejected, providing a final acceptance yield of 99.1 %. Out of the 6886 accepted cards, 6681 are being installed in the central detector and the Cherenkov water pool veto system, 25 will be used by OSIRIS [36], while the remaining 180 will be kept as backup.
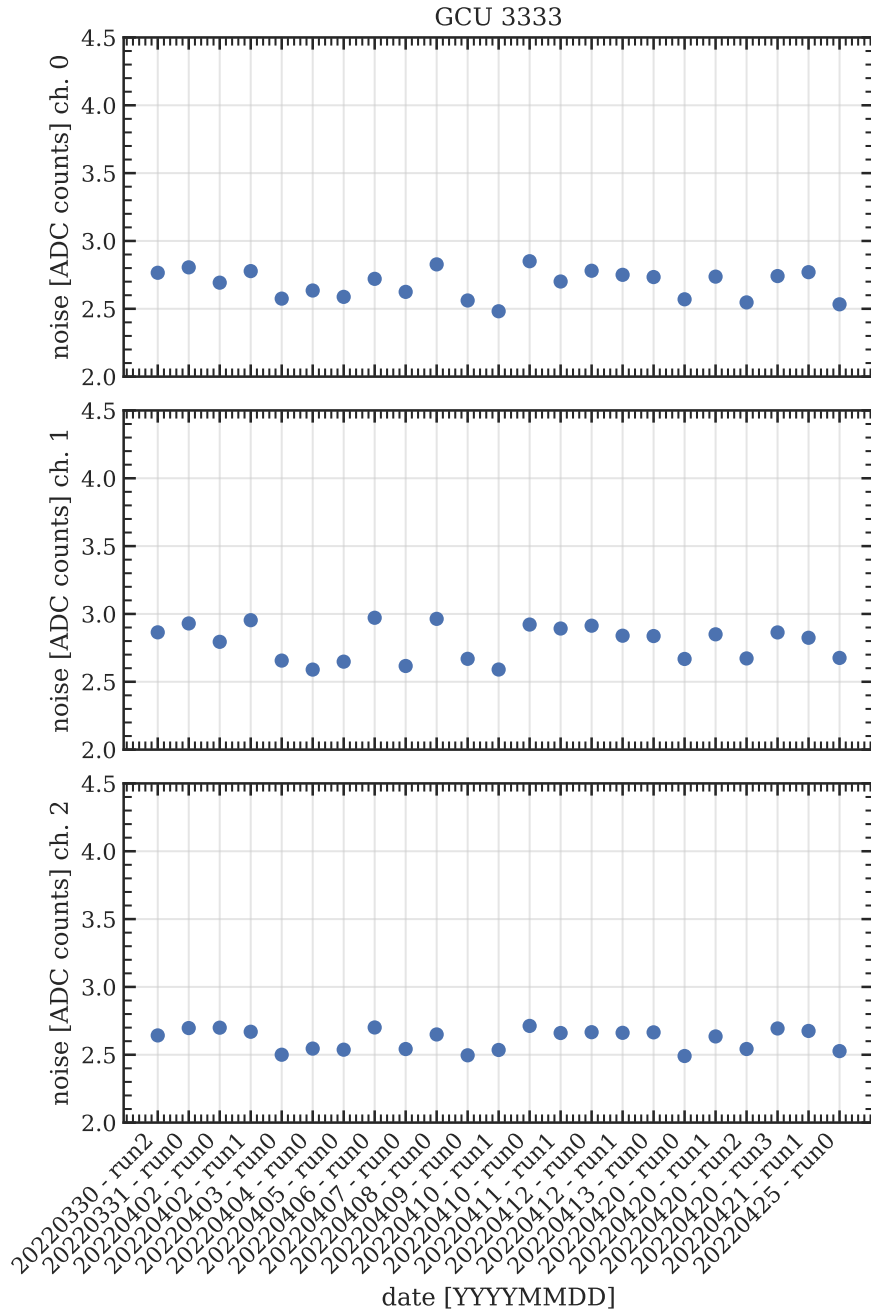
Figure 5.11. Results of the stability test from several runs for GCU 3333 are shown. The three panels show the values of the noise for channel 0 (top), channel 1 (middle) and channel 2 (bottom). The noise for all channels is stable and within the acceptance range over a period of more than 25 days.
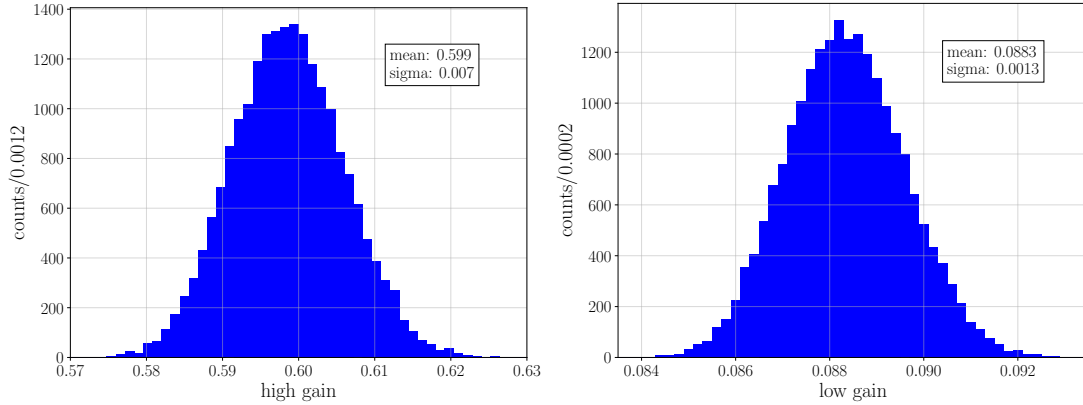
(a) *Gain distribution for the high-gain stream.* **(b)** *Gain distribution for the low-gain stream.*

Figure 5.12. Distributions of the gain obtained from the linearity test for **(a)** the high-gain stream and **(b)** the low-gain stream. The distribution of the high gain has mean and standard deviation equal to 0.599 and 0.007, respectively; the distribution of the low gain has mean and standard deviation equal to 0.0883 and 0.0013, respectively. For both histograms, the gains of all the three channels of 6900 GCUs are included, for a total of 20700 entries; the gains from the first 50 tested GCUs are not included.

Table 5.1. Acceptance range for the baseline, noise, high gain, and low gain, used as acceptance criteria for the evaluation of the performance of each GCU.

Parameter	Acceptance range
baseline	11000 - 12000 ADC counts
noise	2 - 4.5 ADC counts
high gain	0.5 - 0.65
low gain	0.05 - 0.095

Status of the installation

The installation of the 20-inch PMT readout electronics started in fall 2022, after the end of the mass testing in Kunshan. Figure 5.13 shows a sector of the stainless steel structure with three Underwater Boxes installed on top of the structure supporting the PMTs; the connections of each box to three 20-inch PMTs are also visible. Each box is also connected to the trigger electronics and the power supplies which are located in two electronics rooms. The box are also connected to the DAQ servers, and tests similar to the ones presented in this chapter have been done. In December 2022, a first light-off test with a subset of installed boxes, with the main goal of acquiring dark noise data from the PMTs, was done and was successful. The installation is currently on going.

Figure 5.13. Picture of a sector of the stainless steel structure with three Underwater Boxes installed on the detector. Each box is connected to three 20-inch PMTs, whose bases are also visible.

Chapter 6

Precision measurements of the solar oscillation parameters

During the first year of data-taking, the JUNO experiment is expected to collect enough statistics to provide a new estimation of the solar oscillation parameters, Δm_{21}^2 and $\sin^2 \theta_{12}$, with unprecedented precision. In the analysis of the oscillated reactor spectrum, background uncertainties are found to be one of the major contributions in the evaluation of the systematic uncertainties. In particular, geo-neutrinos populate the low energy part of the spectrum affecting the first solar minimum of the oscillation pattern, hence their impact has to be investigated thoroughly. Furthermore, the uncertainty on the reactor rate also plays a role, especially for $\sin^2 \theta_{12}$, so its impact has to be evaluated in detail.

In section 6.1, we introduce the signal and the main backgrounds in the analysis of the oscillated reactor spectrum; then, in section 6.2, we exploit the specific signature of the IBD process to tag the signal events and reduce backgrounds; the statistical method and the analysis framework are presented in section 6.3; in section 6.4, we study the impact of the systematic uncertainties; finally, we conclude in section 6.5.

6.1 Signal and backgrounds

6.1.1 The signal

As already seen in sections 3.1 and 4.2.1, after the interaction of a $\overline{\nu}_e$ with a proton of the liquid scintillator through inverse beta decay, we are left with a positron and a neutron in the final state. The energy released by the final-state positron through ionization and subsequent annihilation constitutes the prompt signal, which is proportional to the antineutrino energy, E_ν, and is used to build the signal spectrum. The final-state neutron thermalizes, and, following an exponential law with a characteristic time of about $200\,\mu s$, gets captured by an hydrogen (99 %) or carbon (1 %) atom with the emission of a $2.2\,\text{MeV}$ or $4.94\,\text{MeV}$ gamma-ray, respectively, which constitutes the delayed signal. It is possible to exploit the time and spatial coincidence between the prompt and the delayed signals to tag candidate antineutrino interactions, and suppress backgrounds, as

detailed in section 6.2.2.

The energy distribution of prompt events, *i.e.*, the signal spectrum, is computed starting from the unoscillated spectrum of $\overline{\nu}_e$ at the source, S_{rea}, introduced in chapter 3 and shown in blue in Fig. 6.1a. Then, the survival probability in matter, Eq. (1.22), is applied to obtain the oscillated spectrum, S_{osc}, shown in orange in the same figure. In the evaluation of the survival probability, a constant matter density of $2.45\,g/cm^3$ [29] and the oscillation parameters listed in Table 1.2 are used. As shown in Fig. 6.1a, the position and the depth of the minimum of the slow oscillation are driven by the solar oscillation parameters, Δm_{21}^2 and $\sin^2\theta_{12}$, respectively. On the other hand, the atmospheric mass splitting, Δm_{31}^2, and $\sin^2\theta_{13}$ determine the frequency and the amplitude of the fast oscillations, respectively.

(a) *Unoscillated and oscillated spectra.*   **(b)** *Effect of the baseline distribution.*
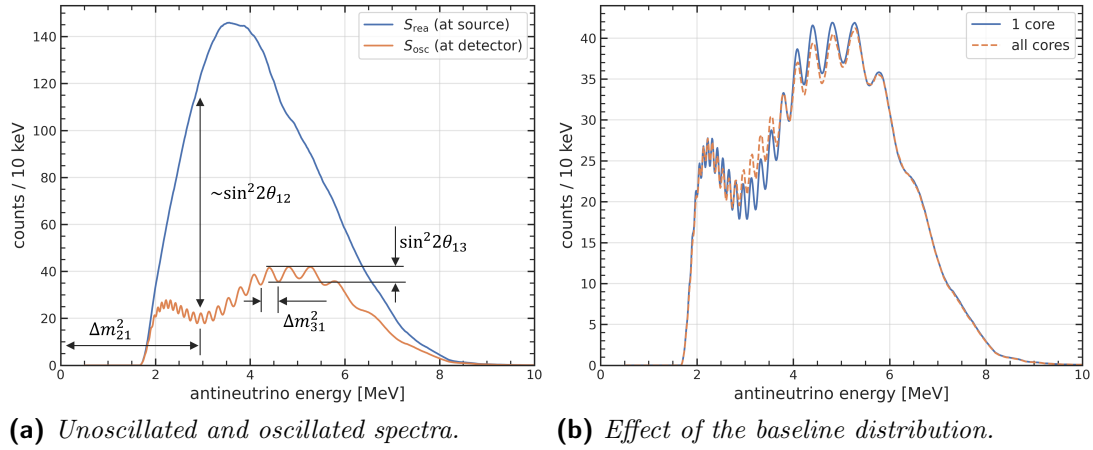
Figure 6.1. **(a)** Signal spectrum at the source without oscillations (blue), S_{rea}, and at the detector with oscillations (orange), S_{osc}. The spectra are evaluated for one year of data-taking and by considering only one reactor core with a total thermal power of $26.6\,GW$ at a mean baseline of $52.5\,km$; normal mass ordering is considered for the oscillated spectrum. **(b)** Comparison between the oscillated spectrum from one equivalent core (blue) and the oscillated spectrum with the actual distribution of the reactor cores (orange).

Figure 6.1a is obtained by considering a single reactor equivalent to the contribution of the 8 near reactor cores, with a total power of $26.6\,GW$ and a mean baseline of $52.5\,km$. In reality, the actual baseline distribution of the 8 near cores of the Yangjian and Taishan nuclear power plants must be taken into account, since it introduces distortions in the oscillated spectrum, as shown in Fig. 6.1b. In order to achieve this, the baselines and thermal powers listed in Table 2.2 are used in equations (3.1) and (3.2). The contribution of the Daya Bay nuclear power plant is also accounted for in the analysis.

SNF and non-equilibrium contributions

The spent nuclear fuel (SNF) and non-equilibrium (NonEq) correction are additional sources of IBD events that are not included in the reactor model used to evaluate S_{rea}; they contribute to the signal rate and spectrum at low energies,

as described in chapter 3. The spectra are inherited by the Daya Bay experiment [81] and are shown in Fig. 6.2 for one year of data-taking. They increase the event yield below 4 MeV. The survival probability in matter is also applied.
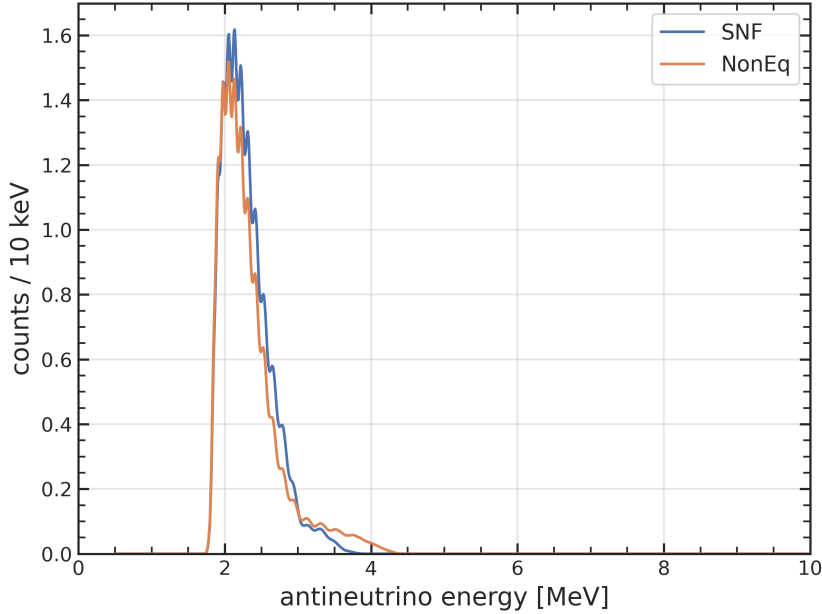
Figure 6.2. The spectra of the spent nuclear fuel (SNF) and non-equilibrium (NonEq) contributions are shown. The spectra are evaluated for a data-taking period of one year and are shown at the detector, so neutrino oscillations in matter are applied. The spectra start at 1.8 MeV due to the threshold of the IBD cross section.

6.1.2 Backgrounds

Backgrounds can either mimic the prompt-delayed signature of the signal (*correlated background*) or contribute as single events (*uncorrelated background*), which can result in fake coincidences.

There are five main sources of backgrounds:

1. $\overline{\nu}_e$ from natural processes occurring in the Earth;

2. $\overline{\nu}_e$ from artificial sources other than the Yangjian, Taishan, and Daya Bay reactors;

3. secondary particles produced by the interaction of cosmic muons in the detector;

4. natural radioactivity;

5. interaction of atmospheric neutrinos in the detector.

A brief description of each background source is now given.

Irreducible backgrounds: geo-neutrinos and $\overline{\nu}_e$ from world reactors

Irreducible backgrounds have the same IBD signature as the reactor $\overline{\nu}_e$ of interest, and consist of $\overline{\nu}_e$ from natural processes occurring in the Earth, also called geo-neutrinos, and from far reactors.

Geo-neutrinos are produced from the β decay of nuclides of the ^{238}U and ^{232}Th decay chains, which are stored inside the Earth. They contribute mainly to the low energy range of the spectrum, below 2.5 MeV.

On the contrary, $\overline{\nu}_e$ from reactor cores of nuclear power plants located more than 300 km from the JUNO experiment are considered to be a background. In fact, given that the energy of reactor antineutrinos is of the order of a few MeV, the oscillation pattern at long baselines does not allow to extract the oscillation parameters we are interested in. Nonetheless, this contribution cannot be neglected because it distorts the spectral shape.

Cosmogenic backgrounds

Cosmogenic backgrounds are events produced by the interaction of muons with ^{12}C atoms of the liquid scintillator, resulting in the production of unstable isotopes and fast neutrons, typically by spallation.

Among the isotopes with cosmogenic origin, we are mainly interested in ^{9}Li and ^{8}He since their decay results in a prompt-delayed coincidence. In fact, they β decay with the emission of a neutron, the so-called β–n decay, with the β and the neutron being the prompt and delayed signals, respectively. Given an overburden of 1800 m.w.e. and an expected muon rate of 4 Hz, their rate is expected to be of the order of tens of events per day. Most of the events can be tagged, and therefore suppressed, by means of the muon veto, which will be introduced in section 6.2.

Cosmogenic fast neutrons are also likely to result in correlated signature. In fact, the neutron recoils on a proton of the LS, producing a prompt signal, and then gets captured, producing a delayed signal.

Radiogenic background

Radiogenic events arise from the α, β, and γ decay of natural radioactivity in the materials of the detector. An estimation of the radioactivity budget of the JUNO experiment has been recently done [117] by measuring the radioactive contamination of the raw materials used to build and to assemble the detector. The radiopurity target for the acrylic vessel and the liquid scintillator were already reported in chapter 2.

The main contributions to the radioactivity budget come from the decay chains of ^{238}U and ^{232}Th, from ^{40}K, and from ^{210}Pb, which is part of the ^{238}U decay chain but is considered as a component out of secular equilibrium. Figure 6.3 shows the simulated cumulative spectra from all radiogenic backgrounds which are uniformly distributed in the liquid scintillator volume, in the top panel, and which are uniformly distributed in the acrylic vessel, in the bottom panel. The radiogenic spectrum is especially prominent at low energies, but covers an energy range up to about 5 MeV. In the top panel, all particles generated in

the liquid scintillator release their energy in the liquid scintillator, and the peaks corresponding to the α particles are clearly visible. On the contrary, α and β particles produced in the acrylic do not reach the liquid scintillator, hence the spectrum on the bottom is mainly composed of γ-rays, whose peaks are clearly visible. Since γ-rays can deposit a fraction of their energy in the acrylic before reaching the liquid scintillator, they produce a continuum spectrum at the left of each peak in a similar way to what happens with γ calibration sources enclosed in an assembly (see section 4.3).
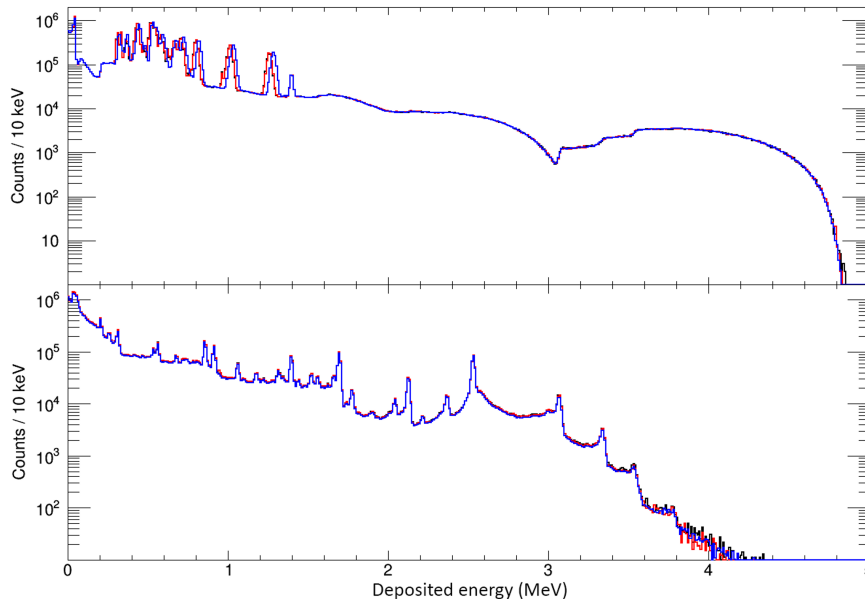
Figure 6.3. Simulated cumulative spectra of all radiogenic backgrounds uniformly distributed in the liquid scintillator (top) and the acrylic vessel (bottom). The curves shown are obtained from different simulations where different α quenching factors are used [117].

Radiogenic events are mainly single events, thus they constitute an uncorrelated background. The only significant exception is a correlated process whose deposited energies are consistent with the ones of the signal, for example, when an α particle from the radioactivity of the ^{238}U and ^{232}Th decay chains gets captured by a carbon atom, ^{13}C, of the liquid scintillator, producing an atom of oxygen, ^{16}O, with the emission of a neutron: ^{13}C$(\alpha, n)^{16}$O. If the neutron is fast enough, it may induce a prompt proton recoil and then get captured, mimicking an IBD signal and thus being a correlated background. Alternatively, the oxygen may be produced in an excited state; the gamma emitted from the oxygen de-excitation may mimic the prompt signal, while the neutron capture may constitute the delayed one.

Atmospheric neutrinos

Atmospheric neutrinos of any flavors are produced by the decay of hadrons generated in the interaction of the cosmic rays with the Earth's atmosphere. Atmospheric neutrinos interact mainly with ^{12}C nuclei of the liquid scintillator via

neutral-current interactions, producing neutrons, protons, α particles, and light nuclei in an excited state. The excited nuclei decay shortly after production by emitting a γ-ray, and if followed by a neutron capture, they can mimic the prompt-delayed IBD signature.

6.2   Event selection

By exploiting the prompt-delayed signature of the IBD process, it is possible to apply selection cuts to tag IBD events and suppress backgrounds in the energy range of interest. The energy selection cuts are applied on JUNO reconstructed energy, $E_{\rm rec}$. For this reason, we first recap the steps in going from the antineutrino energy, E_ν, to $E_{\rm rec}$; then, we detail the selection criteria and their effect on the signal and the backgrounds.

6.2.1   From the reactor spectrum to the reconstructed spectrum

The reconstructed energy spectrum of signal events is computed from the oscillated spectrum in antineutrino energy, $S_{\rm osc}$, shown in blue in Fig. 6.4, by applying the detector response discussed in section 4.2.
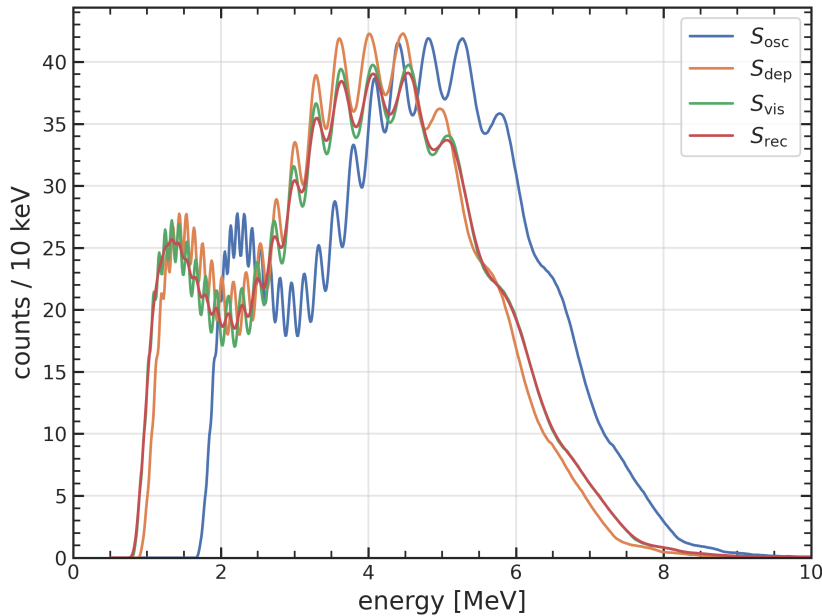
Figure 6.4. The detector response is applied to the oscillated IBD spectrum at the detector, $S_{\rm osc}$, expressed in antineutrino energy (blue): first IBD kinematics is applied to get the deposited energy spectrum, $S_{\rm dep}$ (orange); then, the non-linearity of light emission produces the visible energy spectrum, $S_{\rm vis}$ (green); finally, the reconstructed energy spectrum, $S_{\rm rec}$, is obtained by applying energy resolution (red). The spectra are evaluated for one year of data-taking and by considering only one reactor core with a total thermal power of 26.6 GW at a medium baseline of 52.5 km.

First, the IBD kinematics is applied to get the spectrum of the energy deposited by the positron in the scintillator, S_{dep}, which is shown in orange; it mainly results in shifting the spectrum towards lower energies and accounts for the neutron recoil.

The spectral distortion caused by the non-linearity of the scintillation mechanism is applied, yielding the so called visible energy spectrum, S_{vis}, shown in green, which is both stretched and shifted with respect to the deposited energy spectrum. For this study, the light emission non-linearity includes both the quenching and Cherenkov effects and is implemented by taking the nominal non-linearity curve, f_{nominal}, from the Daya Bay experiment [118], and by rescaling it to match JUNO light emission. In this implementation, we use four additional curves and nuisance parameters to account for the uncertainty:

$$f_{\text{NL}} = f_{\text{nominal}} + \sum_{i=0}^{3} \alpha_i f_i, \tag{6.1}$$

where f_i are the additional correction curves, and α_i are the nuisance parameters, with a Gaussian prior centered in 0 and with width $\sigma = 1$. The ratios of the non-linearity correction curves, f_i, to the nominal curve, f_{nominal}, are shown in Fig. 6.5 as a function of the deposited energy.
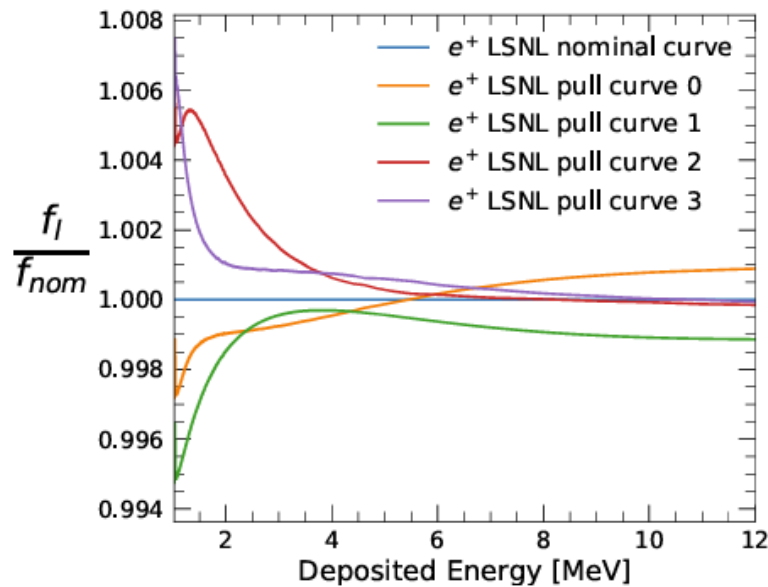
Figure 6.5. Ratios of the non-linearity correction curves, f_i, to the nominal curve, f_{nominal}, as a function of the deposited energy, taken from the Daya Bay experiment [118].

Finally, the reconstructed energy spectrum, S_{rec}, is obtained by applying the energy resolution, which reduces the amplitude of the oscillation pattern, especially at low energies, as shown by the red curve. The values of the energy resolution parameters are $a = 2.614\,\%$, $b = 0.6401\,\%$, and $c = 1.205\,\%$ and are to be fed into Eq. (4.17); the values are taken from the latest study on the JUNO energy resolution [99].

6.2.2   Selection criteria

Given the presence of a prompt and a delayed signals, it is possible to apply selection criteria to select IBD candidates and reduce the background contamination in the IBD sample. The selection criteria to be used in JUNO are the following:

- fiducial volume cut: $r < 17.2\,\text{m}$;
- prompt energy cut: $E_{\text{prompt}} \in [0.7, 12.0]\,\text{MeV}$;
- delayed energy cut: $E_{\text{delayed}} \in [1.9, 2.5] \cup [4.4, 5.5]\,\text{MeV}$;
- prompt-delayed time cut: $\Delta T_{p-d} < 1.0\,\text{ms}$;
- prompt-delayed distance cut: $R_{p-d} < 1.5\,\text{m}$;
- the muon veto.

The quantity r is the radial distance of the event from the detector center, while E_{prompt} and E_{delayed} are the reconstructed energies of the prompt and delayed signals, respectively. The quantities ΔT_{p-d} and R_{p-d} are the time interval and the spatial distance between the prompt and delayed signals, respectively. The time and distance cuts require the prompt and delayed signals to be near in time and space to be tagged as an IBD event.

The muon veto is a complex system which exploits the Cherenkov water pool and the Top Tracker constituting the veto system, described in section 2.1.3. Due to its position and geometry, the Top Tracker is efficient in tagging about 50 % of the downwards moving muons. Tagged muons can be studied in the Cherenkov pool and the central detector, and the way the detectors respond can be used to identify the 50 % of muons which are not tagged. The overall muon veto system is thus efficient in muon detection and can be used to suppress cosmogenic backgrounds. Recently, the muon veto has been optimized for the IBD selection and uses different veto time window depending on the candidate event's proximity to a recent muon track or spallation neutron capture; more information can be found in [29].

Selection criteria applied to the IBD signal A breakdown of the effect of the selection criteria on IBD events is given in Table 6.1: the individual efficiency of each cut is given in the central column, while the column on the right shows the cumulative effect of the selection on the IBD rate. In JUNO, 57.4 IBD signal events per day are expected. After the application of the selection criteria, which combine to give a total efficiency of 82.2 % [29, 119], 47.1 IBD signal events per day are anticipated.

The selection criteria are also applied to the spent nuclear fuel and non-equilibrium contributions, which both yield 0.3 IBD events per day, as summarized in Table 6.2.

Selection criteria applied to the backgrounds The IBD selection criteria introduced in the previous section help suppressing most of the backgrounds; nonetheless, we are left with residual backgrounds, whose rates are summarized in Table 6.2.

Table 6.1. Efficiency of the IBD selection criteria [29, 119]. Efficiencies are given for single cuts, while the last row show the combined efficiency of 82.2 %. The column on the right shows the expected IBD events per day after the selecion criteria are progressively applied.

Selection cut	Efficiency [%]	IBD rate [day^{-1}]
All IBDs	100	57.4
Fiducial volume	91.3	52.4
Energy range	99.9	52.35
Time correlation	99.0	51.8
Spatial correlation	99.3	51.5
Muon veto	91.6	47.1
Combined	82.2	47.1

Irreducible backgrounds have the same IBD signature of the signal, thus the selection criteria have the same efficiency as of the signal. In the end, we are left with an event rate of 0.9/day and 0.3/day for geo-neutrinos from the ^{238}U and ^{232}Th decay chains, respectively, while the world reactors contribute one event per day. The muon veto mainly helps reducing the cosmogenic backgrounds, leading to 0.8 events per day from ^{9}Li and ^{8}He combined (^{9}Li-^{8}He) and 0.1 events per day from fast neutrons. Finally, atmospheric neutrinos only contribute 0.16 events per day.

Table 6.2. Rate of the contribution from the spent nuclear fuel and the non-equilibrium effect [81] and of the residual backgrounds after applying the IBD selection criteria [31, 119]. The rate and shape uncertainties are also listed [31].

	Rate [day^{-1}]	Rate uncertainty [%]	Shape uncertainty [%]
Signal contribution			
Spent nuclear fuel	0.3	14	-
Non-equilibrium	0.3	28	-
Background			
^{238}U geo-ν	0.9	30	5
^{232}Th geo-ν	0.3	30	5
Accidentals	0.18	1	-
Cosmogenic ^{9}Li-^{8}He	0.8	20	10
Fast neutrons	0.1	100	20
^{13}C$(\alpha, n)^{16}$O	0.05	50	50
World reactors	1.0	2	5
Atmospheric ν	0.16	50	50

As far as the radiogenic events are concerned, a detailed study of the effect of the selection criteria has been done and presented in [117]. Figure 6.6a shows the rate of radiogenic events as a function of the lower energy threshold for the prompt energy cut: the rate decreases drastically by increasing the threshold, in fact most of the radiogenic events are concentrated in the low energy part of the spectrum, as shown in Fig. 6.3. Having fixed the lower energy threshold at 0.7 MeV, Fig. 6.6b shows the effect of the fiducial volume cut: reducing the fiducial

volume radius allows us to exclude the radioactivity coming from the acrylic vessel and other materials of the detector surrounding the liquid scintillator. This is true until about a FV radius of $17\,\mathrm{m}$, when the contribution from the liquid scintillator itself starts dominating. A FV cut at $17.2\,\mathrm{MeV}$ is found to be optimal to suppress radioactivity from the detector materials other than the liquid scintillator while not affecting the IBD selection.

(a) *Background rate as a function of the lower energy threshold.* (b) *Background rate as a function of the fiducial volume cut.*
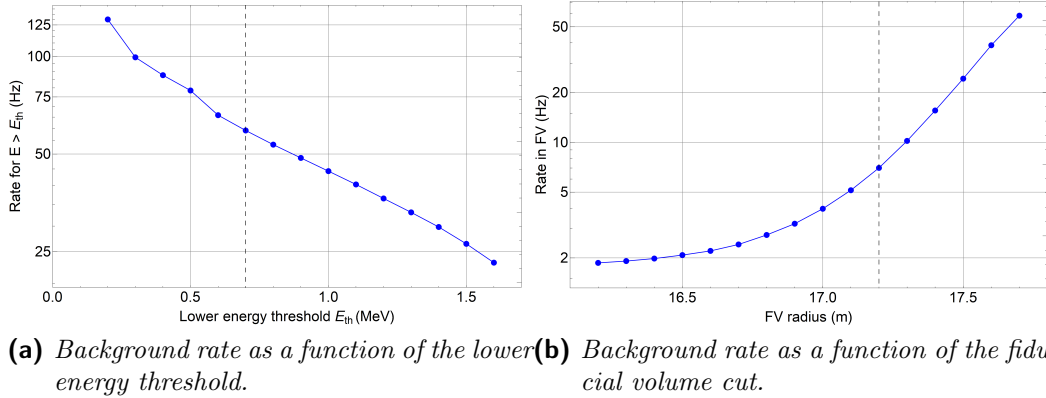
Figure 6.6. Simulation of the radiogenic background from all detector components [117]. **(a)** Radioactivity event rate as a function of the lower energy threshold in the full detector volume. The dotted vertical line refers to the nominal $0.7\,\mathrm{MeV}$ threshold. **(b)** Radioactivity event rate as a function of the fiducial volume cut, with $E > 0.7\,\mathrm{MeV}$. The dotted vertical line corresponds to the nominal cut, $r < 17.2\,\mathrm{m}$.

As already anticipated, radiogenic events are single events constituting an uncorrelated background. Nonetheless, they can result in a fake coincidence, forming the so-called *accidental background*.

Accidental background The accidental background consists of random coincidences that can occur between different processes, mainly radiogenic events. The rate of this background for the given time coincidence window, $\Delta T_{p-d} < 1.0\,\mathrm{ms}$, is of the order of 10^4 events per day. However, since it mainly consists of radiogenic events which are concentrated in the low energy part of the spectrum, as shown in Fig. 6.3, the accidental background dominates the low energy range of the spectrum, and its rate can be strongly suppressed by applying the energy cuts. In addition, requiring the prompt and delay signals to be near in space, with a distance $R_{p-d} < 1.5\,\mathrm{m}$, has a significant impact on rejecting most of the residual accidental background. The final expected rate of the accidental background is 0.18 events per day [119].

Figure 6.7 shows the distribution of the IBD signal events and accidental background based on the space distance ΔR and time interval Δt between the prompt and delayed signals. Most of the IBD events are located in the area with $\Delta R < 1.5\,\mathrm{m}$ and $\Delta t < 1\,\mathrm{ms}$, justifying the choice of the selection criteria introduced earlier. On the contrary, accidentals are characterized by a flat Δt distribution, and only a small fraction of all events has $\Delta R < 1.5\,\mathrm{m}$.

As it can be seen in the 2-dimensional plot, the time and distance cuts correspond to a box, which contains mostly IBD events. Actually, the IBD 2D distribution displays a different shape, and new IBD cuts are currently under study in order to optimize the selection and further reduce the accidental background. A study on the selection criteria by means of machine learning techniques is also on going. This study aims at using equiprobability curves, like the ones shown in black and different shades of grey in Fig. 6.7, to optimize the selection criteria.
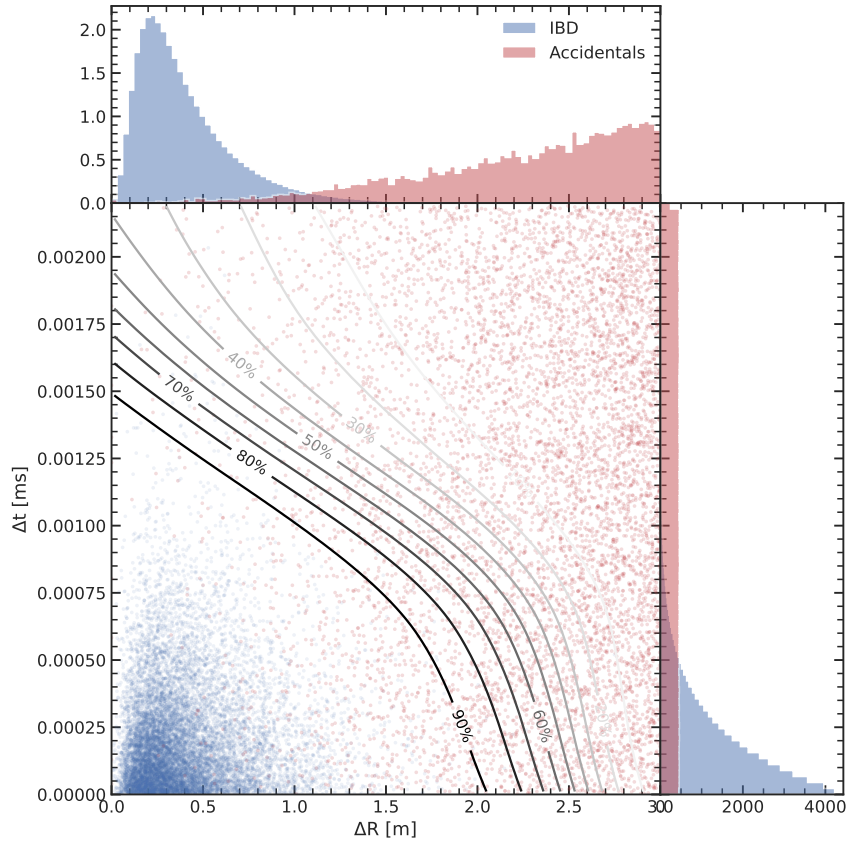
Figure 6.7. Distribution of the IBD signal events and accidental background based on the space distance ΔR and time interval Δt between the prompt and delayed signals. Both the IBD and the accidental datasets consist of $1.4 \cdot 10^6$ simulated events; the accidental datasets is evaluated from radiogenic events only. As it can be seen, the IBD signals and the accidentals have significantly different distributions. Plot by A. Serafini.

6.3   Analysis of the signal spectrum

This section is dedicated to the analysis of the signal spectrum. First, we discuss the statistical method used in the analysis: we define the cost function and explain how systematic uncertainties are incorporated in it. Then, we briefly describe the Oscillated Reactor Spectrum Analysis (ORSA) framework used in this work, and finally we provide a breakdown of the impact of systematic uncertainties on the precision measurement of the solar oscillation parameters, Δm_{21}^2 and $\sin^2 \theta_{12}$.

6.3.1   Signal spectrum

The energy spectrum of IBD candidates for the neutrino oscillation analysis is shown in black in Fig. 6.8, normalized to an exposure of one year. Both the signal (reactor, spent nuclear fuel, and non-equilibrium) and the background components are shown; the inset of the figure provides a better visualization of the background spectral shapes.
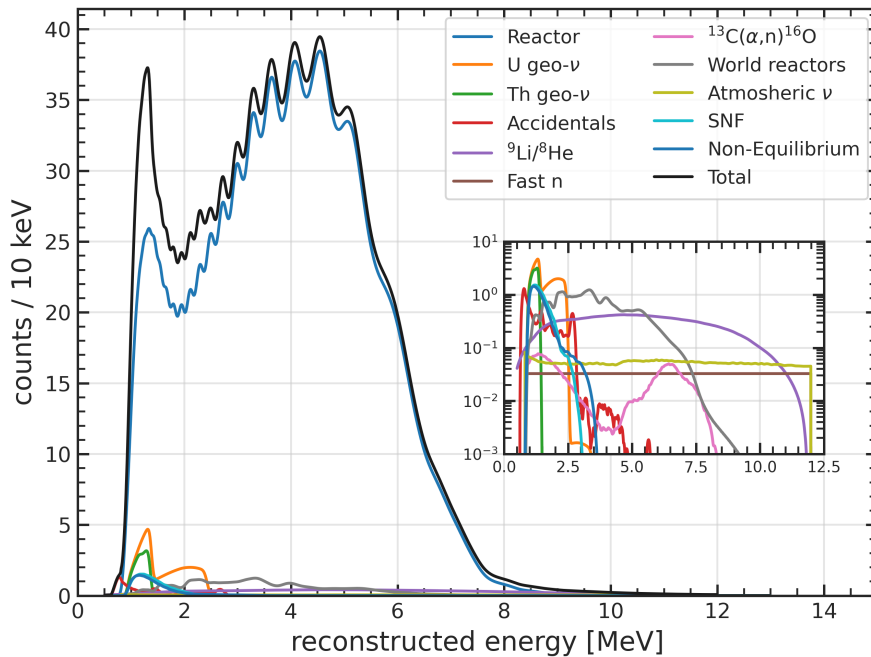
Figure 6.8. The spectra of the reactor IBD signal, in blue, and the backgrounds as expected in JUNO are shown; the black line represents the total spectrum. The reactor spectrum is evaluated taking into account the contributions of all cores. Geo-neutrinos and the accidental background are non-negligible at low energy and play an important role in the distortion of the signal spectrum. The spectra are obtained for a statistic collected in one year of data-taking and are shown in reconstructed energy, E_{rec}. The inset shows the spectral shapes of the backgrounds.

The reactor contribution, in blue, is obtained as explained in section 6.1.1 and by applying the conversion from antineutrino energy E_ν to reconstructed energy E_{rec}, as detailed in section 6.2.1. The SNF and non-equilibrium contributions are obtained by applying the conversion from E_ν to E_{rec} to the Daya Bay spectral shape shown in Fig. 6.2.

As far as backgrounds are concerned, most of them are obtained through Monte Carlo simulations and are already provided in reconstructed energy. Geo-neutrinos are the only exception, since their spectra can be obtained from geological models in terms of antineutrino energy, and then converted to reconstructed energy.

As it can be seen by comparing the reactor spectrum, in blue, with the to-tal spectrum, in black, backgrounds mainly distort the spectrum at low energies below $3\,\mathrm{MeV}$, and geo-neutrinos and accidentals constitute the major contribu-

tions. In particular, they alter the depth of the first solar oscillation minimum, thus distorting the spectrum in the energy range sensitive to the solar oscillation parameters. Geo-neutrinos play a significant role in this respect, as it is further investigated in section 6.4.1.

The spectra shown in Fig. 6.8 are based on Asimov datasets, meaning that the number of entries in each bin is given by the expected number of entries, and no statistical fluctuations are considered. The energy range of the binned histogram spans from $0.8\,\mathrm{MeV}$ to $12\,\mathrm{MeV}$, with a bin width of $10\,\mathrm{keV}$.

6.3.2 Statistical method

To perform the analysis of the reactor spectrum and extract the neutrino oscillation parameters, we compare the complete Asimov spectrum, which is used to mimic the expected spectrum that JUNO will measure after one year of data-taking, as in Fig. 6.8, against the model based on the standard parametrization of neutrino oscillations, as illustrated in section 1.2. The parameter estimation is performed through the minimization of a cost function, defined as:

$$\chi^2(\boldsymbol{\theta}, \boldsymbol{\eta}) = (\boldsymbol{M} - \boldsymbol{\mu}(\boldsymbol{\theta}, \boldsymbol{\eta}))^T \cdot \left(V^{\mathrm{stat}} + V^{\mathrm{b2b}}\right)^{-1} \cdot (\boldsymbol{M} - \boldsymbol{\mu}(\boldsymbol{\theta}, \boldsymbol{\eta})) + \chi^2_{\mathrm{pull}}(\boldsymbol{\eta}). \quad (6.2)$$

Each term of the cost function is now described in detail:

- The quantity $\boldsymbol{M}$ is the vector of measured events per bin. The number of measured events is evaluated by building the spectrum considering all backgrounds, as shown by the black line in Fig. 6.8; we are considering a binned histogram based on an Asimov dataset, so that statistical fluctuations are not included.

- The quantity $\boldsymbol{\mu}$ is the vector of expected number of events per bin. The expected number of events depends on a set of parameters of interest, $\boldsymbol{\theta}$, which are the four oscillation parameters, and a set of nuisance parameters, generally labelled as $\boldsymbol{\eta}$. The expanded form of the expected number of events is:

$$\boldsymbol{\mu}(\boldsymbol{\theta}, \boldsymbol{\eta}) = \eta_{\mathrm{eff}} \left[N_{\mathrm{rea}} \boldsymbol{S}_{\mathrm{rea}}(\boldsymbol{\theta}, \boldsymbol{\eta}) + N_{\mathrm{SNF}} \boldsymbol{S}_{\mathrm{SNF}}(\boldsymbol{\theta}, \boldsymbol{\eta}) + N_{\mathrm{NE}} \boldsymbol{S}_{\mathrm{NE}}(\boldsymbol{\theta}, \boldsymbol{\eta}) \right] + \\ + \sum_B N_B \boldsymbol{S}_B(\boldsymbol{\eta}), \quad (6.3)$$

  where the index B runs over all backgrounds. The total reactor spectrum, $\boldsymbol{S}_{\mathrm{rea}}$, is obtained by summing together the spectra of the near reactor cores:

$$\boldsymbol{S}_{\mathrm{rea}}(\boldsymbol{\theta}, \boldsymbol{\eta}) = \sum_r R_r \boldsymbol{S}_r(\boldsymbol{\theta}, \boldsymbol{\eta}), \quad (6.4)$$

  where the index r runs over the cores of the Yangjian and Taishan nuclear power plants, and also over the contribution of the Daya Bay nuclear power plant. The quantities R_r are nuisance parameters which describe a relative weight assigned to each reactor, so that the contribution from each reactor is allowed to fluctuate in the fit according to a reactor-uncorrelated rate

uncertainty, as explained later in this section.

Each spectrum is considered as a probability density function, with unitary area, and then is scaled to the expected respective number of events, N_i, which are nuisance parameters in the fit. The single spectra, $\boldsymbol{S}_i$, depend on the oscillation parameters and on other nuisance parameters, which are introduced later in this section. An overall efficiency factor, η_{eff}, is introduced to account for the efficiency in the detection of $\overline{\nu}_{\mathrm{e}}$ from reactors, the spent nuclear fuel (SNF), and the non-equilibrium (NE) effect.

- The quantity V^{stat} is the statistical covariance matrix for the combined Neyman-Pearson χ^2, so that the parameters are not biased due to low statistics in some bins, as it could happen at the beginning of the data-taking. Thus, according to [120], the statistical covariance matrix can be written as:

$$V_{ij}^{\mathrm{stat}} = 3\,\delta_{ij} \bigg/ \left(\frac{1}{M_i} + \frac{2}{\mu_i} \right), \qquad (6.5)$$

  where V_{ij}^{stat} is the matrix element between the i-th and j-th bin, with i and j running over the number of bins, and δ_{ij} is the Kronecker delta.

- The quantity V^{b2b} includes systematic uncertainties in the form of a covariance matrix. In particular, it includes the shape, or bin-to-bin uncorrelated, uncertainties on the signal and background spectra. The shape uncertainty for the reactor signal is based on the expectation from the TAO experiment (see section 2.1.7); in fact, the TAO experiment is expected to provide a reference spectrum for JUNO and a more precise estimation of the spectral shape uncertainties. Since TAO is still under construction, Monte Carlo simulations have been used to extract the shape uncertainty used in this work with the exact binning. The shape uncertainties of the backgrounds are listed in Table 6.2 and are inherited by previous JUNO sensitivity studies [30]. Shape uncertainties reported in the table have been estimated for a bin width of 36 keV, which is not the one used in this work, so they have to be scaled to the desired bin width as:

$$\delta = \delta_{36} \sqrt{\frac{36\,\mathrm{keV}}{\Delta E}}, \qquad (6.6)$$

  where δ_{36} is the relative uncertainty at 36 keV, and ΔE is the new bin width. In the analysis presented here, we use a bin width of 10 keV, so that the scaling factor for the relative uncertainty is about 1.9.

- The quantity $\chi^2_{\mathrm{pull}}(\boldsymbol{\eta})$ is the χ^2 term accounting for the prior knowledge on the nuisance parameters, $\boldsymbol{\eta}$, through Gaussian pull terms.

The expanded form of the last term is the following:

$$
\begin{aligned}
\chi^2_{\text{pull}}(\boldsymbol{\eta}) = \sum_i \frac{(\eta_i - \hat{\eta}_i)^2}{\sigma^2(\eta_i)} = \\
= \left(\frac{N_{\text{rea}} - \hat{N}_{\text{rea}}}{\sigma_{\text{rea}}}\right)^2 + \sum_r \left(\frac{R_r - 1}{\sigma_r}\right)^2 + \\
+ \left(\frac{N_{\text{SNF}} - \hat{N}_{\text{SNF}}}{\sigma_{\text{SNF}}}\right)^2 + \left(\frac{N_{\text{NE}} - \hat{N}_{\text{NE}}}{\sigma_{\text{NE}}}\right)^2 + \\
+ \left(\frac{\rho - \hat{\rho}}{\sigma_\rho}\right)^2 + \sum_B \left(\frac{N_B - \hat{N}_B}{\sigma_B}\right)^2 + \\
+ \left(\frac{\eta_{\text{eff}} - 1}{\sigma_{\text{eff}}}\right)^2 + \sum_{m=a,b,c} \left(\frac{m - \hat{m}}{\sigma_m}\right)^2 + \sum_{l=1}^4 \left(\frac{\alpha_l}{\sigma_l}\right)^2 ,
\end{aligned}
\tag{6.7}
$$

where η_i is the i-th nuisance parameter, and $\hat{\eta}_i$ and $\sigma^2(\eta_i)$ are its expected value and assigned uncertainty, respectively. All terms are now described in detail, and are listed in order of appearance:

1. Pull term on the total number of events from reactors, N_{rea}. The assigned rate uncertainty is 2% and accounts for the uncertainties which are correlated among all reactors: a 2% uncertainty on the total mean cross section per fission (see section 3.3.1), and the mean energy per fission contributing an additional 0.2%.

2. Pull terms on the relative weights R_r assigned to each reactor r in Eq. (6.4) to account for reactor-uncorrelated uncertainties. The sources of uncertainties which are uncorrelated among all reactors are the fission fractions and the thermal power, contributing a 0.6% and a 0.5% uncertainty, respectively. The weights R_r are allowed to fluctuate with a total 0.8% uncertainty.

3. Pull term on the number of events from the spent nuclear fuel, N_{SNF}, with the respective rate uncertainty given in Table 6.2.

4. Pull term on the number of events from the non-equilibrium contribution, N_{NE}, with the respective rate uncertainty given in Table 6.2.

5. Pull term on the matter density ρ used in the evaluation of the survival probability in matter. The matter density is assumed to be constant and known with a relative precision of 6% [29].

6. Pull terms on the numbers of background events, with B running over all backgrounds. The rate uncertainties are listed in Table 6.2.

7. Pull term on the overall detector efficiency. The efficiency is mainly related to the number of proton targets[1] in the liquid scintillator, with a pull term centered in 1 and with a 1% uncertainty.

---

[1]Only protons of hydrogen atoms of the liquid scintillator are considered as a target.

8. Pull terms on the three parameters of the energy resolution, with the central values and uncertainties listed in Table 6.3 and taken from the latest study on JUNO energy resolution [99].

9. Pull terms on the four nuisance parameters used to introduce the uncertainty on the non-linearity curve, as in Eq. (6.1). The parameters α_l are assigned a Gaussian pull centered in zero with absolute uncertainty $\sigma_l = 1$.

The terms from 1 to 4 refer to reactor-related nuisance parameters, while the terms from 7 to 9 refer to nuisance parameters related to the detector response. The expected values and the uncertainties of all nuisance parameters introduced in Eq. (6.7) are summarized in Table 6.3. The expected values of the number of entries for the signal and the backgrounds are not given since they depend on the data-taking time, and they were varied during the analysis to probe different exposure scenarios. In total, the cost function of Eq. (6.2) has 29 nuisance parameters.

Table 6.3. Summary of the nuisance parameters implemented in the cost function. The uncertainties are relative uncertainties, except for the nuisance parameters related to the liquid scintillator non-linearity. The expected numbers of events for the signal and the backgrounds are not reported, since they depend on the data-taking period.

Nuisance η	Expected value $\hat{\eta}$	Uncertainty $\sigma(\eta)$
N_{rea}	-	2 %
R_r (9 parameters)	1	0.8 %
N_{SNF}, N_{NE}	-	Table 6.2
ρ	2.45 g/cm^3	6 %
N_{B} (8 parameters)	-	Table 6.2
η_{eff}	1	1 %
a	0.02614	0.20 %
b	0.00640	0.43 %
c	0.01205	1.15 %
α_l (4 parameters)	0	1

6.3.3   ORSA: An analysis framework

The Oscillation Reactor Spectrum Analysis (ORSA) is an analysis framework currently under development by a research group of the University of Padua, Italy. In particular, ORSA is a fitting framework meant primarily for the analysis of the oscillated spectrum from reactors to extract the neutrino mass ordering and provide an estimation of the oscillation parameters.

In ORSA, it is possible to define different cost functions, like the χ^2 and the likelihood. In this work, we use the ORSA implementation of the χ^2 introduced in the previous section. The minimization of the cost function is performed by means of the `iminuit` package, which is a Python interface for the *Minuit2* C++ library by CERN's ROOT team [121, 122] and is handled directly by ORSA. A key feature of ORSA is the implementation of multithreading on CPUs and GPUs to highly reduce computational time.

The use of Markov Chain Monte Carlo is also implemented in ORSA, but since it provides results comparable to the ones obtained with the `iminuit` minimization, only results from the latter are shown here.

6.3.4 Breakdown of systematic uncertainties

In this section, we provide a breakdown of how the systematic uncertainties listed in Table 6.3 affect the expected precision of the oscillation parameters, Δm_{21}^2 and $\sin^2\theta_{12}$.
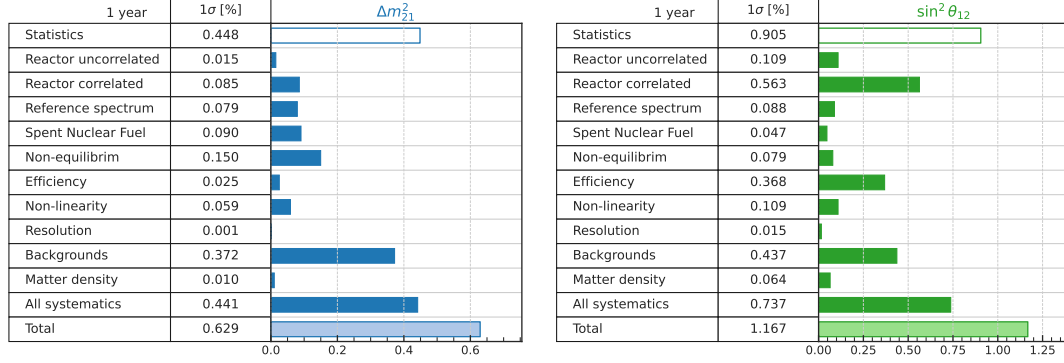
First, we perform the minimization of the cost function, Eq. (6.2), fixing all the nuisance parameters, *i.e.*, without considering the systematic contributions, to get the statistical uncertainty on the oscillations parameters, σ_{stat}. Then, we "switch on" one systematic contribution at a time, we get the total uncertainty from the minimization of the cost function, σ_{tot}, and evaluate the single systematic contribution as:

$$\sigma_{\text{syst}} = \sqrt{\sigma_{\text{tot}}^2 - \sigma_{\text{stat}}^2}. \qquad (6.8)$$
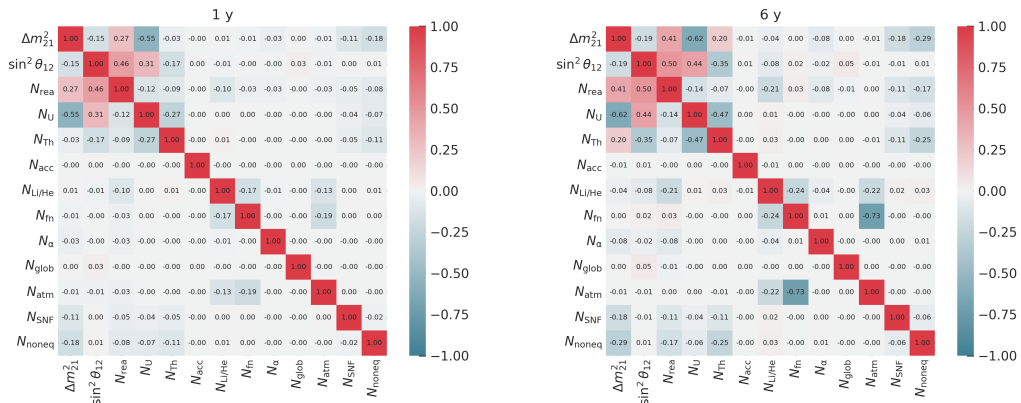
When evaluating the background contribution, both the rate and shape uncertainties are considered. The breakdowns of the systematic contributions to the uncertainty of Δm_{21}^2 and $\sin^2\theta_{12}$ are shown in Figs. 6.9a and 6.9b, respectively. Both the rate and shape uncertainties of backgrounds are considered as systematic uncertainties because the evaluation of the background rate and shape is based on the efficiency of the selection criteria and muon tagging, or we have to rely on Monte Carlo simulations where we use parameters that are not known with a very good precision. So, any error in the evaluation of the background rate or shape is propagated to the final result, *i.e.*, the uncertainty on the oscillation parameters. For both parameters, these uncertainties constitute a major contribution to the systematic uncertainty. For $\sin^2\theta_{12}$, the reactor normalization and the detector efficiency also play a significant role. The impact of these systematic sources are further investigated in the next sections.

It is worth noting that the procedure of Eq. (6.8) is used to highlight the relevance of each systematic source, but it does not take into account the possible correlations arising when "switching on" all systematics in the χ^2 minimization. In fact, the total systematic uncertainty obtained in the latter case, $\sigma_{\text{syst\_all}}$, corresponding to the second to last row of Fig. 6.9, labelled as "all systematics", is different from the sum in quadrature of the single σ_{syst} contributions. The last row reports the total uncertainty, obtained by summing in quadrature the statistical and systematic contributions: $\sigma = \sqrt{\sigma_{\text{stat}}^2 + \sigma_{\text{syst\_all}}^2}$.

Figures 6.10a and 6.10b show the post-fit correlation matrices between the solar oscillation parameters and the number of events of the signal and of each background contribution for 1 and 6 years of data-taking, respectively. Correlations arise since the beginning of the data-taking and strengthen with time. We are mostly interested in the background contributions which correlate with the solar oscillation parameters and with the number of unoscillated reactor events: geo-neutrinos and the cosmogenic ^{9}Li-^{8}He. The impact of these two sources of background is studied in more detail in the next sections.

1 year	1σ [%]	Δm^2_{21}
Statistics	0.448	
Reactor uncorrelated	0.015	
Reactor correlated	0.085	
Reference spectrum	0.079	
Spent Nuclear Fuel	0.090	
Non-equilibrim	0.150	
Efficiency	0.025	
Non-linearity	0.059	
Resolution	0.001	
Backgrounds	0.372	
Matter density	0.010	
All systematics	0.441	
Total	0.629	

1 year	1σ [%]	$\sin^2\theta_{12}$
Statistics	0.905	
Reactor uncorrelated	0.109	
Reactor correlated	0.563	
Reference spectrum	0.088	
Spent Nuclear Fuel	0.047	
Non-equilibrim	0.079	
Efficiency	0.368	
Non-linearity	0.109	
Resolution	0.015	
Backgrounds	0.437	
Matter density	0.064	
All systematics	0.737	
Total	1.167	

(a) *Uncertainty breakdown for Δm^2_{21}.*   **(b)** *Uncertainty breakdown for $\sin^2\theta_{12}$.*

Figure 6.9. Breakdown of the systematic uncertainties for **(a)** Δm^2_{21} and **(b)** $\sin^2\theta_{12}$ for one year of data-taking; the uncertainties in the tables are relative uncertainties. For both oscillation parameters, backgrounds constitute a major contribution to the systematic uncertainty. For $\sin^2\theta_{12}$, the reactor normalization and the detector efficiency also play a significant role. The total uncertainty in the last row is obtained by the sum in quadrature of the statistical uncertainty (first row) and the total systematic uncertainty (second to last row). Plots by V. Cerrone.

1 y

	Δm^2_{21}	$\sin^2\theta_{12}$	N_{rea}	N_{U}	N_{Th}	N_{acc}	$N_{\mathrm{Li/He}}$	N_{fn}	N_{α}	N_{glob}	N_{atm}	N_{SNF}	N_{noneq}
Δm^2_{21}	1.00	-0.15	0.27	-0.55	-0.03	-0.00	0.01	-0.01	-0.03	0.00	-0.01	-0.11	-0.18
$\sin^2\theta_{12}$	-0.15	1.00	0.46	0.31	-0.17	0.00	-0.01	-0.00	-0.00	0.03	-0.01	0.00	0.01
N_{rea}	0.27	0.46	1.00	-0.12	-0.09	-0.00	-0.10	-0.03	-0.03	-0.00	-0.03	-0.05	-0.08
N_{U}	-0.55	0.31	-0.12	1.00	-0.27	-0.00	0.00	0.00	-0.00	-0.00	-0.00	-0.04	-0.07
N_{Th}	-0.03	-0.17	-0.09	-0.27	1.00	-0.00	0.01	-0.00	-0.00	-0.00	-0.00	-0.05	-0.11
N_{acc}	-0.00	0.00	-0.00	-0.00	-0.00	1.00	-0.00	-0.00	-0.00	0.00	0.00	-0.00	-0.00
$N_{\mathrm{Li/He}}$	0.01	-0.01	-0.10	0.00	0.01	-0.00	1.00	-0.17	-0.01	-0.00	-0.13	0.00	0.01
N_{fn}	-0.01	-0.00	-0.03	0.00	-0.00	-0.00	-0.17	1.00	-0.00	-0.00	-0.19	0.00	0.00
N_{α}	-0.03	-0.00	-0.03	-0.00	-0.00	-0.00	-0.01	-0.00	1.00	-0.00	-0.00	-0.00	-0.00
N_{glob}	0.00	0.03	-0.00	-0.00	-0.00	0.00	-0.00	-0.00	-0.00	1.00	-0.00	-0.00	-0.00
N_{atm}	-0.01	-0.01	-0.03	-0.00	-0.00	-0.00	-0.13	-0.19	-0.00	-0.00	1.00	0.00	-0.00
N_{SNF}	-0.11	0.00	-0.05	-0.04	-0.05	-0.00	0.00	0.00	-0.00	-0.00	0.00	1.00	-0.02
N_{noneq}	-0.18	0.01	-0.08	-0.07	-0.11	-0.00	0.01	0.00	-0.00	-0.00	-0.00	-0.02	1.00

6 y

	Δm^2_{21}	$\sin^2\theta_{12}$	N_{rea}	N_{U}	N_{Th}	N_{acc}	$N_{\mathrm{Li/He}}$	N_{fn}	N_{α}	N_{glob}	N_{atm}	N_{SNF}	N_{noneq}
Δm^2_{21}	1.00	-0.19	0.41	-0.62	0.20	-0.01	-0.04	0.00	-0.08	0.00	-0.01	-0.18	-0.29
$\sin^2\theta_{12}$	-0.19	1.00	0.50	0.44	-0.35	0.01	-0.08	0.02	-0.02	0.05	-0.01	-0.01	0.01
N_{rea}	0.41	0.50	1.00	-0.14	-0.07	-0.00	-0.21	0.03	-0.08	-0.01	0.00	-0.11	-0.17
N_{U}	-0.62	0.44	-0.14	1.00	-0.47	0.00	0.01	-0.00	-0.00	-0.00	0.00	-0.04	-0.06
N_{Th}	0.20	-0.35	-0.07	-0.47	1.00	-0.00	0.03	-0.00	0.00	-0.00	-0.01	-0.11	-0.25
N_{acc}	-0.01	0.01	-0.00	0.00	-0.00	1.00	-0.01	0.00	-0.00	0.00	-0.00	-0.00	-0.00
$N_{\mathrm{Li/He}}$	-0.04	-0.08	-0.21	0.01	0.03	-0.01	1.00	-0.24	-0.04	-0.00	-0.22	0.02	0.03
N_{fn}	0.00	0.02	0.03	-0.00	-0.00	0.00	-0.24	1.00	0.01	0.00	-0.73	-0.00	-0.00
N_{α}	-0.08	-0.02	-0.08	-0.00	0.00	-0.00	-0.04	0.01	1.00	-0.00	-0.00	0.00	0.01
N_{glob}	0.00	0.05	-0.01	-0.00	-0.00	0.00	-0.00	0.00	-0.00	1.00	0.00	-0.00	-0.00
N_{atm}	-0.01	-0.01	0.00	0.00	-0.01	-0.00	-0.22	-0.73	-0.00	0.00	1.00	-0.00	-0.00
N_{SNF}	-0.18	-0.01	-0.11	-0.04	-0.11	-0.00	0.02	-0.00	0.00	-0.00	-0.00	1.00	-0.06
N_{noneq}	-0.29	0.01	-0.17	-0.06	-0.25	-0.00	0.03	-0.00	0.01	-0.00	-0.00	-0.06	1.00

(a) *1-year correlation matrix.*   **(b)** *6-year correlation matrix.*

Figure 6.10. Correlation matrix between solar oscillation parameters and number of events of reactor and all backgrounds, where all backgrounds are only constrained in the fit.

6.4 Understanding the impact of systematic uncertainties

In this section, we study the impact of systematic uncertainties in the precision measurement of the solar oscillation parameters, Δm_{21}^2 and $\sin^2\theta_{12}$, for a data-taking period of one year. First, we focus on the impact of backgrounds which are a significant contribution for both oscillation parameters, especially geo-neutrinos and cosmogenic ^{9}Li-^{8}He; then, we consider the effect of the rate uncertainty of the reactor flux.

6.4.1 The impact of backgrounds

Now we provide the breakdown of the impact of backgrounds. In this analysis, all detector response parameters and the matter density are kept fixed during the fit, while the oscillation parameters are free parameters in the fit. The number of reactor events prior to neutrino oscillations, N_{rea}, is always free with a Gaussian prior of 2 %.

The Asimov dataset used as mock data includes the signal and all sources of backgrounds, as shown in Fig. 6.8; a data-taking period of one year is considered. First, we evaluate the reference uncertainty by keeping all backgrounds fixed in the fit, σ_{fixed}, shown in the first column of Figs. 6.11a and 6.11b for Δm_{21}^2 and $\sin^2\theta_{12}$, respectively.

(a) *Background impact on Δm_{21}^2.*

(b) *Background impact on $\sin^2\theta_{12}$.*
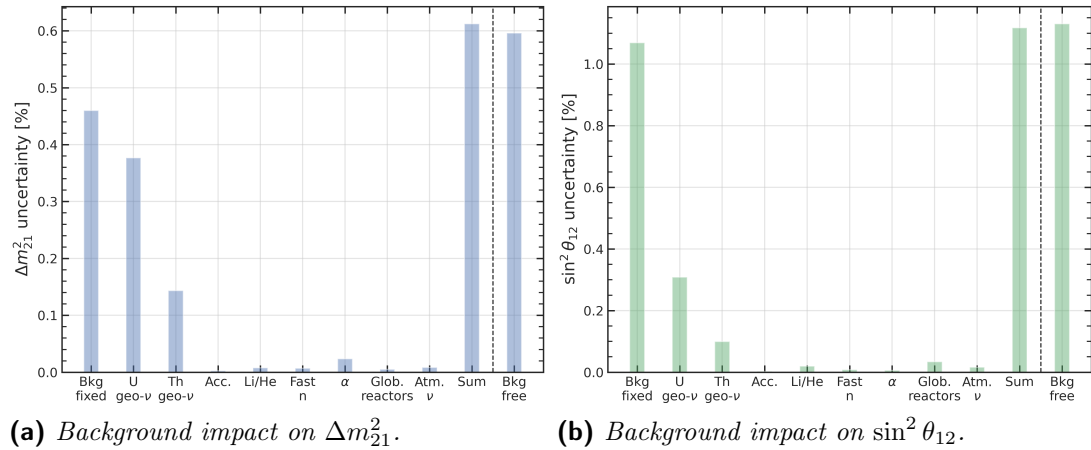
Figure 6.11. Breakdown of the impact of backgrounds on **(a)** Δm_{21}^2 and **(b)** $\sin^2\theta_{12}$ with nominal background rates evaluated for one year of data-taking, and rate and shape uncertainties listed in Table 6.2. The column "Bkg fixed" is obtained by keeping all backgrounds fixed in the fit; the column "Sum" is the sum in quadrature of all columns to its left; the column "Bkg free" is evaluated by allowing all backgrounds to vary; the central columns are obtained by allowing the background labelled on the axis to vary while fixing all other backgrounds. See the text for more detail.

Then, each background contribution is allowed to vary in the fit according to its rate and shape uncertainties; we get the total uncertainties from the fit, σ_{tot};

and finally, we evaluate the contribution of each background as:

$$\sigma_{\text{bkg}} = \sqrt{\sigma_{\text{tot}}^2 - \sigma_{\text{fixed}}}. \tag{6.9}$$

The quantity σ_{bkg} is shown in Fig. 6.11 for each backgrounds, from the second to the third to last columns. The second to last column, labelled as "Sum", is the sum in quadrature of all columns on the left, and provides an estimation of the total systematic uncertainty due to backgrounds. Nonetheless, the sum in quadrature does not take into account possible correlations among backgrounds, which are present as seen in Fig. 6.10. So, the last column in Fig. 6.11, labelled as "Bkg free", is obtained by allowing all backgrounds to vary at the same time according to their uncertainties. In fact, we see that in this case, the uncertainty differs from the one obtained by summing all contributions due to correlations.

It is also worth noticing that the effect of correlations among backgrounds is opposite for the two oscillation parameters: in the case of Δm_{21}^2, the uncertainty is reduced, while for $\sin^2 \theta_{12}$ it increases. Furthermore, it is evident that the backgrounds with the major impact are geo-neutrinos.

Geo-neutrinos

In the study presented here, the matter density, the detector-related nuisance parameters and all backgrounds except for geo-neutrinos are fixed in the fit.

Geo-neutrinos come from ^{238}U and ^{232}Th stored inside the Earth. So far, a fixed Th/U ratio has been used to evaluate the overall geo-neutrinos spectrum and consider it as a single background. The current most precise measurement of the Th/U mass ratio of 3:9 comes from the KamLAND experiment [123], with a precision of 15 %. Thus, the ratio is not known with a very high precision, and it could also differ in different locations based on the different Earth composition. In fact, fixing the Th/U ratio to a wrong value in the fit might introduce a bias in the measurement of the solar oscillation parameters. To test this, we build the spectrum with the true Th/U ratio of 3:9 by KamLAND [123], and fit it by considering geo-neutrinos as a single contribution with the true Th/U ratio. As a reference, results are shown in orange in Fig. 6.12. Then, we fit the same spectrum by considering geo-neutrinos as a single contribution with a wrong Th/U ratio, set to 4:8; the results are shown in red in the figure. By comparing the results with the wrong ratio (red) to the results with the true ratio (orange), we see a bias of 0.13 % and -0.32 % arising in the estimation of Δm_{21}^2 and $\sin^2 \theta_{12}$, respectively. The fact that the estimation of the solar oscillation parameters depends on the geo-neutrinos might be explained by considering Fig. 6.8, where it is clearly visible that the spectra from ^{238}U and ^{232}Th highly impact the spectrum below 4 MeV, where the JUNO experiment is most sensitive to Δm_{21}^2 and $\sin^2 \theta_{12}$.

On the contrary, by leaving the two contributions from ^{238}U and ^{232}Th free and independent in the fit, we see no bias in the estimation of the solar oscillation parameters, as shown in green in Fig. 6.12. The only drawback in this approach is that the uncertainty on $\sin^2 \theta_{12}$ worsens slightly, while no difference arises for Δm_{21}^2. The values of the uncertainties for the orange (fixed ratio) and green (free ratio) cases are also listed in Table 6.4.
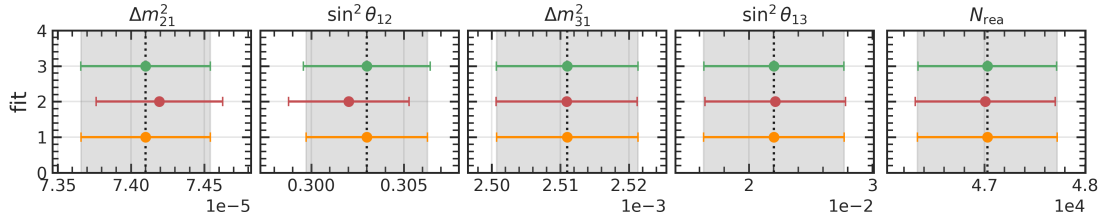
Figure 6.12. From the bottom: the results obtained by fitting the spectrum with the same fixed ratio as in the mock dataset (orange); results obtained by fitting the spectrum with a wrong fixed ratio (red); results obtained by fitting the spectrum with a free ratio, so by keeping both ^{238}U and ^{232}Th backgrounds as separate contributions with separate constraints (green). The vertical dotted lines correspond to the nominal value of the parameter. The grey area corresponds to the uncertainties of the first case, in orange. Fitting the spectrum with the wrong ratio introduces a bias in the central values of the solar oscillation parameters, while keeping the contributions as independent, we see no bias; in the latter case, only the precision on $\sin^2 \theta_{12}$ is slightly worse.

Table 6.4. Comparison of the expected precision on the measurement of the solar oscillation parameters, Δm^2_{21} and $\sin^2 \theta_{12}$, between the case of fixed Th/U ratio and free Th/U ratio, for one year of data-taking.

σ [%]	fixed ratio	free ratio
Δm^2_{21}	0.60	0.60
$\sin^2 \theta_{12}$	1.08	1.13

As we aim to leave the Th/U ratio free in the fit, we investigate the correlation between the oscillation parameters and these two background components. We follow a procedure similar to the one already described in section 6.4.1 to evaluate the contribution of each background. First, we evaluate the uncertainty on the solar parameters by keeping the normalization of both ^{238}U and ^{232}Th fixed, σ_{fixed}; the results are listed in Table 6.5 and shown in Fig. 6.13 in orange. The figure shows the contour plots between Δm^2_{21}, $\sin^2 \theta_{12}$, N_{rea}, N_{U}, and N_{Th}, and their posterior probabilities. By keeping the two geo-neutrinos contributions fixed, we see no correlation between the two solar oscillation parameters, as reported in Table 6.6.

Table 6.5. Expected precision of the measurement of the solar oscillation parameters, Δm^2_{21} and $\sin^2 \theta_{12}$, for different configurations of the geo-neutrinos in the analysis for one year of data-taking. See the text for more detail.

[%]	σ_{fixed} (U, Th fixed)	σ_{U} (U free, Th fixed)	σ_{Th} (U fixed, Th free)	σ_{sum}	σ_{free} (U, Th free)
Δm^2_{21}	0.46	0.38	0.14	0.61	0.60
$\sin^2 \theta_{12}$	1.07	0.31	0.10	1.12	1.13

Then, we keep the normalization of ^{232}Th fixed while N_{U} is allowed to vary within its constraint; results are shown in red in the figure, while the uncertainty
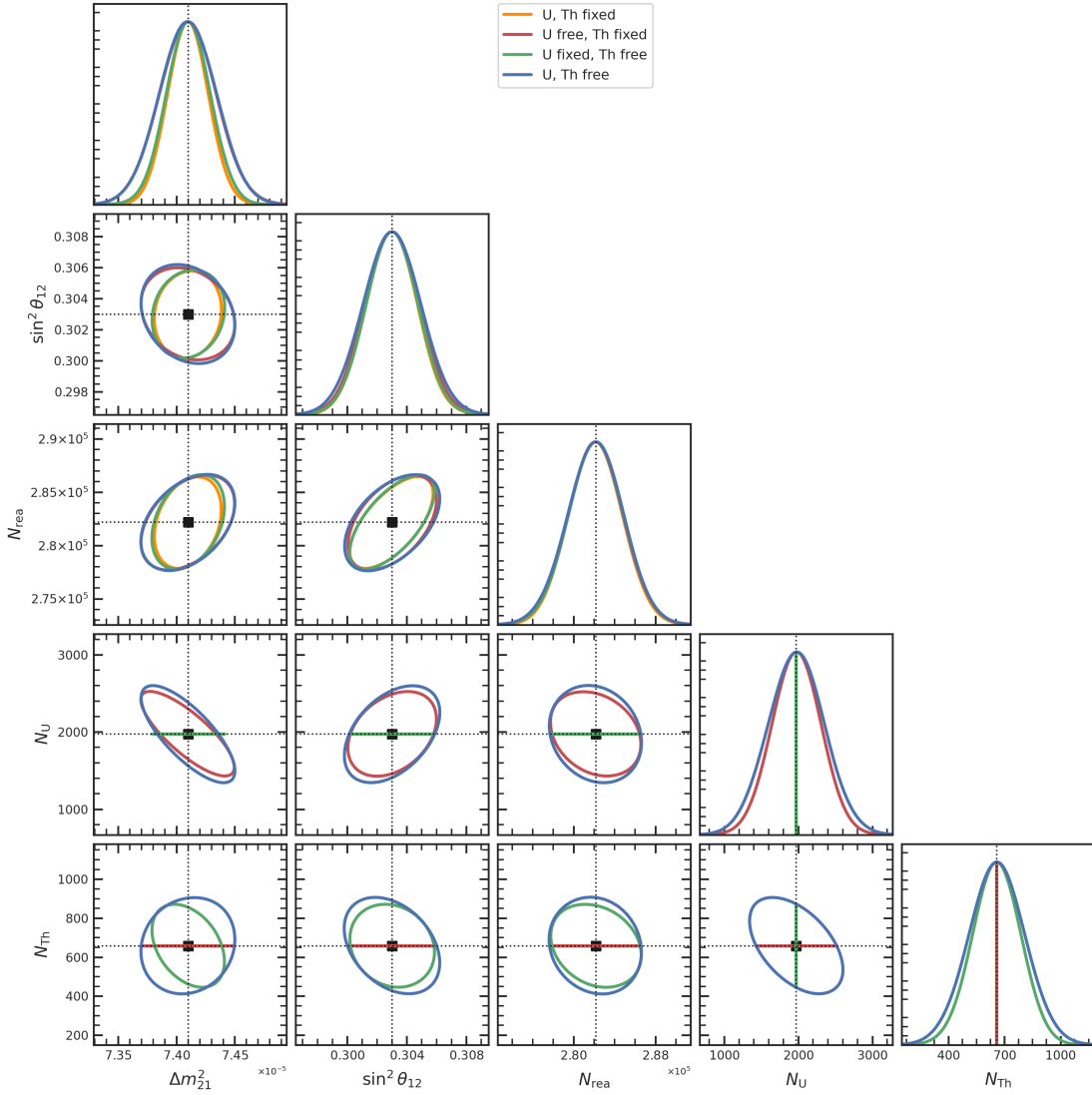
Figure 6.13. Correlation plots among geo-neutrinos background components and the oscillation parameters Δm^2_{21} and $\sin^2 \theta_{12}$. For the sake of clarity, only contour curves at $68\,\%$ confidence level are shown.

listed in the table is evaluated as:

$$\sigma_{\mathrm{U}} = \sqrt{\sigma^2_{\mathrm{fit}} - \sigma^2_{\mathrm{fixed}}}. \qquad (6.10)$$

We see that by varying only the ^{238}U normalization in the fit, a correlation between the two solar oscillation parameters arises, with a correlation coefficient of -0.17. We also notice that N_{U} is highly anti-correlated with Δm^2_{21} and correlated with $\sin^2 \theta_{12}$; the correlation coefficients are listed in Table 6.6.

Then, we do the same with ^{232}Th, by keeping the normalization of ^{238}U fixed; results are shown in green in Fig. 6.13 and also listed in the Table 6.5. In this case, we see no correlation between the two solar parameters, and a slight anti-correlation between N_{Th} and Δm^2_{21} and also $\sin^2 \theta_{12}$. The correlation coefficients are reported in Table 6.6.

Finally, we keep the normalization of both ^{238}U and ^{232}Th free; results are

Table 6.6. Correlations between the solar oscillation parameters, Δm_{21}^2 and $\sin^2\theta_{12}$, and the number of events from reactors, N_{rea}, and from geo-neutrinos, N_{U} and N_{Th}, for one year of data-taking.

ρ	U, Th fixed	U free, Th fixed	U fixed, Th free	U, Th free
$\Delta m_{21}^2 - \sin^2\theta_{12}$	0.01	-0.17	0.03	-0.16
$N_{\text{rea}} - \Delta m_{21}^2$	0.20	0.26	0.23	0.26
$N_{\text{rea}} - \sin^2\theta_{12}$	0.53	0.46	0.53	0.46
$N_{\text{U}} - \Delta m_{21}^2$	-	-0.63	-	-0.59
$N_{\text{U}} - \sin^2\theta_{12}$	-	0.28	-	0.31
$N_{\text{U}} - N_{\text{rea}}$	-	-0.16	-	-0.13
$N_{\text{Th}} - \Delta m_{21}^2$	-	-	-0.30	-0.06
$N_{\text{Th}} - \sin^2\theta_{12}$	-	-	-0.09	-0.17
$N_{\text{Th}} - N_{\text{rea}}$	-	-	-0.15	-0.10
$N_{\text{Th}} - N_{\text{U}}$	-	-	-	-0.29

shown in blue in the figure and the uncertainties, σ_{free}, are listed in the last column of the table. A correlation with $\rho = -0.29$ between the two backgrounds arises, leading to a change in correlation between N_{Th} and Δm_{21}^2. Also, an anti-correlation between the two solar parameters is present, with a coefficient of -0.16. All correlation coefficient related to this configuration are listed in the last column of Table 6.6. We can then evaluate the sum in quadrature, $\sigma_{\text{sum}} = \sqrt{\sigma_{\text{fixed}}^2 + \sigma_{\text{U}}^2 + \sigma_{\text{Th}}^2}$, which does not take into account correlations, and is different from σ_{free}, as expected. In particular, from the comparison of the last two columns of Table 6.5, we find that by keeping both ^{238}U and ^{232}Th free, correlations play a role by slightly improving the precision in the measurement of Δm_{21}^2, while worsening a bit the precision of $\sin^2\theta_{12}$.

Cosmogenic ^{9}Li-^{8}He

We want to estimate the impact of the cosmogenic ^{9}Li-^{8}He background, since its bell-like shape is very similar to the unoscillated reactor spectrum, and indeed the number of events from reactors and from ^{9}Li-^{8}He are correlated, as shown in Fig. 6.10. In the analysis presented here, the matter density, the detector-related nuisance parameters, and all other backgrounds are fixed in the fit; a data-taking time of one year is considered.

First, we intentionally bias the rate of cosmogenic ^{9}Li-^{8}He. To do so, we create an Asimov dataset using the nominal number of events for the signal and all the backgrounds, and initialize the fit first with $N_{\text{Li-He}} = \tilde{N}_{\text{Li-He}} + 1\sigma_{\text{Li-He}}$ and then with $N_{\text{Li-He}} = \tilde{N}_{\text{Li-He}} - 1\sigma_{\text{Li-He}}$, where $\tilde{N}_{\text{Li-He}}$ is the nominal value and $\sigma_{\text{Li-He}}$ is the ^{9}Li-^{8}He rate uncertainty. In both cases, no impact on the estimation of Δm_{21}^2 and $\sin^2\theta_{12}$ is observed. This is probably due to the fact that the ^{9}Li-^{8}He spectrum covers the whole energy range of interest and does not distort the spectrum in the region most sensitive to the solar oscillation parameters. The precise measurement of Δm_{21}^2 and $\sin^2\theta_{12}$ is thus robust to a wrong estimation of the ^{9}Li-^{8}He background rate.

Since the rate of this background is related to the selection criteria, in particular it depends on the muon veto, it is worth investigating also the impact of

changing the rate of the background and see if it is worth tightening or loosening the veto cuts. To do so, we vary the amount of cosmogenic ^{9}Li-^{8}He by factors of 0.01, 0.1, 10, and 100, both in the Asimov data sample and in the fit prediction. Results are shown in Fig. 6.14 and also listed in Table 6.7.

Table 6.7. Impact of a different rate of cosmogenic ^{9}Li-^{8}He background on the precision measurement of the solar oscillation parameters, at one year of data-taking.

$N_{\mathrm{Li-He}}$	$\times 0.01$	$\times 0.1$	nominal	$\times 10$	$\times 100$
$\sigma(\Delta m^2_{21})$	$0.608\,\%$	$0.608\,\%$	$0.610\,\%$	$0.631\,\%$	$0.905\,\%$
$\sigma(\sin^2\theta_{12})$	$1.124\,\%$	$1.125\,\%$	$1.130\,\%$	$1.187\,\%$	$1.965\,\%$

The central black points correspond to the nominal rate of cosmogenic ^{9}Li-^{8}He. The red and orange points corresponds to having the number of ^{9}Li-^{8}He events reduced by factors of 0.01 and 0.1, respectively. We see that by tightening the veto cuts and having a lower ^{9}Li-^{8}He rate, there is no much gain in the precision of the solar oscillation parameters. Having 10 times more background, which is shown in green, is not affecting much the precision on the solar oscillation parameters, while having 100 times more background, in blue, has a large impact: uncertainties for Δm^2_{21} and $\sin^2\theta_{12}$ increases by about $50\,\%$ and $75\,\%$, respectively. Loosening the veto cuts shows a degradation in JUNO expected sensitivity.
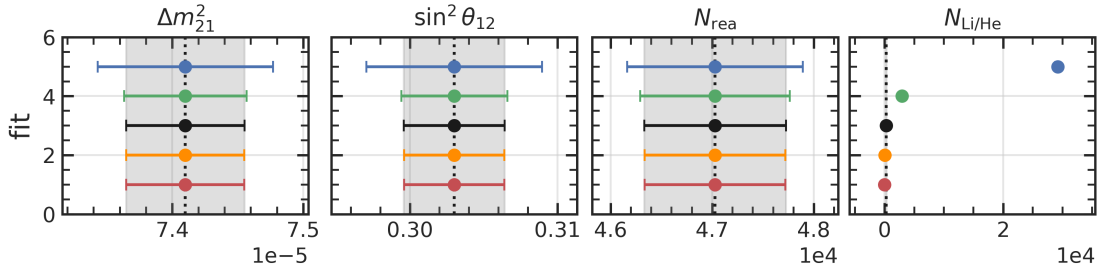
Figure 6.14. Impact of a different rate of cosmogenic ^{9}Li-^{8}He background on the precision measurement of the solar oscillation parameters, at one year of data-taking. The nominal results are in black, while the cases of a rate multiplied by 0.01, 0.1, 10, and 100 are shown in red, orange, green, and blue, respectively. The vertical dotted lines correspond to the nominal value of the parameter. The grey area corresponds to the uncertainties of the nominal case.

Changing rate and shape uncertainties of the backgrounds

When the detector is switched on at the beginning of data-taking, and during the first year which is the period considered in these studies, backgrounds will not be known with a great precision. For this reason, we would like to investigate the impact of using more conservative background uncertainties in the fit.

The procedure followed here is the same as the one explained at the beginning of section 6.4.1 used to obtain Fig. 6.11; to ease the comparison, the results shown in Fig. 6.11 are also reported in transparent colors in Fig. 6.15 and are labelled

as "nominal". In the evaluation of the contribution of each background, both the rate and shape uncertainties are multiplied by a factor of 2, and the results are shown in solid colors in Fig. 6.15.

(a) *Background impact on Δm_{21}^2.*   **(b)** *Background impact on $\sin^2 \theta_{12}$.*
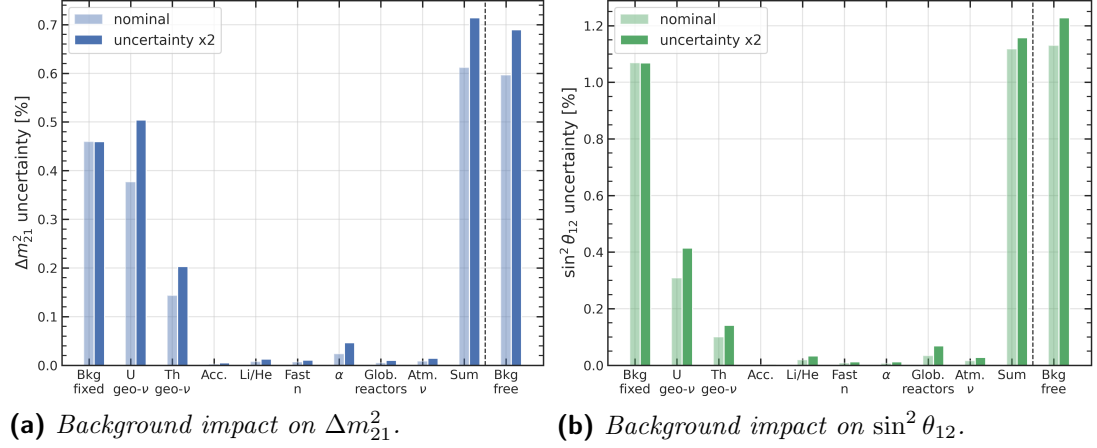
Figure 6.15. The impact of backgrounds on **(a)** Δm_{21}^2 and **(b)** $\sin^2 \theta_{12}$ with nominal background rate, but by increasing both the rate and shape uncertainties by a factor of 2, is shown in solid colors. For comparison, the results with nominal uncertainties are shown in transparent colors. See the text for more detail on the meaning of each column.

We see a similar behavior compared to the nominal case, with each background showing a greater contribution. The effect of the correlations that can be seen by comparing the column "Sum" with the column "Bkg free" is also maintained. The uncertainty on Δm_{21}^2 and $\sin^2 \theta_{12}$ due to backgrounds increases by about 15 % and 10 %, respectively. Using more conservative uncertainties on the backgrounds does not have a big impact, resulting in a small worsening of the precision on the measurement of the solar oscillation parameters.

6.4.2   Impact of the reactor rate uncertainty

From Fig. 6.9, we can see that a significant source of uncertainty, especially for $\sin^2 \theta_{12}$, is given by the reactor rate (reactor correlated) uncertainty. The value of 2 % listed in Table 6.3 is inherited by the measurement of the flux by the Daya Bay experiment [84].

The aim of this section is to estimate the impact of the reactor rate uncertainty on the precision measurement of the solar oscillation parameters. In this study, the matter density, the detector-related nuisance parameters, and all backgrounds are fixed in the fit; only the oscillation parameters and N_{rea} are free parameters of the fit. To do so, we scan the reactor rate uncertainty from a very optimistic value of 0.1 % to the pessimistic estimation of 100 %. The scan is performed for 1, 6, and 20 years of data-taking; the results are shown in Figs. 6.16a and 6.16b for Δm_{21}^2 and $\sin^2 \theta_{12}$, respectively.

As it can be seen in Fig. 6.16a, the parameter Δm_{21}^2 is only slightly affected by the reactor rate uncertainty, with the precision being constant for all three data-taking periods.

(a) *Expected precision on Δm_{21}^2.*   **(b)** *Expected precision on $\sin^2\theta_{12}$.*
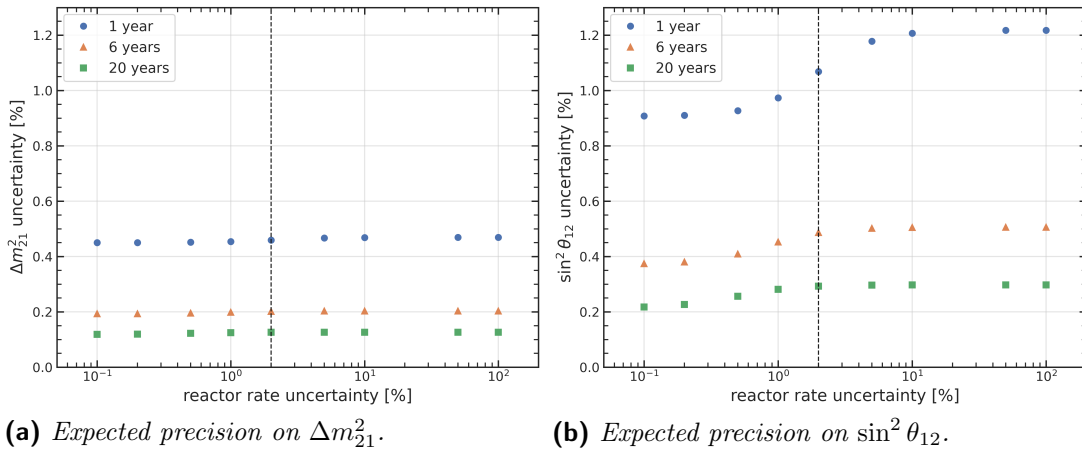
Figure 6.16. Expected precision on **(a)** Δm_{21}^2 and **(b)** $\sin^2\theta_{12}$ as a function of the reactor rate uncertainty for 1 (blue), 6 (orange), and 20 (green) years of data-taking. The vertical dashed line refers to the nominal rate uncertainty of 2 %.

On the contrary, the precision of $\sin^2\theta_{12}$ has a significant dependence on the value of the reactor rate uncertainty, with different behaviors for different data-taking times. In fact, at one year of data-taking, the statistics is low and the rate of reactor $\overline{\nu}_e$ still plays an important role: the precision on $\sin^2\theta_{12}$ varies from about 0.9 % in the most optimistic scenario to about 1.2 % in the most pessimistic one. At the nominal value, identified with the vertical dashed line, we are exactly in the middle of the transition between the two scenarios. For this reason, it is crucial to investigate the model of the reactor spectrum as done in chapter 3 and provide a precise estimation not only of the shape but also of the flux, so that we could improve the precision on $\sin^2\theta_{12}$.

On the other hand, at 20 years of data-taking, we see a smaller separation between the two opposite scenarios. In fact, for longer data-taking periods, we are no longer statistically dominated and the precision is driven by the shape of the spectrum which can be affected and distorted by systematic uncertainties. In particular, the shape is affected by the light emission non-linearity and the energy resolution of the detector response, thus it is important to study it in detail, as proposed in chapter 4.

6.5   Results and discussion

In this section, we report the final estimation of the expected precision in the measurement of the solar oscillation parameters, Δm_{21}^2 and $\sin^2\theta_{12}$.

The JUNO experiment is expected to achieve an unprecedented sub-percent precision in the measurement of the solar oscillation parameters. In fact, after 1 year of data-taking the expected precision is 0.62 % and 1.16 % for Δm_{21}^2 and $\sin^2\theta_{12}$, respectively, already improving the current precision of 2.39 % and 4.23 % from PDG2022 [2]. The results are obtained by including all expected sources of systematic uncertainties in the fit. From Fig. 6.13, we can see that the two

parameters are not correlated with each other.
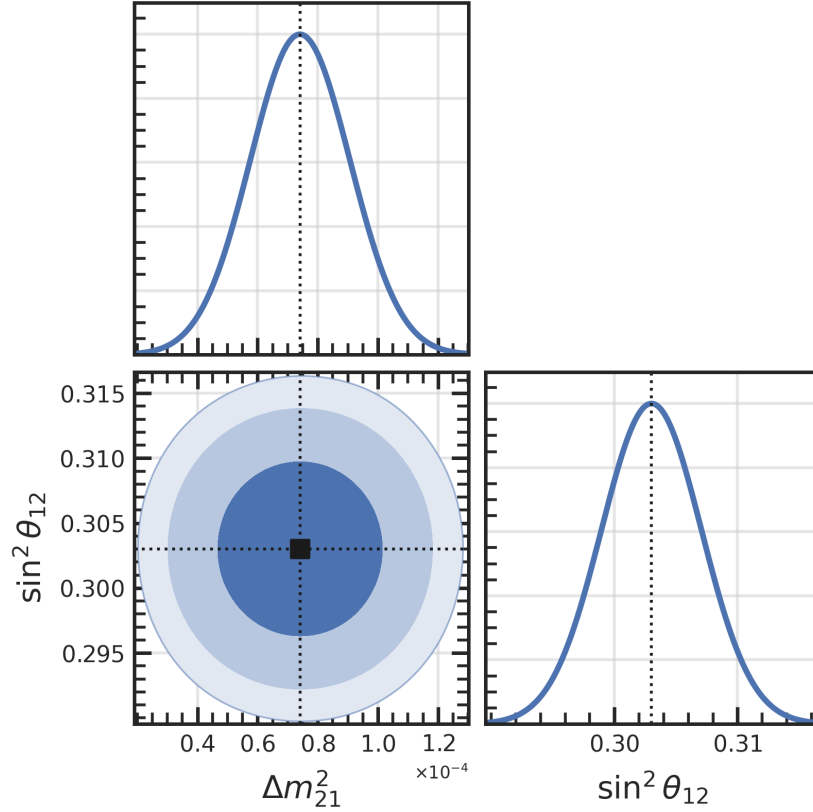
Figure 6.17. The plot at the bottom left shows the contour plot between Δm_{21}^2 and $\sin^2\theta_{12}$ at 68 %, 95 %, and 99 % confidence level; the two parameters show no correlation. The other two plots show the posterior distributions of the two solar oscillation parameters

Furthermore, the measurement done with reactor neutrinos could be further checked by the independent measurement performed with solar neutrinos, as anticipated in section 2.2.

Table 6.8. Precision on the measurement of Δm_{21}^2 and $\sin^2\theta_{12}$ for different data-taking periods. For comparison, the current precision from the Particle Data Group global fit is shown in the last column.

σ	1 year	6 years	20 years	PDG2022 [2]
Δm_{21}^2	0.62 %	0.34 %	0.24 %	2.39 %
$\sin^2\theta_{12}$	1.16 %	0.58 %	0.39 %	4.23 %

In Table 6.8, the expected precision at 6 years and 20 years of data-taking are listed together with the precision at one year and the current precision, while Fig. 6.18 shows the χ^2 profile for Δm_{21}^2 on the left and $\sin^2\theta_{12}$ on the right for the three different exposures. As it can be seen, there is a big improvement in the precision by going from one year to six years, while a smaller increase of the precision is obtained for longer data-taking periods. This can be explained with

the help of Fig. 6.19, which shows the evolution in time of the precision of the two solar parameters. At the beginning of data-taking, the precision is dominated by the statistical uncertainty, which decreases in time. On the contrary, for long exposures, the results are dominated by systematic uncertainties, and the precision saturates. To improve the precision also for longer exposures, systematics uncertainties should be studied and reduced.
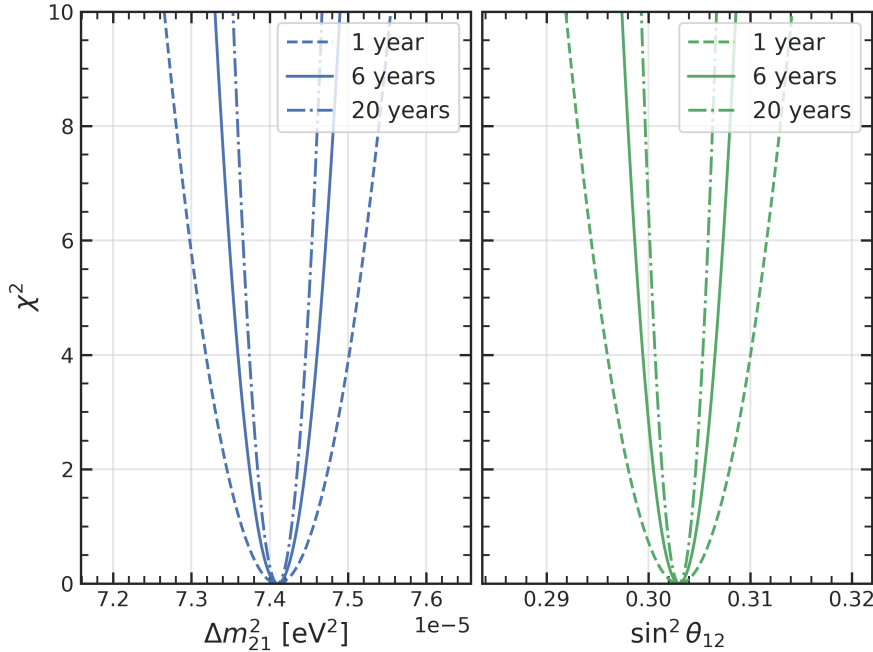
Figure 6.18. Profile of the cost function, χ^2, for Δm_{21}^2 (left) and $\sin^2\theta_{12}$ (right) at 1 year, 6 years, and 20 years of data-taking. All sources of systematic uncertainties are included in the fit.

Conclusion

The JUNO experiment is expected to measure the solar oscillation parameters with unprecedented sub-percent precision. After one year of data-taking, JUNO will reach a sub-percent precision as far as Δm_{21}^2 is concerned, while it will improve the precision on $\sin^2\theta_{12}$ compared to the state-of-the-art.

In parallel to JUNO, there are other neutrino detectors currently under construction and that will begin data-taking shortly after JUNO: DUNE and Hyper-K. DUNE is a neutrino beam experiment with the main goal of determining the neutrino mass ordering and the CP violation; nonetheless, it will also provide an improved measurements of the solar oscillation parameters, although not competitive with JUNO. Hyper-K, that will detect mainly beam neutrinos and atmospheric neutrinos, will also be sensitive to the neutrino mass ordering and the CP violation in the neutrino sector, and is sensitive to the atmospheric oscillation parameters, while it's not competitive with JUNO in the solar sector.
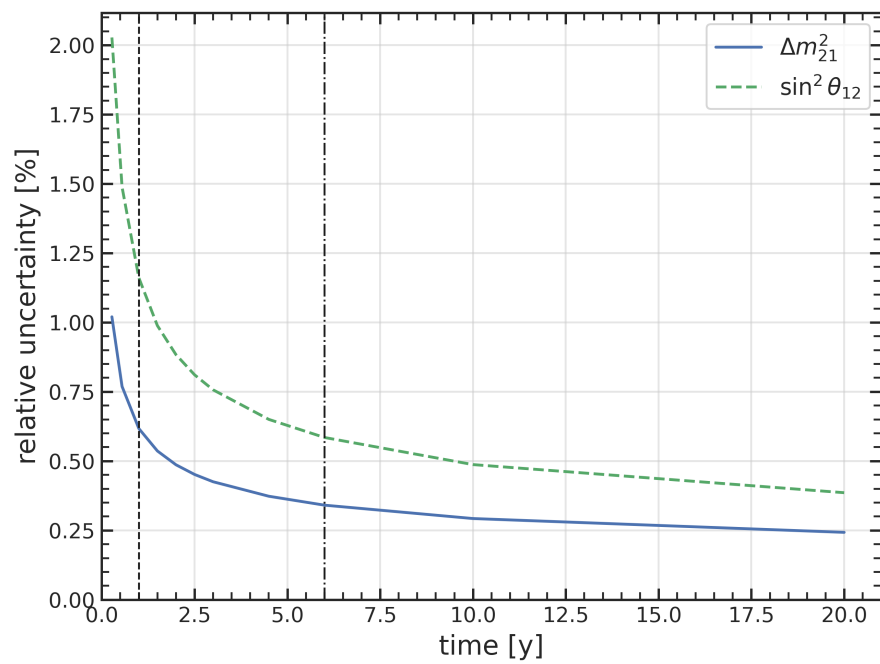
Figure 6.19. Evolution of the relative uncertainties of Δm_{21}^2 (blue) and $\sin^2 \theta_{12}$ (orange) with data-taking time. The dashed vertical line corresponds to one year of data-taking, while the dashed-dotted vertical line corresponds to six years of data-taking.

Conclusion

JUNO is a multi-purpose neutrino experiment that is currently being built to further investigate the quantum phenomenon of neutrino oscillations. JUNO will detect electron antineutrinos produced at nearby nuclear reactors and is expected to the determine the neutrino mass ordering with a 3σ significance in about six years of data-taking and to measure three of the oscillation parameters (Δm_{21}^2, Δm_{31}^2, and $\sin^2\theta_{12}$) with an unprecedented sub-percent precision. In this work, I focused on the estimation of the expected precision that the JUNO experiment can reach in the measurement of the *solar* oscillation parameters, Δm_{21}^2 and $\sin^2\theta_{12}$, after one year of data-taking. To this end, I addressed some experimental issues relevant to the analysis that could possibly spoil JUNO results if not properly addressed: modelling the electron antineutrinos source; modelling the relationship between the deposited energy in the detector and the light emitted by the liquid scintillator, which is a key component of the detector response; the mass testing of the photomultiplier readout boards; and finally the impact of backgrounds in the analysis.

In chapter 3, I presented a method to evaluate the prediction for JUNO reactor spectrum based on recent data from the Daya Bay experiment. This method is to be preferred to the currently employed model developed by Huber and Mueller, because it takes into account the proper flux normalization and the spectral distortion, which are not included in the Huber Mueller model. I also investigated the effect of the changes in the fuel composition, and thus in the fission fractions, during one operational cycle of a reactor core, showing that both the rate and shape of the antineutrino spectrum are affected.

Finally, I focused on the evaluation of the uncertainty budget of the prediction of the reactor spectrum. In particular, I devoted great effort to study the 2D interpolation of the covariance matrix in order to match JUNO finer binning. The study on the uncertainty presented here does not provide a definite answer yet and further studies are needed.

In chapter 4, I presented a novel method based on a simple output of Geant4 simulations to model the scintillation non-linearity with just one free parameter, the Birks' constant k_B. I built and tuned the model based on the scintillation light detected when deploying the gamma calibration sources; the value of the Birks' constant obtained from the tuning was found to be within 1% from the input value. Then, I applied the model to e^- and e^+ to obtain the respective non-linearity curves, so that all particles are treated with the same approach. For all particles, the comparison between the model prediction and the mock data shows a relative difference within 0.1%, providing a good consistency check

of the model.

The non-linearity model presented in this work only describes the non-linearity of the light emission through the scintillation process. An additional source of non-linearity is introduced by the Cherenkov effect, so future studies could focus in trying to incorporate this effect into the non-linearity model. In addition, it might also be interesting to study the effect of the production cut in the Geant4 simulations on the model, as already investigated by the Daya Bay collaboration [88].

In chapter 5, I described the mass testing of 6950 electronics readout boards for the 20-inch PMT system. I developed the test protocol so that it could also be operated remotely since the mass testing lasted for about ten months during the Covid pandemic. The protocol consisted of several tests to check the connectivity of the devices to the local network, to check basic features of the collected waveforms, $e.g.$, the noise, and to monitor several slow control parameters of the board, like the internal temperature. Only 8 GCUs were discarded on the basis of the tests presented and the established criteria; another 56 GCUs were discarded due to issues that arose during the assembling procedure. In total, 6886 GCUs were accepted, while only 64 were rejected, providing a final acceptance yield of 99.1 %.

Finally, I evaluated the expected precision in the measurement of the solar oscillation parameters, Δm_{21}^2 and $\sin^2\theta_{12}$, as reported in chapter 6. The results were obtained by including all expected sources of systematic uncertainties in the fit. The values of the expected precision at three different data-taking periods are listed in the following table:

σ	1 year	6 years	20 years	PDG2022 [2]
Δm_{21}^2	0.62 %	0.34 %	0.24 %	2.39 %
$\sin^2\theta_{12}$	1.16 %	0.58 %	0.39 %	4.23 %

After 1 year of data-taking, the expected precision is 0.62 % and 1.16 % for Δm_{21}^2 and $\sin^2\theta_{12}$, respectively, already improving the current precision of 2.39 % and 4.23 % from PDG2022 [2]. The expected precision at 6 years and 20 years of data-taking are also listed. There is a big improvement in the precision by going from one year to six years, while a smaller increase of the precision is obtained for longer data-taking periods. In fact, at the beginning of data-taking, the precision is dominated by the statistical uncertainty, which decreases in time. On the contrary, for long exposures, the results are dominated by systematic uncertainties, and the precision saturates. Systematic uncertainties should be studied and reduced to improve the precision also for longer exposures.

In this work, I found that background uncertainties constitute a major source of systematic uncertainty for both solar parameters; in particular, geo-neutrinos play a significant role. For the solar mixing angle, $\sin^2\theta_{12}$, I found that the uncertainty on the reactor rate also plays a role, especially at short exposures.

In parallel to JUNO, there are other neutrino detectors currently under construction and that will begin data-taking shortly after JUNO, $i.e.$, DUNE and Hyper-K, although none of them will be competitive with JUNO in the solar sector.

Appendix A

Uncertainty treatment in the modelling of the reactor spectrum: Supplemental material

Supplemental material related to the treatment of uncertainties in the modelling of the reactor spectrum described in chapter 3 is now presented.

A.1 Tabulated spectra and uncertainties

The tabulated spectrum and uncertainties for ^{241}Pu from the conversion method by Huber [73] are listed in Table A.1, while for ^{238}U from the *ab initio* method by Mueller *et al.* [75] are listed in Table A.2; the tabulated values for ^{235}U and ^{239}Pu are not shown since the spectra from Daya Bay are used in the antineutrino-driven model. The values are tabulated for the antineutrino energy ranging from 2 MeV to 8 MeV with a bin width of 0.25 MeV. The spectrum is give in units of antineutrino per fission per MeV, while uncertainties are given in percent at 1σ (68 % CL).

For ^{241}Pu, the uncertainties in columns 3 and 4 are related to the conversion procedure and are fully uncorrelated between bins, while the uncertainties in columns 5 and 6 are theoretical uncertainties and are fully correlated between bins. Finally, the uncertainty in column 7 is related to the normalization of the original ILL data and is fully correlated between bins. For more details on the uncertainties refer to [73].

For ^{238}U, the uncertainty in column 3 is obtained by propagating the uncertainties from nuclear databases to the antineutrino spectrum and has partial correlation among bins below 3.5 MeV; this partial correlation is investigated in section A.3. The uncertainties in columns 4 and 5 are theoretical uncertainties, with the former being uncorrelated between bins and the latter fully correlated between bins. Finally, the uncertainty in column 6 is related to the missing information of the nuclear databases and is uncorrelated between bins. For more details on the uncertainties refer to [75].

The uncertainties related to the Daya Bay spectra are already available in the form of a covariance matrix in the supplemental material of [67]; the spectra are

149

also provided as supplemental material.

Table A.1. Tabulated spectrum and uncertainties for ^{241}Pu from the conversion method by Huber [73]. The first and second columns are the antineutrino energy and the antineutrino spectrum, respectively, while the other columns list various sources of uncertainties, which are given in percent at 1σ (68 % CL). The uncertainties in columns 3 and 4 are related to the conversion procedure and are fully uncorrelated between bins. On the other hand, the uncertainties in columns 5 and 6 are theoretical uncertainties and are fully correlated between bins. The uncertainty in column 7 is related to the normalization of the original ILL data and is fully correlated between bins.

E_ν [MeV]	$\bar\nu$ spectrum fission^{-1} MeV^{-1}	stat. [%]	bias err. [%]	$\bar Z$ [%]	WM [%]	norm. [%]
2.00	1.26	1.7	0.18	$^{+0.16}_{0}$	$^{0}_{-0.18}$	1.8
2.25	1.08	1.6	0.34	$^{+0.13}_{0}$	$^{0}_{-0.12}$	1.8
2.5	$8.94 \cdot 10^{-1}$	1.4	0.33	$^{+0.079}_{0}$	$^{+0.099}_{-0.23}$	1.8
2.75	$7.77 \cdot 10^{-1}$	1.4	0.2	$^{+0.024}_{0}$	$^{+0.24}_{-0.34}$	1.8
3.00	$6.41 \cdot 10^{-1}$	1.6	0.12	$^{+0}_{-0.041}$	$^{+0.38}_{-0.46}$	1.8
3.25	$5.36 \cdot 10^{-1}$	1.6	0.15	$^{+0}_{-0.12}$	$^{+0.52}_{-0.57}$	1.8
3.5	$4.39 \cdot 10^{-1}$	1.6	0.22	$^{+0}_{-0.2}$	$^{+0.65}_{-0.68}$	1.8
3.75	$3.46 \cdot 10^{-1}$	1.4	0.2	$^{+0}_{-0.29}$	$^{+0.79}_{-0.8}$	1.8
4.00	$2.82 \cdot 10^{-1}$	1.5	0.11	$^{+0}_{-0.39}$	$^{+0.93}_{-0.91}$	1.8
4.25	$2.2 \cdot 10^{-1}$	1.9	0.17	$^{+0}_{-0.5}$	$^{+1.1}_{-1.}$	1.9
4.5	$1.66 \cdot 10^{-1}$	2.5	0.29	$^{+0}_{-0.62}$	$^{+1.2}_{-1.1}$	1.9
4.75	$1.25 \cdot 10^{-1}$	2.5	0.48	$^{+0}_{-0.75}$	$^{+1.3}_{-1.2}$	1.9
5.00	$9.74 \cdot 10^{-2}$	2.3	0.033	$^{+0}_{-0.89}$	$^{+1.5}_{-1.4}$	1.9
5.25	$7.47 \cdot 10^{-2}$	2.3	0.14	$^{+0}_{-1.}$	$^{+1.6}_{-1.5}$	1.9
5.5	$5.58 \cdot 10^{-2}$	2.6	0.13	$^{+0}_{-1.2}$	$^{+1.8}_{-1.6}$	1.9
5.75	$4.11 \cdot 10^{-2}$	3.2	0.21	$^{+0}_{-1.4}$	$^{+1.9}_{-1.7}$	1.9
6.00	$3.05 \cdot 10^{-2}$	4.	0.09	$^{+0}_{-1.5}$	$^{+2.}_{-1.8}$	1.9
6.25	$1.98 \cdot 10^{-2}$	4.4	0.33	$^{+0}_{-1.7}$	$^{+2.2}_{-1.9}$	1.9
6.5	$1.54 \cdot 10^{-2}$	4.5	0.43	$^{+0}_{-1.9}$	$^{+2.3}_{-2.}$	1.9
6.75	$1.09 \cdot 10^{-2}$	4.7	0.074	$^{+0}_{-2.1}$	$^{+2.5}_{-2.2}$	1.9
7.00	$7.75 \cdot 10^{-3}$	4.8	0.39	$^{+0}_{-2.3}$	$^{+2.6}_{-2.3}$	1.9
7.25	$4.47 \cdot 10^{-3}$	6.3	0.36	$^{+0}_{-2.5}$	$^{+2.7}_{-2.4}$	2.
7.5	$2.9 \cdot 10^{-3}$	7.7	0.3	$^{+0}_{-2.8}$	$^{+2.9}_{-2.5}$	2.
7.75	$1.78 \cdot 10^{-3}$	8.3	0.063	$^{+0}_{-3.}$	$^{+3.}_{-2.6}$	2.
8.00	$1.06 \cdot 10^{-3}$	12.	0.63	$^{+0}_{-3.3}$	$^{+3.2}_{-2.7}$	2.

A.2 Covariance matrix interpolation: Fit of ToyMC spectra

More details on the fit of the ToyMC spectra used to interpolate the covariance matrix introduced in section 3.5 are now presented. We start by discussing the procedure taking ^{241}Pu as an example, and in the following section we present the results also for ^{238}U.

Table A.2. Tabulated spectrum and uncertainties for ^{238}U from the *ab initio* method by Mueller *et al.* [75]. The first and second columns are the antineutrino energy and the antineutrino spectrum, respectively, while the other columns list various sources of uncertainties, which are given in percent at 1σ (68 % CL). The uncertainty in column 3 is obtained by propagating the uncertainties from nuclear databases to the antineutrino spectrum and has partial correlation among bins below 3.5 MeV. The uncertainties in columns 4 and 5 are theoretical uncertainties, with the former being uncorrelated between bins and the latter fully correlated between bins. The uncertainty in column 6 is related to the missing information of the nuclear databases and is uncorrelated between bins.

E_ν [MeV]	$\overline{\nu}$ spectrum fission^{-1} MeV^{-1}	Nuclear databases [%]	Forbid. treatment [%]	$A_{C,W}$ corrections [%]	Missing info. [%]
2.00	1.43	1.2	0.2	0.1	10
2.25	1.26	1.3	0.2	0.2	10
2.50	1.12	1.3	0.1	0.3	10
2.75	$9.80 \cdot 10^{-1}$	1.3	0.1	0.3	10
3.00	$8.70 \cdot 10^{-1}$	1.4	0.4	0.4	10
3.25	$7.57 \cdot 10^{-1}$	1.6	0.7	0.5	10
3.50	$6.40 \cdot 10^{-1}$	1.7	0.1	0.5	10
3.75	$5.39 \cdot 10^{-1}$	1.9	1.3	0.6	10
4.00	$4.50 \cdot 10^{-1}$	2.2	1.6	0.6	10
4.25	$3.67 \cdot 10^{-1}$	2.5	1.6	0.7	10
4.50	$2.94 \cdot 10^{-1}$	2.8	1.4	0.8	10
4.75	$2.32 \cdot 10^{-1}$	3.2	1.0	0.8	10
5.00	$1.83 \cdot 10^{-1}$	3.8	0.5	0.9	10
5.25	$1.43 \cdot 10^{-1}$	4.4	0.2	0.9	10
5.50	$1.10 \cdot 10^{-1}$	5.2	0.2	0.9	15
5.75	$8.35 \cdot 10^{-2}$	6.1	0.2	0.9	15
6.00	$6.21 \cdot 10^{-2}$	7.1	0.2	1.0	15
6.25	$4.70 \cdot 10^{-2}$	8.0	0.3	1.0	15
6.50	$3.58 \cdot 10^{-2}$	9.0	0.4	1.1	15
6.75	$2.71 \cdot 10^{-2}$	10.1	0.4	1.1	15
7.00	$1.95 \cdot 10^{-2}$	10.9	0.5	1.1	20
7.25	$1.32 \cdot 10^{-2}$	11.0	0.7	1.1	20
7.50	$8.65 \cdot 10^{-3}$	10.7	0.8	1.1	> 20
7.75	$6.01 \cdot 10^{-3}$	11.1	0.8	1.2	> 20
8.00	$3.84 \cdot 10^{-3}$	13.3	1.2	1.3	> 20

Fit of ^{241}Pu sampled spectra

The sampled spectra are fitted using the `scipy.optimize.curve_fit` function. Three different fit modes are used: (1) a χ^2-like function with no uncertainty (equivalently, a χ^2 fit with the uncertainty at the denominator fixed to 1); (2) a standard χ^2 fit, where the uncertainties are taken equal to the square root of the diagonal values of the covariance matrix; (3) a χ^2 fit taking into account the whole covariance matrix.

The same set of sampled spectra is used with the three fitting modes. The distributions of the best-fit parameters are shown in Fig. A.1. For the case of no uncertainties used in the fit, the distributions of the parameters are not symmetric, as it is clearly visible in Fig. A.1a. Comparing Figs. A.1b and A.1c, it can be seen that the use of the covariance matrix in the fit has an impact on the resulting best-fit parameters. The expected best-fit values from Huber are also shown as vertical solid black lines; the parameter distributions for the third case, where the covariance matrix is used, are peaked at the expected values; in the other case, a bias is visible.

Figure A.2 shows the reduced χ^2 distributions for the three fitting modes; the number of degrees of freedom is the number of bins (25) minus the number of parameters (6) of the fitting function, Eq. (3.16), hence $25 - 6 = 19$. The slight difference in the distribution between the second and third modes is another proof of the impact of the covariance matrix in the fit.

Figure A.3 shows a few best-fit curves for the three fitting modes. As a reference, the Asimov spectrum is also shown as black dots. From the comparison between the best-fit curves and the Asimov dataset, it can be seen that the parametric fit function, Eq. (3.16), is smoother than the Asimov, thus it is not able to reproduce the finer structures of the original spectrum. The covariance matrices for the three fitting modes where the Asimov spectrum is used as the expectation value in Eq. (3.15), displayed in the middle row of Fig. 3.21 (panels **(d)**, **(e)**, and **(f)**), show features that are not present in the original matrix and are probably introduced by the difference in smoothness between the Asimov and the fit function.

Then, the mean spectrum is evaluated from all best-fit curves, which is shown as red dots in Fig. A.3. As it can be seen, the mean spectrum does not match the Asimov dataset and is a better representative of the best-fit curves. The mean spectrum is used as the expectation value in Eq. (3.15) and the resulting matrices are shown in the bottom row of Fig. 3.21. The matrix in panel **(g)** is still not matching the original matrix, and this is probably related to the fact that no uncertainty was used in the fit. On the other hand, the matrices in panels **(h)** and **(i)** show a good resemblance with the original matrix, as far as the correlation pattern is concerned, but are not able to retrieve the diagonal.

We can conclude that the use of a smooth fit function allows us to reproduce the correlation between bins, while it gives no information on bin-to-bin uncorrelated uncertainties (which should be statistical Poissonian fluctuations) and is not able to describe fine structures of the spectrum. The best fit configuration is the one corresponding to panel **(i)**, where fitting mode (3) with the covariance matrix is used and the mean spectrum is used as the expectation value in Eq. (3.15).

(a) *Best-fit parameters with no uncertainty.*

**(b)** *Best-fit parameters with uncertainties but no correlation.*

(c) *Best-fit parameters with the covariance matrix.*
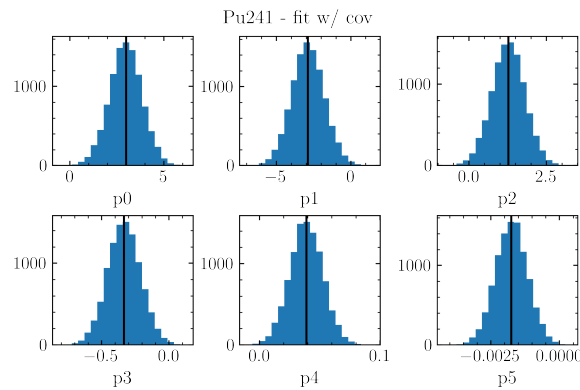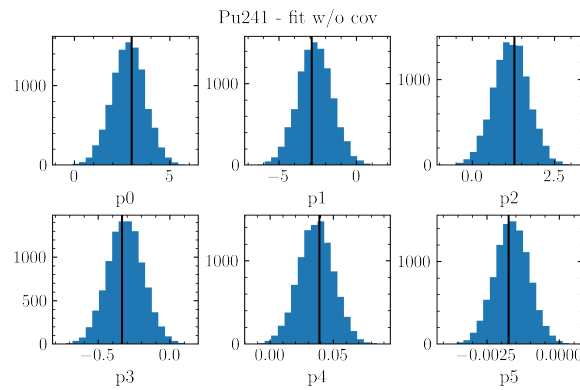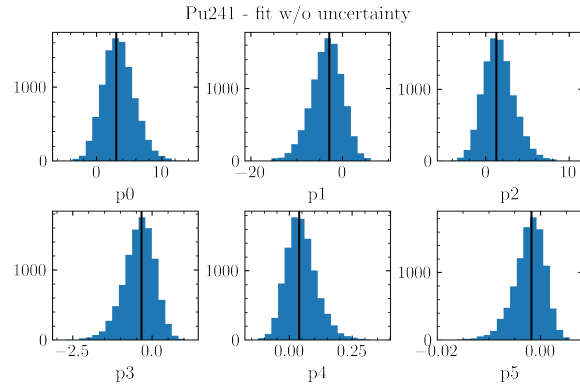
Figure A.1. Parameter distributions from the fits on ^{241}Pu ToyMC spectra: **(a)** no uncertainty is used in the fit; **(b)** the diagonal elements of the covariance matrix are used as uncertainties in the fit; **(c)** the covariance matrix is used in the fit. The vertical solid black lines are the expected best-fit values from Huber; the distributions for case **(c)** are peaked at the expected values. A slight difference from case **(b)** to **(c)** indicates the impact of a non-diagonal covariance matrix in the fit.
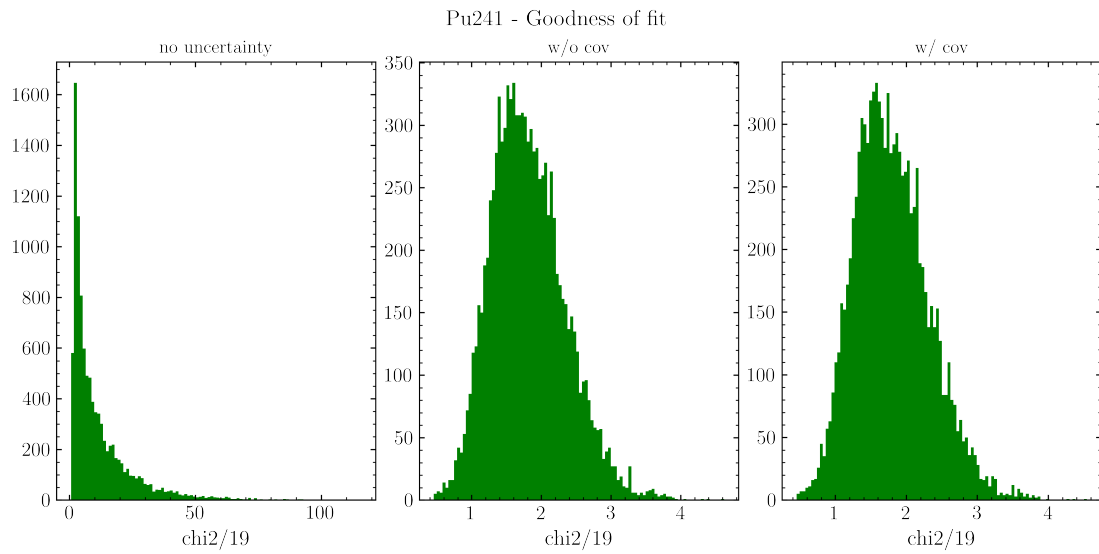
Figure A.2. Goodness of fit for ^{241}Pu ToyMc spectra: the distributions of the reduced χ^2 are shown for the fit with no uncertainty (left), with uncertainties but no covariance matrix (middle), and with the covariance matrix (right).
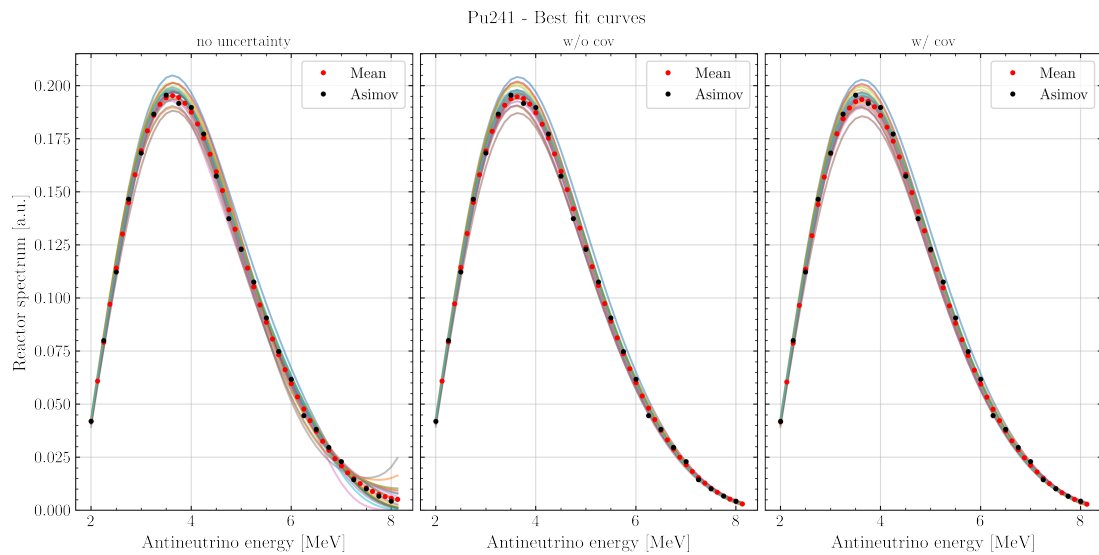
Figure A.3. The plot shows 20 best-fit curves from the fitting of ^{241}Pu ToyMC spectra for the fit with no uncertainty (left), with uncertainties but no covariance matrix (middle), and with the covariance matrix (right). The Asimov (black dots) and the mean (red dots) spectra are also shown.

Fit of ^{238}U sampled spectra

We now present the same analysis for ^{238}U.

Figure A.4 shows the distributions of the parameters from the fit of the ^{238}U ToyMC spectra. Since the covariance matrix for this isotope is almost diagonal, there is not much difference in the fit with or without the covariance matrix, as can be seen by the comparison between Figs. A.4b and A.4c. The expected best-fit values from Mueller *et al.* are also shown as vertical solid black lines. The distributions, even in the case with the covariance matrix, are not centered around the expected values, because we are using the spectrum from Estienne *et al.* which cannot be described with Mueller's parameters; Estienne *et al.* do not provide new estimates of the parameters for their new ^{238}U spectrum based on the parametrization of Eq. (3.16).

Figure A.5 shows the reduced χ^2 distributions for the three fitting methods. Also in this case, we can see no difference between the distributions of the second and third fitting modes, because the covariance matrix is almost diagonal.

Figure A.6 shows a few best-fit curves for the first and the third fitting modes; the second mode is not shown because it's identical to the third one. From the left plot of the figure, it can be seen that without any uncertainties in the fit, the use of a smooth 6-parameter curve introduces non-physical features in the spectrum, especially around the peak and in the high energy part of the spectrum.

The Asimov spectrum is shown as black dots in Fig. A.6. The Asimov spectrum is used as the expectation value in the evaluation of the covariance matrix, Eq. (3.15); the resulting covariance matrices are shown in the middle row of Fig. 3.22, in panels (**d**), (**e**), and (**f**). Similarly to ^{241}Pu, these matrices display features which are not present in the original matrix.

Then, we use the mean spectrum as the expectation values, since it better describes the best-fit curves; the resulting matrices are shown in the bottom row of Fig. 3.22, in panels (**g**), (**h**), and (**i**). Contrary to what happened with ^{241}Pu, we see no improvement by going from the Asimov to the mean spectrum. This is probably due to the fact that the covariance matrix is almost diagonal, and we concluded with ^{241}Pu that this method works fine to reproduce the correlation between bins, but not the diagonal contribution.

A.3   Impact of partial correlation in the ^{238}U uncertainty budget

In the uncertainty budget of ^{238}U by Mueller *et al.*, the contribution from the nuclear databases presents a partial correlation between bins in the low energy part of the spectrum, in the range from 2 MeV to 3.5 MeV. In the studies done in section 3.5, this contribution is considered as bin-to-bin uncorrelated, hence a diagonal matrix. In this section, we investigate the impact of the additional partial correlation.

The total covariance matrix with the partial correlation contribution can be seen in Fig. A.7 on the right; for comparison, the matrix without the contribution is shown on the left. The effect of this contribution is small, and is visible in the
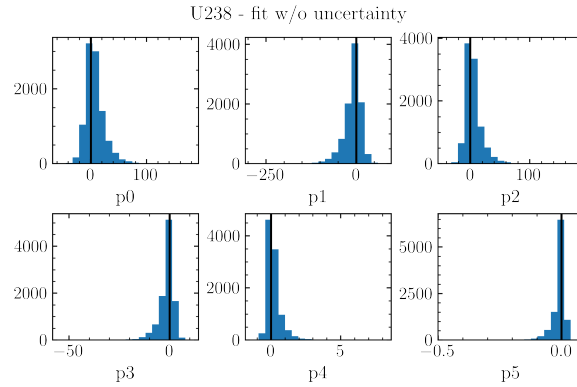
(a) *Best-fit parameters with no uncertainty.*
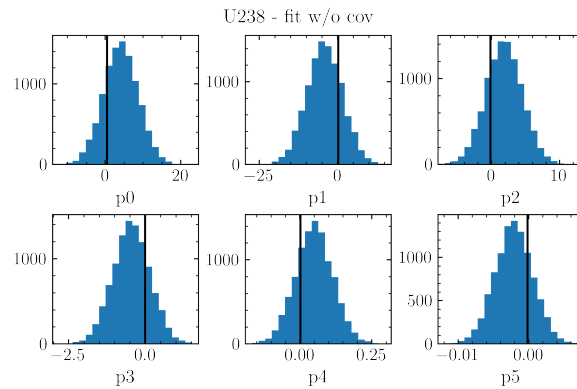
(b) *Best-fit parameters with uncertainties.*
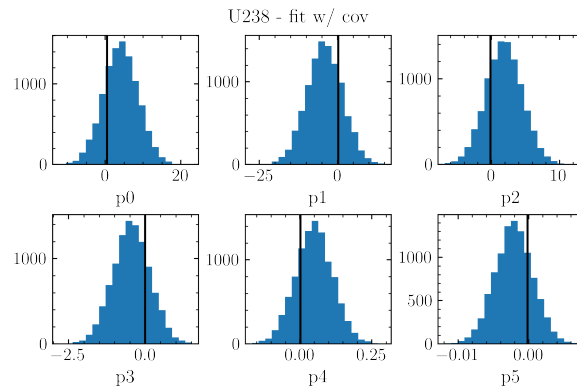
(c) *Best-fit parameters with covariance matrix.*

Figure A.4. Parameter distributions from the fits on ^{238}U ToyMC spectra: **(a)** no uncertainty is used in the fit; **(b)** the diagonal elements of the covariance matrix are used as uncertainties in the fit; **(c)** the covariance matrix is used in the fit. The vertical solid black lines are the expected best-fit values from Mueller *et al.*, which are not retrieved by the fit since we are using the Asimov spectrum from Estienne *et al.* Since the ^{238}U covariance matrix is almost a diagonal matrix, there is no significant difference between **(b)** and **(c)**.
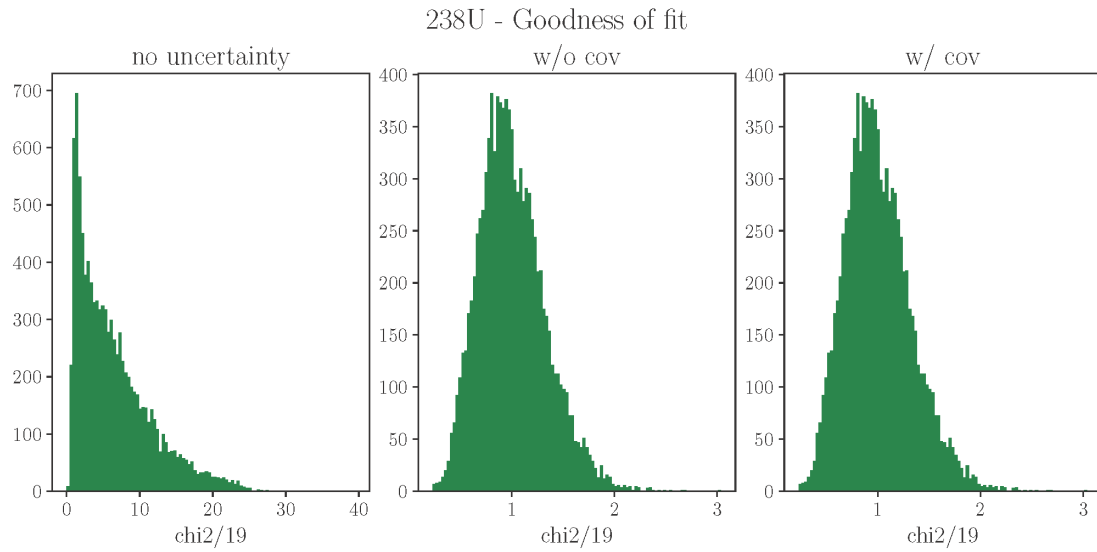
Figure A.5. Goodness of fit for ^{238}U ToyMc spectra: the distributions of the reduced χ^2 are shown for the fit with no uncertainty (left), and with uncertainties but no covariance matrix (middle), with the covariance matrix (right).
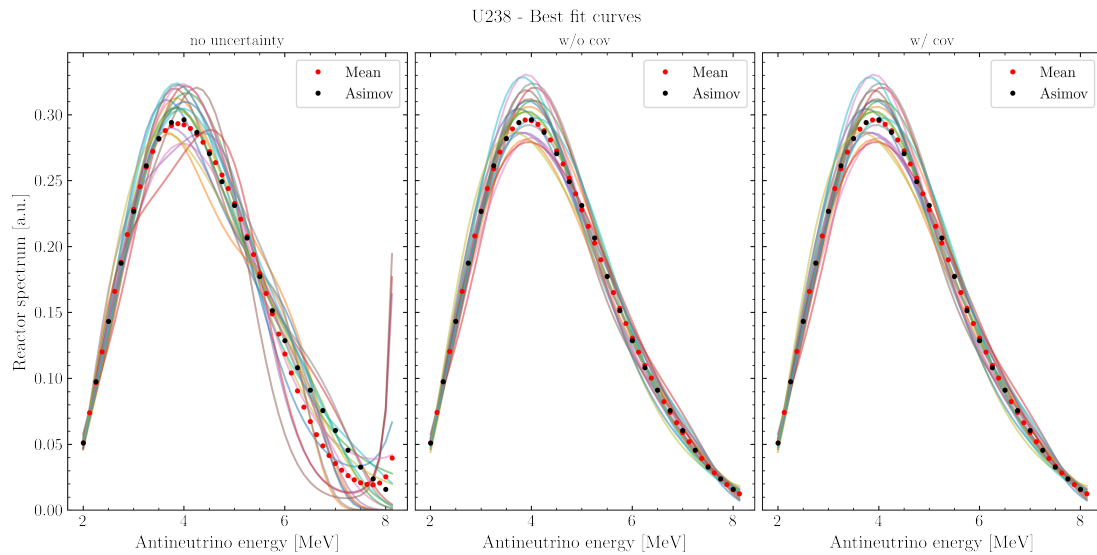
Figure A.6. The plot shows 20 best-fit curves from the fitting of ^{238}U ToyMC spectra for the fit with no uncertainty (left), and with the covariance matrix (right); the case with uncertainty and no covariance matrix is not shown because there is not difference from the covariance matrix case. The Asimov (black dots) and the mean (red dots) spectra are also shown. From the plot on the left, it is clearly visible that the fit without any uncertainties is not able to well reproduce the expected spectrum.

bottom left corner of the matrix as a correlation pattern between the first 6 bins.

238U total covariance matrix
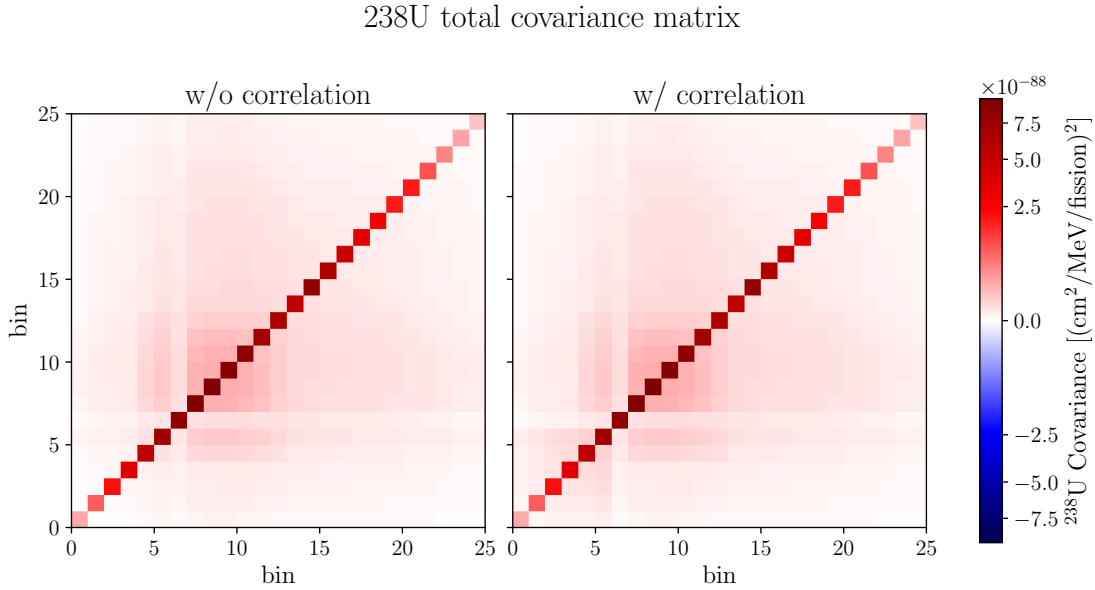
Figure A.7. Covariance matrices for ^{238}U without partial correlation (left) and with partial correlation (right).

To check the impact of the partial correlation to the uncertainty budget, 10k ToyMC spectra were generated for both matrices of Fig. A.7. The heat maps of the generated spectra are shown in Fig. A.8 for the matrix without partial correlation, on the left, and with partial correlation, on the right. The two matrices seem to produce the same uncertainty band. As a reference, the Asimov dataset is also shown in black dots.

Following the same procedure done for the comparison of the different interpolation methods in section 3.5.3, we evaluate the 16-th, median, and 84-th percentile curves for the two datasets. Finally, a comparison of the curves from the two matrices is presented in Fig. A.9: the 16-th percentile on the left, the median in the middle, and the 84-th percentile on the right. Solid lines correspond to the dataset obtained without the inclusion of the partial correlation, while dashed lines correspond to the dataset with this additional contribution. It can be seen that the relative difference, displayed in the bottom panels, is below 1% for all three curves in the whole energy range. Furthermore, the difference at low energies, where this contribution should have an impact, is lower than at high energies, where relative uncertainties are higher.

We can conclude that the partial correlation of the contribution from the nuclear databases to the ^{238}U uncertainty budget has a negligible impact, thus not affecting the study done in section 3.5.3.
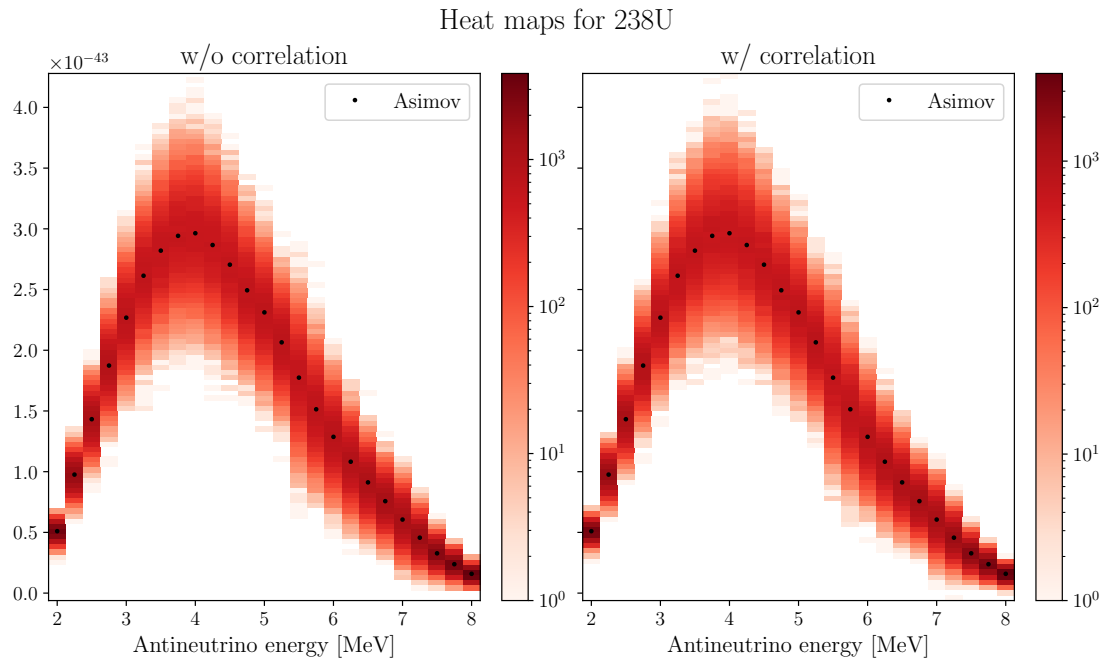
Figure A.8. Heat maps evaluated from the generated spectra for ^{238}U with the covariance matrix without partial correlation (left) and with the matrix with partial correlation (right). The Asimov spectrum is also shown.
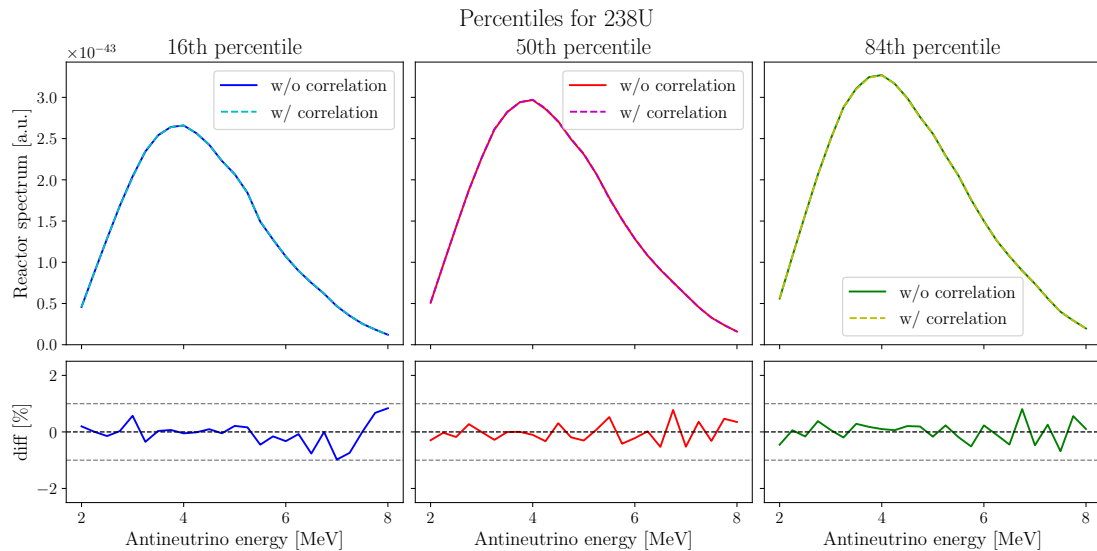
Figure A.9. Comparison of the 16-th (left), 50-th (middle), and 84-th (right) percentile curves for ^{238}U between the covariance matrices without (solid lines) and with (dashed lines) the partial correlation. In the bottom panels, the relative difference is displayed.

Appendix B

Geant4-based model of the light emission: Supplemental material

Supplemental material to the modelling of the scintillation light emission in a liquid scintillator of chapter 4 is now presented.

B.1 Liquid scintillator composition and parameters in the stand-alone Geant4 framework

The composition of JUNO liquid scintillator mixture is listed in Table B.1, while Table B.2 summarizes some of its properties.

Table B.1. Composition of JUNO liquid scintillator, inherited from the Daya Bay experiment.

Element	Concentration [%]
C	0.87924
H	0.1201
O	0.00034
N	0.00027
S	0.00005

Table B.2. Properties of JUNO liquid scintillator, as defined in Geant4.

Property	Value
Density	$0.859 \, \mathrm{g/cm^3}$
Radiation length	$51.667 \, \mathrm{cm}$
Nuclear interaction length	$80.778 \, \mathrm{cm}$
Mean ionization energy	$57.890 \, \mathrm{eV}$
Temperature	$293.15 \, \mathrm{K}$
Pressure	$1.00 \, \mathrm{atm}$

B.2 Geant4 production cuts

A cut in the production of secondary particles is introduced in the Geant4 simulation framework for those processes with a divergent cross section at low energies, like ionization and Bremsstrahlung, to reduce the computational time and resources that are needed. The production cut is provided as a distance, which is then converted in a threshold energy based on the particle and the material. The production cuts as threshold energies are listed in Table B.3 for γ, e^-, and e^+ for JUNO liquid scintillator mixture and for various cut lengths.

When a primary particle no longer has enough energy to produce secondary particles which travel at least the given threshold length, the discrete energy loss stops and no more secondaries are produced. Then, the primary particle is tracked down to zero energy using a continuous energy loss; in this way, the correct stopping location of the primary particle is preserved.

The presence of production cuts influences the number and the energy distribution of the secondary particles, as described in the next section.

Table B.3. Production cuts converted from a length threshold to an energy threshold for γ, e^-, and e^+ for JUNO liquid scintillator.

threshold [keV]	$1000\,\mu m$	$100\,\mu m$	$10\,\mu m$	$1\,\mu m$
γ	2.2	$10 \cdot 10^{-3}$	$10 \cdot 10^{-3}$	$10 \cdot 10^{-3}$
e^-	324.7	79.7	11.6	$193.2 \cdot 10^{-3}$
e^+	316.4	78.7	11.4	$191.1 \cdot 10^{-3}$

B.3 Distributions of secondary particles

The number and energy distributions of secondary particles for e^-, γ, and e^+ in JUNO liquid scintillator are now discussed. The production cut is set to $100\,\mu m$ for e^- and e^+ and to $1000\,\mu m$ for γ.

B.3.1 Distributions of secondary particles for e^-

Electrons are simulated at various initial energies: from $0.1\,\mathrm{MeV}$ to $1.0\,\mathrm{MeV}$ with a step of $0.1\,\mathrm{MeV}$, $5.0\,\mathrm{MeV}$, and $10.0\,\mathrm{MeV}$.

Figure B.1a shows the distribution of the number of secondary charged particles produced by the interaction of electrons with JUNO liquid scintillator. The peak on the left is populated by delta-rays produced during the ionization process; the shoulder on the right is populated by low-energy electrons after having undergone Compton scattering by Bremsstrahlung gammas. The energy distribution of the secondary charged particles is shown in Fig. B.1b. The sharp edge at about $80\,\mathrm{keV}$ is due to the production cut on the ionization process, which is set to $100\,\mu m$ (see Table B.3). Below $80\,\mathrm{keV}$, the energy spectrum is populated by electrons undergoing Compton scattering, which has no divergent term at low energy, thus no production cut is applied.

(a) *Number of secondary charged particles.*   **(b)** *Energy of secondary charged particles.*
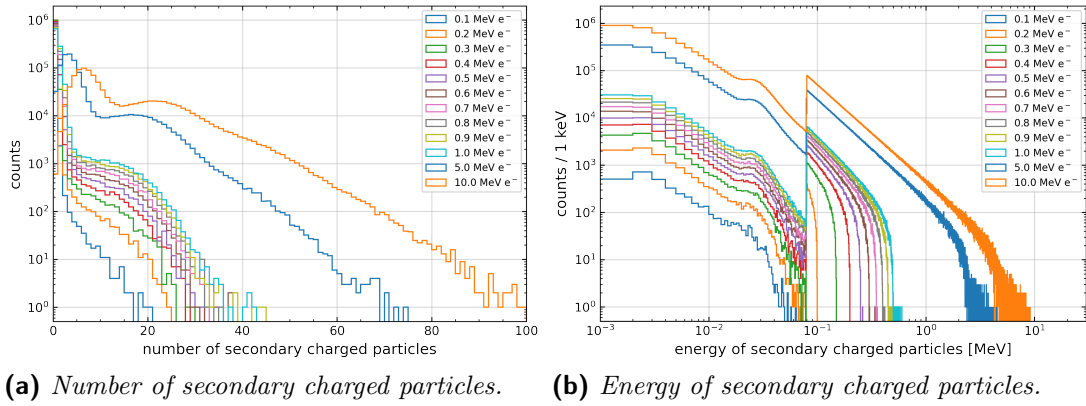
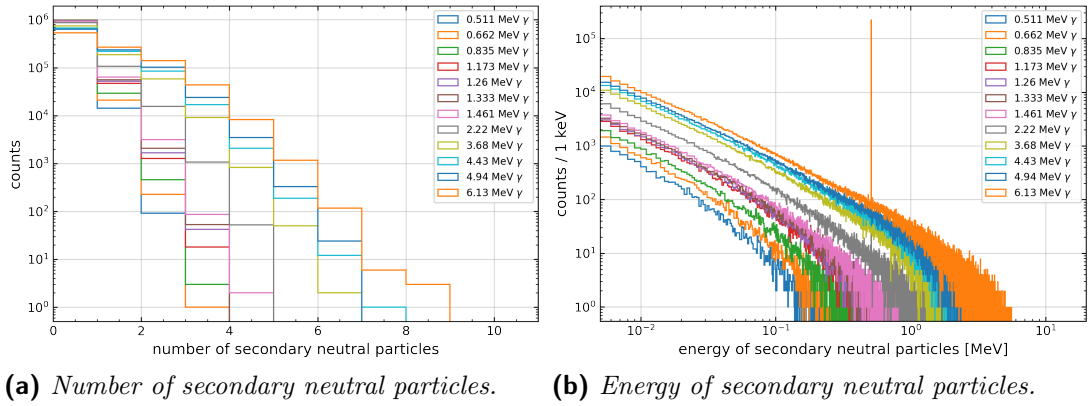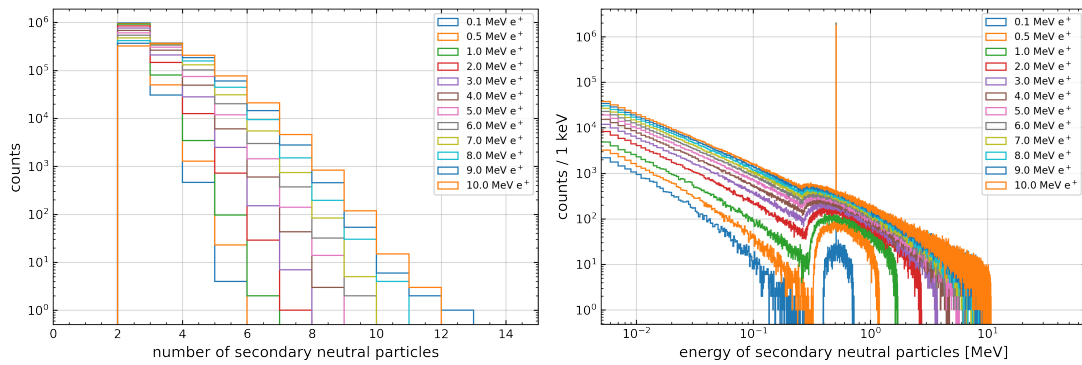**Figure B.1.** **(a)** Distribution of the number and **(b)** energy distribution of secondary charged particles produced by the interaction of electrons with JUNO liquid scintillator, for different values of the electron initial energy.

Figure B.2a shows the distribution of the number of secondary neutral particles produced by the interaction of electrons with JUNO liquid scintillator. The energy distribution of the secondary neutral particles is shown in Fig. B.2b. A production cut is applied also to the Bremsstrahlung process, in fact, a sharp edge similar to the one in Fig. B.1b is visible at about 2 keV, corresponding to a cut of 1000 μm; the region below 2 keV is not populated since gammas are not produced at such low energies in any other processes. For electron initial energy above a few megaelectronvolts, Bremsstrahlung gammas have enough energy to undergo conversion into an electron-positron pair; then, the positron interacts with an electron of the medium producing two annihilation gammas, which are visible in Fig. B.2b as a sharp peak at 511 keV.

(a) *Number of secondary neutral particles.*   **(b)** *Energy of secondary neutral particles.*
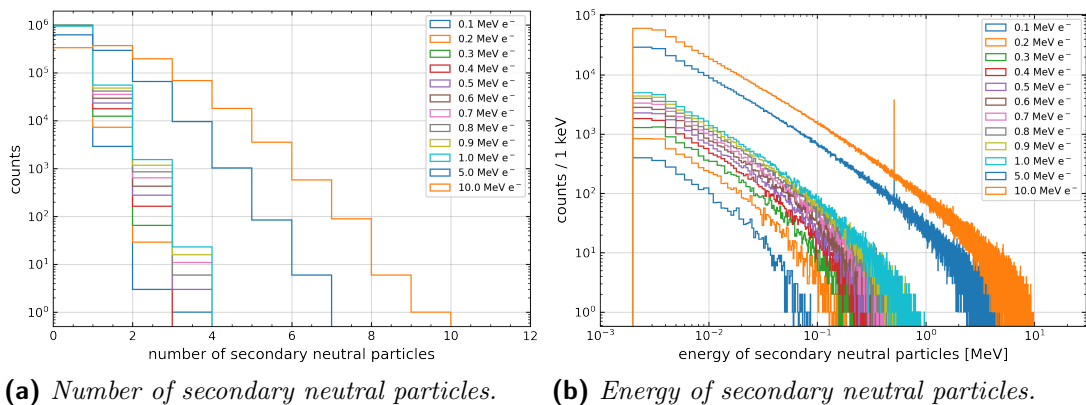
Figure B.2. **(a)** Distribution of the number and **(b)** energy distribution of the secondary neutral particles produced by the interaction of electrons with JUNO liquid scintillator, for different values of the electron initial energy.

B.3.2   Distributions of secondary particles for γ

Gammas are simulated at various initial energies, corresponding to the single γ peaks of JUNO calibration sources, as listed in Table 4.1.

Figure B.3a shows the distribution of the number of secondary charged particles produced by the interaction of gammas with JUNO liquid scintillator. The peak on the left is populated by electrons undergoing Compton scattering by the primary γ. The shoulder on the right arises by the fact that high energy gammas might convert to an electron-positron pair; both the electron and positron produce gammas through Bremsstrahlung, which then undergo Compton scattering producing additional charged secondaries. The energy distribution of the secondary charged particles is shown in Fig. B.1b and was already discussed in section 4.1.
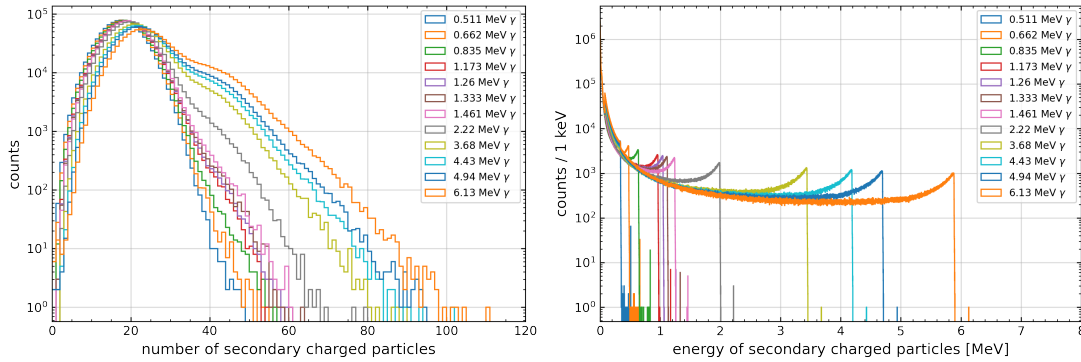
(a) *Number of secondary charged particles.*   **(b)** *Energy of secondary charged particles.*

Figure B.3. **(a)** Distribution of the number and **(b)** energy distribution of secondary charged particles produced by the interaction of gammas with JUNO liquid scintillator, for different values of the gamma initial energy.

Figure B.4a shows the distribution of the number of secondary neutral particles produced by the interaction of gammas with JUNO liquid scintillator. The energy distribution of the secondary neutral particles is shown in Fig. B.4b. Secondary neutral particles are produced by secondary charged particles through Bremsstrahlung. Since high energy gammas can undergo pair production, a sharp peak at 511 keV due to positrons annihilating in the medium is clearly visible.

B.3.3   Distributions of secondary particles for e^+

Positrons are simulated at various initial energies: 0.1 MeV, 0.5 MeV, and from 1.0 MeV to 10.0 MeV with a step of 1.0 MeV.

Figure B.5a shows the distribution of the number of secondary charged particles produced by the interaction of positrons with JUNO liquid scintillator. Charged secondary particles are mainly produced by Compton scattering of the two annihilation gammas; in fact, the peak of the distribution is almost twice the one corresponding to a 511 keV γ shown in Fig. B.3b. At higher energies, the peak shifts towards the right due to additional Bremsstrahlung gammas un-

(a) *Number of secondary neutral particles.*   **(b)** *Energy of secondary neutral particles.*

Figure B.4. **(a)** Distribution of the number and **(b)** energy distribution of the secondary neutral particles produced by the interaction of gammas with JUNO liquid scintillator, for different values of the gamma initial energy.

dergoing Compton scattering. The energy distribution of the secondary charged particles is shown in Fig. B.5b.

(a) *Number of secondary charged particles.*   **(b)** *Energy of secondary charged particles.*
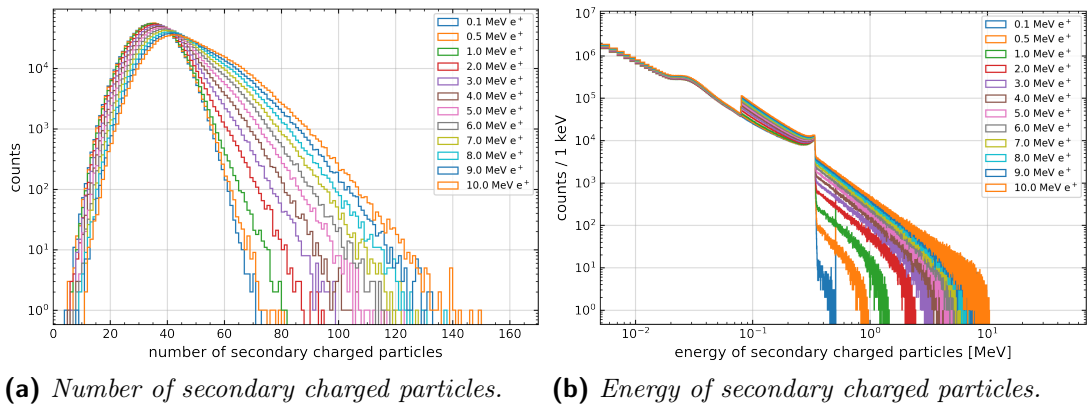
Figure B.5. **(a)** Distribution of the number and **(b)** energy distribution of secondary charged particles produced by the interaction of positrons with JUNO liquid scintillator, for different values of the positron initial kinetic energy.

Figure B.6a shows the distribution of the number of secondary neutral particles produced by the interaction of positrons with JUNO liquid scintillator. Since positrons always annihilate in the medium, there are at least two secondary gammas; other secondary gammas are produced through Bremsstrahlung. The energy distribution of the secondary neutral particles is shown in Fig. B.6b. The peak at 511 keV from the positron annihilation is clearly visible.

(a) *Number of secondary neutral particles.*   **(b)** *Energy of secondary neutral particles.*

Figure B.6. **(a)** Distribution of the number and **(b)** energy distribution of the secondary neutral particles produced by the interaction of positrons with JUNO liquid scintillator, for different values of the positron initial kinetic energy.

Bibliography

[1]   The Nobel Prize in Physics 2015. URL: https://www.nobelprize.org/prizes/physics/2015/press-release/ (visited on 11/20/2023).

[2]   R. L. Workman et al. "Review of Particle Physics". In: *PTEP* 2022 (2022), p. 083C01. DOI: 10.1093/ptep/ptac097.

[3]   John N. Bahcall et al. "Standard Solar Models and the Uncertainties in Predicted Capture Rates of Solar Neutrinos". In: *Rev. Mod. Phys.* 54 (1982), p. 767. DOI: 10.1103/RevModPhys.54.767.

[4]   Raymond Davis Jr. et al. "Search for neutrinos from the sun". In: *Phys. Rev. Lett.* 20 (1968), pp. 1205–1209. DOI: 10.1103/PhysRevLett.20.1205.

[5]   Aldo Serenelli. "Alive and well: A short review about standard solar models". In: *The European Physical Journal A* 52.4 (Apr. 2016). ISSN: 1434-601X. DOI: 10.1140/epja/i2016-16078-1.

[6]   J. N. Abdurashitov et al. "Solar neutrino flux measurements by the Soviet-American Gallium Experiment (SAGE) for half the 22 year solar cycle". In: *J. Exp. Theor. Phys.* 95 (2002), pp. 181–193. DOI: 10.1134/1.1506424. arXiv: astro-ph/0204245.

[7]   W. Hampel et al. "GALLEX solar neutrino observations: Results for GALLEX IV". In: *Phys. Lett. B* 447 (1999), pp. 127–133. DOI: 10.1016/S0370-2693(98)01579-2.

[8]   K. S. Hirata et al. "Observation of B-8 Solar Neutrinos in the Kamiokande-II Detector". In: *Phys. Rev. Lett.* 63 (1989), p. 16. DOI: 10.1103/PhysRevLett.63.16.

[9]   Y. Fukuda et al. "Measurements of the solar neutrino flux from Super-Kamiokande's first 300 days". In: *Phys. Rev. Lett.* 81 (1998). [Erratum: Phys.Rev.Lett. 81, 4279 (1998)], pp. 1158–1162. DOI: 10.1103/PhysRevLett.81.1158. arXiv: hep-ex/9805021.

[10]   K. Abe et al. "Solar Neutrino Measurements in Super-Kamiokande-IV". In: *Phys. Rev. D* 94.5 (2016), p. 052010. DOI: 10.1103/PhysRevD.94.052010. arXiv: 1606.07538 [hep-ex].

[11]   Q. R. Ahmad et al. "Direct evidence for neutrino flavor transformation from neutral current interactions in the Sudbury Neutrino Observatory". In: *Phys. Rev. Lett.* 89 (2002), p. 011301. DOI: 10.1103/PhysRevLett.89.011301. arXiv: nucl-ex/0204008.

[12]   M. Agostini et al. "Comprehensive measurement of pp-chain solar neutrinos". In: *Nature* 562.7728 (2018), pp. 505–510. DOI: 10.1038/s41586-018-0624-y.

[13]   D. Basilico et al. "Final results of Borexino on CNO solar neutrinos". In: *Phys. Rev. D* 108.10 (2023), p. 102005. DOI: 10.1103/PhysRevD.108.102005. arXiv: 2307.14636 [hep-ex].

[14]   M. Agostini et al. "First Simultaneous Precision Spectroscopy of pp, ^{7}Be, and pep Solar Neutrinos with Borexino Phase-II". In: *Phys. Rev. D* 100.8 (2019), p. 082004. DOI: 10.1103/PhysRevD.100.082004. arXiv: 1707.09279 [hep-ex].

[15]   M. Agostini et al. "Improved measurement of ^{8}B solar neutrinos with 1.5 kt·y of Borexino exposure". In: *Phys. Rev. D* 101.6 (2020), p. 062001. DOI: 10.1103/PhysRevD.101.062001. arXiv: 1709.00756 [hep-ex].

[16]   K. S. Hirata et al. "Observation of a small atmospheric muon-neutrino / electron-neutrino ratio in Kamiokande". In: *Phys. Lett. B* 280 (1992), pp. 146–152. DOI: 10.1016/0370-2693(92)90788-6.

[17]   Y. Fukuda et al. "Evidence for oscillation of atmospheric neutrinos". In: *Phys. Rev. Lett.* 81 (1998), pp. 1562–1567. DOI: 10.1103/PhysRevLett.81.1562. arXiv: hep-ex/9807003.

[18]   N. Agafonova et al. "Final Results of the OPERA Experiment on ν_τ Appearance in the CNGS Neutrino Beam". In: *Phys. Rev. Lett.* 120.21 (2018). [Erratum: Phys.Rev.Lett. 121, 139901 (2018)], p. 211801. DOI: 10.1103/PhysRevLett.120.211801. arXiv: 1804.04912 [hep-ex].

[19]   K. Eguchi et al. "First results from KamLAND: Evidence for reactor antineutrino disappearance". In: *Phys. Rev. Lett.* 90 (2003), p. 021802. DOI: 10.1103/PhysRevLett.90.021802. arXiv: hep-ex/0212021.

[20]   A. Gando et al. "Reactor On-Off Antineutrino Measurement with KamLAND". In: *Phys. Rev. D* 88.3 (2013), p. 033001. DOI: 10.1103/PhysRevD.88.033001. arXiv: 1303.4667 [hep-ex].

[21]   F. P. An et al. "Observation of electron-antineutrino disappearance at Daya Bay". In: *Phys. Rev. Lett.* 108 (2012), p. 171803. DOI: 10.1103/PhysRevLett.108.171803. arXiv: 1203.1669 [hep-ex].

[22]   Y. Abe et al. "Indication of Reactor $\bar{\nu}_e$ Disappearance in the Double Chooz Experiment". In: *Phys. Rev. Lett.* 108 (2012), p. 131801. DOI: 10.1103/PhysRevLett.108.131801. arXiv: 1112.6353 [hep-ex].

[23]   J. K. Ahn et al. "Observation of Reactor Electron Antineutrino Disappearance in the RENO Experiment". In: *Phys. Rev. Lett.* 108 (2012), p. 191802. DOI: 10.1103/PhysRevLett.108.191802. arXiv: 1204.0626 [hep-ex].

[24]   D. Adey et al. "Measurement of the Electron Antineutrino Oscillation with 1958 Days of Operation at Daya Bay". In: *Phys. Rev. Lett.* 121.24 (2018), p. 241805. DOI: 10.1103/PhysRevLett.121.241805. arXiv: 1809.02261 [hep-ex].

[25]   Steve Boyd. *Lecture notes on Neutrino Oscillations*. May 2016.

[26]   Ivan Esteban et al. "The fate of hints: updated global analysis of three-flavor neutrino oscillations". In: *JHEP* 09 (2020), p. 178. DOI: `10.1007/JHEP09(2020)178`. arXiv: `2007.14792 [hep-ph]`.

[27]   Ivan Esteban et al. *NuFIT 5.2*. 2022. URL: `http://www.nu-fit.org/`.

[28]   Amir N. Khan et al. "Why matter effects matter for JUNO". In: *Phys. Lett. B* 803 (2020), p. 135354. DOI: `10.1016/j.physletb.2020.135354`. arXiv: `1910.12900 [hep-ph]`.

[29]   Angel Abusleme et al. "Sub-percent precision measurement of neutrino oscillation parameters with JUNO". In: *Chin. Phys. C* 46.12 (2022), p. 123001. DOI: `10.1088/1674-1137/ac8bc9`. arXiv: `2204.13249 [hep-ex]`.

[30]   Fengpeng An et al. "Neutrino Physics with JUNO". In: *J. Phys. G* 43.3 (2016), p. 030401. DOI: `10.1088/0954-3899/43/3/030401`. arXiv: `1507.05613 [physics.ins-det]`.

[31]   Angel Abusleme et al. "JUNO physics and detector". In: *Prog. Part. Nucl. Phys.* 123 (2022), p. 103927. DOI: `10.1016/j.ppnp.2021.103927`. arXiv: `2104.02565 [hep-ex]`.

[32]   Zelimir Djurcic et al. "JUNO Conceptual Design Report". In: (Aug. 2015). arXiv: `1508.07166 [physics.ins-det]`.

[33]   F. P. An et al. "The muon system of the Daya Bay Reactor antineutrino experiment". In: *Nucl. Instrum. Meth. A* 773 (2015), pp. 8–20. DOI: `10.1016/j.nima.2014.09.070`. arXiv: `1407.0275 [physics.ins-det]`.

[34]   Dewen Cao et al. "Light Absorption Properties of the High Quality Linear Alkylbenzene for the JUNO Experiment". In: *Nucl. Instrum. Meth. A* 927 (2019), pp. 230–235. DOI: `10.1016/j.nima.2019.01.077`. arXiv: `1801.08363 [physics.ins-det]`.

[35]   A. Abusleme et al. "Optimization of the JUNO liquid scintillator composition using a Daya Bay antineutrino detector". In: *Nucl. Instrum. Meth. A* 988 (2021), p. 164823. DOI: `10.1016/j.nima.2020.164823`. arXiv: `2007.00314 [physics.ins-det]`.

[36]   Angel Abusleme et al. "The design and sensitivity of JUNO's scintillator radiopurity pre-detector OSIRIS". In: *Eur. Phys. J. C* 81.11 (2021), p. 973. DOI: `10.1140/epjc/s10052-021-09544-4`. arXiv: `2103.16900 [physics.ins-det]`.

[37]   Angel Abusleme et al. "The JUNO experiment Top Tracker". In: *Nucl. Instrum. Meth. A* 1057 (2023), p. 168680. DOI: `10.1016/j.nima.2023.168680`. arXiv: `2303.05172 [hep-ex]`.

[38]   T. Adam et al. "The OPERA experiment target tracker". In: *Nucl. Instrum. Meth. A* 577 (2007), pp. 523–539. DOI: `10.1016/j.nima.2007.04.147`. arXiv: `physics/0701153`.

[39]   Liang-Jian Wen et al. "A quantitative approach to select PMTs for large detectors". In: *Nucl. Instrum. Meth. A* 947 (2019), p. 162766. DOI: `10.1016/j.nima.2019.162766`. arXiv: `1903.12595 [physics.ins-det]`.

[40]   Angel Abusleme et al. "Mass testing and characterization of 20-inch PMTs
       for JUNO". In: *Eur. Phys. J. C* 82.12 (2022), p. 1168. DOI: 10.1140/epjc/
       s10052-022-11002-8. arXiv: 2205.08629 [physics.ins-det].

[41]   Chuanya Cao et al. "Mass production and characterization of 3-inch PMTs
       for the JUNO experiment". In: *Nucl. Instrum. Meth. A* 1005 (2021), p. 165347.
       DOI: 10.1016/j.nima.2021.165347. arXiv: 2102.11538 [physics.ins-det].

[42]   Angel Abusleme et al. "Calibration Strategy of the JUNO Experiment".
       In: *JHEP* 03 (2021), p. 004. DOI: 10.1007/JHEP03(2021)004. arXiv:
       2011.06405 [physics.ins-det].

[43]   Jiaqi Hui et al. "The automatic calibration unit in JUNO". In: *JINST*
       16.08 (2021), T08008. DOI: 10.1088/1748-0221/16/08/T08008. arXiv:
       2104.02579 [physics.ins-det].

[44]   Yuanyuan Zhang et al. "Laser Calibration System in JUNO". In: *JINST*
       14.01 (2019), P01009. DOI: 10.1088/1748-0221/14/01/P01009. arXiv:
       1811.00354 [physics.ins-det].

[45]   Yuanyuan Zhang et al. "Cable loop calibration system for Jiangmen Un-
       derground Neutrino Observatory". In: *Nucl. Instrum. Meth. A* 988 (2021),
       p. 164867. DOI: 10.1016/j.nima.2020.164867. arXiv: 2011.02183
       [physics.ins-det].

[46]   Yuhang Guo et al. "Design of the Guide Tube Calibration System for the
       JUNO experiment". In: *JINST* 14.09 (2019), T09005. DOI: 10.1088/1748-
       0221/14/09/T09005. arXiv: 1905.02077 [physics.ins-det].

[47]   K. Feng et al. "A novel remotely operated vehicle as the calibration system
       in JUNO". In: *JINST* 13.12 (2018), T12001. DOI: 10.1088/1748-0221/
       13/12/T12001.

[48]   Yang Han. "Dual Calorimetry for High Precision Neutrino Oscillation Mea-
       surement at JUNO Experiment". PhD thesis. Université Paris Cité, France,
       2020. URL: https://theses.hal.science/tel-03295420.

[49]   Yu-Feng Li et al. "Unambiguous Determination of the Neutrino Mass Hi-
       erarchy Using Reactor Neutrinos". In: *Phys. Rev. D* 88 (2013), p. 013008.
       DOI: 10.1103/PhysRevD.88.013008. arXiv: 1303.6733 [hep-ex].

[50]   G. Mention et al. "The Reactor Antineutrino Anomaly". In: *Phys. Rev.
       D* 83 (2011), p. 073006. DOI: 10.1103/PhysRevD.83.073006. arXiv:
       1101.2755 [hep-ex].

[51]   Feng Peng An et al. "Measurement of the Reactor Antineutrino Flux
       and Spectrum at Daya Bay". In: *Phys. Rev. Lett.* 116.6 (2016). [Erratum:
       Phys.Rev.Lett. 118, 099902 (2017)], p. 061801. DOI: 10.1103/PhysRevLett.
       116.061801. arXiv: 1508.04233 [hep-ex].

[52]   Y. J. Ko et al. "Sterile Neutrino Search at the NEOS Experiment". In:
       Phys. Rev. Lett. 118.12 (2017), p. 121802. DOI: 10.1103/PhysRevLett.
       118.121802. arXiv: 1610.05134 [hep-ex].

[53] G. Bak et al. "Measurement of Reactor Antineutrino Oscillation Amplitude and Frequency at RENO". In: *Phys. Rev. Lett.* 121.20 (2018), p. 201801. DOI: 10.1103/PhysRevLett.121.201801. arXiv: 1806.00248 [hep-ex].

[54] H. de Kerret et al. "Double Chooz θ_{13} measurement via total neutron capture detection". In: *Nature Phys.* 16.5 (2020), pp. 558–564. DOI: 10.1038/s41567-020-0831-y. arXiv: 1901.09445 [hep-ex].

[55] Angel Abusleme et al. "TAO Conceptual Design Report: A Precision Measurement of the Reactor Antineutrino Spectrum with Sub-percent Energy Resolution". In: (May 2020). arXiv: 2005.08745 [physics.ins-det].

[56] The JUNO collaboration. *Prospects for identifying the neutrino mass ordering with reactor antineutrinos in JUNO*. Paper in preparation.

[57] Angel Abusleme et al. "JUNO sensitivity to ^{7}Be, pep, and CNO solar neutrinos". In: *JCAP* 10 (2023), p. 022. DOI: 10.1088/1475-7516/2023/10/022. arXiv: 2303.03910 [hep-ex].

[58] Angel Abusleme et al. "Feasibility and physics potential of detecting ^{8}B solar neutrinos at JUNO". In: *Chin. Phys. C* 45.2 (2021), p. 023004. DOI: 10.1088/1674-1137/abd92a. arXiv: 2006.11760 [hep-ex].

[59] Jie Zhao et al. "Model Independent Approach of the JUNO ^{8}B Solar Neutrino Program". In: (Oct. 2022). arXiv: 2210.08437 [hep-ex].

[60] Angel Abusleme et al. "JUNO sensitivity to low energy atmospheric neutrino spectra". In: *Eur. Phys. J. C* 81 (2021), p. 10. DOI: 10.1140/epjc/s10052-021-09565-z. arXiv: 2103.09908 [hep-ex].

[61] Angel Abusleme et al. "Real-time monitoring for the next core-collapse supernova in JUNO". In: *JCAP* 01 (2024), p. 057. DOI: 10.1088/1475-7516/2024/01/057. arXiv: 2309.07109 [hep-ex].

[62] Angel Abusleme et al. "Prospects for detecting the diffuse supernova neutrino background with JUNO". In: *JCAP* 10 (2022), p. 033. DOI: 10.1088/1475-7516/2022/10/033. arXiv: 2205.08830 [hep-ex].

[63] Angel Abusleme et al. "JUNO sensitivity to the annihilation of MeV dark matter in the galactic halo". In: *JCAP* 09 (2023), p. 001. DOI: 10.1088/1475-7516/2023/09/001. arXiv: 2306.09567 [hep-ex].

[64] Angel Abusleme et al. "JUNO sensitivity on proton decay $p \to \nu K^+$ searches*". In: *Chin. Phys. C* 47.11 (2023), p. 113002. DOI: 10.1088/1674-1137/ace9c6. arXiv: 2212.08502 [hep-ex].

[65] Jun Wang et al. "Damping signatures at JUNO, a medium-baseline reactor neutrino oscillation experiment". In: *JHEP* 06 (2022), p. 062. DOI: 10.1007/JHEP06(2022)062. arXiv: 2112.14450 [hep-ex].

[66] X. B. Ma et al. "Improved calculation of the energy release in neutron-induced fission". In: *Phys. Rev. C* 88.1 (2013), p. 014605. DOI: 10.1103/PhysRevC.88.014605. arXiv: 1212.6625 [nucl-ex].

[67] F. P. An et al. "Antineutrino energy spectrum unfolding based on the Daya Bay measurement and its applications". In: *Chin. Phys. C* 45.7 (2021), p. 073001. DOI: 10.1088/1674-1137/abfc38. arXiv: 2102.04614 [hep-ex].

[68] Alessandro Strumia et al. "Precise quasielastic neutrino/nucleon cross-section". In: *Phys. Lett. B* 564 (2003), pp. 42–54. DOI: 10.1016/S0370-2693(03)00616-6. arXiv: astro-ph/0302055.

[69] K. Schreckenbach et al. "Absolute measurement of the beta spectrum from 235 U fission as a basis for reactor antineutrino experiments". In: *Phys. Lett. B* 99 (1981), pp. 251–256. DOI: 10.1016/0370-2693(81)91120-5.

[70] F. Von Feilitzsch et al. "Experimental beta spectra from Pu-239 and U-235 thermal neutron fission products and their correlated anti-neutrinos spectra". In: *Phys. Lett. B* 118 (1982), pp. 162–166. DOI: 10.1016/0370-2693(82)90622-0.

[71] K. Schreckenbach et al. "Determination of the anti-neutrino spectrum from U-235 thermal neutron fission products up to 9.5 MeV". In: *Phys. Lett. B* 160 (1985), pp. 325–330. DOI: 10.1016/0370-2693(85)91337-1.

[72] A. A. Hahn et al. "Anti-neutrino Spectra From ^{241}Pu and ^{239}Pu Thermal Neutron Fission Products". In: *Phys. Lett. B* 218 (1989), pp. 365–368. DOI: 10.1016/0370-2693(89)91598-0.

[73] Patrick Huber. "On the determination of anti-neutrino spectra from nuclear reactors". In: *Phys. Rev. C* 84 (2011). [Erratum: Phys.Rev.C 85, 029901 (2012)], p. 024617. DOI: 10.1103/PhysRevC.85.029901. arXiv: 1106.0687 [hep-ph].

[74] URL: https://universe-review.ca/F14-nucleus04.htm.

[75] Th. A. Mueller et al. "Improved Predictions of Reactor Antineutrino Spectra". In: *Phys. Rev. C* 83 (2011), p. 054615. DOI: 10.1103/PhysRevC.83.054615. arXiv: 1101.2663 [hep-ex].

[76] N. Haag et al. "Experimental Determination of the Antineutrino Spectrum of the Fission Products of ^{238}U". In: *Phys. Rev. Lett.* 112.12 (2014), p. 122501. DOI: 10.1103/PhysRevLett.112.122501. arXiv: 1312.5601 [nucl-ex].

[77] V. I. Kopeikin et al. "Measurement of the Ratio of Cumulative Spectra of Beta Particles from ^{235}U and ^{239}Pu Fission Products for Solving Problems of Reactor-Antineutrino Physics". In: *Phys. Atom. Nucl.* 84.1 (2021), pp. 1–10. DOI: 10.1134/S1063778821010129.

[78] V. Kopeikin et al. "Reevaluating reactor antineutrino spectra with new measurements of the ratio between ^{235}U and ^{239}Pu β spectra". In: *Phys. Rev. D* 104.7 (2021), p. L071301. DOI: 10.1103/PhysRevD.104.L071301. arXiv: 2103.01684 [nucl-ex].

[79] V. I. Kopeikin. "Flux and spectrum of reactor antineutrinos". In: *Phys. Atom. Nucl.* 75 (2012), pp. 143–152. DOI: 10.1134/S1063778812020123.

[80] M. Estienne et al. "Updated Summation Model: An Improved Agreement with the Daya Bay Antineutrino Fluxes". In: *Phys. Rev. Lett.* 123.2 (2019), p. 022502. DOI: 10.1103/PhysRevLett.123.022502. arXiv: 1904.09358 [nucl-ex].

[81] D. Adey et al. "Extraction of the ^{235}U and ^{239}Pu Antineutrino Spectra at Daya Bay". In: *Phys. Rev. Lett.* 123.11 (2019), p. 111801. DOI: 10.1103/PhysRevLett.123.111801. arXiv: 1904.07812 [hep-ex].

[82] F. P. An et al. "Joint Determination of Reactor Antineutrino Spectra from ^{235}U and ^{239}Pu Fission by Daya Bay and PROSPECT". In: *Phys. Rev. Lett.* 128.8 (2022), p. 081801. DOI: 10.1103/PhysRevLett.128.081801. arXiv: 2106.12251 [nucl-ex].

[83] H. Almazán et al. "Joint Measurement of the ^{235}U Antineutrino Spectrum by Prospect and Stereo". In: *Phys. Rev. Lett.* 128.8 (2022), p. 081802. DOI: 10.1103/PhysRevLett.128.081802. arXiv: 2107.03371 [nucl-ex].

[84] Feng Peng An et al. "Improved Measurement of the Reactor Antineutrino Flux and Spectrum at Daya Bay". In: *Chin. Phys. C* 41.1 (2017), p. 013002. DOI: 10.1088/1674-1137/41/1/013002. arXiv: 1607.05378 [hep-ex].

[85] F. P. An et al. "Improved Measurement of the Evolution of the Reactor Antineutrino Flux and Spectrum at Daya Bay". In: *Phys. Rev. Lett.* 130.21 (2023), p. 211801. DOI: 10.1103/PhysRevLett.130.211801. arXiv: 2210.01068 [hep-ex].

[86] *Operating Experience with Nuclear Power Stations in Member States*. Operating Experience with Nuclear Power Stations in Member States. Vienna: INTERNATIONAL ATOMIC ENERGY AGENCY, 2021. URL: https://www.iaea.org/publications/15004/operating-experience-with-nuclear-power-stations-in-member-states.

[87] F. P. An et al. "Evolution of the Reactor Antineutrino Flux and Spectrum at Daya Bay". In: *Phys. Rev. Lett.* 118.25 (2017), p. 251801. DOI: 10.1103/PhysRevLett.118.251801. arXiv: 1704.01082 [hep-ex].

[88] D. Adey et al. "A high precision calibration of the nonlinear energy response at Daya Bay". In: *Nucl. Instrum. Meth. A* 940 (2019), pp. 230–242. DOI: 10.1016/j.nima.2019.06.031. arXiv: 1902.08241 [physics.ins-det].

[89] Philipp Kampmann et al. "A semi-analytical energy response model for low-energy events in JUNO". In: *JINST* 15.10 (2020), P10007. DOI: 10.1088/1748-0221/15/10/P10007. arXiv: 2006.03461 [physics.ins-det].

[90] Miao Yu et al. "A universal energy response model for determining the energy nonlinearity and resolution of $e^{\pm}$ and γ in liquid scintillator detectors". In: *Eur. Phys. J. C* 83.5 (2023), p. 403. DOI: 10.1140/epjc/s10052-023-11541-8. arXiv: 2211.02467 [hep-ex].

[91] S. Agostinelli et al. "Geant4 — A simulation toolkit". In: *Nuclear Instruments and Methods in Physics Research Section A: Accelerators, Spectrometers, Detectors and Associated Equipment* 506.3 (2003), pp. 250–303. ISSN: 0168-9002. DOI: https://doi.org/10.1016/S0168-9002(03)01368-8.

[92] J. Allison et al. "Geant4 developments and applications". In: *IEEE Transactions on Nuclear Science* 53.1 (2006), pp. 270–278. DOI: 10.1109/TNS.2006.869826.

[93] J. Allison et al. "Recent developments in Geant4". In: *Nuclear Instruments and Methods in Physics Research Section A: Accelerators, Spectrometers, Detectors and Associated Equipment* 835 (2016), pp. 186–225. ISSN: 0168-9002. DOI: https://doi.org/10.1016/j.nima.2016.06.125.

[94] Martin Berger et al. *ESTAR, PSTAR, and ASTAR: Computer Programs for Calculating Stopping-Power and Range Tables for Electrons, Protons, and Helium Ions (version 1.21)*. Jan. 1999. URL: http://physics.nist.gov/Star.

[95] M.J. Berger et al. *XCOM: Photon Cross Sections Database*. 1998. URL: https://www.nist.gov/pml/xcom-photon-cross-sections-database.

[96] F. Capozzi et al. "Neutrino mass hierarchy and electron neutrino oscillation parameters with one hundred thousand reactor events". In: *Phys. Rev. D* 89.1 (2014), p. 013001. DOI: 10.1103/PhysRevD.89.013001. arXiv: 1309.1638 [hep-ph].

[97] J. B. Birks. "Scintillations from Organic Crystals: Specific Fluorescence and Relative Response to Different Radiations". In: *Proc. Phys. Soc. A* 64 (1951), pp. 874–877. DOI: 10.1088/0370-1298/64/10/303.

[98] I. M. Frank et al. "Coherent visible radiation of fast electrons passing through matter". In: *Compt. Rend. Acad. Sci. URSS* 14.3 (1937), pp. 109–114. DOI: 10.3367/UFNr.0093.196710o.0388.

[99] The JUNO collaboration. *Prediction of energy resolution in the JUNO experiment*. Paper in preparation.

[100] M.-M. Bé et al. *Table of Radionuclides*. Vol. 8. Monographie BIPM-5. Pavillon de Breteuil, F-92310 Sèvres, France: Bureau International des Poids et Mesures, 2016. ISBN: 978-92-822-2264-5. URL: http://www.bipm.org/utils/common/pdf/monographieRI/Monographie_BIPM-5_Tables_Vol8.pdf.

[101] Debertin, K. and Helmer, R.G. "Gamma- and X-ray spectrometry with semiconductor detectors". In: Netherlands: North-Holland, 1988. Chap. 3.

[102] Rosa Maria Guizzetti. "Studio della risposta del rivelatore JUNO alle sorgenti di calibrazione e determinazione degli effetti di non linearità nella ricostruzione di energia". Bachelor's thesis, University of Padua, Italy. 2022. URL: https://hdl.handle.net/20.500.12608/35406.

[103] M. Bellato et al. "Embedded readout electronics R&D; for the large PMTs in the JUNO experiment". In: *Nucl. Instrum. Meth. A* 985 (2021), p. 164600. DOI: 10.1016/j.nima.2020.164600. arXiv: 2003.08339 [physics.ins-det].

[104] The JUNO collaboration. *The JUNO experiment large-PMT read-out and trigger electronics.* Paper in preparation.

[105] Andrea Serafini. "The JUNO large PMT readout electronics". In: *Nucl. Instrum. Meth. A* 1043 (2022), p. 167499. DOI: 10.1016/j.nima.2022.167499.

[106] Alberto Coppi. "Design and development of Data Quality Monitoring protocols for the integration tests of the JUNO large PMT electronics". Bachelor's thesis, University of Padua, Italy. 2021. URL: https://hdl.handle.net/20.500.12608/1067.

[107] Riccardo Triozzi. "Mass testing of Large-PMT electronics at Kunshan for the JUNO experiment". In: *PoS* ICHEP2022 (Nov. 2022), p. 1062. DOI: 10.22323/1.414.1062.

[108] Alberto Coppi et al. "Mass testing of the JUNO experiment 20-inch PMT readout electronics". In: *Nucl. Instrum. Meth. A* 1052 (2023), p. 168255. DOI: 10.1016/j.nima.2023.168255. arXiv: 2301.04379 [physics.ins-det].

[109] Vanessa Cerrone et al. "Validation and integration tests of the JUNO 20-inch PMT readout electronics". In: *Nucl. Instrum. Meth. A* 1053 (2023), p. 168322. DOI: 10.1016/j.nima.2023.168322. arXiv: 2212.08454 [physics.ins-det].

[110] Filippo Marini. "Development and Testing of the large PMTs Front-End Electronics for the JUNO Experiment". PhD thesis. University of Padua, Italy, 2021. URL: https://hdl.handle.net/11577/3443916.

[111] Riccardo Triozzi et al. "Implementation and performances of the IPbus protocol for the JUNO Large-PMT readout electronics". In: *Nucl. Instrum. Meth. A* 1053 (2023), p. 168339. DOI: 10.1016/j.nima.2023.168339. arXiv: 2302.10133 [physics.ins-det].

[112] D. Pedretti et al. "Nanoseconds Timing System Based on IEEE 1588 FPGA Implementation". In: *IEEE Transactions on Nuclear Science* 66.7 (2019), pp. 1151–1158. DOI: 10.1109/TNS.2019.2906045.

[113] C. Ghabrous Larrea et al. "IPbus: a flexible Ethernet-based control system for xTCA hardware". In: *JINST* 10.02 (2015), p. C02019. DOI: 10.1088/1748-0221/10/02/C02019.

[114] Vanessa Cerrone. "Characterization of the final read-out electronics for the large PMTs of the JUNO experiment". Bachelor's thesis, University of Padua, Italy. 2021. URL: https://hdl.handle.net/20.500.12608/936.

[115] Rene Brun et al. "ROOT - An Object Oriented Data Analysis Framework". In: *Nucl. Inst. & Meth. in Phys. Res. A* 389 (1996). Proceedings AIHENP'96 Workshop, Lausanne, Sep. 1996, pp. 81–86.

[116] Xilinx. *Kintex-7 FPGAs Data Sheet: DC and AC Switching Characteristics*. 2021. URL: https://docs.xilinx.com/v/u/en-US/ds182_Kintex_7_Data_Sheet.pdf.

[117] Angel Abusleme et al. "Radioactivity control strategy for the JUNO detector". In: *JHEP* 11 (2021), p. 102. DOI: 10.1007/JHEP11(2021)102. arXiv: 2107.03669 [physics.ins-det].

[118] Feng Peng An et al. "Measurement of electron antineutrino oscillation based on 1230 days of operation of the Daya Bay experiment". In: *Phys. Rev. D* 95.7 (2017), p. 072006. DOI: 10.1103/PhysRevD.95.072006. arXiv: 1610.04802 [hep-ex].

[119] Vanessa Cerrone. "Probing the atmospheric mass splitting with reactor antineutrino oscillations at JUNO". Master's thesis, University of Padua, Italy. 2023. URL: https://hdl.handle.net/20.500.12608/48924.

[120] Xiangpan Ji et al. "Combined Neyman–Pearson chi-square: An improved approximation to the Poisson-likelihood chi-square". In: *Nucl. Instrum. Meth. A* 961 (2020), p. 163677. DOI: 10.1016/j.nima.2020.163677. arXiv: 1903.07185 [physics.data-an].

[121] Hans Dembinski et al. "scikit-hep/iminuit". In: (Dec. 2020). DOI: 10.5281/zenodo.3949207.

[122] F. James et al. "Minuit: A System for Function Minimization and Analysis of the Parameter Errors and Correlations". In: *Comput. Phys. Commun.* 10 (1975), pp. 343–367. DOI: 10.1016/0010-4655(75)90039-9.

[123] S. Abe et al. "Abundances of uranium and thorium elements in Earth estimated by geoneutrino spectroscopy". In: (May 2022). DOI: 10.1029/2022GL099566. arXiv: 2205.14934 [physics.geo-ph].